MICROFABRICATED ACOUSTIC AND THERMAL FIELD-FLOW FRACTIONATION SYSTEMS

A Thesis
Presented to
The Academic Faculty

by

Thayne L. Edwards

In Partial Fulfillment
Of the Requirements for the Degree
Doctor of Philosophy in the
School of Electrical
and Computer Engineering

Georgia Institute of Technology

May 2005

MICROFABRICATED ACOUSTIC AND THERMAL

FIELD-FLOW FRACTIONATION SYSTEMS

Approved by:

Dr. A. Bruno Frazier, Committee Chair
School of Electrical and Computer Engineering
Georgia Institute of Technology

Dr. John Papapolymerou
School of Electrical and Computer Engineering
Georgia Institute of Technology

Dr. Faramarz Fekri
School of Electrical and Computer Engineering
Georgia Institute of Technology

Dr. Mark G. Allen
School of Electrical and Computer Engineering
Georgia Institute of Technology

Dr. Levent Degertekin
School of Mechanical Engineering
Georgia Institute of Technology

Date Approved:

December 2004

To my wife Amber,

for undying patience, support and love.

ACKNOWLEDGEMENTS

First and foremost I need to thank my family: my wife, Amber, and our two children, Marinda and Ethan. Without their support this project would never have been completed or even started. Amber has been understanding and patient with long hours, late nights, and extended graduation deadlines; not to mention the several endurance trials we faced in Georgia including a car wreck and quite of few illnesses. This dissertation honors her commitment to her husband and children.

Appreciation is given to the other researchers of the Micro Instrumentation Research Lab at Georgia Tech and, initially, at the University of Utah. This gratitude is not only due to the insightful discussions on research topics, without which I would have had great difficulty in completing this project, but, also with regards to friendships made. I would also like to thank my advisor, Bruno Frazier, for providing me with the opportunity to come to Georgia and for encouraging me to complete my doctorate.

Many thanks are due to the staff of the Microelectronics Research Center at Georgia Tech, especially Gary Spinner. Their diligence in maintaining and continually improving the cleanroom is one of the reasons this dissertation is possible.

Finally, I acknowledge God for the talents and knowledge that I possess, which have enabled my progression toward the completion of my life goals.

TABLE OF CONTENTS

LIST OF TABLES

LIST OF FIGURES

LIST OF SYMBOLS

Symbol	Physical Units	Description
F_{Ac}	N	Acoustic force on a small spherical particle
r	m	Radius of spherical particle
k	m^{-1}	Acoustic wave number or propagation factor
$\bar{E}$	J/m^3	Energy density of acoustic field
u	m/s	Particle velocity
ρ', ρ_0	g/m^3	Density of carrier fluid
ρ	g/m^3	Density of particle
λ_a	m	Acoustic wavelength
γ', β	Pa^{-1}	Volumetric compressibility of carrier fluid
γ, β_s	Pa^{-1}	Volumetric compressibility of particle
$f(\gamma,\rho)$	*dimensionless*	Density/compressibility contrast factor
x	m	Distance from transducer face or channel wall.
v_{zone}	m/s	Velocity of a zone of particles of a particular size, density, compressibility, or thermal diffusion coefficient
$\langle v \rangle$	m/s	Average velocity of the carrier fluid.
R	*dimensionless*	Retention parameter
$c(x)$	m^{-3}	Concentration profile of zone of particles of a particular size, density, compressibility, or thermal diffusion coefficient
$\langle c(x) \rangle$	m^{-3}	Mean concentration of particles of a particular size, density, compressibility, or thermal diffusion coefficient
w	m	Fluid channel width (also l, layer thickness)
k_B	J/K	Boltzmann constant (1.380658×10^{-23})
T	K	Fluid channel temperature

Symbol	Physical Units	Description
λ	*dimensionless*	Fraction of channel occupied by particle zones of a particular size, density, compressibility, or thermal diffusion coefficient
F_{max}	N	Maximum acoustic force on a spherical particle
d	m	Diameter of particle
f'	*dimensionless*	Compressibility/density factor associated with high retention assumption
t	s, min	Time
ω	rad/s	Angular frequency of acoustic wave
U, U^+, U^-	m/s	Acoustic velocity standing, forward and backward waves
l	m	Layer thickness
p	Pa	Pressure of acoustic wave
Z_0	Rayl, kg/m^2-s	Material characteristic acoustic impedance
c	m/s	Speed of sound in medium
j	*dimensionless*	Imaginary number, phase indicator, $(-1)^{1/2}$
T	N/m^2	Stress tensor in a medium
S	m/m	Strain tensor in a medium
c	N/m^2	Stiffness matrix
v	m/s	Velocity tensor
∇_s	m/m^4	Strain gradient
Γ	N/m^2	Christoffel matrix
l	*dimensionless*	Direction matrix
Z	Rayl, kg/m^2-s	Acoustic impedance
u_0	m/s	Maximum velocity at transducer face
e	*dimensionless*	Piezoelectric matrix
ε	*dimensionless*	Permittivity matrix
ε_0	F/m	Permittivity of free space (8.8542×10^{-12})
λ_e	N/m^2	Eigen values of Christoffel matrix
v_a	m/s	Acoustic phase velocity
K	*dimensionless*	Piezoelectric coupling constant

Symbol	Physical Units	Description
k_t	*dimensionless*	Piezoelectric coupling coefficient
$\boldsymbol{s}$	s/m	Slowness of an acoustic wave phase (inverse velocity)

SUMMARY

This dissertation presents arguments for miniaturization of a thermal field-flow fractionation system (μ-ThFFF) and fabrication of a micro-scale acoustic field-flow fractionation system (μ-AcFFF) using similar methods. The idea stemmed from a recent advancement in miniaturization of FFF systems, specifically an electrical FFF system. The basis for completion of this work is founded upon history, current scientific needs, and the prospect of advancements beyond current comprehension. This general statement is qualified in the following chapters.

Motivation for miniaturization of ThFFF systems was established by examining the geometrical scaling of the fundamental ThFFF theory. Miniaturization of conventional macro-scale ThFFF systems was made possible through utilization of micromachining technologies. Fabrication of the μ-ThFFF system was discussed in detail. The μ-ThFFF system was characterized for plate height versus flow rate, single component polystyrene retention, and multi-component polystyrene separations. Retention, thermal diffusion coefficients, and maximum diameter-based selectivity values were extracted from separation data and found comparable with macro-scale ThFFF system results. Retention values ranged from 0.33 to 0.46. Thermal diffusion coefficients were between 3.0×10^{-8} and 5.4×10^{-8} $cm^2/sec\cdot K$. The maximum diameter-based selectivity was 1.40.

While the concept of an acoustic FFF sub-technique has been around for decades, the fabrication methods have not been available until recently. The theory was developed in full including relating sample physical properties to retention time in the FFF system. includes acoustic proagation in crystals and amorphous solids. In addition to the theory, the design and fabrication of the μ-AcFFF was presented. Design results from an acoustic modeling program were presented with the determination of the acoustic resonant frequency. The acoustic-based systems was designed around the model results and characterized by electrical input impedance, fluidic, plate height, polystyrene suspension retention, and polystyrene mixture separation studies.

The μ-AcFFF system was able to retain a series of nanometer scale polystyrene samples. However, the retention data did not follow normal mode retention but did reveal the location of the steric inversion point for the power level used, around 200 nm. The results of the multiple component separation confirmed this results as the sample, which contained 110, 210, and 300 nm diameter samples, was not resolved but only broadened.

The experiments performed in this work indicate a feasible method for implementation of the acoustic FFF system and also miniaturization of the thermal FFF system on the microscale. Future work may expand upon the principles and ideas presented herein including characterization of other materials (dissolved polymers, biological materials, environmental samples, etc.), integration with other MEMS devices, and investigation of other FFF fields.

CHAPTER 1

INTRODUCTION

Scope of Work

In this work, surface and bulk micromachining was applied to designing and fabrication of chromatographic separation and purification systems. Micromachining was the term used to refer to this collection of microscale fabrication techniques. Field-flow fractionation was the chromatographic type separation system that was being miniaturized. The basis of separation in a field-flow fractionation (FFF) channel depends upon the subtype used. In particular, the research focuses on two types of field-flow fractionation systems, thermal-based (ThFFF) and acoustic-based (AcFFF).

ThFFF is a powerful separation, analysis and purification tool. Much work has been done in expanding knowledge of this tool; however, there are still many unknowns to be explored and limitations to be overcome. One example of the limitations in using ThFFF is the analysis time. Acquiring data such as thermal diffusion constants for many different samples is very time intensive. Certain advantages are gained as the geometry of the ThFFF channel is scaled down, such as analysis time. These advantages were explored in this thesis by expanding the theory behind ThFFF. The motivations behind designing and fabricating a reduced scale ThFFF system were to reduce analysis time,

reduce the sample size requirement, and build a portable, disposable ThFFF system. The knowledge of microfabrication techniques as well as the knowledge gained from ThFFF theory was applied in designing a micromachined thermal field-flow fractionation (μ-ThFFF).

In contrast to ThFFF, one of the least understood and most recent FFF technique to be investigated is acoustic field-flow fractionation (AcFFF). Only a few publications have been presented on the subject starting only about a decade ago. The problems with trying to use typical FFF theory with the acoustic force will be explained. The theory of particle retention in AcFFF will be calculated using rigorous methods and compared to a previously reported approximation for the relationship between the retained particle time and particle properties. Using bulk and surface micromachining technology, a μ-AcFFF system was built. Characterization was accomplished through evaluating system plate height and in retaining and fractionating polystyrene particle samples.

The ultimate goal of this project, but not included within the scope of the early work comprising this thesis, was to integrate the μ-ThFFF and μ-AcFFF systems into a portable device that can be associated with a micro-Total Analysis System (μ-TAS) or integrated into a "lab-on-a-chip." A brief description of some of the work already accomplished in this area will be presented. Future work for this system may consist of integrating each of the macroscale components with the microchannel.

Sample Preparation and Bioinstrumentation

Sample preparation is the equipment and process involved in modifying a raw sample in various ways prior to analysis of the desired sample component. Modifications may include reactions, purification, and concentration. Although sensors can be made

quite selective toward a particular analyte, sample preparation is usually necessary to eliminate sensor fouling and false measurements, as well as improve detectability through sample concentration and other means. Sample preparation is one of several required components of a complete analysis system.

In addition to sample preparation, researchers and clinicians are often interested in physical parameters of a particular material. The material must first be detected and possibly isolated in some way before the properties (e.g., molecular weight, surface chemistry, and bulk chemistry) can be measured. For materials that are on the order of nanometers to microns, processes such as chromatography and electrophoresis work well for both highly specific isolation of materials and determination of material properties. Field-flow fractionation (FFF) was an elution separation method comparable in many ways to chromatography. In general, both the materials and size range of materials separated in FFF systems was complimentary to those analyzed using electrophoresis and liquid chromatography.

Other methods such as mass spectrometry, infrared spectrometry, and XPS work extremely well in determination of material composition. However, the machines used for these analyses are generally expensive and large. Some chromatographic and FFF systems also have the same problem. However, in some cases an inexpensive, portable device is desirable. For example, the home blood glucose monitor used by millions of diabetics. This device has made possible frequent testing of blood glucose levels that otherwise would not be time or cost effective for the patient. Microfabricated systems can, in some instances, provide a method for a low cost, portable analysis and separation system.

A large endeavor has been made toward a total analysis system in which all components are integrated: pumps, valves, injection, preparation, sensing, detection, sorting, and collection. This effort is evidenced by conferences (e.g. *Micro Total Analytical Systems* or *μ-TAS*) and journals (*Lab-on-a-Chip*) dedicated solely to the integrated micro lab concept. Acoustics has recently made a larger appearance in this area, in particular in particle sorting [1]. Arguably, the most researched application is in the area of biology and the quantification of related systems.

Bioinstrumentation is the measurement of a physical signal or quantity associated with a biological based material and converting the signal through transducers and electronic means to useful instrumentation. Bioinstrumentation covers many areas such as imaging, biopotential measurement, osmotic measurements, chemical and biomaterial detection, pressure and flow measurements, material separation and purification, drug delivery and measurement devices, acoustic systems, heat transfer systems, and many more [2-6].

One important area of interest is the biochemical and material separation, purification, and analysis systems. These systems include many variations of electrophoresis, chromatography, FFF, distillation, centrifugation, filter, dialysis, osmosis, and others.

Miniaturization of chromatographic-based separation and analysis systems using micromachining technologies has yielded significant performance advantages when compared to larger, macro scale counterparts [7, 8]. The primary advantages include a decrease in the analysis time, a decrease in the sample / reagent consumption, an increase

in the number of parallel analyses, an increase in the integrated system functionality, and the possibility of system portability and disposability.

Field-flow Fractionation

Field-flow fractionation is an elution separation method comparable in many ways to chromatography. FFF was first introduced by J. C. Giddings in 1966 in the first edition of Separation Science [9]. The idea was introduced as a process applicable to not only chromatographic-type separations but also to macromolecule and colloidal separations. This advantage comes because of the single-phase nature of FFF. In the following two years, Giddings proved the concept by retaining polystyrene samples in toluene using a thermal gradient [10, 11].

In FFF, the separation field is applied perpendicular to the direction of separation. A carrier fluid with nonuniform flow characteristics is present in the direction of separation. Because of this arrangement, the samples need only to diffuse short distances under considerable smaller field strengths than would be typically required for an equivalent direct field method. Some of the fields proposed for separation by Giddings were electrical, centrifugal, and thermal. [9-11]

Separation in an FFF system occurs as a differential migration of fields which travel unidirectionally through a ribbon-like flow channel. This separation configuration is similar to chromatography. The samples are eluted in order of those retained from shortest to longest periods of time. Retention time is based on the interaction between the mobile phase or the sample (physiochemical characteristics) and the stationary phase or the column packing. Unlike some forms of chromatography, FFF does not require a

stationary phase other than the walls of the channel that provide a “no slip” condition for the carrier fluid.

There are several variations or subtypes of chromatographic separations. The most common is where a carrier fluid is passed through a long column (tube) in which the stationary phase is packed or the walls coated. The samples adsorb to the stationary phase or are slowed by the tortuous pathways. One variation is called electrophoresis where an electric field was applied across the stationary phase. The samples migrate through this phase according to size and charge. Like chromatography, several subtypes of FFF are based on the field applied across the channel. Thermal field-flow fractionation is introduced in the next section while other subtypes are introduced in the next chapter.

Thermal FFF

ThFFF Thermal field-flow fractionation (ThFFF) has been typically applied to separation, purification and analysis of polymers. ThFFF can be used for determination of molecular weight [12], particle diameter [13], thermal diffusion coefficient [14]-[16], physiochemical and surface properties [13], [16], [17], and sample polydispersity [18], [19]. Separations of suspended particles or dissolved polymers are performed in a solvent carrier such as methanol, THF, acetonitrile, DMSO and others, [20]-[23]. Water is not typically used because of its low thermal diffusion coefficient with many common polymers. However, water is a desirable carrier fluid because it was inexpensive, common, and non-toxic. A study on aqueous suspensions of polystyrene beads has been reported [13] and was used in this study for comparison of results.

In a ThFFF system, the sample reacts to an applied temperature difference across the width of the flow channel by diffusing toward the cold wall via the thermal diffusion mechanism. The relation between the physiochemical properties and degree of susceptibility is expressed in the empirically determined thermal diffusion constant. Samples that are more susceptible to the thermal field are compacted more against the cold wall than samples that are less susceptible. Due to the laminar velocity profile of the carrier fluid, samples that compact less will have a higher average velocity than the samples that compact more toward the sidewall of the flow channel. The difference in average velocity results in the spatial and temporal separation of the sample components at the output of the ThFFF channel.

Attempts have been made to understand and predict the thermal diffusion constant; however, thermal diffusion was still not understood well in liquids. Despite the lack of understanding in thermal diffusion mechanisms, theory of retention in ThFFF has been well developed based upon the thermal diffusion coefficient. The mathematical relationships relate known quantities such as elution sample volume to physical parameters such as molecular weight, polydispersity, thermal diffusion coefficient, molecular weight and size, and possibly chemical composition. Thus, ThFFF can be used as an analysis tool as well as a separation device.

Acoustic Field-flow Fractionation

The use of acoustic forces in a field-flow fractionation system is not a new concept. The idea was originally presented by Semenov and Maslow in 1988 [24]. A few years later, theory for AcFFF was published by Martin and Williams in 1992 [25]. Nearly a decade later Tri and Beckett presented at the Field-flow Fractionation

conference in Paris, France the concept and theory behind acoustic separation techniques in thin channels, including FFF and SPLITT [26]. The following year, Beckett presented preliminary research results with an acoustic SPLITT system [27]. In this research a size-based binary system of polystyrene particles was fractionated continuously into the individual components. The research of Tri and Beckett has most recently been accepted for journal publication [28].

The basis of fractionation in AcFFF is centered around a density and compressibility contrast factor. Size is also a large factor in discriminating samples. These factors will be elicited in the theory chapter through the acoustic force equation. While fractionating based on size is not unique to AcFFF, the density/compressibility basis is exclusive. This distinctive ability is the primary motivation for creating an AcFFF system that can easily be fabricated, thus expanding the capabilities available to researchers using FFF.

Micromachining techniques have previously been used to construct an electric field-flow fractionation system (μ-ElFFF) [29]. Using similar microfabrication technologies and design parameters, μ-ThFFF and μ-AcFFF systems and have been fabricated.

Microsystems Technology

For nearly 40 years silicon has been used as a substrate for fabrication of microelectronic integrated circuits [30]. The use of these circuits has revolutionized the electronics, making possible the fabrication of very fast computers that are small in terms of size and weight. The applications of these systems are endless. These processes have not been used solely for microelectronics though. In the late 1960s and early 1970s these

fabrication technologies including diffusion, etching, deposition, and photolithography were investigated for fabrication of sensors, actuators, and structures. The collection of processes used for fabrication of these types of systems was termed micromachining [31].

Micromachining or microfabrication technologies are typically subdivided into two groups of processes, those that add to the substrate or *surface* micromachining, and those that subtract from the substrate, *bulk* micromachining. Surface micromachining includes processes such as thin-film deposition, metal deposition, and diffusion. Bulk micromachining uses process such as potassium hydroxide etching, laser ablation, laser milling, ion reaction etching, and other wet and dry etching processes. Micromachined systems sometimes referred to as micro-electro-mechanical systems (MEMS) in many cases require processes in both categories.

Possibly because of the large influence from the microelectronics industry, silicon was used in most cases as the substrate. Single crystal silicon was used in many cases for its crystal planes but also because of its availability. Other substrates that have been used are glass, quartz, diamond, sapphire, gallium arsenide, metals, and plastics.

As mentioned earlier, an area of great interest to the micromachining community was research of a "lab-on-a-chip" or micro-Total Analysis System (μ-TAS). This research has focused on two main approaches, the microarray and the microchannels [32]. The first approach involves a substrate covered with an array of sensors. The sensors are covered or "flooded" with the material to be analyzed. The second approach utilizes fluidic channels to direct the sample through a process. One important step of this process may include a separation system such as chromatography or FFF. Integration of the ThFFF system into a μ-TAS was the ultimate goal of this project.

The application of microsystems technologies to biological based instruments was sometimes referred to as bio-MEMS. Micromachined bioinstrumentation research has included polymerase chain reaction (PCR) [33-36], electrophoresis [37-40], free-flow electrophoresis [41,42], gas chromatography [43-45], and liquid chromatography [46,47], and field-flow fractionation [48-50]. Several benefits are gained when scaling the physical parameters of these systems. The general scaling benefits include system cost size and cost reduction including the possibility of a portable analysis system, small sample size requirements, shorter analysis times, and improvements in analyses including extension of analysis range. Other areas of interest and importance to these systems are the injection, motion, and liquid placement [36,51]. Accurate and precise volumes must be correctly positioned in microchannels for proper mixing, reactions, and separations [36]. Fabrication of a microscale ThFFF system and a microscale-AcFFF system using micromachining technologies have the benefits just described as well as additional benefits that will be explored in detail in this thesis.

Chapter Outlines

The theory behind a general form of field-flow fractionation, acoustic field-flow fractionation, and thermal field-flow fractionation will be addressed in some detail in Chapter 2. The theory will be presented with equations that have been developed from past researchers in the FFF field. This chapter will also contain theoretical effects from scaling channel dimensions such as the channel width and will provide the motivation for fabrication of a miniaturized ThFFF system. Theory specific to acoustic wave propagation in isotropic and anisotropic media, as well as piezoelectricity, is described in detail with respect to the selection of materials and calculations for design.

Fabrication of both the μ-AcFFF and the μ-ThFFF system was included in Chapter 3. This chapter will cover basic techniques of microfabrication technology associated with the manufacturing of the μ-ThFFF system. These techniques include channel and heater fabrication as well as the fluidic, electrical, and thermal interconnects between the microscale and macroscale system components. The experiments used to characterize the systems will be described in detail, such as AcFFF resonant frequency, electrode (heater) resistivity, channel dimensions, and particle standard suspension retention.

The fourth chapter contains results from the fabrication process and from the experiments for the acoustic system. These results include images of the channel and completed system, profiles of the channel, electrical input impedance, system band broadening effects, single component polystyrene retention, and multiple component polystyrene separation.

Chapter 5 is the results chapter for characterization of the ThFFF system parameters that are presented in Chapter 2. Comparison of the μ-ThFFF system with a macroscale system will also be covered. Results presented will be similar to that obtained for AcFFF with a few differences. Characterization of the integrated heater will be one of these exceptions.

The last chapter is the conclusion to the thesis. A review of the work that was done and the results will be briefly recanted. An evaluation of the accomplishements toward the goals of this project will be made. Future work for this project will also be proposed and discussed.

CHAPTER 2

ACOUSTIC, THERMAL AND FFF THEORY

Recent work on scaling effects in an electrical field-flow fractionation system (ElFFF) was published recently by Gale [52]. In this dissertation, reference was also made to the possibility of scaling a thermal field-flow fractionation system. This chapter describes the theory of FFF and points out the specific benefits of reducing the channel geometry of ThFFF systems.

Field-flow fractionation is a chromatographic separation process [54, 55]. FFF is an elution separation technique in which a field is applied to retain the sample in the column for a time based upon its physical parameters. For this reason, FFF is often compared to chromatographic separations or is evaluated based upon common chromatographic system evaluation methods. However, there are key differences between FFF and chromatography that require an exploration into the direct effect that a change in system parameters will have on the outcome of the system tested [56]. Giddings [57] explored the effects of miniaturization of the general FFF channel through both experimental evidence and theory. In comparison to a capillary, chromatographic separation, he concluded, "There is no compelling fundamental reason . . . to reduce the thickness of FFF channels."

Possibly, because of this comparison with chromatography, very little attention has been given to reducing the channel size in FFF systems. Giddings, in this same paper, did search through FFF theory to find advantages and disadvantages of scaling the FFF channel. Even though this has been done in general, no scaling work, to date, has been done specifically for the ThFFF system. This will be accomplished here.

The purpose of the ThFFF system is separation of a multicomponent sample, analysis of a sample, or both. The goals of separation and analysis are then sample selectivity that can be accurately related to the sample physical parameter of interest, complete separation eluting sample zones, and separation and analysis times that are as short as possible. Miniaturization of the ThFFF system will be related to these goals.

Other benefits are still gained from a reduction in channel geometry in the ThFFF system. These benefits are clearly stated by Giddings and will be reiterated in this work. These benefits are:

- Reduced solvent consumption (solvent carrier fluids are common in ThFFF)
- Sample dilution reduction (improves detectability)
- Sample overloading for detectability is reduced (less peak broadening)
- Reduced required sample size (good for expensive or hard to obtain samples)
- Shorter relaxation time (decreased separation/analysis time)
- Smaller instrument size (portability)
- Channel edge effects on the flow profile is reduced (less peak broadening)

Some of these benefits, such as the ones that deal with reducing the distortion of the sample peak, apply to all systems. Other benefits may only apply to certain applications of the system. One potential use of this micro ThFFF system is as the

separation component of a portable analysis device commonly referred to as a micro Total Analysis System (μ-TAS) or as a "lab-on-a-chip." In this case, the benefits of a reduced solvent flow, smaller instrument size, smaller sample volume requirement, and reduced dilution of sample for better detection are of extreme importance.

General Field-flow Fractionation Theory

The theory behind the retention and separation mechanism in FFF has been well developed and is available in many different references. To provide a clear understanding of the scaling effects on FFF and to understand the subtle differences that may cause error in ThFFF, the equations will be expanded again in this chapter.

The basic theory applies to all subtechniques of FFF since the basis of separation in each technique is the same. The difference between the subtechniques is in the field applied to the samples to cause the retention. First, the theory common to all subtechniques will be laid out; then, the theory specific to the thermal subtype of FFF will be given.

Channel Geometry

Field-flow fractionation is a chromatographic-type separation that occurs in a rectangular channel where the breadth, b, is typically 100 times that of the width, w, see Figure . Because of these dimensions, the channel can be considered as two infinite parallel plates. The separation channel in conventional ThFFF systems is constructed by cutting the shape of the channel from a thin Mylar sheet. The sheet is then clamped between two thick slabs of metal with bolts. The surfaces of the metal slabs are

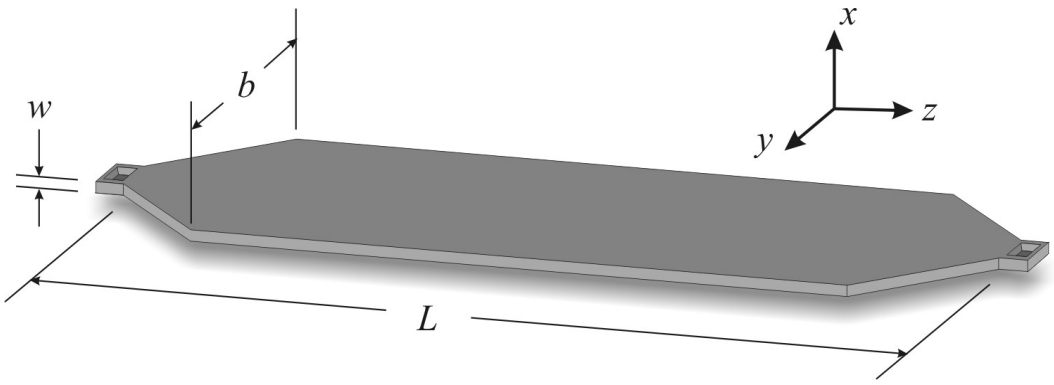

Figure 1. This is a typical shape of an FFF separation channel showing the dimensions of width, w, breadth, b, and length, L. The breadth to width ratio is usually over 100, under which conditions the velocity flow profile is laminar and two-dimensional.

typically polished and sometimes modified to make possible the subtype of FFF desired [58,59].

The size of w needs to be small enough to create a laminar velocity profile of the carrier fluid for a given flow rate of the fluid. The sample migrates, via diffusion, normal to the carrier flow under an applied field. The different fields used give rise to the different subtypes of FFF. The size of w again needs to be small enough that the diffusion distance is not too great. Otherwise, the time required for a sample to come to equilibrium will be very large, making the separation or analysis impractical. The channel thickness in a conventional ThFFF system is typically 254μm, 127μm, or 51μm. These thicknesses are sometimes referred to as normal, thin, and ultrathin [55]. Other thicknesses are common though [53,60]. The length of the channel, L, may vary in size. It is long enough to allow enough time for the separation to occur under given process conditions. A typical size of L is around 25 – 90 cm [55,59,61] but can be as high as 184 cm [62]. The larger L and smaller b and w, the more difficult it is to maintain constant channel dimensions in fabrication. These spatial variations in w may disturb the laminar flow profile and/or affect the separation and analysis of the sample.

Void Time and Void Volume

Two important parameters that deal with the geometry of the channel are the void time, t^0, and the void volume, V^0. These parameters are determined by the volume of fluid required to sweep out one volume of the channel and the time required to sweep out this volume. These parameters are important because they represent the peak position of the sample that is not retained due to the applied field. It will be shown later that samples

that are retained can be compared to the unretained sample and the important physical constants of the sample can be related to this ratio.

FFF Fields and Subtypes

In FFF, a field is applied normal to the flow of the carrier fluid to cause a flux of the sample toward one wall. In chromatography, the field is applied in the direction of the carrier or separation. This parallel configuration requires an additional degree of resolution in the direction of the field and in turn, an additional amount of energy to achieve that resolution [63]. Figure shows a cross-sectional view a FFF channel and a field applied across the channel. In this case, the field is a thermal field with a high temperature at the top wall and a cold temperature at the bottom wall.

A number of different fields have been used to cause a migration of sample toward one of the walls. Some of the more common fields used are electric (EFFF or ElFFF) [52,63-83], thermal (TFFF or ThFFF), steric (SFFF) [84-112], flow (FlFFF) [113-145], and sedimentation (SdFFF or SedFFF) [146-207]. Other types have still been tried but are not as common such as, magnetic (MFFF or MgFFF) [208-213], acoustic (AFFF or AcFFF), gravitational (GFFF) [214-221], and dielectricphoresis (depFFF) [222-225], as well as any combination or variation of these fields.

Sample Concentration Profile and Thickness

The flux, J_F, of a sample induced by a field is dependent on the drift velocity, U, and the concentration gradient, $c(x)$, across the channel. This relation is expressed in Equation 1.

$$J_F = U\,c(x) \tag{1}$$

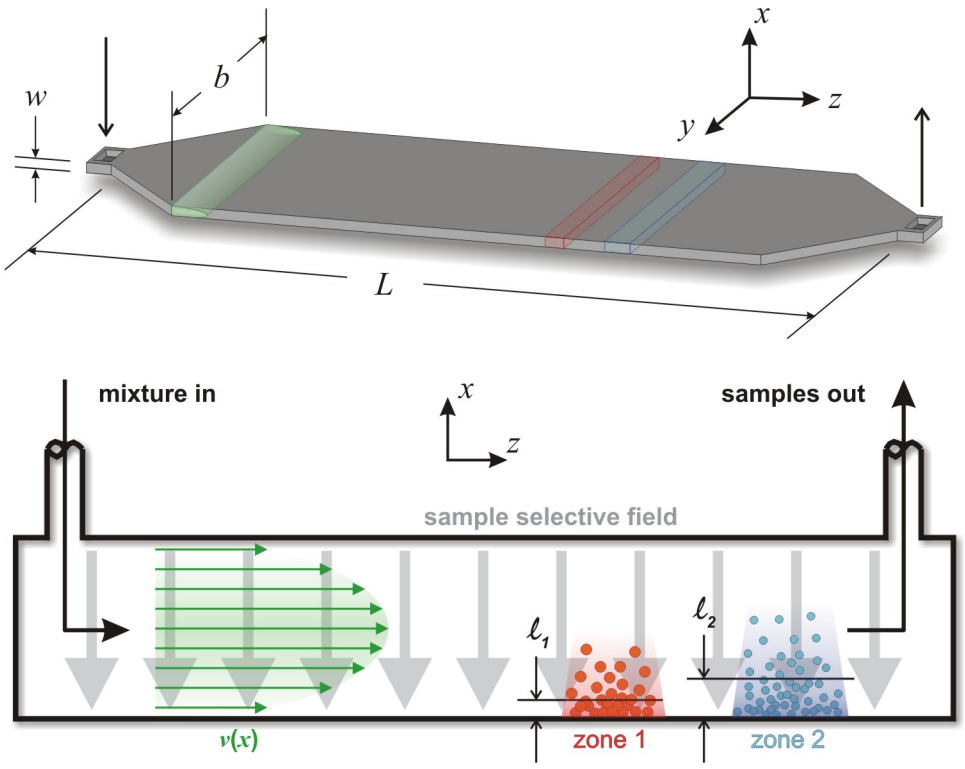

Figure 2. A schematic of an FFF channel. The carrier fluid enters at one end and exits at the other while maintaining a laminar velocity profile along the length of the channel. A field is applied normal to flow of the carrier. For this case, it is a thermal field. The samples react at different degrees and compact more or less at one of the walls. Each sample zone of a specific diameter, d, (or molecular weight, MW) then has a different layer thickness, l, and in turn, a different average velocity, v. The difference in v between the zones translates to a spatial separation along the length of the channel.

The drift velocity, U, of the samples is given by Equation 2 and depends on the type and strength of the field.

$$U = \frac{S'\phi}{f} \tag{2}$$

The drift velocity is a function of the field strength, *S'*, the sample-specific field susceptibility parameter, ϕ, and the friction factor, *f*. For a complete description of these parameters for each of the major subtypes of FFF, see Caldwell [63, 75].

As the samples concentrate at one wall due to the applied field, a concentration gradient gives rise to a flux in the opposite direction driven by normal Fickian diffusion, J_D. This diffusion is represented in Equation 3 where the concentration gradient is approximated by $\Delta c/w$, and the sample/carrier binary diffusion constant or diffusivity, *D*.

$$J_D = D\frac{\Delta c}{w} \tag{3}$$

The sample comes to equilibrium when the fluxes, J_D and J_F, are equal. The sample forms an exponential concentration gradient across the channel with the highest concentration, c_0, at the accumulation wall. This concentration gradient is shown schematically in grayscale in Figure for both the large diameter and small diameter particle zones. The sample concentration as a function of distance, *x*, from the accumulation wall is given by Equation 4.

$$c(x) = c_0 \exp\left(-\frac{x}{l}\right) = c_0 \exp\left(-\frac{x}{\lambda w}\right) \tag{4}$$

The sample layer thickness, l, or its dimensionless analog, λ ($=l/w$), is defined as the center of mass of the sample. This layer thickness, λ, is related to U in Equation 2 by Equation 5.

$$\lambda = \frac{D}{Uw} \tag{5}$$

Flow Profile

Because of the slow fluid flow and the thin channel, assumed to be infinite, parallel plates, the carrier fluid velocity profile is laminar. This velocity is represented schematically in Figure and is related to position relative to the accumulation wall by Equation 6 [20].

$$v(x) = 6\langle v\rangle\left[\left(\frac{x}{w}\right) - \left(\frac{x}{w}\right)^2\right] \tag{6}$$

This parabolic velocity profile is derived from the differential form of the Navier-Stokes equation with flow driven by a pressure gradient, dP/dz, and a constant viscosity is assumed. The average velocity of the channel is given by <v>. The shape of the velocity profile is critical to the separation. Because the samples compact at the accumulation wall at varying degrees, according to the sample layer thickness, λ in Equation 5, the average velocity for a particular sample will differ from another sample. The samples then form zones that are spatially separated as they travel along the length of the channel. This spatial separation is shown schematically in Figure .

Because the samples are eluted at different times, they can be collected in purified form. Complete purification is generally not obtained if the samples are not

monodisperse in size or molecular weight, or if the zones are not completely resolved from each other. These effects will be looked at later.

The flow profile is theoretically a parabola, as shown in Figure . Next, will be shown the exact mathematical relation between the time the sample is eluted, which is a direct function of the flow profile, and the sample susceptibility parameters. In this way, the sample can be analyzed and the molecular weight, diameter, or other parameter that is susceptible to the field can be determined. This relation is expressed in the retention parameter.

Retention

Retention of the sample in the channel for a specific amount of time relative to the void time is dependent on the sample susceptibility to the field, the flow profile, the carrier fluid properties, and the strength of the field applied across the channel. Retention is also defined as the ratio of sample average velocity, $\langle v \rangle_{sample}$, to the carrier fluid average velocity, $\langle v \rangle_{carrier}$, given by Equation 7.

$$R = \frac{\langle v \rangle_{sample}}{\langle v \rangle_{carrier}} \tag{7}$$

Because the distance traveled for both the retained sample and the carrier fluid is the same, Equation 7 can be related to the elution time of the retained sample, t_r, and the elution time of the carrier fluid, t^0. Earlier, the void time, t^0, was defined as the time required to sweep one channel volume of fluid from the channel, called the void volume, V^0. Using t^0 or V^0, Equation 7 is transformed to Equation 8.

$$R = \frac{V^0}{V_r} = \frac{t^0}{t_r} \tag{8}$$

The parameter V_r is the volume of carrier fluid needed to flush the retained sample through the channel. Both t_r and t^0 are easily measured from experimental data; the retention ratio, *R*, can then be calculated from these times.

For the parabolic velocity profile in Equation 6, *R* can be related to the sample layer thickness by Equation 9.

$$R = 6\lambda\left(\coth\left(\frac{1}{2\lambda}\right) - 2\lambda\right) \tag{9}$$

This equation has a limiting form when the sample layer thickness is very small (i.e. when $\lambda << 1$). The layer thickness is often very small and the limiting form, found in Equation 10, carries an error of no greater than 5% for an *R*-value of 0.2 (an upper limit for the retention ratio).

$$R \approx 6\lambda \tag{10}$$

By combining and rearranging equations 2, 5 and 10, the field susceptibility parameter, ϕ, is related to *R* (or to the elution times of Equation 8), in Equation 11.

$$\phi = \frac{6Df}{S'wR} = \frac{6Df}{S'w}\frac{t_r}{t^0} \tag{11}$$

From ϕ, the sample physical constants are determined depending upon the field used. It is noted that in the case of ThFFF, the value *R* is not affected by scaling the width, *w*, of the channel. This point will be shown later.

Steric Mode FFF

Retention in equations 9 through 11 is for normal mode FFF. This is the case where the radius of the particle is much smaller than the layer thickness. Once the radius of the particle exceeds the theoretical layer thickness calculated from the diameter of the

particle, the elution order of the particles is reversed (i.e., larger particles travel faster than smaller particles). This mode of operation is called Steric Field-flow fractionation. The retention ratio for this mode is given by Equation 12.

$$R = \frac{3\gamma d}{w} \tag{12}$$

Here, the retention ratio, regardless of the field used, is always affected by the scaling effect of the channel.

Selectivity

Selectivity shows the ability of a system to resolve samples based on differences in molecular weight or size. A theoretical maximum selectivity exists for systems that are operating under the condition of high retention, and is shown mathematically in Equation 13.

$$S_{max} = \left|\frac{\mathrm{d}(\ln V_r)}{\mathrm{d}(\ln d)}\right| = \left|\frac{\mathrm{d}(\ln V_r)}{\mathrm{d}(\ln MW)}\right| \tag{13}$$

Under conditions of much lower retention, the maximum selectivity is reduced by the differential equation found in Equation 14 [63].

$$S = \left|\frac{\mathrm{d}(\ln V_r)}{\mathrm{d}(\ln \lambda)}\right| S_{\max} = 3\left(\frac{R}{36\lambda^2} + 1 - \frac{1}{R}\right) S_{\max} \tag{14}$$

The latter equality in Equation 14 is found by differentiating Equation 9. The maximum selectivity depends on the subtechnique used but may range from 0.2 to 1 for molecular weight and from 1 to 3 for diameter based separations. [226]

Plate Height and Band Broadening Factors

Plate height is the measure of zone spreading or sample peak distortion after the sample has passed through the channel. By this definition, plate height can be represented by Equation 15 if a Gaussian shaped sample peak is assumed.

$$H = \frac{d\sigma^2}{dz} \approx \frac{\sigma^2}{L} \tag{15}$$

Plate height is approximated by the peak variance, σ^2, divided by the distance the peak travels, or simply, the length of the channel, L. Three main factors play a role in zone spreading. They are nonequilibrium (H_n), instrument and operational effects (H_i), and polydispersity (H_p). The combined plate height, H, is shown in Equation 16.

$$H = H_n + \sum H_i + H_p \tag{16}$$

The term, H_n, is generated because a sample is distributed over a wide range of velocities. As portions of the sample move from regions of high velocity to regions of low velocity, and back again, the various portions of the sample move away from each other and spread the zone. This term is the dominant effect in the total plate height and is a complex function of the layer thickness, $\chi(\lambda)$, as shown in Equation 17. [227, 228, 229]

$$H_n = \frac{\chi(\lambda) w^2 \langle v \rangle}{D} \approx \frac{24\lambda^3 w^2 \langle v \rangle}{D} \tag{17}$$

As the sample layer thickness becomes very small (i.e. $\lambda \rightarrow 0$) the function $\chi(\lambda) \rightarrow 24\lambda^3$.

The collection of terms, H_i, are the effects of such things as channel shape, channel surface roughness, injection plug width, fluidic interconnects and tubing, detector, and channel edge effects. These parameters are controllable by building a better ThFFF system. The operating procedure will affect such things as the sample injection

plug width. Recently, Gale [230] introduced an on-board electrical impedance detector for the μ-ElFFF system. With the detector placed just before the outlet of the channel, the band broadening due to the tubing from the channel to the detector and in the detector itself it eliminated. Other types of detectors may be implemented instead of the electrical impedance detector.

As mentioned earlier, channel shape is also important to separation time and accuracy. Research has been done on the effects of decreased volume channel ends to reduce broadening of the sample peak [59]. This design was implemented in both the μ-ElFFF and the μ-ThFFF systems. The tapered ends are shown schematically in Figure .

Polydispersity is an important parameter in polymers. It is represented by the standard deviation of a particle diameter, σ_d, or the polydispersity index, μ, which is the weight average molecular weight divided by the number average molecular weight (MW_w/MW_n). Caldwell [63] pointed out that H_p is the only term in Equation 16 that depends on <v>. For this reason, FFF can be used to determine σ_d of a sample by retaining the sample several times at constant field strength and varying carrier flow rates. The slope is the H_n term and if H_i is neglected, the intercept is the H_p term. The polydispersity can be determined using the relation in Equation 18.

$$H_p = LS_M^2\left(1-\frac{1}{\mu}\right) = LS_d^2\left(\frac{\sigma_d}{d}\right)^2 \tag{18}$$

The selectivity is determined from Equation 14.

A common alternative representation of plate height is the number of theoretical plates, *N*. This value *N* is equal to *L*/*H*. From data, N can be calculated using Equation 19 [231].

$$N = 5.54\left(\frac{t_r}{w_{½}}\right)^2 = \frac{L}{H} \tag{19}$$

Resolution

The ability of a system to separate components of a mixture can be quantified by the resolution index, *Rs*. Simply stated, the resolution index describes the amount of overlapping of two peaks. In mathematical terms, it is shown in Equation 20 and is the scaled ratio of the difference in the two retention volumes, ΔV_r, or retention times, Δt_r, and the average standard deviation of the two peaks, σ_v or σ_t, see Figure.

$$Rs = \frac{\Delta V_r}{4\sigma_V} = \frac{\Delta t_r}{4\sigma_t} \tag{20}$$

The index, *Rs*, can also be represented by the theory developed so far and is expressed in Equation 21.

$$Rs = \frac{\sqrt{L}}{4}\frac{\Delta MW}{MW_{ave}}\frac{S_M}{\sqrt{H}} = \frac{\sqrt{L}}{4}\frac{\Delta d}{d_{ave}}\frac{S_d}{\sqrt{H}} \tag{21}$$

The difference in molecular weight or diameter of the two samples is ΔMW and Δd, respectively. The average molecular weight and average diameter is MW_{ave} and d_{ave}, respectively.

Relaxation Time

The equations defined for retention, plate height, and resolution all assume that the equilibrium condition between the normal diffusion flux and the field-induced flux

was obtained instantaneously. In fact, there is a finite space of time between when the sample is introduced to the field and the equilibrium condition. This finite time is called the relaxation time, τ. The relaxation time is a function of the channel width and thus is scaled with the channel. The relation between τ and w is shown in Equation 22.

$$\tau = \frac{w^2}{D\pi^2} \tag{22}$$

This time, τ, can be significant in some cases. To overcome the non-equilibrium effect during this time a stop-flow routine is often employed. After the sample has been introduced into the field, the carrier flow is stopped for a time greater than τ. This time is typically around 10 minutes for macroscale ThFFF channels. From Equation 22, the benefit of reducing w on this time and subsequently on the overall separation and analysis time is scaled to the square power.

Separation Time and Speed

For a given Rs (see Figure) the amount of time required for the separation, t_a, is fixed with all other separation constants fixed. The relationship between t_a and Rs was determined by Caldwell [63] (Equation 23).

$$t_a = const\left(\frac{Rs}{S'}\right)^2 = const\left(Rs\frac{w}{\Delta T}\right)^2 \tag{23}$$

From Equation 23, it can be seen that the analysis time is scaled by the square power with the width of the channel. Looking at the required separation time from another standpoint, for a given t_a and Rs, the temperature difference, ΔT, must be scaled with w to achieve the same separation. This drop in ΔT reduces the power requirement to the system.

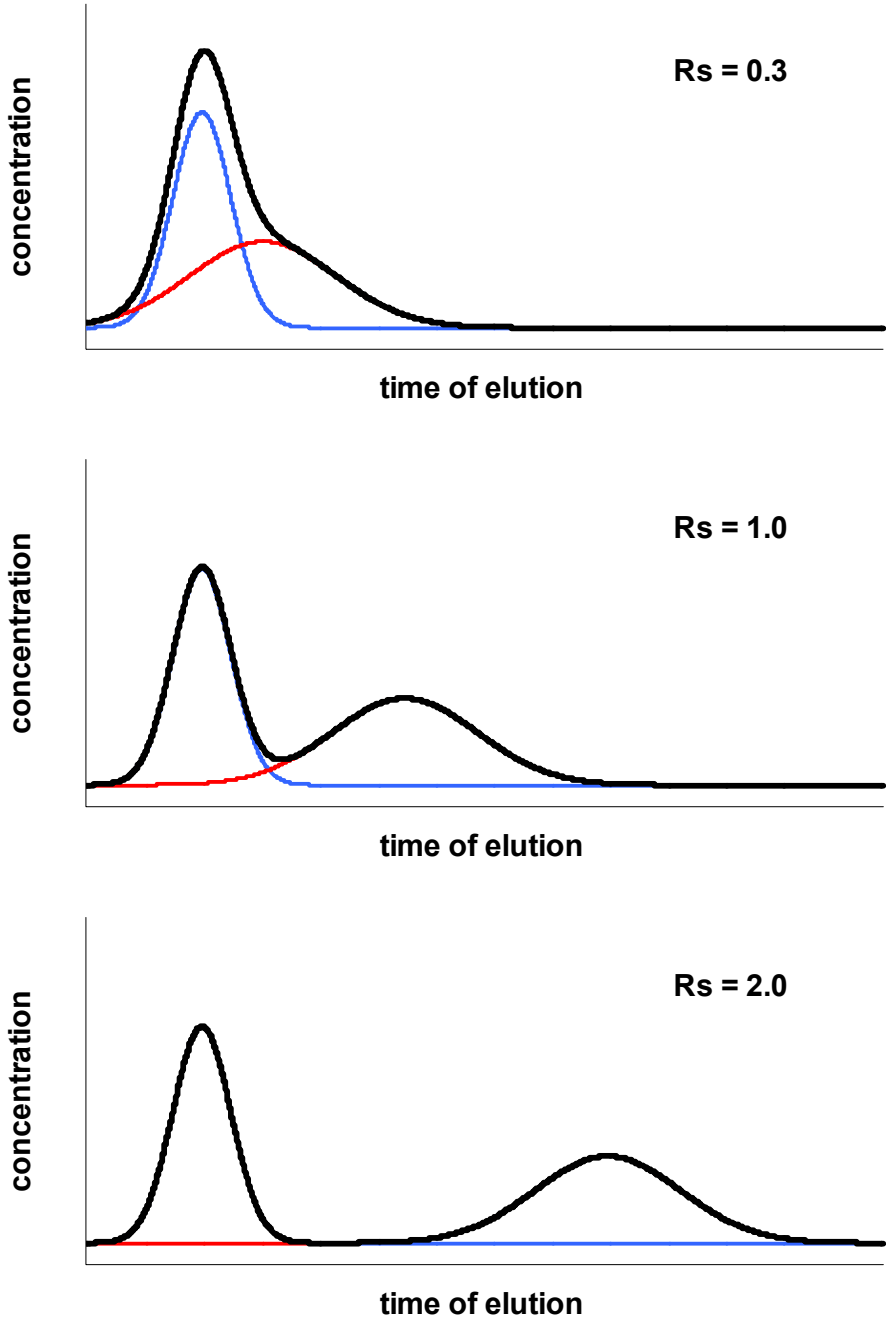

Figure 3. Theoretical resolutions calculated from Equation 20. For Rs = 0 the two peaks overlap completely. In this figure, for Rs = 0.3 the two peaks still sum to a single peak. A baseline separation is indicated with Rs = 1.0. The peaks continue to separate with increasing Rs values as indicated with Rs = 2.0. As Rs → ∞ then Δtr → ∞.

AcFFF Theory

In this section, the theory for AcFFF will be developed from the basic acoustic force equation and the foundation equations of FFF. Theory will also be presented from a previously published article [24], in which an assumption was used to simplify the acoustic force and make possible the easy integration with existing FFF theory. In addition, the basic theory governing standing waves in resonating chambers is developed to aid in understanding the basis for the design and is presented in the folowing sections. Finally, material properties will also be shown to be important through the governing wave equations in solids and liquids.

Acoustic Force

Developed theory for retention in an FFF channel for most field types is based on a force that is constant in the direction normal to the separation. This assumption is valid for all the common applied separation fields such as electrical, gravitational, flow, and thermal. This assumption is not at all valid with an acoustic based system except under conditions of high retention. The force from an acoustic field on a particle of radius, r, much smaller than the wavelength, λ_a, is given by Yosioka and Kawasima [232] in Equation 24.

$$F_{Ac} = \left(-\frac{4}{3}\pi r^3 \right) k\bar{E} f(\rho, \gamma) \sin(2kx) \tag{24}$$

From this equation it is obvious that the force varies in the x-direction, the direction of the field. The variables in this equation include the particle radius, r, acoustic wave number, $k=2\pi/\lambda_a$, average acoustic energy density, $\bar{E}=\frac{1}{2}\rho' u^2$, and the

density-compressibility factor, $f(\rho,\gamma)$, defined below. The energy density is calculated from the density of the carrier fluid, ρ', and the acoustic wave velocity amplitude, u.

This equation also elucidates the mechanisms by which particles can be separated. First, particles of identical physiochemical properties can still be separated based on size, with a third-order dependence on the particle radius, r^3. This third-order dependence means a high resolution for even small differences in diameter.

In addition to separation based on size, AcFFF is also able to differentiate between samples of different density and compressibility through the factor $f(\rho,\gamma)$ in Equation 24. This factor is defined in Equation 25 [232].

$$f(\rho,\gamma)=\frac{5\rho-2\rho'}{2\rho+\rho'}-\frac{\gamma}{\gamma'} \tag{25}$$

In this equation the primed variables are the density, ρ, and compressibility, γ, of the carrier fluid and the unprimed are for the particle properties. Thus, a separation based on the contrast of acoustic properties, of the particles to the medium, is possible.

Acoustic Field-flow Fractionation

Because the acoustic force on the particle is not constant, a more rigorous approach to solving the zone velocity and retention parameter is necessary. The retention of a zone of particles with a particular diameter and acoustic property is generally defined by the ratio of the zone velocity, v_{zone} to the average fluid velocity $\langle v \rangle$ or,

$$R=\frac{v_{zone}}{\langle v\rangle}=\frac{\langle c(x)\cdot v(x)\rangle}{\langle c(x)\rangle\cdot\langle v(x)\rangle}=\frac{\frac{1}{w}\int_0^w c(x)\cdot v(x)dx}{\langle v\rangle\cdot\frac{1}{w}\int_0^w c(x)} \tag{26}$$

The carrier fluid velocity profile is obtained by assuming the particle concentration is small and so the viscosity of the fluid constant. For this case, in infinite

parallel plates, the flow profile is constant in the *y*-direction (along channel breadth) and in the x-direction is

$$v(x) = 6\langle v \rangle \left[\frac{x}{w} - \left(\frac{x}{w} \right)^2 \right] \tag{27}$$

The concentration profile is determined through setting the flux of the particles, due to acoustic force, equal to the opposing concentration-based diffusion flux and solving the differential equation. The resulting profile is

$$c(x) = c_0 \exp\left[\frac{-F_{\max}}{2kk_B T} \sin(2kx) \right] \tag{28}$$

where c_o is the concentration at the accumulation wall, F_{max} is the collection of constants in equations 24 and 25, k_B is the Boltzmann constant, and T is the channel temperature.

From Equation 26, the retention is related experimentally to the ratio of the elution time to the void time. While this number is easily obtained from experiments it is difficult to relate to the diameter or acoustic properties based on the complex nature of the concentration profile. As in the case of typical FFF systems, the use of a dimensionless parameter, $\lambda = l/w$, is necessary to bridge R to physiochemical properties (Equation 24). This parameter is defined in Equation 29.

$$\lambda = \frac{1}{w} \frac{\int_0^w x c(x) dx}{\int_0^w c(x) dx} \tag{29}$$

Under the assumption of high retention, and thus a constant force, Martin and Williams [25] published a relationship between λ and the particle properties,

$$\lambda = \frac{48kT}{\pi^2 \rho u^2 d^3 |f'|} \tag{30}$$

The compressibility density factor, f', in this equation is defined as,

$$f' = 1 - \frac{\beta_s}{\beta} + \frac{3\left(\rho/\rho' - 1\right)}{2\rho/\rho' + 1} \tag{31}$$

where, β_s and β is the compressibility of the particle and liquid, respectively, and ρ and ρ' are defined as before. This equation will be evaluated against the rigorous approach using Equation 11 with experiments using polystyrene bead standards.

Acoustic Standing Waves

The following acoustic theory is important for design of the system and selection of the appropriate construction materials. The fabrication details will be presented in Chapter 3. The acoustic system will consist of three layers: the transducer, channel and reflector plate. The transducer is expected to operate at the fundamental frequency in the longitudinal mode with no shear components. The thicknesses of the other layers will be designed around this fundamental resonant frequency (i.e. the crystal thickness is equal to one-half the wavelength). The channel layer is comprised of the channel walls (solid) and the fluid channel (liquid). The theory will only treat the regions of the fluid channel and will ignore the channel walls. The reflector plate is not only used to help establish the appropriate acoustic standing wave, but also serves as the fluidic channel bottom wall and substrate for electrodes. Figure 4 illustrates a basic resonating system from which the following equations are based.

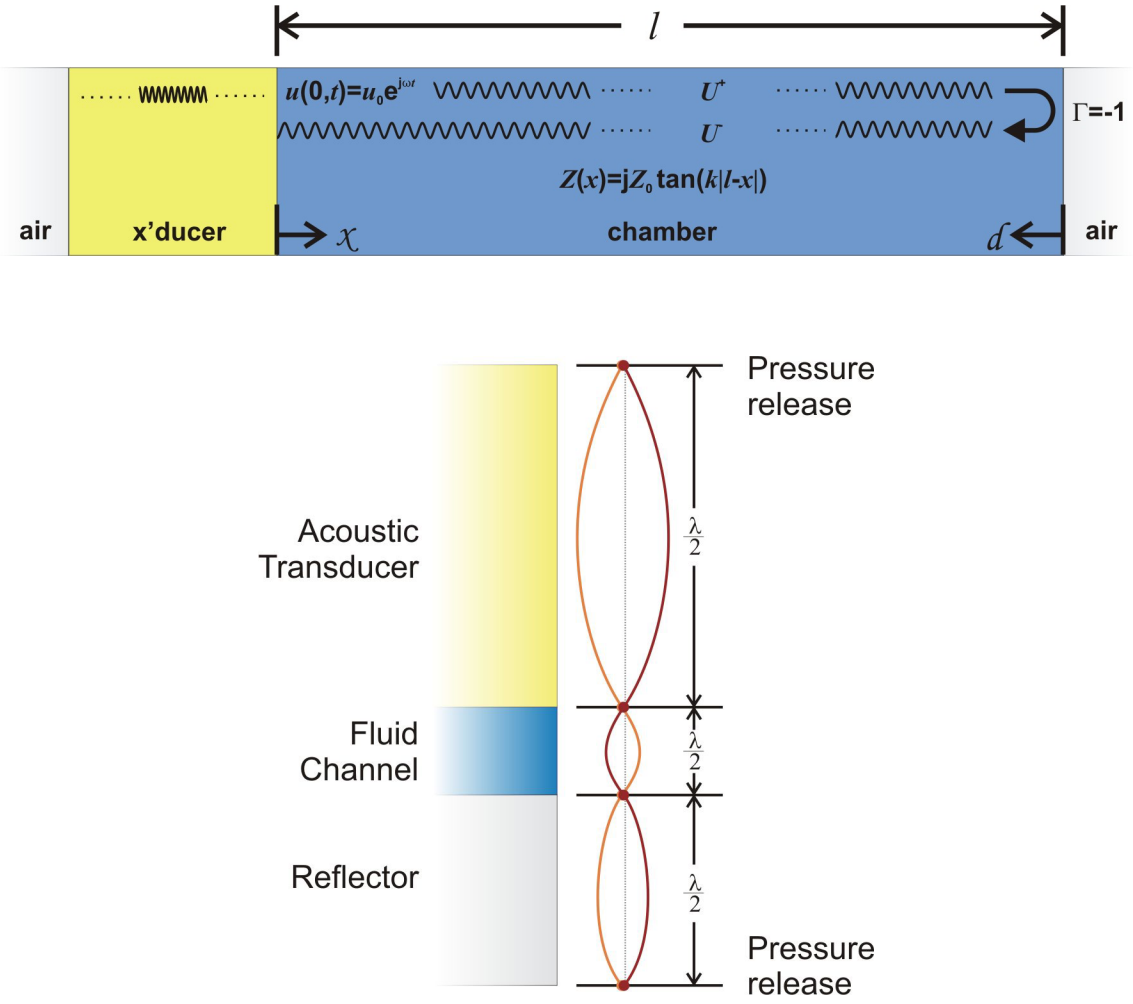

Figure 4. (Top) Acoustic transducer and chamber combine to form a resonating cavity. The forward and backward waves add to form the standing wave profile. At a pressure release boundary the entire wave is reflected and the standing wave has maxima and minima located at quarter wavelength intervals. (Bottom) The overall design of the three layer acoustic FFF system is to place these nodes and antinodes at each of the material boundaries.

If the system is surrounded by air, the silicon/air interface will give a pressure release boundary due to the extreme impedance mismatch. The reflection coefficient is close to -1. Nearly the entire wave will be reflected at this point. One solution to the 1-D wave equation results in a sinusoidal velocity wave in both space and time, $u(x,t)$.

$$u(x,t) = U(x)e^{j\omega t} \tag{32}$$

In a standing wave, the forward, U^+, and backward, U^-, traveling waves combine to form a spatially stagnant wave. Figure 2a shows a graphical representation of the forward and backward traveling waves with a reflection coefficient of 0.5. Figure 2b shows how these waves combine to form a standing wave envelope. Because of total reflection these terms are equal and opposite. Unlike Figure 2b, the velocity nodes in a standing wave with a total reflection will be near zero. The total spatial wave is given by

$$\frac{U}{U^+} = e^{jkd} + e^{-jkd} \tag{33}$$

.

The wave is represented in space and time by

$$u(x,t) = U^+ e^{j\omega t}\left[e^{jkd} + e^{-jkd}\right] \tag{34}$$

.

Or by using a simply trigonometric identity, it is

$$u(x,t) = 2U^+ e^{j\omega t}\cos(kd) \tag{35}$$

If the transducer/channel interface is driven sinusoidally at a given amplitude,

$$u(0,t) = u_0 e^{j\omega t} \tag{36}$$

then,

$$u(0,t) = 2U^+ e^{j\omega}\cos(kl) = u_0 e^{j\omega} \tag{37}$$

$$U^+ = \frac{u_0}{2\cos(kl)}, \tag{38}$$

$$u(x,t) = u_0 e^{j\omega} \frac{\cos(k[l-x])}{\cos(kl)} \tag{39}$$

Resonance occurs when $kl = n + \pi/2$, where n=0, 1, 2, ... The resonance condition can be more easily visualized from a graphical representation of several reflected waves. If the waves are only partially reflected in a single cavity, then Figure 5 properly represents the resulting standing wave.

Using the momentum equation,

$$\rho_0 u_t + p_x = 0 \tag{40}$$

The pressure component of the wave equation can be derived,

$$p_x = -j\omega\rho_0 u_0 e^{j\omega} \frac{\cos(k[l-x])}{\sin(kl)} \tag{41}$$

$$p(x,t) = j\omega \frac{\rho_0}{k} e^{j\omega t} \frac{\sin(k[l-x])}{\cos(kl)} . \tag{42}$$

The characteristic impedance of the material is,

$$Z_0 = \rho_0 c = \frac{\rho_0 \omega}{k} \tag{43}$$

$$p(x,t) = jZ_0 u_0 e^{j\omega} \frac{\sin(k[l-x])}{\cos(kl)} . \tag{44}$$

The acoustic impedance as a function of space can be calculated from the ratio of the pressure wave to the velocity wave,

$$Z(x) = \frac{p(x,t)}{u(x,t)} = jZ_0 \tan(k[l-x]) . \tag{45}$$

This equation means that every quarter wavelength the impedance will transform from either infinite impedance to zero or vice versa, but is time invariant, Figure 6.

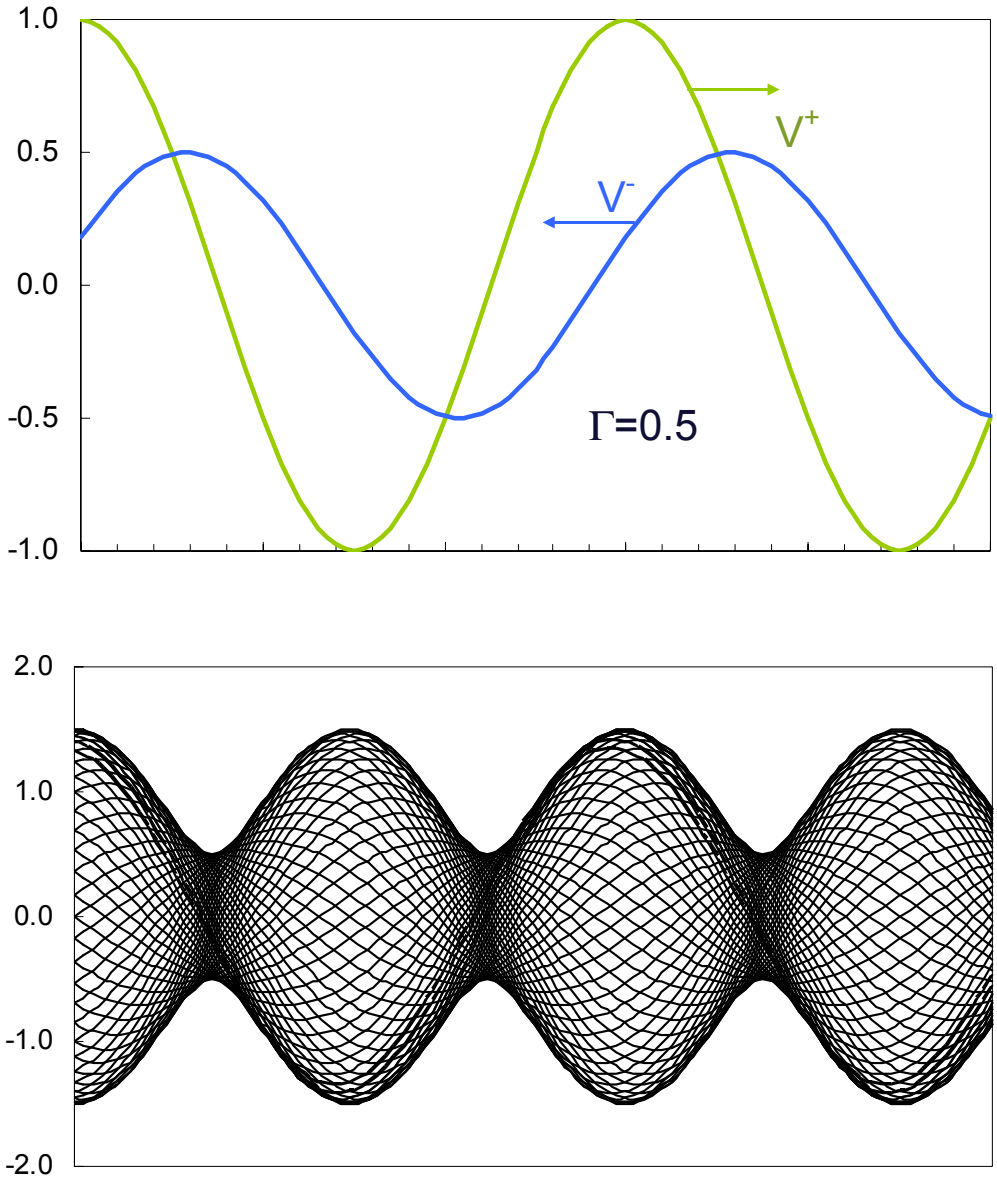

Figure 5. (Top) The forward and backward velocity components of an acoustic wave. The backward wave is a reflection of the forward wave at the right wall. The reflection coefficient in this case is 0.5. (Bottom) The resulting standing wave envelope of summation of the waves that are reflected back and forth.

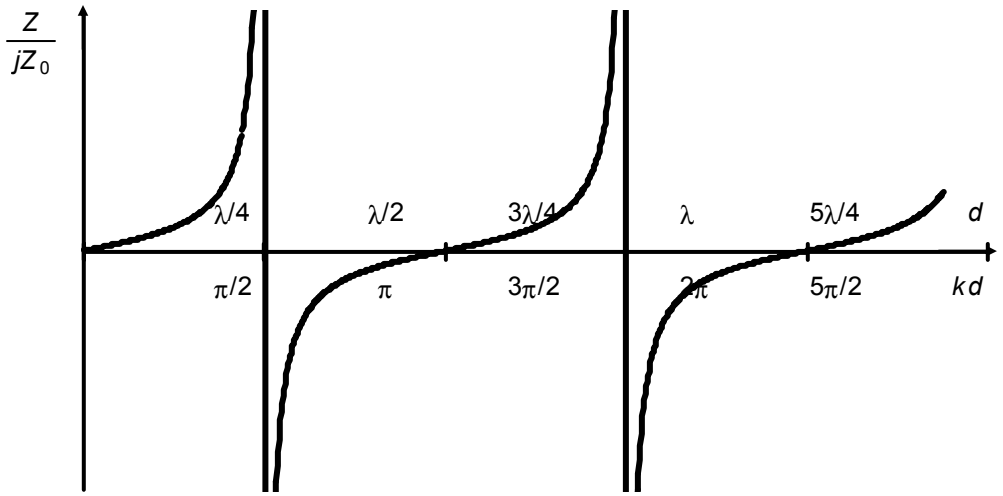

Figure 6. The acoustic impedance, Z, normalized to the material characteristic impedance, Z_0, is plotted as a function of distance, d or kd, from pressure release wall in cavity due to the established standing wave pattern.

This knowledge will aid in designing the thickness of each of the layers since the position of the maxima and minima are critical to the behavior of the separation process as described earlier. In addition, placement of the maxima and minima at the proper interfaces will benefit the system in allowing power to be introduced into and confined primarily to the channel.

Transmission Line Models

A more rigorous approach to predicting the acoustic fields in this layered system is by using transmission line models. Acoustic waves and electromagnetic waves are similar and the theory of one can be used to describe the other. In this section, traditional transmission line theory will be used with some variable substitution ($I \rightarrow v$ and $V \rightarrow p$) to describe the acoustic system. Passive layers will be modeled as a 2-port network while the piezoelectric layer will be modeled as a 3-port network, all in series, Figure 7.

The piezoelectric crystal layer has two acoustic ports, as in the passive layer model, and an additional electric port. Krimholtz, Leedom and Mattaei [233] developed a model (KLM), based on the *Mason* model, for broadband transduction of acoustic and electric energy. This KLM model is shown in Figure 7 *bottom*. It is based on an electrical port tapped into the center of the transducer, halfway between to the two acoustic ports. The conversion of electric to acoustic (or vice versa) energy is represented as a transformer with a ϕ:1 turn ratio, with

$$\phi = k_T \sqrt{\frac{\pi}{\omega_0 C_0 Z_c}} \operatorname{sinc}\left(\frac{\omega}{2\omega_0}\right) \tag{46}$$

In this equation k_T is the acoustic-electric constant defined below in Equation 62. The function is also evaluated at the operating frequency, ω, with respect to the resonant

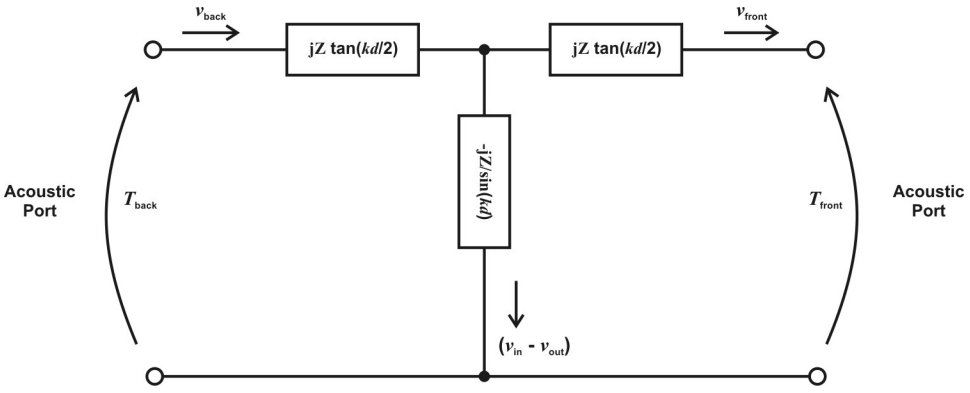

Two-port network

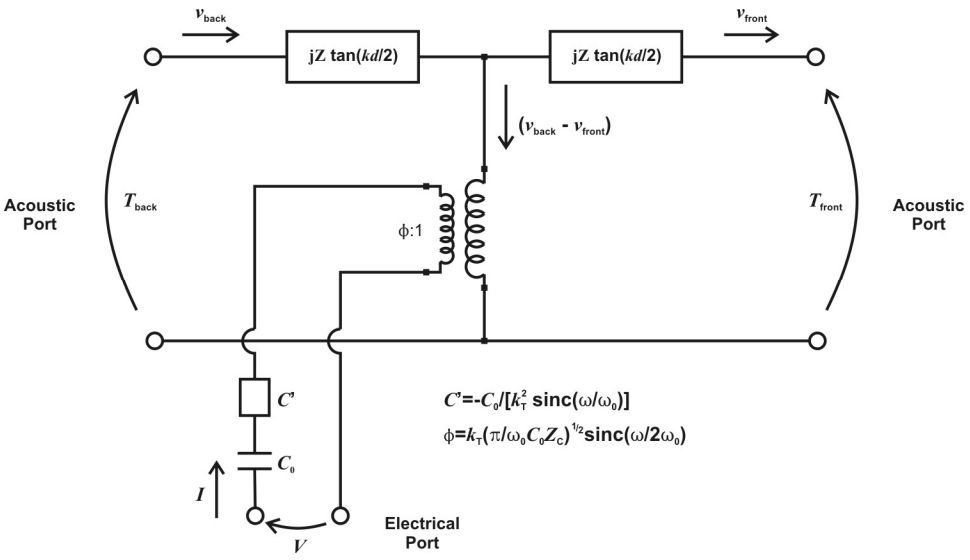

Three-port network

Figure 7. Network models of acoustic layers. (Top) Two-port network model of non-piezoelectric material. (Bottom) Three-port network model of piezoelectric material, including one electrical port and two acoustic ports.

frequency, ω_0. Also in this equation are the electrical capacitance, C_0, and the characteristic impedance, Z_c, of the transducer. This model also includes a fictitious negative capacitance, C', in series with C_0 and is defined as

$$C' = \frac{-C_0}{k_T^2 \operatorname{sinc}\left(\frac{\omega}{\omega_0}\right)}. \tag{47}$$

Wave Propagation in Solids (Crystals)

Since there are no isotropic solids used in this study, the theory will be confined to the specific case of acoustic propagation in crystals. The wave equation is determined by four principle equations: Hooke's law, Newton's law, definition of particle velocity, and definition of strain.

Hooke's law in three dimensions is used to relate normal stress (T_{xx}, T_{yy}, T_{zz}) and shear stress (T_{xy}, T_{yz}, T_{xz}) to normal strain (S_{xx}, $\boldsymbol{S}_{yy}$, S_{zz}) and shear strain (S_{xy}, S_{yz}, S_{xz}) through the stiffness matrix, $\mathbf{c}_{ijkl}$.

$$\mathbf{T}_{ij} = \mathbf{c}_{ijkl}\mathbf{S}_{kl} \tag{48}$$

Newton's law is that a force is the product of the mass and acceleration. This relation in terms of stress, **T**, and density, ρ, in three dimensions is

$$\nabla \cdot \mathbf{T} = \rho \frac{\partial \mathbf{v}}{\partial t} \tag{49}$$

The definition of particle velocity is the change in position, **u**, relative to time

$$\mathbf{v} = \frac{\partial \mathbf{u}}{\partial t}. \tag{50}$$

The definition of strain is the relative change in displacements with a change in position

$$\mathbf{S} = \nabla_s \mathbf{u} \tag{51}$$

The strain gradient, ∇_s, is used to transform the displacement vector, **u**, to the strain.

The wave equation in terms of velocity and in three dimensions, is derived from these four equations to be

$$\nabla \cdot \mathbf{c} : \nabla_S \mathbf{v} = \rho_0 \frac{\partial^2 \mathbf{v}}{\partial t^2} . \tag{52}$$

Simplifying and solving this wave equation results in the Christoffel equation

$$k^2 \mathbf{\Gamma}_{ij} \mathbf{v}_j = \rho_0 \omega^2 \mathbf{v}_i \tag{53}$$

and the Christoffel matrix, $\mathbf{\Gamma}_{ij}$, where *i* and *j* are from 1 to 3

$$\mathbf{\Gamma}_{ij} = \mathbf{l}_{iK} \mathbf{c}_{KL} \mathbf{l}_{Lj} . \tag{54}$$

The indices K and L are from 1 to 6 (xx, yy, zz, zy, zx, yx). This matrix is used to describe the propagation of mechanical waves in the three dimensions, where the direction is given by

$$\mathbf{l}_{iK} = \begin{bmatrix} l_x & 0 & 0 & 0 & l_z & l_y \\ 0 & l_y & 0 & l_z & 0 & l_x \\ 0 & 0 & l_z & l_y & l_x & 0 \end{bmatrix} \tag{55}$$

and

$$\mathbf{l}_{Lj} = \begin{bmatrix} l_x & 0 & 0 \\ 0 & l_y & 0 \\ 0 & 0 & l_z \\ 0 & l_z & l_y \\ l_z & 0 & l_x \\ l_y & l_x & 0 \end{bmatrix} \tag{56}$$

By solving the Eigen value problem with Γ_{ij}, the resulting Eigen values, λ_e are used to determine the three phase velocities possible, all of which are orthogonal to each other. The acoustic phase velocities, v_a are determined by

$$v_a = \sqrt{\frac{\lambda_e}{\rho}}\,. \tag{57}$$

The phase velocity is used in conjunction with Equation 45, the impedance in an acoustic standing wave, to determine the appropriate thickness of the layer.

Equation 54 is sufficient to describe a crystal in which its strain is only coupled to a shear, see the section on *Silicon* below. This is not the case in a piezoelectric crystal where the strain is also coupled to an electric field, as described in the *Lithium Niobate* section below. Two more terms are required in the Christoffel matrix to describe this coupling: the piezoelectric matrix, **e** and the permittivity matrix, **ε**. For a piezoelectric material the Christoffel equation remains the same but the Christoffel matrix becomes

$$\mathbf{\Gamma}_{ij} = \mathbf{l}_{iK}\left(\mathbf{c}_{KL} + \frac{\mathbf{e}_{Kj}\mathbf{l}_j\mathbf{l}_i\mathbf{e}_{iL}}{\mathbf{l}_i\boldsymbol{\varepsilon}_{ij}\mathbf{l}_j}\right)\mathbf{l}_{Lj}\,. \tag{58}$$

The one dimensional direction vectors are defined as

$$l_i = \begin{bmatrix} l_x & l_y & l_z \end{bmatrix} \tag{59}$$

and

$$l_j = \begin{bmatrix} l_x \\ l_y \\ l_z \end{bmatrix}. \tag{60}$$

Again, by solving for the Eigen values of the Christoffel matrix, the phase velocities can be determined. This velocity can be used to determine the fundamental and harmonic frequencies of the crystal. The fundamental and harmonic frequencies of the crystal occur when the thickness is equal to odd multiples of half wavelengths, as described earlier.

In a piezoelectric medium, the phase velocities determined by Equation 58 are termed *stiffened*. There are also fictitious *unstiffened* phase velocities in a piezoelectric material determined by Equation 54. The difference between these two velocities is the degree at which the material couples the electrical energy to acoustic energy. This term is called the piezoelectric coupling coefficient, K^2, and is determined by

$$K^2 = \frac{\lfloor v_a \rfloor_{unstiffened} - \lfloor v_a \rfloor_{stiffened}}{\lfloor v_a \rfloor_{unstiffened}}. \tag{61}$$

The acoustic-electric coupling coefficient is defined as

$$k_t^2 = \frac{K^2}{1+K^2}. \tag{62}$$

A plot of k_t for each wave (one longitudinal and two shear) as a function of different cuts is useful in determining the appropriate cut based on the degree of coupling for both the wanted wave and the unwanted waves. This tool is used in the *Lithium Niobate* section below.

Silicon

The material used as the reflector plate is a lightly doped <100> silicon. For purposes of calculations the doping is ignored and pure crystal Si is assumed. This assumption is made due to the fact that the ability to control the thickness of the Si is limited to approximately ±5 μm (using the methods used in this thesis), which is above the error that is introduced from the change in phase velocity due to light doping.

Silicon is a cubic crystal system, class m3m; see Figure 8. The stiffness matrix, **c**, of Hooke's law for silicon is

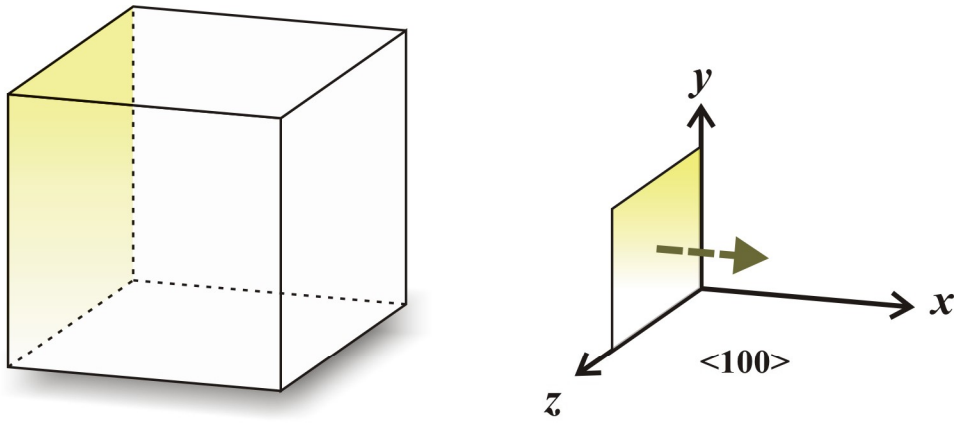

Silicon - *Cubic*

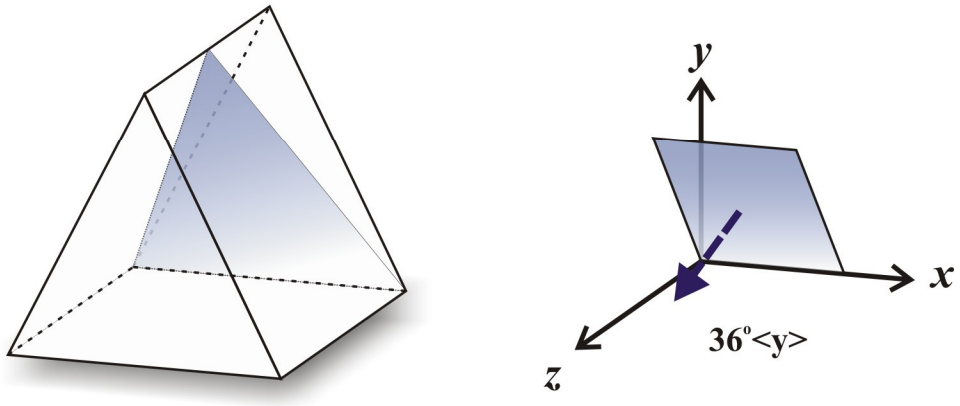

LiNbO3 - *Trigonal*

Figure 8. Crystal structure of two materials used in fabrication of the acoustic FFF system. The transducer is 36o y-cut Lithium Niobate (LiNbO3) and the reflector plate is <100> Silicon (Si). The vector shows the propagation direction of the longitudinal or quasi longitudinal wave.

$$\mathbf{c}=\begin{bmatrix} c_{11} & c_{12} & c_{12} & 0 & 0 & 0 \\ c_{12} & c_{11} & c_{12} & 0 & 0 & 0 \\ c_{12} & c_{12} & c_{11} & 0 & 0 & 0 \\ 0 & 0 & 0 & c_{44} & 0 & 0 \\ 0 & 0 & 0 & 0 & c_{44} & 0 \\ 0 & 0 & 0 & 0 & 0 & c_{44} \end{bmatrix} \tag{63}$$

with $c_{11}=166\times10^9$ N/m^2, $c_{12}=64\times10^9$ N/m^2, and $c_{44}=80\times10^9$ N/m^2. The specific gravity of silicon is 2.33.

For propagation normal to the surface of <100> Si (i.e. $l_x=1$, $l_y=0$, $l_z=0$), the Christoffel matrix becomes

$$\mathbf{\Gamma}=\begin{bmatrix} c_{11} & 0 & 0 \\ 0 & c_{44} & 0 \\ 0 & 0 & c_{44} \end{bmatrix}. \tag{64}$$

Solving the Christoffel matrix of a cubic system for the longitudinal wave along a major axis gives a phase velocity of

$$v_x=\sqrt{\frac{c_{11}}{\rho}}=8441\,{}^{m}\!/_{s}\,. \tag{65}$$

Plotting the inverse of the velocities, slowness in seconds per meter, of all three waves as a function of angle around the propagating axis, which in this case is a major axis, yields the results shown in Figure 9. The two shear waves are slower by nearly half over the longitudinal wave. The purpose for plotting slowness instead of velocity is to give an idea of how the power is either spread or focused. The power flow angle is normal to the surface of the slowness curve. Along the major axis, the power flow is in the direction of the axis and no spreading occurs.

The characteristic impedance for the longitudinal wave is

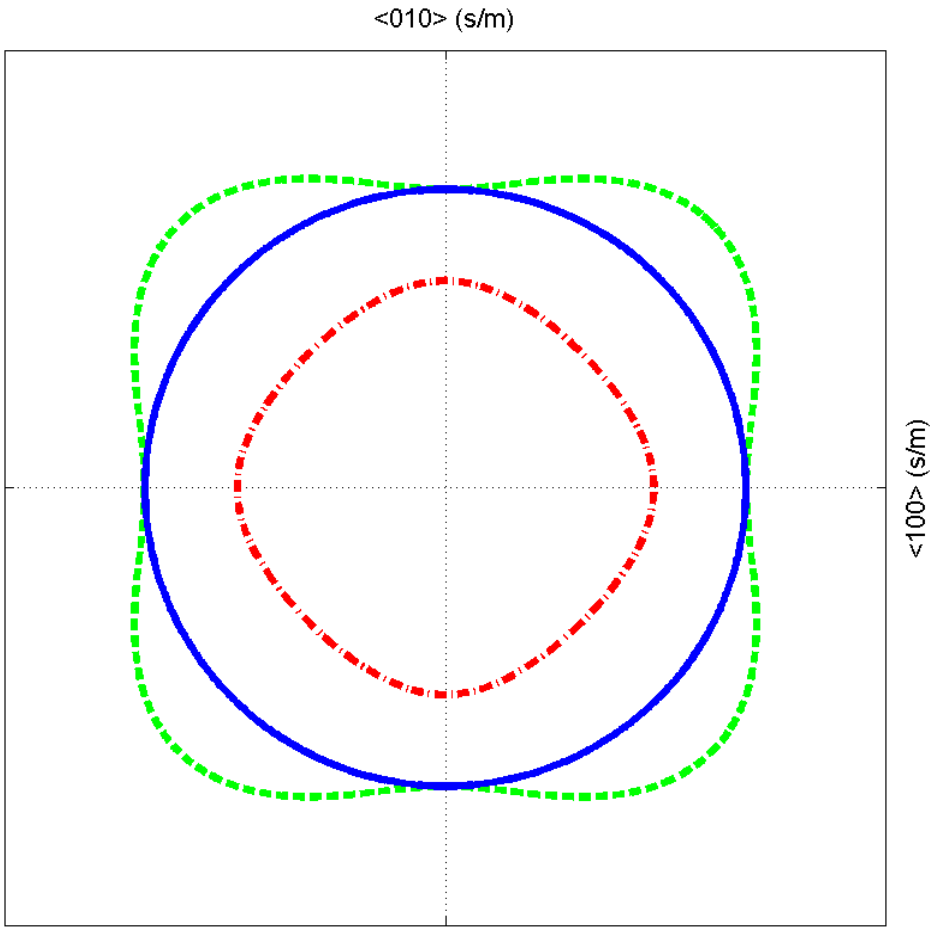

Figure 9. Slowness curve for single crystal silicon in two of the major planes. The inner ring (dash-dot curve) is the quasi-longitudinal wave; the two outer rings are the shear and waves. For propagation along a major axis (i.e. 0º, 90º, 180º, and 270º) the longitudinal wave has a velocity of 8441 m/s.

$$Z_0 = \rho v_x = 21 \text{ Mrayl} \tag{66}$$

Lithium Niobate ($LiNbO_3$ or LN)

The electrical to acoustic energy transducer used in this system was single crystal lithium niobate (LN). The design of the system (layer thicknesses) was based on the characteristics (piezoelectric coupling coefficient, speed of sound, thickness, and permittivity) of the LN crystal. The LN crystal orientation (cut) was chosen based on the following theory.

LN is a trigonal system crystal, class 3m, with 6 independent components. It is symmetric (3m) with respect to the *z*-axis, Figure 8. For this type of crystal, Hooke's law stiffness matrix is

$$\mathbf{c} = \begin{bmatrix} c_{11} & c_{12} & c_{13} & c_{14} & 0 & 0 \\ c_{12} & c_{11} & c_{13} & -c_{14} & 0 & 0 \\ c_{13} & c_{13} & c_{33} & 0 & 0 & 0 \\ c_{14} & -c_{14} & 0 & c_{44} & 0 & 0 \\ 0 & 0 & 0 & 0 & c_{44} & 2c_{14} \\ 0 & 0 & 0 & 0 & 2c_{14} & c_{66} \end{bmatrix}. \tag{67}$$

For LN, the values of **c** are: c_{11}=203×10^9 N/m^2, c_{12}=53×10^9 N/m^2, c_{13}=75×10^9 N/m^2, c_{33}=245×10^9 N/m^2, c_{14}=9×10^9 N/m^2, c_{44}=60×10^9 N/m^2, and $c_{66} = \frac{c_{11} - c_{12}}{2}$.

Two other matrices are necessary to describe the LN crystal because of its piezoelectricity. These matrices are the piezoelectric matrix, **e**, and the permittivity matrix, **ε**. The piezoelectric matrix for a trigonal 3m crystal is,

$$\mathbf{e} = \begin{bmatrix} 0 & 0 & 0 & 0 & e_{15} & 2e_{21} \\ e_{21} & -e_{21} & 0 & e_{15} & 0 & 0 \\ e_{31} & e_{31} & e_{33} & 0 & 0 & 0 \end{bmatrix}. \tag{68}$$

LN values of **e** are: e_{15}=3.7, e_{21}=2.5, e_{31}=0.3, e_{33}=1.3. The permittivity matrix for LN is given by Equation 69.

$$\boldsymbol{\varepsilon} = \begin{bmatrix} \varepsilon_{11} & 0 & 0 \\ 0 & \varepsilon_{11} & 0 \\ 0 & 0 & \varepsilon_{33} \end{bmatrix} \tag{69}$$

LN values of $\boldsymbol{\varepsilon}$ are ε_{11}=44 and ε_{33}=29. The specific gravity of lithium niobate is 4.64.

Because the symmetry about the *z*-axis of LN, it can be shown (it is not included in this these) to be less useful than cuts in other planes, such as about the *x*-axis. Phase velocities of the three waves in cuts about the *x*-axis are calculated by the stiffened and unstiffened Christoffel matrix and the results are shown in Figure 10, in terms of slowness, *s* (inverse velocity).

From the polar plot in Figure 10 and *x*-*y* plot in Figure 11 there are a few interesting features of LN around the *x*-axis. First, the longitudinal velocity, the inner curve, always has a higher phase velocity than the two shear waves. Second, one of the shear waves appears to have no piezoelectric coupling. And finally, there appears to be a few interesting angles at which there is a nearly maximum coupling to either the longitudinal or shear wave and complete isolation from the other. This can be seen more clearly by plotting k_t as a function of the angle in the *y*-*z* plane.

The first important angle is at 30° <*y*> where the longitudinal wave has maximum coupling. However, at an angle of 36° <*y*> the coupling is still quite high but the shear wave coupling is zero, so the longitudinal wave can be isolated.

The other two angles of importance correspond to the shear wave. Although the shear wave was not used in this research, it should be possible to build an acoustic-based FFF system with this cut as well as the longitudinal cut. The first angle matches with the

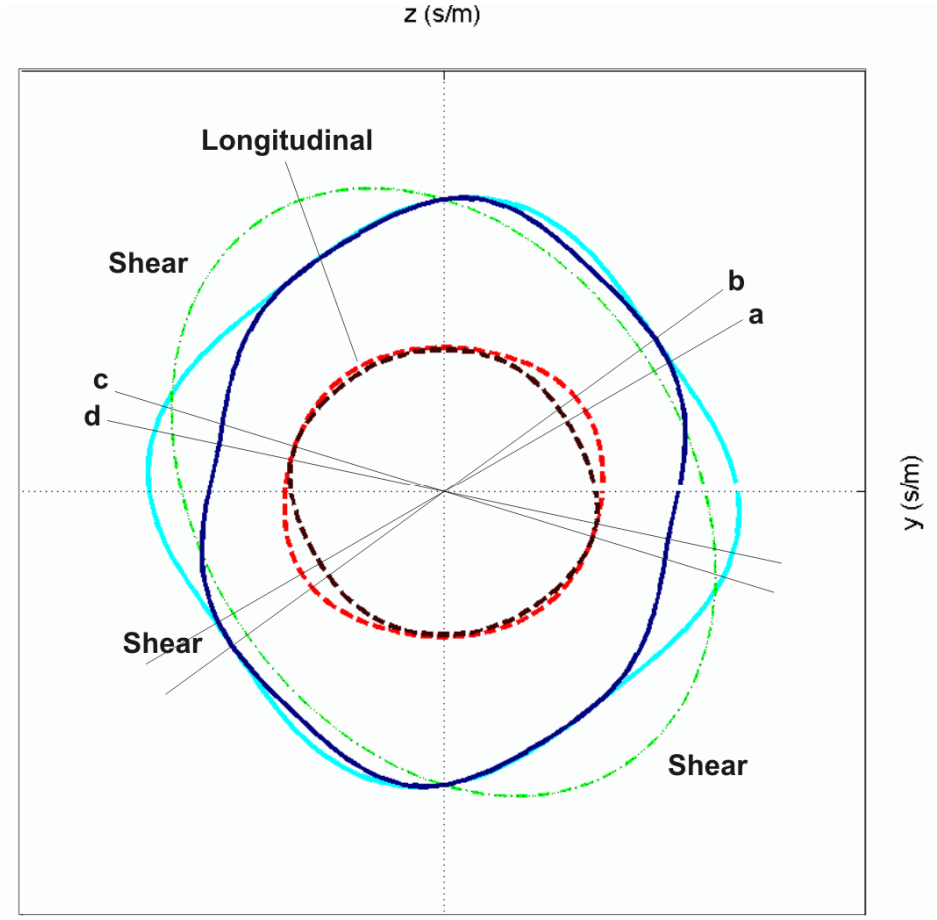

Figure 10. Slowness curve for single crystal Lithium Niobate. The three pair of curves are for unstiffened and stiffened phase velocities. The two outer pair is for the shear modes and the inner pair is the longitudinal mode. Cut a at30° <y> is the maximum longitudinal coupling (dash) while cut b at 36° <y> has no shear (solid) coupling. Cut c at 163° <y> is the maximum shear coupling while cut d at 168° <y> has no longitudinal coupling. The second shear mode (dash-dot) has no coupling at any angle.

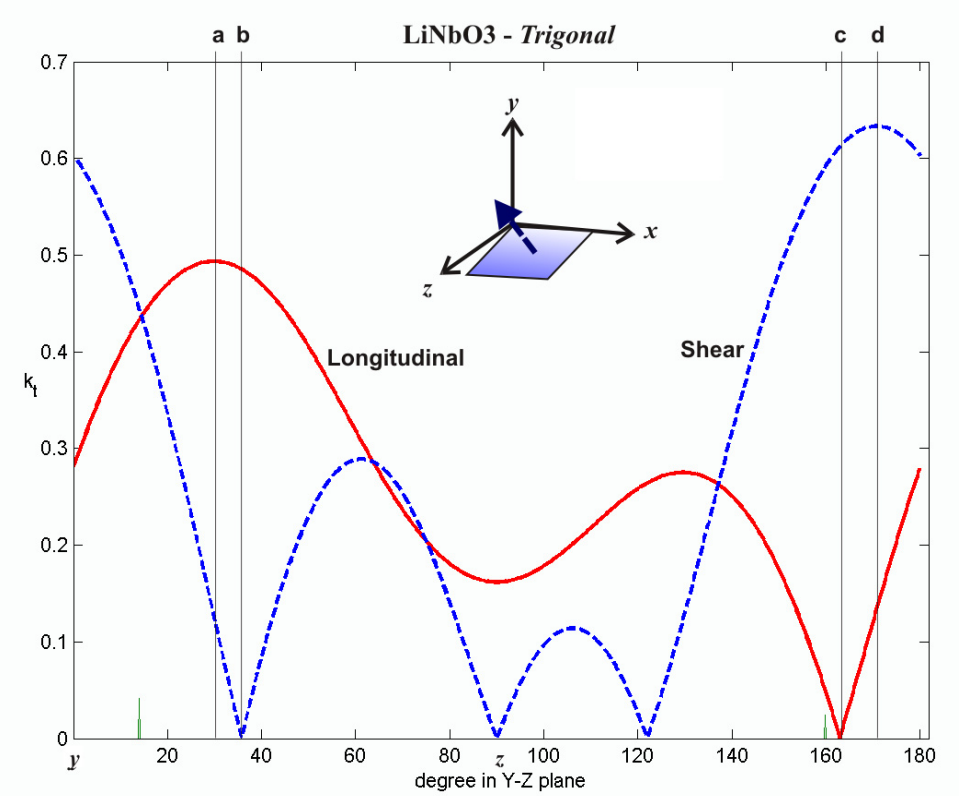

Figure 11. Plot of piezoelectric coupling in Lithium Niobate as a function of the angle around the x-axis. Cut a at 30° <y> is the maximum longitudinal coupling (solid) while cut b at 36° <y> has no shear (dash) coupling. Cut c at 163° <y> is the maximum shear coupling while cut d at 168° <y> has no longitudinal coupling. The second shear mode has no coupling at any angle.

maximum coupling of the shear wave at 163° <*y*>. At 168° <*y*>, there is zero coupling of the longitudinal wave but still high coupling of the shear wave.

The cut chosen is the 36° <*y*> LN. The phase velocity of the longitudinal wave at this angle is determined to be 7387 m/s. This thickness of the crystal obtained was 505 μm. The resonant frequency of the system then is calculated to be about 6.08 MHz.

Thermal Field-flow Fractionation Theory

When field-flow fractionation was first introduced by Giddings in 1966 in a Communication in the journal, *Separation Science*, he mentioned a few possible subtechniques of FFF. These subtechniques were electrical, magnetic, thermal, and gravitational, as well as any other force field that could be thought of. Although ThFFF is a subtechnique of FFF and in general does follow the theory outlined for general FFF systems, there are specifics not covered in the general FFF theory and even some deviations from this theory that are important to note. These deviations may introduce error into the calculation of physical parameters from the experimental measurements, such as retention ratios.

Solvents and Samples

Besides the field employed to induce sample migration, another major difference in ThFFF from other FFF subtypes is the carrier fluid used. In ElFFF and other subtypes, it is common to use low ionic concentration water. Water is typically inexpensive and easy to come by. It also is compatible with many of the FFF systems in terms of degradation and operation. This is not the case for ThFFF. Water was traditionally not used for several reasons. First, ThFFF was originally used primarily for dissolved

polymer separations. One common solvent/sample system that is commonly used for calibration of ThFFF is linear polystyrene dissolved in tetrahydrofuran (THF). Water typically does not dissolve polymers well. The second reason is that water does not support thermal diffusion well. Solvents such as THF have a much higher thermal diffusion than does water.

Dissolved samples, polymers in particular, were originally used for ThFFF retention and separation experiments whereas solid particles were not typically used. Some common polymers that have been used are: polystyrene (PS), polymethylmythacrylate (PMMA), polycarbonate (PC), polybutadiene (ABS), and others.

Retention in ThFFF

One of the unique characteristics of ThFFF that separates it from the other FFF subtechniques is its ability to retain samples based on factors other than just size. While ElFFF is capable of doing this to a degree, because its retention is based on the charge of the particle, ThFFF still is able to distinguish between even more complex samples than just a difference in charge or size. In this section, a review of the retention parameters involved in ThFFF will be explored.

As stated in the previous section, a sample layer of specific thickness is established when equilibrium between two opposing flux forces is achieved. One of these fluxes in induced by a field applied across the channel. As the sample concentrates due to this first force, a flux in the opposite direction is induced by the concentration gradient. This flux, J_D, is commonly known as ordinary diffusion or Fickian diffusion. A one-dimensional representation of this flux in the x-direction is given by Equation 70.

$$J_D = D\frac{\mathrm{d}c(x)}{\mathrm{d}x}. \tag{70}$$

Here the concentration gradient is given by $\mathrm{d}c(x)/\mathrm{d}x$ and the diffusion constant or diffusivity is given by D.

In ThFFF, the induced field is a thermal gradient, $\mathrm{d}T(x)/\mathrm{d}x$, in the x-direction. This is simply set up by maintaining a hot wall temperature and a cold wall temperature. The effect of a thermal gradient on a sample in the carrier fluid is a flux toward the cold wall. This flux is due to a phenomenon known as thermal diffusion. The one-dimensional equation for thermal diffusion, J_T, in the x-direction, see Equation 71, is identical to ordinary diffusion.

$$J_T = D_T\frac{\mathrm{d}T(x)}{\mathrm{d}x}c(x) \tag{71}$$

The thermal diffusion coefficient is represented by D_T. This constant is strictly empirical at this point, because it is still not well understood. The relation between D_T and the sample's physical characteristics gives ThFFF its unique separation abilities. The constants D and D_T will be talked about shortly.

At equilibrium, Equation 70 will be equal to Equation 71. The differential equation established at equilibrium is found in Equation 72.

$$\frac{1}{c(x)}\frac{\mathrm{d}c(x)}{\mathrm{d}x} = \frac{D_T}{D}\frac{\mathrm{d}T(x)}{\mathrm{d}x} \tag{72}$$

Solving for the concentration profile as a function of channel position, x, and using the approximation $\mathrm{d}T(x)/\mathrm{d}x \approx \Delta T/w$, gives

$$c(x) = c_0\exp\left[-\left(\frac{D_T}{D}\right)\left(\frac{\Delta T}{w}\right)x\right]. \tag{73}$$

The cold wall concentration of the sample is c_0. The value D_T/D is referred to as the Soret Coefficient and has a value typically between 0.001 K^{-1} and 0.01 K^{-1}. Equation 73 is equivalent to the general FFF theory, Equation 4. By equating the arguments in the exponent, an expression for λ can be obtained as in Equation 74.

$$\lambda \approx \frac{1}{\Delta T}\frac{D}{D_T} \tag{74}$$

This equation is also related to the sample drift velocity, U,

$$U \approx D_T \frac{\Delta T}{w}. \tag{75}$$

This relation also satisfies Equation 1 in the general FFF theory. The field strength, S', and the sample susceptibility, ϕ, parameters are found through the relation shown in Equation 76.

$$S'\frac{\phi}{f} = \frac{\Delta T}{w} D_T \tag{76}$$

Since the field strength is simply the temperature gradient (i.e., $S' \approx \Delta T/w$), then ϕ must be the ratio of D_T to the friction factor, f. These parameters, as well as the parameters for other FFF subtechniques are found in Caldwell [21].

Equation 76 shows that layer thickness and field strength in ThFFF is based on three factors: ΔT, D, and D_T. The parameter D and D_T "describe" the particle.

Ordinary diffusion is well known and has been related to the diameter of the particle, Equation 77, or the molecular weight of the dissolved sample, Equation 78.

$$D = \frac{kT}{3\pi\eta d} \tag{77}$$

$$D = \frac{kT}{3\pi\eta}\left[\frac{10\pi N_A}{3[\eta]MW}\right]^{1/3} \quad (78)$$

In these equations, kB is Boltzmann constant, T is the average temperature of the sample, η is the average carrier fluid viscosity, d is the diameter of the particle, N_A is Avogadro's constant, $[\eta]$ is the intrinsic viscosity of the dissolved sample, and MW is the viscosity average molecular weight of the dissolved sample. In Equation 78, $[\eta]MW$ is a measure of the sample hydrodynamic volume.

The thermal diffusion constant, D_T, is also related to sample physical parameters. However, thermal diffusion is not well understood despite its discovery nearly 150 years ago in 1856 [234]. Much research has been accomplished on the subject since then, but with few results in determining the mechanism behind the flux in liquids. Theory for gas thermal diffusion has been more successful [234]. Some researchers have tried to predict thermal diffusion with thermodynamics as an entropic effect, but often predicted the sign wrong. To date, the thermal diffusion constant is strictly empirical. For this reason, more data needs to be acquired to be able to establish the mechanism. Some papers have been published on sample compositional effects in polymers and block copolymers and carrier fluid composition effects. By reducing the analysis time in ThFFF for samples of known diameter or molecular weight, the collection of thermal diffusion constants can be obtained on a much larger scale. This benefit is one of the motivations behind the research of the μ-ThFFF system.

Retention data in ThFFF can be used to predict the diameter of the particle or molecular weight of the dissolved sample if D_T is known for the sample. If the sample d or MW is known then the thermal diffusion constant can be predicted. Often times the

ratio of D_T to the ordinary diffusion coefficient is reported as the Soret coefficient, σ, of the sample/solvent binary system.

Because of the dependence of retention on D and D_T, separations can be based on size difference for samples that have the same composition, chemical make up of the sample for samples of the same size, or a combination of them both. For this reason, ThFFF is an even more powerful analysis and purification tool over other FFF subtechniques. However, it is also much more complicated than other FFF subtechniques.

Plate Height

Band broadening, as represented by the plate height term, for general FFF was shown in equations 16, 17 and 18. Equation 18 represents the term due to polydispersity and is ignored at this point because it is not dependent on channel dimensions. Equation 16 is dominated by the nonequilibrium term and becomes equal to Equation 17. Appling equations for layer thickness (Equation 5), λ, and drift velocity for a thermal field (Equation 73), U, to Equation 17, yields the relation for plate height in a ThFFF channel, see Equation 79.

$$H = \frac{24D^2\langle v\rangle}{D_T^3}\left(\frac{w^2}{\Delta T^3}\right) \tag{79}$$

In this equation, the channel scaling effects on plate height in a thermal field are shown to be proportional to the width squared. In other words, the sample peak will sharpen as the separation proceeds, reducing the time required for the separation. However, the plate height is also dependent on the temperature difference across the channel to the third power. If the temperature difference is reduced to maintain a

constant temperature gradient, then the plate height will actually increase proportional to the channel width squared.

Resolution

The resolution for a general FFF channel, as given by Equation 21, is inversely proportional to the square root of the plate height. If the temperature difference is held constant for a separation, the resolution will be inversely proportional to the channel width, *w*. This effect is seen in Equation 80.

$$Rs = \frac{const}{\sqrt{H}} = \frac{const}{\boldsymbol{w}\, D}\sqrt{\frac{D_{\mathrm{T}}^{3}\Delta T^{3}}{24\langle v\rangle}} \tag{80}$$

However, if the temperature gradient is held constant for a given separation, as stated in the previous section, *Rs* will actually decrease in proportion to the square root of the width.

Analysis Time

The time required to separate a sample at a given resolution is given by Asten, et al. [235], as found in Equation 81.

$$t_a = \frac{64}{b^2} Rs^2 \left(\frac{\Delta M}{M_{avg}}\right)^2 \frac{D}{D_T^{2`}} \left(\frac{w}{\Delta T}\right)^2 \tag{81}$$

Similar to the analysis time for general FFF, the analysis time for ThFFF is proportional to the width of the channel squared.

Temperature Gradient and Cold-wall Effects

The discussion on retention in ThFFF in this thesis was based on several assumptions. These assumptions are a constant viscosity and thermal conductivity across

the channel. The discussion also ignored the dependence of retention on the cold-wall temperature. It is because of these effects that a universal calibration method for ThFFF channels has been difficult to come by. These effects have been studied, however. A universal calibration method for ThFFF was recently published [236]. This calibration is system or instrument transferable and takes into account the temperature gradient and cold-wall temperature. This calibration makes possible the accurate determination of polymer physical constants as a function of temperature even under different operating conditions. However, the calibration does not yet apply to different families of polymers and different solvent/polymer systems.

Retention is ThFFF is most importantly affected by the distortion of the velocity profile. The parabolic profile assumed in the general FFF model is due to a constant viscosity across the channel. In reality, the viscosity has a strong dependence on the temperature and is a function of the carrier used. Belgaid, et al. [20] state that differential form the Navier-Stokes equation, see Equation 82, used to determine the parabolic velocity profile in Equation 6 is not correct even when using the position dependent viscosity function, $\eta(x)$, in place of η.

$$\eta \frac{d^2 v}{dx^2} = \frac{dP}{dx} \tag{82}$$

In order for Equation 82 to be correct, a $d\eta/dx$ term must be included.

A further complication of solving the dependence of the flow profile on temperature is that dT/dx is not constant across the channel. This variation is due to the temperature dependence of thermal conductivity, $\alpha(x)$. This effect is generally small.

A complete treatment of these effects is found in Belgaid, et al. [20]. Only the results are presented in this thesis. The velocity profile is now given by Equation 83.

$$v(x) = 6\langle v\rangle\left[(1+v)\frac{x}{w} - (1+3v)\left(\frac{x}{w}\right)^2 + 2v\left(\frac{x}{w}\right)^3\right] \tag{83}$$

The parameter v can be obtained by equating the results of a rigorous determination of the velocity profile and the shear rate at the cold wall (from equation 35 [235], $6\langle v\rangle[1+v]x/w$). A plot of velocity profiles as a function of the parameter v is found in Figure 12. From this figure, the deviation from a parabolic flow profile, $v = 0$, can be significant. The result is applied to the concentration profile in equation 4 and the retention ratio, R, is isolated. The result from this treatment is found in equation 36.

$$R = 6\lambda\left\{v + (1-6\lambda v)\left[\coth\left(\frac{1}{2\lambda}\right) - 2\lambda\right]\right\} \tag{84}$$

Cao, et al. [236] state that this Equation 84is not necessarily accurate. The reason for this inaccuracy is from the strong, direct dependence of D on temperature, T, and the indirect dependence of D on temperature through the viscosity, η, and diameter, d, terms. Because the samples are compacting at the cold wall, the effects on retention are related to the temperature of the cold wall. The details, in accounting for the cold wall effect in determining a universal calibration, are found in Cao, et al. [236] and are not be reiterated in this thesis.

Scaling Effects in ThFFF

An examination of scaling effects in ThFFF will provide insightful information as to whether it is beneficial or not to use micromachining technologies to fabricate a ThFFF system. This examination will be done with a detailed look into the scaling each of the important process and system parameters that affect a separation and sample analysis in ThFFF. Although microfabrication methods have improved, made possible, and even

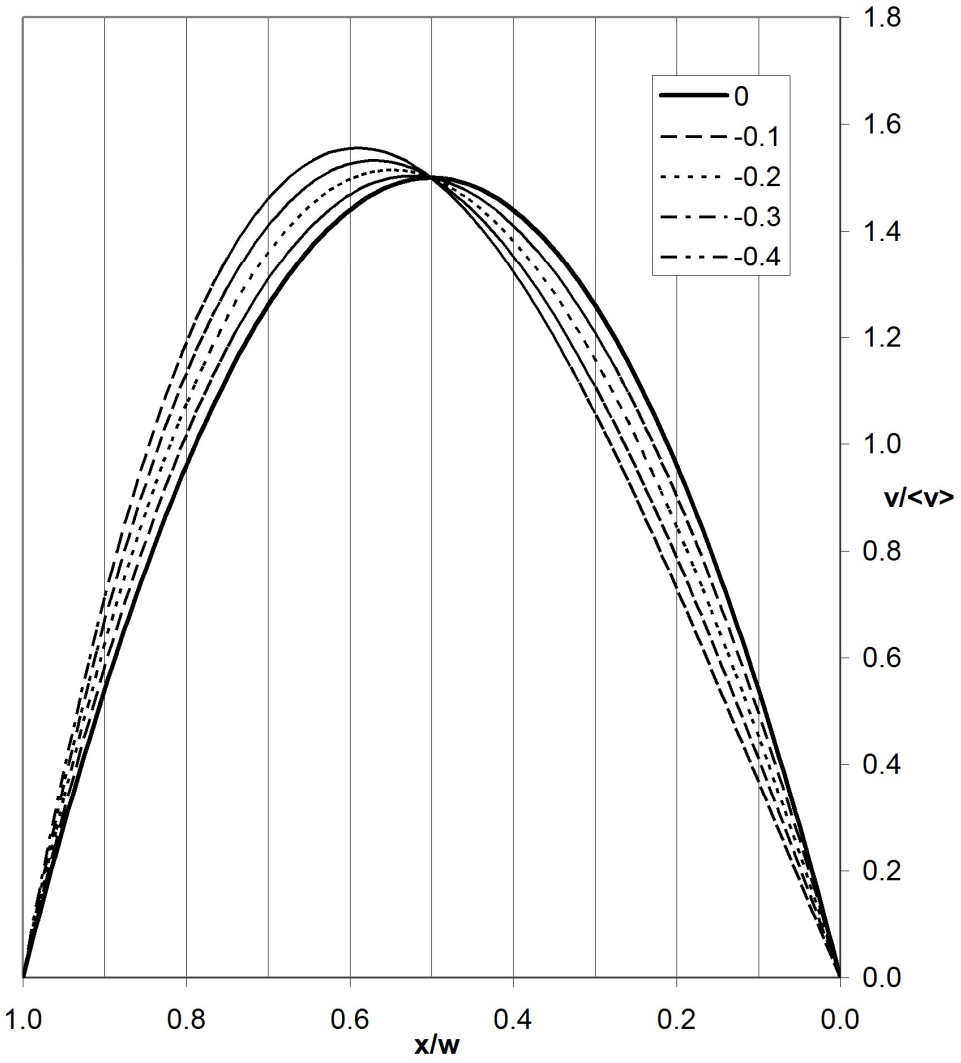

Figure 12. Velocity profiles of the carrier fluid for different values of v according to equation 36. The distortion of the velocity profile can be significant with values of v below –0.2.

revolutionized certain systems, it is not always beneficial to use such methods or even scale down a system. In some cases, macroscale or mesoscale fabrication methods are more cost efficient, or the system does not improve or may even regress in performance with smaller scale fabrication. It is important for the researcher to investigate all effects of scaling with a particular system before attempting miniaturization of the system.

Gale has presented detailed scaling information on both the general FFF and the ElFFF systems. To be consistent with his examination, the information for the general FFF system will be used from this source and compared with the ThFFF system.

Table 1 shows the scaling effects both for the general FFF system and for the ThFFF system. Afterward a detailed look into each of the listings in the table will be reviewed and discussed.

Sample size requirement, carrier fluid consumption, and instrument size: Both sample size and carrier fluid consumption are related to the void volume, V^0, of the system. The void volume depends upon three geometric parameters, so these parameters scale with the third power, s^3. Sample size is important in some cases where the sample is expensive or hard to obtain. This scaling parameter, however, is also limited on the lower end by the system detection limit. Sample overloading may also result if the sample is not scaled appropriately.

If the ThFFF system is to be as a portable analysis device in the field, the amount of carrier that the researcher carries may be of importance. The instrument size is typically dominated by the length. The width and height are typically much smaller, so the instrument size is more closely proportional to s. However, in ThFFF the heaters and cooling chamber add significantly to size and weight. With a scaled channel using

Table 1. Summary of scaling effects in general FFF and ThFFF systems. The scaling parameter, s, is typically the channel width, w, except in the cases of required sample size, instrument size, and solvent consumption, and Hp.

System Parameter	General FFF Scaling Factor	Advantage or Disadvantage	Thermal FFF Scaling Factor	Advantage or Disadvantage
Instrument Size	s^3	Advantage	s^3	Advantage
Carrier Fluid Consumption	s^3	Advantage	s^3	Advantage
Required Sample Size	s^3	Both	s^3	Both
Drift Velocity, U_x	1	Neither	$\frac{1}{s}$	Potential Advantage
Concentration Profile, $c(x)$	1	Neither	Exp(s)	Potential Disadvantage
Retention Ratio, R	$\frac{1}{s}$	Disadvantage	1	Potential Advantage
Steric Retention, R_{steric}	$\sim\frac{1}{s}$	Potential Advantage	$\sim\frac{1}{s}$	Potential Advantage
Plate Height from Nonequilibrium, H_n	$\frac{1}{s}$	Disadvantage	s^2	Potential Advantage
Plate Height from Polydispersity, H_p	s	Potential Disadvantage	s	Potential Disadvantage
Resolution, Rs	s	Disadvantage	$\frac{s(L)}{s(w)}$	Potential Advantage
Relaxation Time, τ	s	Advantage	s^2	Advantage
Analysis Time, t_a	s^2	Potential Advantage	s^2	Advantage

microfabrication technology, it has been shown that a portable ThFFF device can be manufactured on a three-inch, silicon wafer.

Drift velocity, U: This parameter is often used in FFF relationships. Improvements in the drift velocity lead to improvements in resolution, plate height, and analysis time. In general FFF systems, this parameter is not affected by the channel width if all other factors are held constant. However, because of the dependence of the field strength on w in ThFFF, the drift velocity becomes inversely proportional w. This relationship means improvements in U as the channel width is reduced.

Concentration profile, $C(x)$: The exponential dependence of the concentration distribution on the width will lead to a more tightly packed sample against the channel wall when the channel width is reduced. This effect may lead to sample overloading and increased sample-wall interactions, both of which are typically undesirable.

Retention ratio, R: It is desirable to increase the amount of retention (lower R value) of a sample while decreasing such parameters as size, power, and solvent consumption. Because of the inversely proportional relationship between w and R in general FFF, it is not advantageous to decrease the channel height. The retention ratio in ThFFF is not affected by the channel dimensions and so can be scaled without losing retention.

Steric Retention, R_{steric}: Retention in the steric mode is increased with scaling the channel width. This is only a potential advantage because the steric inversion point is also changed which will limit the range

Plate height from non-equilibrium effects, H_n: From equation 16, it appeared that the scaling effect is proportional to w^2, which is very beneficial when reducing w.

However, in the discussion following, reasons were given that might make a reduction in w a disadvantage. One of the advantages of reducing the size of the system is to conserve energy from the heaters. If this is the case, then the temperature gradient is maintained as channel size is reduced. This means the temperature difference also drops (thus the energy conservation). However, a drop in temperature is scaled by s^3, which gives an overall scaling of H to w, or simply, s. This scaling is equivalent to the general FFF scenario.

Plate height from polydispersity, Hp: This parameter scales with the length of the channel. A larger channel allows the peak to broaden more and so results in a more accurate analysis of the sample polydispersity or particle size distribution.

Resolution, Rs: The argument for Rs is the same as that for H. Assuming a constant temperature drop the resolution of the system scales inversely to the square root of s. If the system is operated under this condition then the effects of reducing w are beneficial. The same effect can be created by simply increasing the temperature of a larger scale system. However, there are limitations to the increase in temperature. These limitations are the boiling point of the carrier and degradation point of the samples. In addition, temperature differences that are too high may cause nonuniformities in the temperature distribution along the channel length. It may also make removal of the heat at the cold wall difficult, which is an important aspect of portable microscale systems.

Relaxation time, τ: This time parameter is not included in the analysis time parameter, but it does directly affect the amount of time required for a separation. In both the case of general FFF and ThFFF, the relaxation time is proportional w^2. Because of this relation, the benefits are excellent in minimizing this extra time requirement on

separations and analysis. This analysis follows that for the drift velocity, which is a basic measure of the relaxation time.

Analysis time, t_a: The time required to separate samples at a given resolution is based on the retention time of the last sample eluted. The analysis time is proportional to w^2. Since time is an important factor in most cases, it is very advantageous to reduce the channel width for improving this parameter. However, other factors are still influence by scaling w and must be considered concurrently.

Summary

Field-flow fractionation is a family of powerful analysis and purification tools similar to chromatography. Often FFF system complement chromatographic systems when combined together to purify samples. Because of the way in which FFF systems in general, retain samples, there are few benefits in reducing channel width. There are actually some disadvantages in scaling down the system channel. This case is for the FFF subtechniques in which the dimensionless layer thickness, or retention parameter, λ, depends on the width of the channel. Only in the case of thermal FFF is λ strictly not dependent on the width. In the case of ElFFF, the field strength is actually dependent on the width, so λ is not necessarily dependent on the channel geometry.

One of the arguments against scaling the channel is that the same beneficial effects on retention, resolution, and analysis time can be made by simply increasing the field strength. This is true. However, there are practical limitations to increasing the field strength. In ThFFF, the temperature gradient is limited by the carrier fluid boiling point and the coolant system used. In viable biological separations, the temperature limit may be the destruction of the cells or biomaterials being separated. Although the samples

are accumulated at the cold wall, they are often introduced at the hot wall and spread the entire channel until equilibrium is finally established.

The ultimate benefit of reducing the channel size is in the form of analysis time and separated sample purity. It was shown that the analysis time is reduced significantly when with the reduction in channel height. However, in the case of general FFF other factors are influenced that reduce the benefit of this scaled geometry. The retention ratio, plate height, and resolution are compromised. This compromise is generally not the case for ThFFF systems and is thus benefited by scaling.

Other important benefits come in the reduced size of the ThFFF system. Portability is important for researchers not in the laboratory. Microfabrication technologies allow integration of bulky heater and cooling systems, as well as the FFF channel, onto a small silicon wafer. The rate of consumption of solvents may be important when operating the system in a remote analysis site. ThFFF systems typically do not use water as a solvent. Carrying large amounts of organic solvents may be expensive and dangerous. The waste from the system is also minimized. Finally, the amount of sample required for a separation may be reduced with channel size. This is important when the sample is expensive or hard to obtain.

The benefits for reducing the ThFFF system are sufficient. For this reason, the fabrication of a μ-ThFFF system is researched and tested in this thesis.

CHAPTER 3

FABRICATION AND EXPERIMENTAL METHODS

Design and fabrication based on MEMS technologies and theory, covered in the previous chapter, will be expounded in detail in this chapter. The experimental tests will also be elucidated in detail for characterization of the microfabricated systems including plate-height examination for off-chip and on-chip detection, single-component polystyrene particle suspension retentions, and multiple component polystyrene component suspension separations. The chapter is divided into two major sections for the acoustic and thermal systems. Each major section is partitioned further into *Design and Fabrication* and *Experimental* subsections. An introduction into standard processes used in the fabrication of these two devices is a suitable place to instigate this chapter.

Microfabrication Techniques

Micromachining or microfabrication techniques originated from the microelectronics industry about 20 years ago. Common techniques used in the microelectronics industry are photolithography, thin film deposition, substrate etching (wet and dry), and others. The methods associated with the steps used in the fabrication of the μ-ThFFF channel and heater are described in detail in this section.

Photolithography

Photolithography is the process of using light to define regions in a photosensitive material that are later removed while the other regions are left behind. Two types of photoresist are used, positive and negative. When positive resist is used, the resist regions exposed to light are removed. Negative resist has the opposite effect. The basic photolithographic procedure, shown in Figure 13, is:

1. Deposit photoresist onto the substrate, usually by spinning.
2. Design mask with pattern to be copied onto substrate.
3. Cover the photoresist with the mask and expose to light.
4. Remove the exposed (positive resist) or the unexposed (negative resist) regions in the photoresist with developer.

Photomasks are typically made from chromium covered quartz plates. The chromium is covered with positive photoresist. Focused light is directed onto the resist while a computer-controlled stage moves either the light source or the mask to generate the pattern. The exposed chromium is etched away leaving the desired pattern. Alternatives to focused light are electron beams and X-rays.

Thin Film Deposition

Thin films are commonly found in micromachining used as masks, structures, membranes, insulators, dielectrics, electrodes, and other purposes. Commonly used films are silicon nitride (Si_3N_4), silicon dioxide (SiO_2), silicon carbide (SiC), metals, organic films, inorganic films, polysilicon, and polycrystalline diamond. In this thesis, Si_3N_4, SiO_2, and titanium metal thin films were used. The addition of films to a substrate is

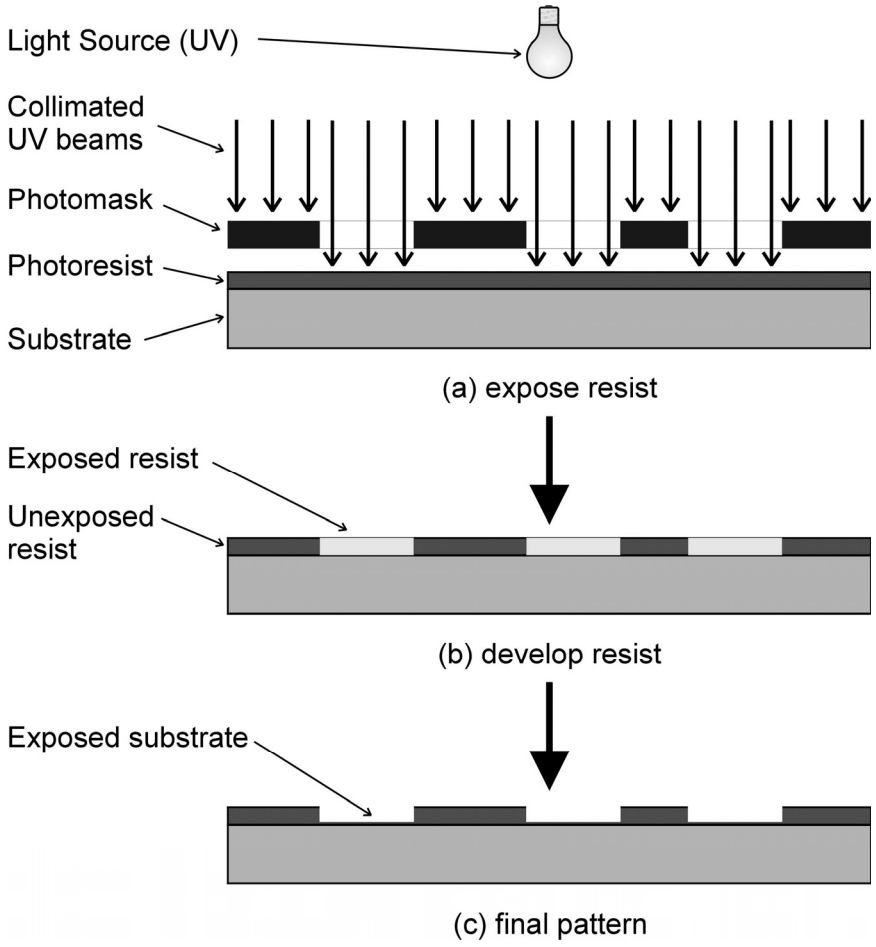

Figure 13. Steps representing the common photolithography technique. Regions of a substrate covered with photoresist are exposed to UV light, (a), as defined by a photomask. The exposed regions are developed, (b), away to expose the substrate, (c).

referred to as an additive process or surface micromachining, as opposed to a subtractive process or bulk micromachining.

Silicon dioxide, SiO_2, was used as an insulator and a mask for potassium hydroxide (KOH) etching of Si. The film thickness required was approximately 1 μm. Dry oxidation results in a high quality film, but is quite slow. For this thickness, a thermally grown "wet" SiO_2 process was used. The chemical reaction to form SiO_2 is

$$Si + 2H_2O \rightarrow SiO_2 + 2H_2 .$$

Two methods were used for wet oxide growth and both were successful. For the first method, the wafer was heated to 900 - 1150°C. Oxygen was distributed through a bubbler containing DI water and then passed through the furnace tube at a flow rate of 33 cm^3/min. This setup is shown in Figure 14(A). The deposition rate was estimated to be 1 μm per 11 hours at 900 °C and 1.5 μm per 6 hours at 1150 °C.

The second method, shown in Figure 14(B), used the same principle as the first method, but with a pyrogenic reaction (H_2 + O_2) to form water instead of the bubbler. The temperature was set to 1150°C. The deposition rate was estimated at 1μm in 1 hour and 45 minutes at this temperature.

An alternative mask to the silicon oxide was silicon nitride, Si_3N_4. It was deposited using plasma enhanced chemical vapor deposition (PECVD) by reacting silane (SiH_4) with ammonia in the presence of plasma. The theoretical reaction to form Si_3N_4 is

$$3SiH_4 + 4NH_3 \rightarrow Si_3N_4 + 12H_2 .$$

The silicon nitride is not always stoichiometric and can include hydrogen. The process may also include "pin-holes" in the film.

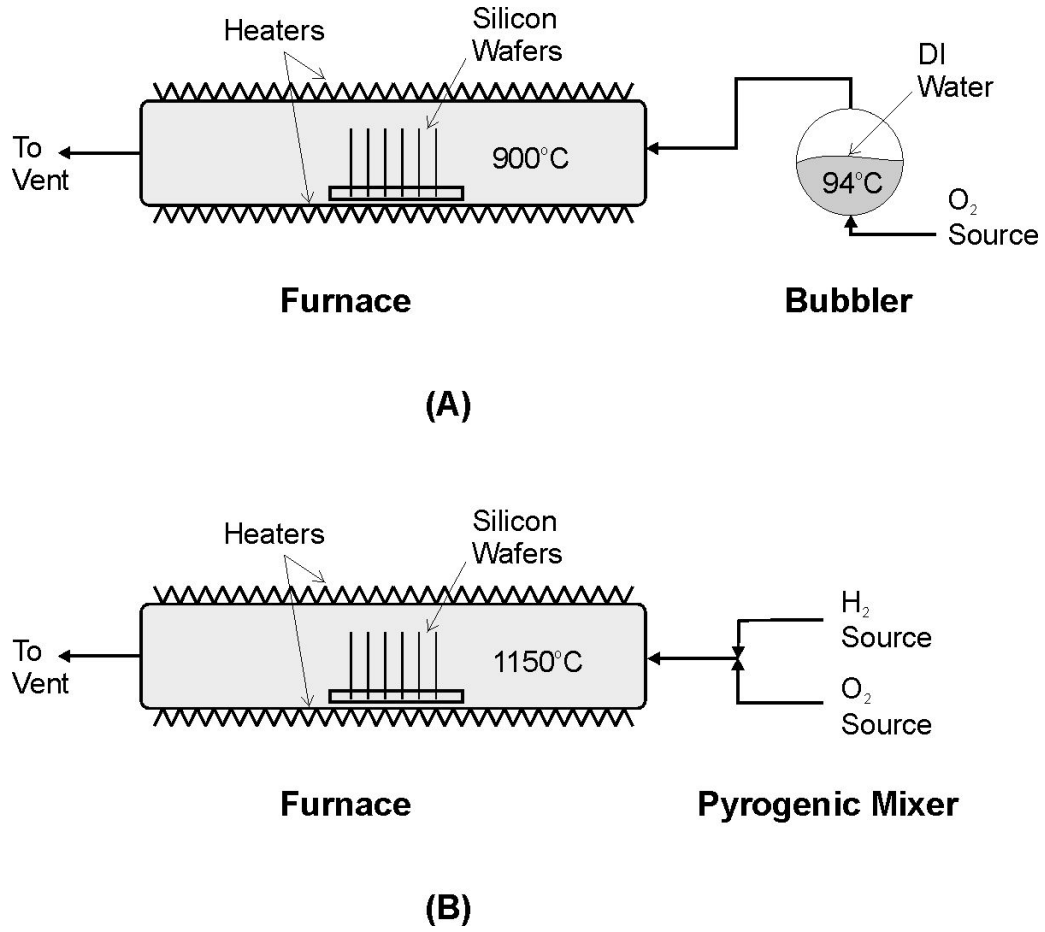

Figure 14. Setup of silicon dioxide deposition furnace. Setup (A) is using oxygen bubbled through DI water. The oxygen flow rate was approximately 33 cc/min. Setup (B) is a pyrogenic furnace where water is formed by combustion of H_2 and O_2.

The gases and flow rates in the deposition were: silane, SiH_4, at 23 mL/min, ammonia, NH_3, at 55 mL/min, and nitrogen, N_2, at 20 mL/min. The recipe alternated between high (8 seconds at 30 W) and low (4 seconds) frequency RF excitation to produce a very low stress film. The cycle ran 30 minutes to deposit 5000 Å Si_3N_4. Although silicon nitride has a negligible etch rate in KOH, the pin holes caused defects during the KOH etch process. The silicon dioxide etched considerably faster, but the film was continuous and left no defects. For this reason, SiO_2 was the film of choice.

Titanium was used for the heater in the μ-ThFFF system and a combination of titanium and gold was used for the electrodes on the AcFFF system. Metal deposition is accomplished in a low vacuum ($<10^{-6}$ Torr) environment. The two techniques used in these experiments were direct current (DC) sputtering and electron beam (E-beam) evaporation.

In DC sputtering the substrate is place in close proximity to the sputter target in the vacuum chamber. The sputter target is mounted to a liquid cooled electrode surrounded by a ground shield. A high potential field (approximately 400 V and 300 VA) is applied from the target to shield which dislodges metal atoms from the target. Under the high vacuum the atoms are able to travel the distance to the substrate. Because these molecules still have considerable energy after striking the surface they will migrate along the surface. For this reason sputtering is a conformal method, useful for depositing electrodes on structural sidewalls.

E-beam evaporation is also accomplished under high vacuum to allow the molecules to travel relatively large distances from the source to the substrate. The source in this case is the desired metal in a carbon (typically) crucible. A high energy electron

beam is deflected into the center of the metal. The energy evaporates the metal to form free drifting metal molecules. The energy of these molecules is much lower and therefore do not migrate upon striking the surface. This technique is useful when highly directional deposition techniques are required, such as in micro stenciling and lift-off processes, described later.

Wet and Dry Etching

Etching of films and substrates is referred to as a subtractive process or bulk micromachining. Bulk micromachining is often used for fabrication of channels, wells, holes or ports, cantilevered beams, membranes, and other structures. Because of the crystal structure of silicon and other materials common to micromachining, etching can be either isotropic or anisotropic depending on the etchants used. Etching can be accomplished either in a sealed chamber with gases (dry) or submerged in a liquid (wet). There are advantages and disadvantages to each but that will not be discussed here.

In the μ-ThFFF system, both wet and dry etching was used. Wet etching was used to pattern the silicon dioxide, create ports through the silicon wafer, thin the silicon wafer, and pattern the titanium heaters. As discussed later in this chapter, the wet etch of silicon is anisotropic when Potassium hydroxide (KOH) in DI water at an elevated temperature is used. The hydroxide ions react with the silicon forming highly soluble silicon compound and hydrogen gas. KOH is a strong base and should be handled carefully; it reacts readily with connective tissues without pain and will cause damage. Silicone dioxide or silicon nitride, as well as some metals, are suitable masks for KOH etching. Photoresists are not used as masks and any residual from previous processes will ruin the etch. Details on the KOH etch are given in the AcFFF fabrication section.

Since anisotropy was not necessary when thinning the wafer, another silicon etch was also tried. This etch is a mixture of hydrofluoric acid, nitric acid, and acetic acid called HNA for short. The etch rate and roughness of the etch is dependant on temperature, concentration and stirring. Gas bubbles form at the reaction site and do not release readily unless vigorous stirring is employed. Reaction rates as high as 400 μm per minute can be achieved but at the expense of rough surface characteristics.

Dry etching was used to pattern the silicon oxide and silicon nitride films and etch through the silicon wafer to form ports or stencil patterns. Dry etching was also used to remove unwanted silicon grass that formed during wet etching of the silicon substrate. One specific form of dry etching is termed reactive ion etching (RIE). This method uses a plasma to drive the reactive ions to the surface and also to aid in removal of the reacted species. For etching silicon with straight sidewalls, an inductively coupled plasma (ICP) RIE was used. This technique uses an inductor to drive the reactive species in a pattern that is highly directional and normal to the surface of the substrate.

Acoustic Field-flow Fractionation

Design and Fabrication

Design and fabrication of the acoustic FFF system is based on previous experience with the microfabricated ThFFF system with the exception of the transducer. Replacement of the thermal transducer with an acoustic transducer requires a look into the acoustic properties and thicknesses of each of the materials so that the proper acoustic standing wave can be established. In addition, the proper acoustic material must be selected so that the resonance frequency will yield a suitable wavelength for the FFF channel. The thickness of the transducer is critical to achieve this resonance frequency

and generate the power required for the acoustic force to drive the separations. The optimum setup is to establish ¼ of the acoustic standing wave in the separation channel. There are a couple of reasons for this setup being the optimum. First, according to Equation 6, the force can either be positive or negative based on the relative acoustic properties. This principle means that particles are driven to either the velocity nodes or anti-nodes. With the channel width at one quarter of the wavelength, there is only one node and one anti-node present, located at opposite walls. A half wavelength is also acceptable because the nodes are symmetric about the center of the channel, see Figure 15. With more nodes or anti-nodes present, the concentration profiles and the resultant retention parameter becomes more challenging to predict and may also lead to separation of identical component zones, resulting in multiple elution times for the same component.

The other reason for designing the channel at a multiples of quarter wavelengths is that the channel becomes a quarter-wave transformer, as in transmission line theory and is described in detail in Chapter 2. The transducer, channel and silicon wafer all act in conjunction to form an acoustic resonator. A quarter-wavelength thickness of the reflector layer will transform zero impedance at the reflector/air interface to maximum impedance at the channel/reflector interface. In the channel, the opposite is true so that a zero impedance will be established at the transducer/channel interface, which is otherwise a large mismatch and thus hard to input energy into this part of the system.

Field-flow fractionation requirements

The success of a FFF system is based on proper channel geometry, materials and configuration. As noted in Chapter 2, one of the requirements for proper fractionation is the establishment of a parabolic profile to allow for discrete sample velocities based on

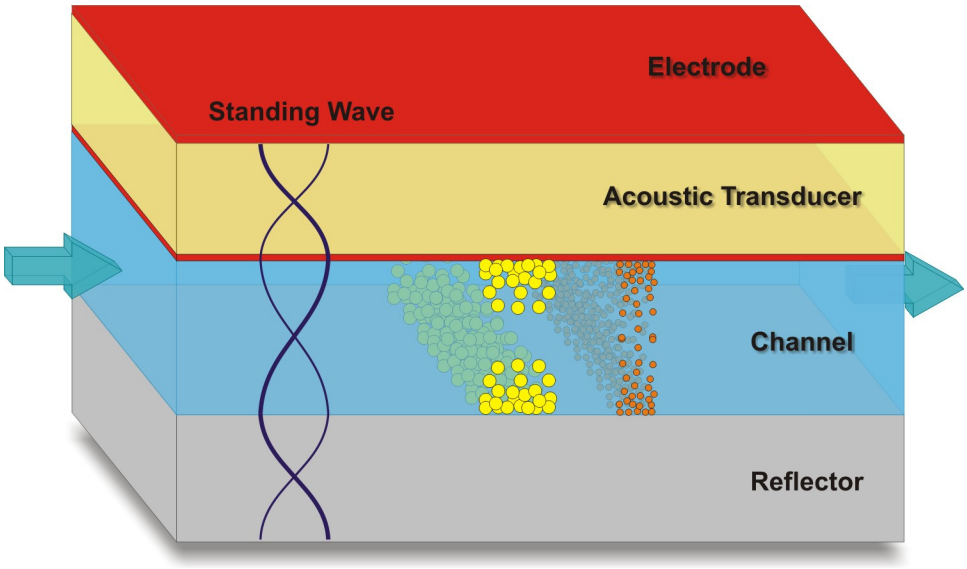

Figure 15. AcFFF separation modes. Particles can concentration at either the velocity nodes or anti-nodes based on their relative density and compressibility. The acoustic force is also based on size of the particle. The transducer is operated at the fundamental frequency of the system.

the sample layer thickness. Because of the rectangular channel geometry, two velocity profiles will exist; however, only one can be used for fractionation, the other will simply distort the sample and lead to secondary dispersion effects [237]. In order to minimize these secondary effects the channel is typically design with a breadth to width ratio of greater than 100. The profile in the breadth direction will more resemble plug flow rather than parabolic flow. The length of the channel must simply be long enough to allow the fractionation to occur to the degree of resolution desired between the constituents.

This channel geometry presents a fabrication challenge when considering channels with dimensions on the order of 10s × 100s × 1000s of microns. The channel is very wide and long relative to its thickness. Since uniformity is also critical to reducing secondary dispersion effects, these channels are difficult to fabricate, especially as the width decreases. Some challenges include channel uniformity with tightly controlled layer thicknesses, complete channel sealing, integration of active components such as the transducer and sample detection, and fluidic interfaces from micro to macro scales and sample introduction methods that will minimize band broadening.

Fabrication

Typical microelectricalmechanical (MEMS) based fabrication techniques were used to make the system. Figure 16 shows the overall process. The steps involved were: 1, wafer Thinning; 2, fluidic port etching; 3, metal electrode deposition; 4, channel patterning; 5, alignment and bonding; and 6, interconnections and test equipment. These steps are outlined in detail in the following sections named after each of the steps.

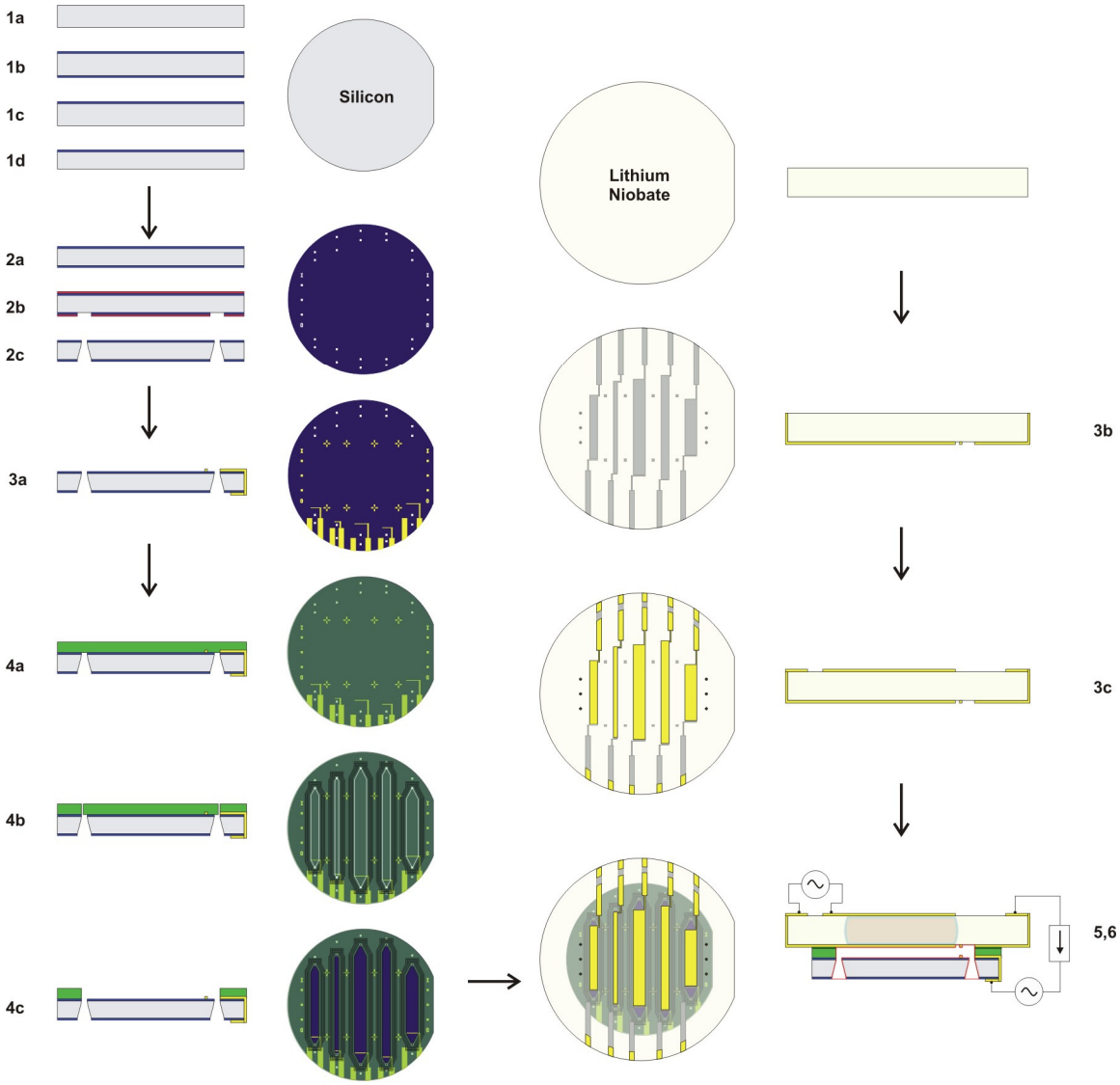

Figure 16. Fabrication steps for the microscale acoustic field-flow fractionation system. See text for details.

Wafer Thinning

Fabrication of the μ-AcFFF separation channels began with thinning a 3-inch, single-side polished, <100> silicon wafer to the appropriate layer thickness. A typical thickness for this wafer is an average of 380 μm. The required thickness is 349 μm to achieve the desired standing wave pattern. Several methods were available to thin the wafer. First, mechanical lapping and polishing was tried. The lapping procedure used a silica solution. The roughness of the silicon wafer was not critical, as the acoustic wavelength was much greater than the roughness, so scattering would not be a problem. This is the preferred method; however, due to inadequate equipment, this method was not reliable.

Chemical etching was also used to thin the wafer. Since one side of the wafer was already polished, it was desirable to mask this side and etch only from the rough side. The polished side was suitable for the channel wall since it was smooth and easier to pattern metal traces on. Two etches were tried, an isotropic and an anisotropic etch.

The isotropic etch was a mixture of hydrofluoric acid (HF), nitric acid (HNO_3) and acetic acid in a ratio of 5:5:90. The etch rate for this mixture was approximately 10 microns per minute. This mixture is referred to as HNA. The problem with this etch was finding a suitable mask for the polished side of the wafer. Any mask that would hold up to HNA, such as platinum, was very difficult to later remove.

The anisotropic method was the easiest to implement and was the method used in the fabrication of this device. For this etch 20 weight percent potassium hydroxide (KOH) was used, Figure 17. To accelerate the etch, the mixture was heated to a high temperature, about 80 – 95 °C. A lower temperature around 60 – 70 °C was used to

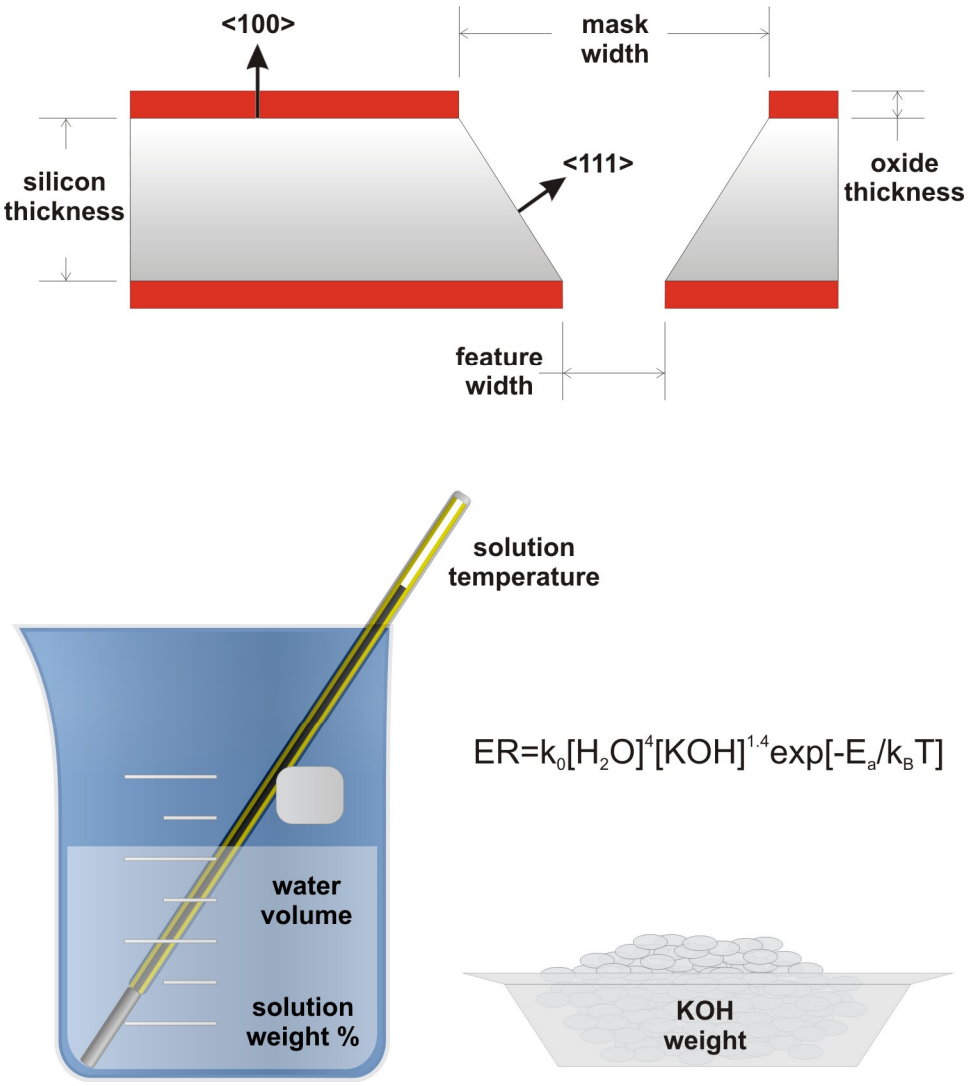

Figure 17. This is a figure of the KOH etch setup. The wafer was placed in the bottom of the graduated beaker and the beaker with solution and wafer was heated on a hot-plate until the desired temperature. The etch rate of <111> Si is much slower than in the <100> direction, as indicated by the top figure. Silicon dioxide, thermally grown was used to mask the silicon during the etch.

control thickness, uniformity, and roughness. The wafer was periodically removed from the etch, cleaned and dried to measure the thickness of the wafer. The thickness was measured using *Chicago* brand calipers with one micron accuracy.

Thermally grown silicon dioxide is a good mask for Si in KOH. The oxide was grown at 1100 °C for 6 hours in a steam injected oxygen environment. The polished side of the wafer was covered with *Shipley* 1813 positive tone photoresist and hard baked at 120 °C for 15 minutes. The wafer was submerged in buffered oxide etch (BOE) until the SiO_2 was removed from the wafer backside. The resist was stripped using acetone and methanol and then rinsed in DI water. The wafer was cleaned with a piranha etch (70% H_2SO_4 / 30% H_2O) and rinsed for 5 minutes in DI water (18 MΩ-cm), Figure 18.

Fluidic Port Etching

Two methods were used for etching fluidic access ports through the thinned Si wafer: inductively coupled plasma reactive ion etching (ICP RIE) and KOH. For the ICP etch a thick negative tone photoresist (*Clairant* AZ4620) was used to mask the front side of the wafer. The resist processing conditions are: 1000 rpm spin coat for 30 seconds, 115 °C soft bake for 2 minutes, i-line exposure for 45 seconds, develop in 4:1 *400k AZ* developer, and post bake 120 °C for 20 minutes. The wafer was mounted to another wafer using *Shipley* 1813 photoresist prior to the hard bake. This etch produced relatively straight sidewalls but took a long time due to equipment scheduling.

The second method was relatively quick and required very little equipment, and so was also much less expensive. The ports were anisotropically etched using KOH, Figure 17 and Figure 19. The mask was thermally grown SiO_2, the same as in the previous step. The mask was patterned using *Shipley 1813* PR with the following process

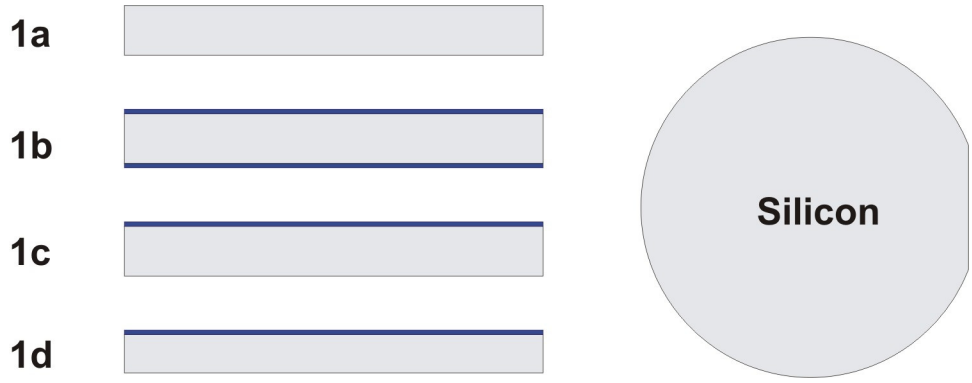

Figure 18. Step 1 of the fabrication process. A 3" <100> Si wafer was used after thinning it to the appropriate thickness. The blue layer is SiO_2, thermally grown to mask the polished side of the wafer.

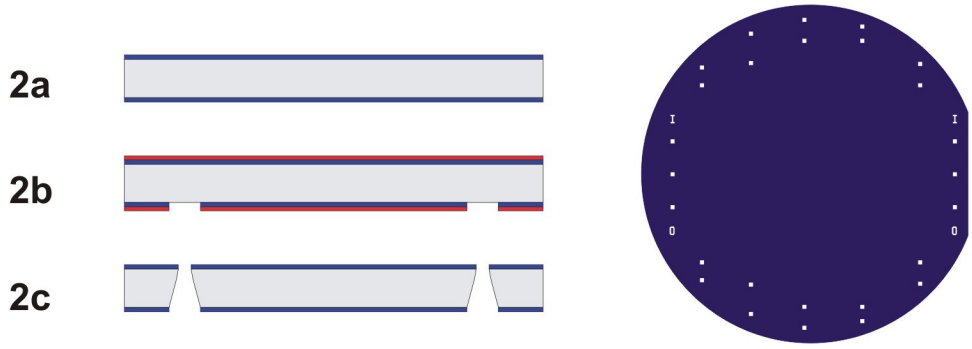

Figure 19. Step 2 in the fabrication process. The fluidic ports were etch through the wafer using KOH, a process similar to that used for the thinning step with the exception of the photolithographic patterning. The red layer is positive tone photoresist used to mask the SiO_2 in the BOE.

conditions for both sides (front side first): 3000 rpm for 30 second spin coat, soft bake at 100 °C for 3 minutes, *i*-line exposure for 8 seconds, develop completely in *Shipley* 352 developer, rinse thoroughly and dry, hard bake 120 °C for 20 minutes. The KOH etch bath was 20% by weight KOH in DI water held at 90 °C. The etch time was approximately 2 hours. The wafer was then cleaned in piranha etch (70% H_2SO_4 and 30% H_2O_2) and rinsed and dried thoroughly as in the previous step.

Metal Electrode Deposition

Metal electrodes are required on both the silicon wafer and the lithium niobate (LN) transducer, Figure 20. The transducer was 36º *y*-cut lithium niobate, 4" in diameter and 525 μm in thickness. The electrodes were all deposited using a micro stenciling technique. A stencil was used to ensure that any incompatibilities of the photolithography processes and metal etchants with the LN were avoided and made the process simpler and faster one the stencils were fabricated.

The stencil made out of silicon was fabricated using a process developed by Mohanty et al [238]. This process is identical to the ICP-RIE process used for etching fluidic ports through the silicon wafer. The electrode pattern to be transferred to the LN or silicon substrate was etched into the silicon stencil. The stencil was placed in contact with the LN or Si substrate and the desired metals were deposited using either sputtering or E-beam evaporation deposition techniques, Figure 21.

Two electrode sets were required for the AcFFF system: transducer electrodes and detector electrodes. The transducer electrodes were arranged on the wafer to define five distinct regions in which the LN could be activated. Each region contained one set of electrodes place on opposite sides of the LN wafer exactly overlapping. The electrode

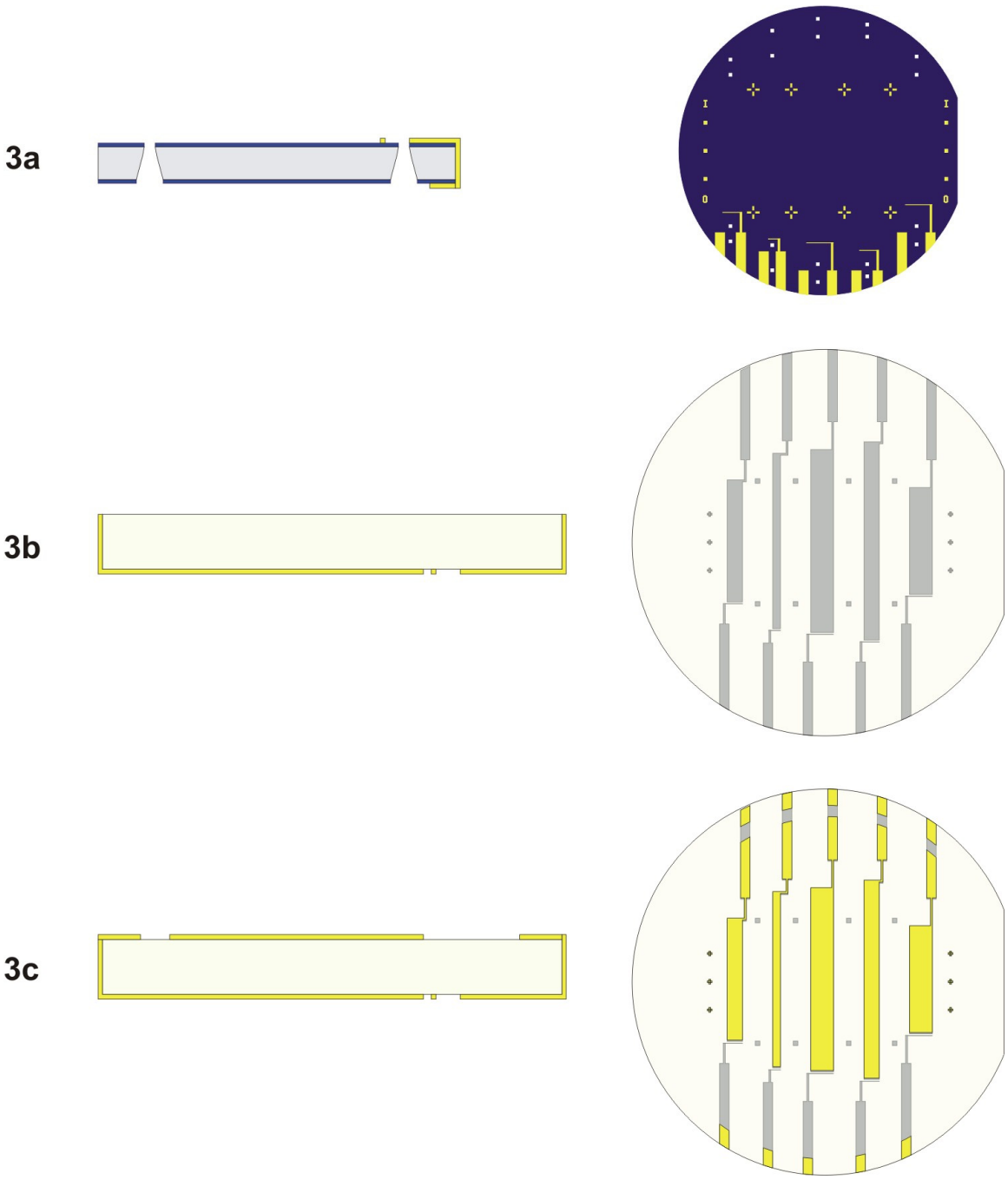

Figure 20. Step 3 of the fabrication process. This step includes metal deposition and patterning through a silicon stencil of detectors electrodes on 3a, silicon wafer, and 3b, front side of lithium niobate, as well as transducer electrodes on both the front and back side of lithium niobate, 3b and 3c. The metals are Ti/Au.

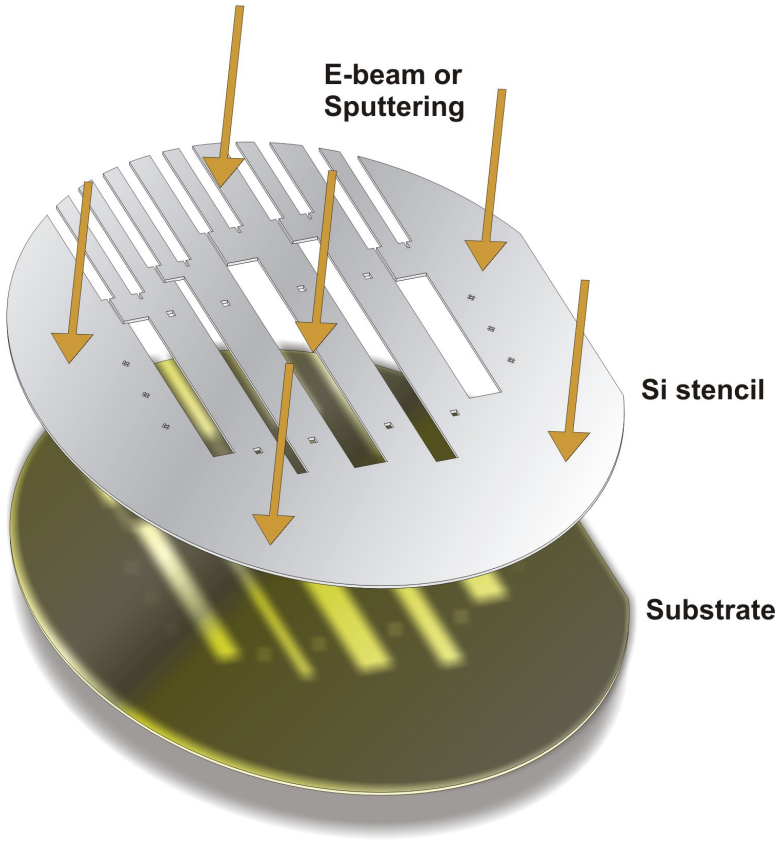

Figure 21. Silicon stencil fabricated by ICP-RIE (*Bosch*). The metal is deposited through the etched pattern onto the substrate. This figure shows a blow-up view of the deposition; in reality the stencil will be in contact with the substrate during the deposition. E-beam and sputtering techniques are used to deposit the Ti/Au electrodes.

on the channel side of the wafer was also wrapped around the edge of the wafer to allow for electrical interconnects to be made. The area of the overlap in the pair of electrodes formed a capacitor, C_0, which was discussed in Chapter 2. The metals used for these electrodes were chromium/gold (Cr/Au, 1000Å/2500Å).

The detector electrodes were thin wires (75 μm) with contact pads. One electrode was located near the end of the transducer electrode on the channel side of the LN wafer. The other electrode was located on the Si substrate (channel side) where it would exactly overlap with the other electrode when the two wafers were placed together to form the channel. The electrodes would be separated by a distance equal to the channel thickness as described in the next section. The detector electrodes were located near the exit region of the channel to be used as a concentration detector by measuring change in impedance as the sample passed by. The metals used for these electrodes were Cr/Au (1000Å/2500Å).

Channel Patterning

Next, the channel walls were formed using polydimethylsiloxane (PDMS), Figure 22. Prior to using this material, other materials (polyimide, SU-8, polycarbonate, polystyrene) were tried but with limited success. The first of these materials was SU-8. The pattern and process used for the μ–ThFFF system, was also used for the μ-AcFFF system. The problems faced with using the SU-8 were non-uniform thicknesses and uncontrolled thicknesses due to the edge bead. Because SU-8 is a rigid epoxy it required the addition of an adhesive to bond the channel to the transducer. This adhesive often changed the channel thickness to an unpredictable amount and also had difficulty in wetting and thus sealing the channel. This method was replaced using PDMS.

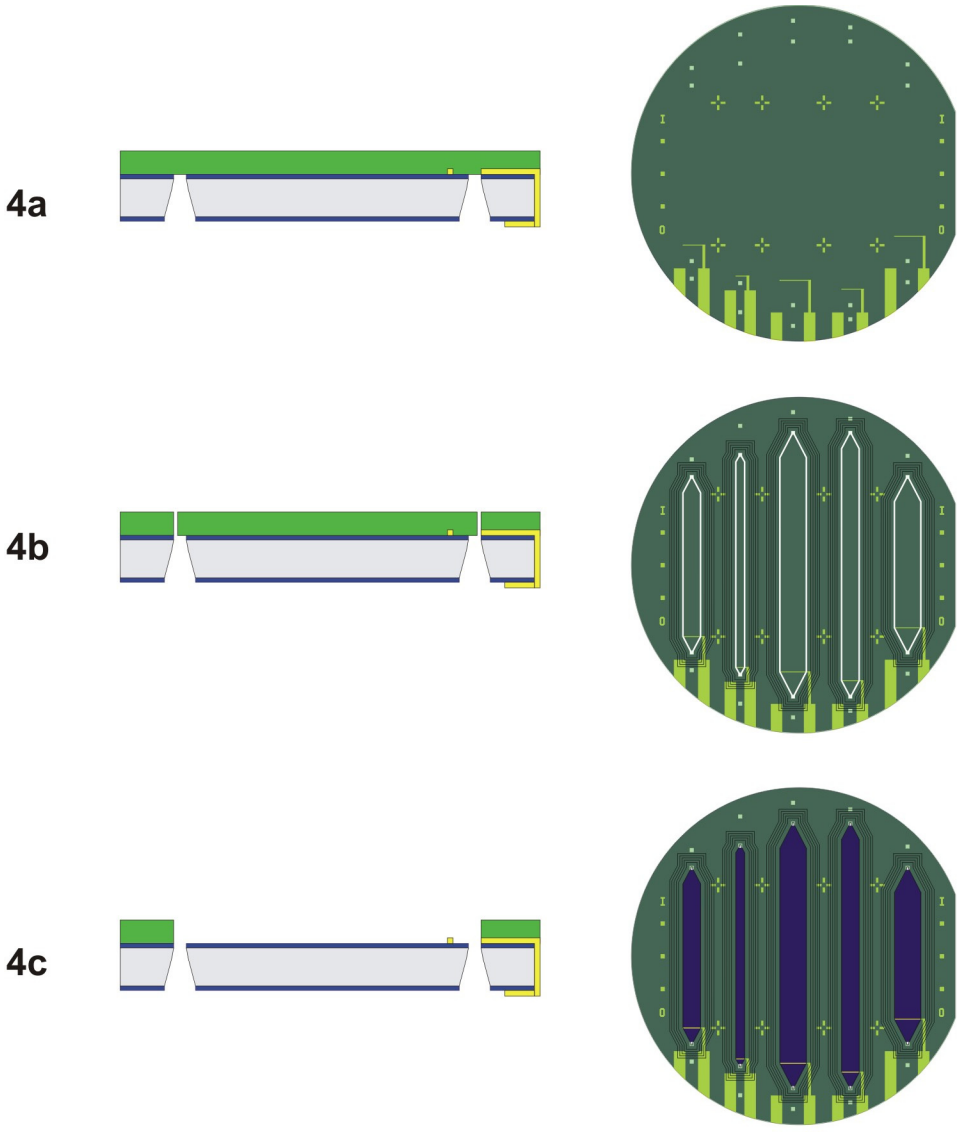

Figure 22. Step 4 of the fabrication process is the channel formation. Five channels were defined on a single wafer. The channels were formed by spin coating the wafer with PDMS, **4a**. The channels were defined in the PDMS using CO_2 laser ablation, **4b**. Finally the PDMS was removed from the channel areas, **4c**.

PDMS is an elastomer in its cured state. The particular PDMS used was *Dow Corning* Sylgard 184. The base and curing agent are mixed in a 10:1 ratio and degassed in a vacuum chamber. The uncured PDMS is then spin coated onto the silicon wafer and cured at the following process conditions: 1800 rpm for 30 seconds spin coat, and bake at 150 °C for four hours, Figure 22 (*top*).

The channel pattern was cut into the PDMS using CO_2 laser ablation. A *Gravograph / New Hermes* model 700XL laser ablation unit was used in conjunction with the associated *Gravostyle* layout software for the etch. The pattern was made in *AutoCAD 2004* and then imported into *Gravostyle.* The process conditions for the etch was: 1200 dpi, 10% power, 25% speed, single pass, air assist on high, and vector mode, Figure 22 (*middle*). The PDMS inside the channel was removed using tweezers and an X-acto knife. The PDMS was cleaned of ablated debris in an isopropanol and DI water rinse, Figure 22 (*bottom*). The formation of the walls completed the silicon half of the system.

Alignment and Bonding

The two wafers were bonded together using the PDMS spacer. Prior to bonding though, the PDMS surface was modified in an oxygen plasma. The oxygen plasma was generated in a RIE at 75 watts and 100 mTorr of O_2 for 5 seconds [239]. Visual alignment with the naked eye was used during placement of the top and bottom pieces, as exact alignment was not critical due to the large dimensions in the breadth and length directions, Figure 23.

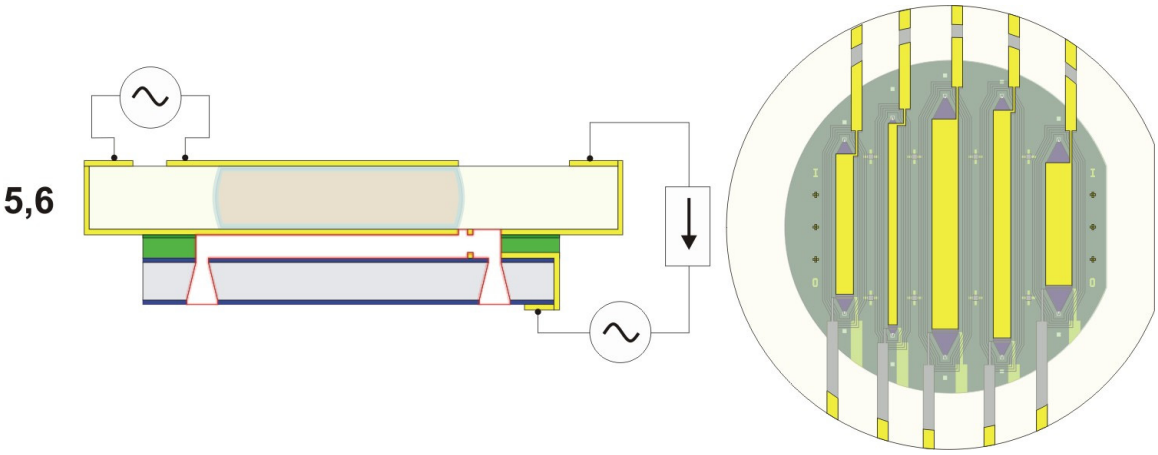

Figure 23. Step 5 of the process is to bond the two halves of the system together by treating the surface of the PDMS spacer with oxygen plasma. If the bonding is not complete then uncured PDMS can be painted onto the surface, bring the two surfaces in contact, and then allow the PDMS to cure. Step 6 of the process is to connect the electrical and fluidic (*not shown*) interconnects to the system and attach to the external equipment as described in the text.

In some cases the two pieces would still not bond completely by simply bringing them into contact with each other. In these cases it was necessary to apply a thin layer of uncured PDMS to the surface of the cured PDMS using a paint brush. Concentric rings were etched around the channel in the same pattern as the channel. These grooves increased the surface area for higher bond strengths, better sealing, and allowed for the extra uncured PDMS to wick away from the surface so as to maintain channel thickness. The PDMS was then allowed to cure at room temperature for 24 hours.

Interconnections and Test Equipment

Fluidic and electrical connections were required for this system. The electrical connections were made by bonding a 30 gauge wire using silver paste. The cure time for the silver past was 24 hours for a complete bond. The wires were also secured to the substrate using PDMS to prevent the silver paste bond from breaking. One wire was connected to each of the transducer electrodes and detector electrodes, four in all, Figure 24.

The two wires on the transducer were connected to a function generator (*Agilent 33250A*). This function generator was capable of 10 volts peak-to-peak maximum at a frequency of up to 80 MHz. The input impedance was also adjustable.

The detector electrodes were also connected to a function generator (*Agilent E3611A*) in series with the current ports in a digital multimeter (DMM, *Agilent 3458A*). This meter was capable of measuring currents from sub-microamperes to amperes. The expected current from the detector was a few to hundreds of microamperes. The DMM also had a GPIB connection to a personal computer (PC) running data acquisition and display software (*LabView 7.0*).

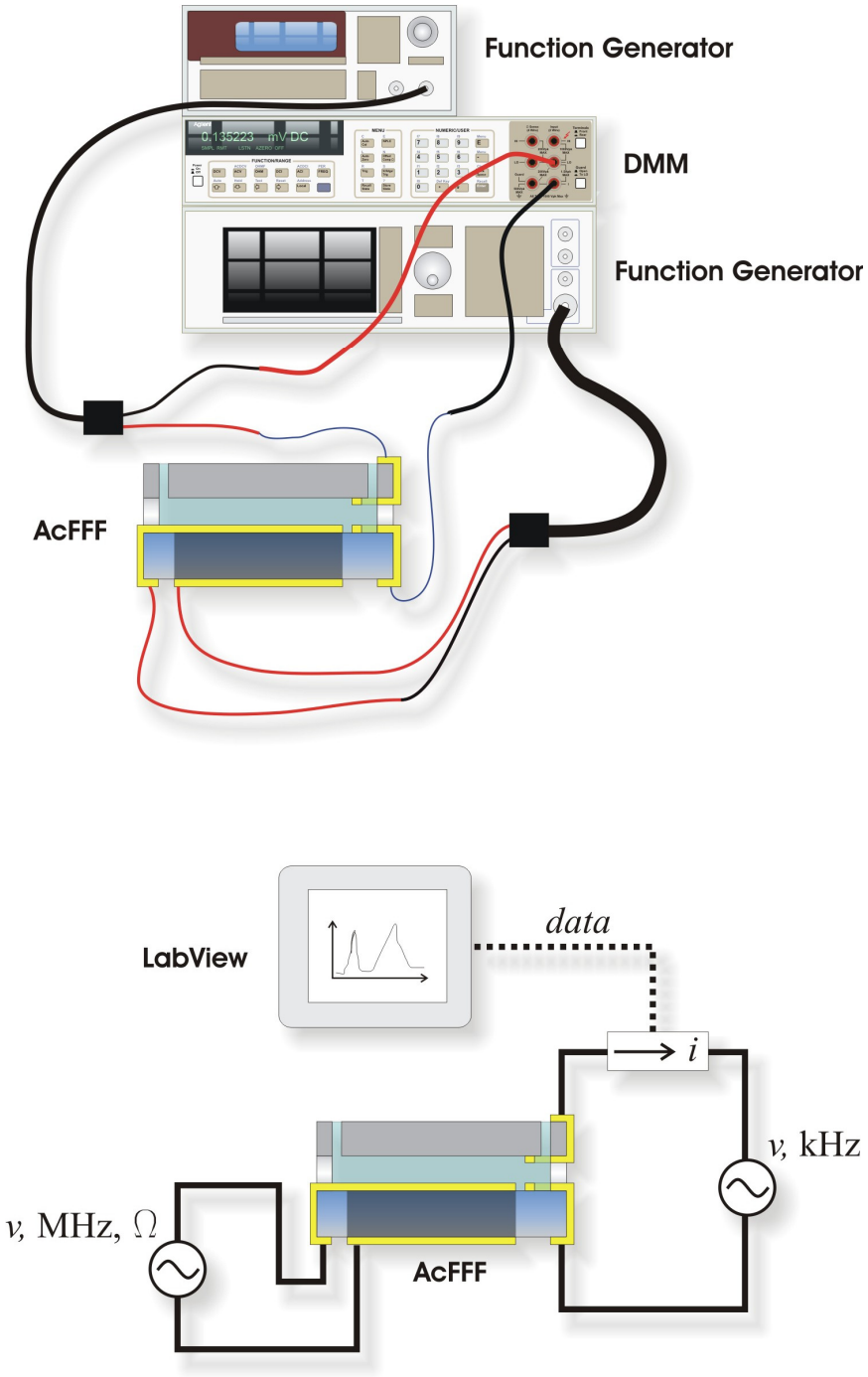

Figure 24. Electrical connections in the AcFFF system. *Top,* Physical layout of connections. *Bottom*, schematic of electrical connections and data acquisition.

A *LabView* program was written to interface with the DMM to acquire data points at an interval of several Hertz and then display the current as a function of time. The data were also recorded to disk in comma delimited ACSII format. The program also allowed for experimental conditions to be recorded as a header to this file. Process conditions included date, time, carrier fluid, carrier fluid flow rate, samples, sample sizes, channel dimensions, transducer operating conditions, detector operating conditions, and stop-flow times (if necessary). Details of the program are included in Appendix A. Sample raw data is shown in Appendix B.

The fluidic interconnection was made by bonding a 6-inch length, 100 μm inner diameter PEEK capillary (*UpChurch Scientific*) to the inlet port using fast cure PDMS (*Sylgard 170*). The capillary was connected to a fluidic tee connector (*UpChurch Scientific*). The opposite side of the tee was connected to a syringe (*Becton Dickinson* 30 mL) and loaded into a syringe pump (*kdScientific 100*) while the side port was stopped with a septum for syringe (*Hamilton* 1 μL*)* injection, Figure 25.

Tubing between the syringe and injection tee was 1/16-inch outer diameter polypropylene (*UpChurch Scientific*). In this line was placed another tee identical to the injection tee. The side port of this tee was connected to a pressure transducer and display (*Sigma PX180-015GV* and *Sigma DP41*). The pressure was measured to determine if the capillary or channel became clogged at any point which was indicated by a gradual rise in pressure.

This device is described in the Proposed Work, μ-AcFFF section. Data acquisition from the on-board impedance detector or the off-board UV extinction detector

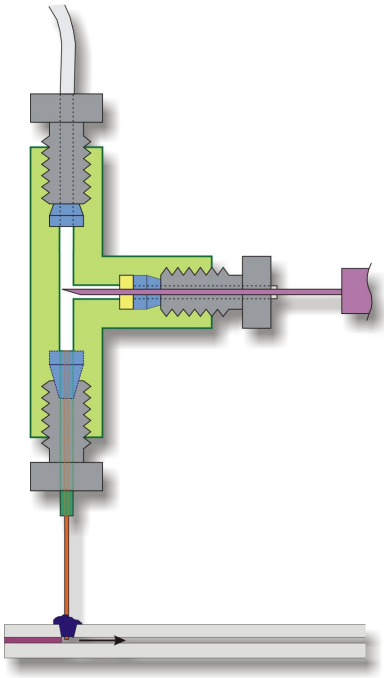

Top

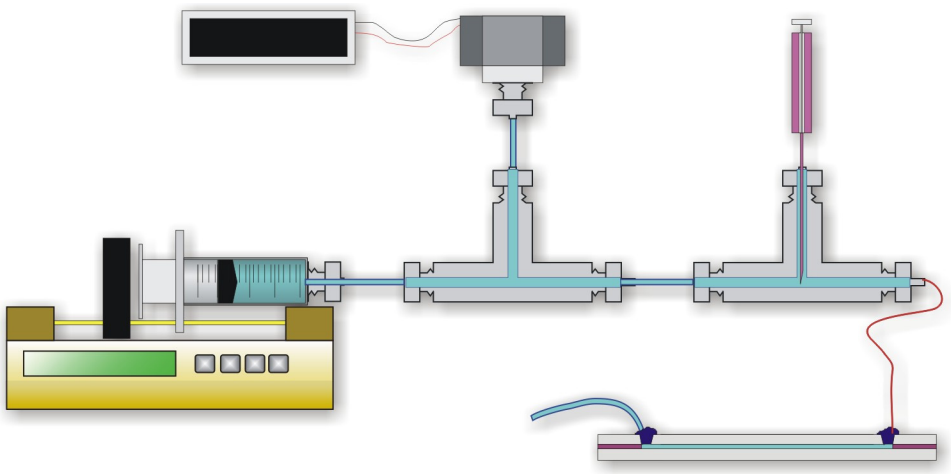

Bottom

Figure 25. *Top*, the fluidic interconnection scheme for introducing sample boluses into the carrier stream. *Bottom*, the overall fluid test setup for the AcFFF system including syringe pump, syringe, tubing, pressure transducer, tees, sample syringe, capillary, and FFF channel.

is accomplished through a multimeter (*Agilent 3458A*) connected through GPIB to a personal computer. The software used for data acquisition, storage and presentation is *LabView 7.0*. The graphical program has been written and tested on the μ-ThFFF system.

System Characterization and Experiments

The set of experiments used to characterize and validate the acoustic FFF system is described in this section. Characterization of the system involved interrogating the acoustic standing wave via the electrical input impedance and determining the instrument plate height. To validate the system was operating as predicted by the theory, a series of experiments in which various sizes of polystyrene particles in suspension were injected into the active system to measure retention and resolution. Each section below details the experimental setup and expected results. The results of these experiments are the focus of the next two chapters.

Modeling and Frequency Analysis

In order to determine the resonant frequency of the system and that the design was correctly implemented, the system input impedance was analyzed. First, the system was modeled used the KLM 3-port network model of a transducer in series with two 2-port network models of the channel and silicon as discussed in Chapter 2. The frequency range that was investigated was 1 MHz to 10 MHz. This frequency range was chosen because the system should be near the fundamental frequency of the crystal, 6.18 MHz.

The resonant frequency was determined by locating the frequency at which the electrical source voltage is in phase with the current. On the input impedance plot this resonant condition occurs where the phase is zero. The anti-resonant frequency also has

a zero phase. The magnitude of the impedance is minimum at resonance and maximum at anti-resonance.

The second portion of this experiment was measuring the input impedance on a fabricated micro-acoustic FFF system both with and without fluid in the channel. An impedance analyzer (*Agilent 4294A*) was used with standard Kelvin test leads (*Agilent 16089B*) for the measurement. The frequency range and analysis followed that for the modeling. The results were then compared with the model results.

In addition, a simple touch test was performed to ensure that the acoustic wave was at resonance throughout the entire system and not isolated to only the transducer. A finger was placed on either the transducer face or the silicon face and the impedance spectrum was recorded.

Plate height

The instrument contribution to band-broadening in the system was measured. The system was injected with a 0.5 μL bolus of 0.068 N NaCl solution in a DI water carrier. The extra-column volume was associated with pre-channel tubing which was 6-inches in length and 150 microns of inner diameter, or 2.69 μL. Also included with the pre-channel volume was the tapered entrance region with a volume of 0.471 μL. The active region of the channel had dimensions of 62 μm × 4 mm × 32.6 mm or 8.08 μL. The flow rate of the carrier was adjusted for each specific run and measurement. The on-chip detector was used to measure the current as the sample passed from the active region to the tapered exit region of the channel. The concentration of the sample was proportional to the current measured. The plate height of the sample can be extracted using the theory in Chapter 2. This plate height was then plotted as a function of the flow rate to give the

instrumental plate height of the system and was compared with other micro and macro-scale FFF systems, including both on-chip and off-chip detection.

Single component polystyrene suspension retention

Various sizes of polystyrene beads in suspension (*Bangs Labs*) were injected into the system in 1.0 microliter boluses to determine retention. The diameters used were 110, 210, 300, 1000, 4350, and 9100 nanometers. The sample concentrations of the 110 to 300 nm solutions were diluted to 0.1 weight percent from the stock solution of 10 weight percent. The 1000 to 9100 nm solutions were diluted to 0.1 weight percent from the stock solution of 1 weight percent. These larger beads were coated to fluoresce; although, fluorescence was not used in these experiments

The system was setup with the *x*-direction (direction of field) normal to gravity to eliminate any effects it may have on the particles, even though its effects were estimated to be very small. The detector electrodes were driven with a 2 kHz, 5 volt peak-to-peak signal. This frequency and voltage were determined by Gale and Frazier [29] to be optimum for measuring polystyrene suspensions.

The transducer was operated at the fundamental resonant frequency as determined by the previous set of experiments. This frequency was 6.08 MHz. The impedance of the function generator was adjusted to match the input impedance of the AcFFF system to ensure maximum power transfer. The voltage was adjusted in increments of 1 volt from 0 to 10 volts. The force on the sample is proportional to the voltage applied, so retention should be increased with increasing voltage. This phenomenon was noted and was also quantified through theory.

Multiple component suspension mixture separation

In addition to single particle retention, the system was also characterized with respect to resolution of multiple component polystyrene suspension mixtures. The samples injected were mixtures of the above mentioned polystyrene samples. The sample size was 1 microliter in each experiment. Sample mixtures used were Mixture A (110, 210, and 300 nm), Mixture B (1000, 4350, and 9100 nm), and Mixture C (110, 210, 300, 1000, 4350, and 9100 nm). All mixtures were made using the equal parts of the diluted 0.1 weight percent solutions from the single component retention experiments. The concentration of each of the components in Mixture A and Mixture B is then 0.033% and the concentration of each component in Mixture C is 0.0166%. The resolution was determined for each pair of adjacent components. The diameter based selectivity was also determined for these experiments.

μ-ThFFF System Component Parameters and Design

The ThFFF system is comprised of several elements that work together to perform the separation and analysis. These parts are the fluidic channel, carrier fluid pump and flow rate controller, heater, heat sink, thermocouple, interconnects, sample injection system, detector, and fraction collector. These components are illustrated in a block, flow diagram, see Figure 26. The heater and heat sink are shown in this figure. The heater is integrated with the channel. The heat sink is not physically attached to the system in any way. Each of the components with their specific design and operating parameters is discussed in detail in this section.

Channel

Fabrication of the fluidic channel is one of the most critical parts of the μ-ThFFF system. Channel geometry must be controlled precisely to minimize the plate height effect from the channel. The fabrication procedure chosen for this step must be able to control the channel height precisely along the length of the channel. Design of the channel shape also will reduce plate height and improve resolution and analysis time. The fabrication procedure must also be able to allow control over semicomplex channel shapes.

The channel width, *w*, is the critical scaling parameter in developing the μ-ThFFF channel. Channels down to ~50 μm can be successfully manufactured using common macroscale techniques. Theoretically, channels with a thickness on the order of 1μm can be fabricated using spin on films such as SU-8. However, channels under ~10μm in width are increasingly difficult to successfully fabricate. Additionally, extremely small channels have design difficulties such as volume matching to minimize band broadening. The limitation on the size of particles that can be separated is decreased and is reflected in the change in the steric transition size. A channel thickness of 25-50 μm is a reasonable goal for this project. Channel width is governed by the breadth to width ratio of 100. Although a longer length is theoretically preferred, the length is restricted by the diameter of the 3-inch silicon wafer. Larger wafers are available but must be supported by the fabrication facilities. Typically, larger wafers mean much more expensive fabrication equipment.

Research on FFF channel shape has been done to minimize the band broadening effect as the sample enters and exits the wide channel through very small ports. A typical

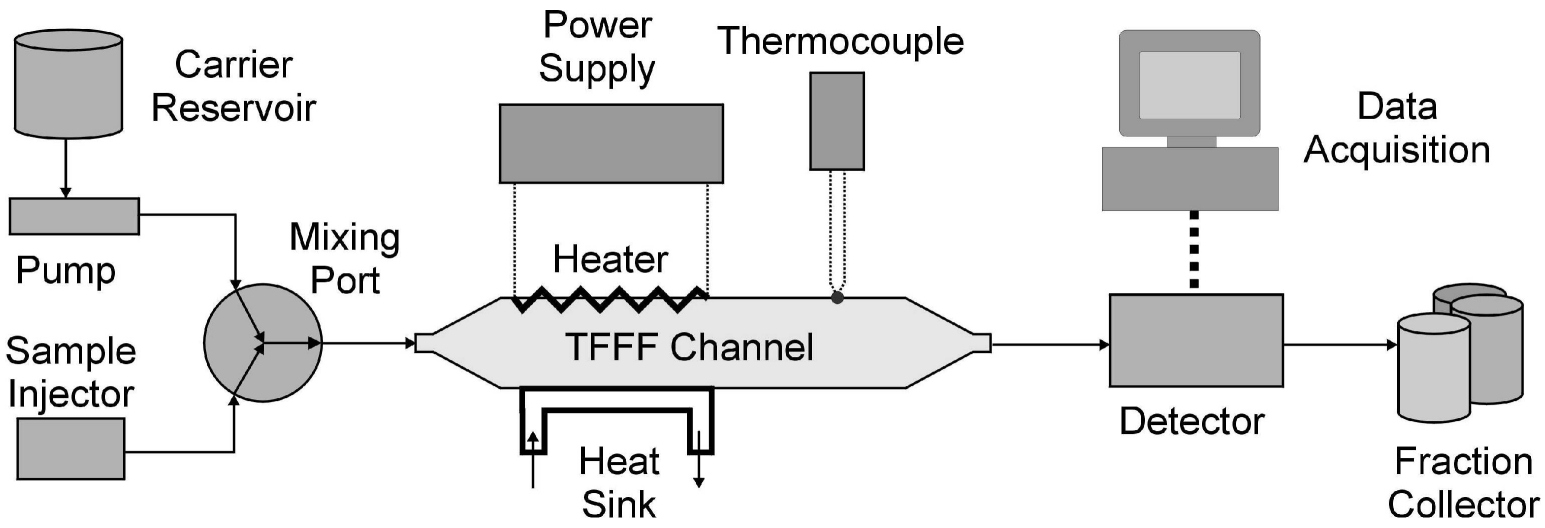

Figure 26. A block flow diagram of the ThFFF system. The carrier fluid is pumped at a constant rate through the mixing port and channel. A sample to be analyzed or separated is injected into the mixing port. The power supply connects to the heater integrated with the channel. The temperatures of the hot wall and cold wall are measured with a thermocouple. The void peak and retained samples pass through the detector which data are then acquired and stored by the computer. The various purified samples are then optionally passed to the fraction collector.

channel shape is shown in Figure 4. The entrance and exit regions are tapered, at an angle of 60°, from the width of the channel to the size of the port.

The materials used in fabricating the channel are important for several reasons. Because of the extremely small scale of the channels, small defects in the surface or variations in the height can cause inaccurate analysis and decreased resolution. Another concern is that of compatibility with the samples to be separated. This is of particular importance when biological samples are separated. Biocompatibility is a broad term that refers to hemolysis of blood cells, protein or biomaterial adhesion, outgassing of solvents, absorption, and others. Many surface modification techniques are available to improve biocompatibility.

Pump

The carrier fluid is pumped through the system at a constant rate. The flow rate is critical to a separation because it defines the velocity profile as well as the time that the void peak is eluted. Under constant retention conditions, if the void peak is eluted too quickly, the other peaks may not be retained long enough to ensure a baseline resolution between peaks. However, if the flow rate is too low, the analysis time for highly retained samples may be too long, even on the order of a day.

An optimum average velocity for the carrier fluid was determined by Giddings [240]. The optimum velocity, $\langle v \rangle_{opt}$, was obtained for minimizing plate height and is found in Equation 85.

$$\langle v \rangle_{opt} = \sqrt{18}\frac{D}{R^2 w} \qquad 85$$

In this equation, D is the normal diffusion coefficient, R is the retention ratio, and w is the channel width. Typical values for small macromolecules under moderate retention are $D = 10^{-6}$ cm^2/sec and $R = 0.1$ [240]. The channel width is approximately 25 μm for the μ-ThFFF channel. These values calculate an average velocity for the carrier fluid of approximately 0.17 cm/sec. If the channel breadth is around 4 cm, then the flow rate that the pump must deliver is 0.61 mL/hr. The pump used in this case was a syringe pump with a Becton-Dickenson, 5 mL plastic syringe as the fluid reservoir.

Heater

Maintaining a constant temperature at the hot wall is important when analyzing samples because of the strict relationship between temperature gradient, layer thickness, retention ratio, and sample properties. The typical heater arrangement for a ThFFF system is two, resistance heater rods inserted through the upper block of the channel. The typical power consumption for one of these rods is about 1.5 kilowatts or a total of 3.0 kilowatts for both. This amount of power is not reasonable if the μ-ThFFF system is to be used as a portable device or integrated into a "lab-on-a-chip" system.

The μ-ThFFF heater must consume as little power as possible to meet these demands. The heater must also be able to maintain a hot wall maximum temperature at the boiling point of the carrier fluid. Sometimes, the channel will be maintained at a high pressure to raise the boiling point of the carrier fluid. In this way, the temperature gradient can be increased and high retentions achieved. This is probably not necessary in the μ-ThFFF channel since the reduction in size increases the gradient for a given temperature difference. Solvents typically have normal boiling points (nbp) lower than that of water. The heater is then required to maintain a temperature of the nbp of water,

around 100°C. The heater must also be able to supply enough power without degrading. The power requirement of the heater is estimated to be about 24 watts.

The heater can be simply integrated into the channel at this point. This design reduces the bulkiness associated with an external heater and reduces the power consumption to a level suitable for portability. The heater band is slightly larger than channel in breadth and length. Two types of heaters have been tried and tested to be successful in terms of both fabrication compatibility and temperature and power output. These two types of heaters are the boron doped silicon heater and the titanium (Ti) deposited heater.

The boron doped silicon is a robust heater but requires high temperatures to fabricate. The heater bands are also difficult to isolate from each other. These points will be discussed later in the fabrication process.

The Ti heaters do not require high processing temperatures but are more susceptible to degradation. To reduce the possibility of degrading the Ti deposited heater (as in the case of a fuse), the current was required to be low while maintaining a power output necessary to heat the hot wall to the 100°C. The metal must also have a reasonably high electrical resistivity. For this reason, titanium metal was chosen. The power to the heater was supplied by a typical power supply capable of at least 1.5 amps and 20 volts.

Heat Sink

The heat sink is also critical to analysis of samples. It is this component that maintains the cold wall temperature and, in part, the temperature gradient. The heat sink must be able to remove the energy from the heater while maintaining a cold wall

temperature of about 10°C. The heat sink is not integrated with the channel at this point. The integration of a heat sink on the same scale as that of the heater is possible and is suggested for further work for this project. Some types of heat sinks to consider include the Joule-Thompson refrigerator and Peltier effect heat pumps [241].

The heat sink used for these studies consisted of a chamber with all the sides and bottom walls made from PVC. The top wall was made from 1/8-inch aluminum. The channel was placed on top of this aluminum wall. Two opposing sidewalls included ports for cold water to enter and exit the chamber. An additional port was located at the top of one of the sidewalls to allow air trapped in the chamber to exit. A typical temperature of the cold wall was about 11°C. The water flow rate could be adjusted as needed to remove the heat generated from the heater.

Thermocouple

Because of the critical nature of maintaining a constant temperature at both the hot and cold wall, there must be a method for measuring these temperatures. For this purpose, a simple thermocouple placed on the surface of the heater or on the surface of the heat sink should be sufficient. The thermocouple range must include the temperatures between 10°C and 100°C. A J-type thermocouple is commonly used for measurements in this temperature range and is widely available. The voltage from the thermocouple is compared to a voltage from an isolated, constant temperature thermocouple and converted through an algorithm to a temperature.

For this work, the thermocouple was external and separate from the system. When placed on the heater or on the aluminum surface the thermocouple wires were electrically isolated with a piece of standard electrical tape.

Microfabricated thermocouples have been demonstrated and could possibly be integrated into the μ-ThFFF system. This thermocouple integration is suggested for further work on this project. Integrating thermocouples into the system may improve the accuracy of the temperature measurement because the location of the thermocouple would be closer to the point of interest. Thermocouples could also be placed along the length of the channel with separate region heaters to provide a more constant temperature in the *z*-direction or programmed temperature control.

Interconnects and Sample Injection System

Fluidic and electrical interconnects tied the miniaturized system components to the macro scale system components. Copper strand wires were bonded to the Ti heater using a conductive adhesive. The resistance was required to be minimized to prevent localized heating at the connection.

The fluidic interconnects required a design that would minimize band broadening due to extra-column volumes. The tubing through which the sample traversed must be as short as possible with an inner diameter as small as possible. The tubing must also be compatible with the solvent and must be inert to the sample (i.e., not promote adhering of the sample to the walls). The tubing must be secured well to the inlet/outlet ports of the channel and have as little "dead-volume" as possible at these joints.

The fluidic interconnects at the inlet of the system must be able to support some type of injection system for the sample to be introduced at any given time while the carrier fluid is constantly pumped through the system. For this type a configuration, the common setup for a chromatography column could be used. In this case, a septum is used to prevent flow through the injection port while allowing a syringe to be inserted

into the stream to inject the sample. The injection system should allow the syringe tip to placed as close to the inlet port as possible to prevent band broadening due to extra-column volume.

Another common configuration is the use of a sample injection loop. A loop of known volume is filled with the sample. A valve with a small dead volume is used to redirect the carrier flow through the sample loop. This method is not preferred yet because of the unavailability of sample loops with volumes small enough for the sample sizes for μ-ThFFF and because of the extra-column tubing between the valve and input port to the channel. The possibility of micromachining a sample injection loop and integrating it with the channel is of interest. This work is also suggested for further work in the μ-FFF systems.

Detector

The detector used was an off chip, *Linear*, model UV-106 ultraviolet extinction detector. The monitor extinction wavelength was 254 nm. While this detector provided satisfactory preliminary results, it is not optimal for the μ-ThFFF system because of the relatively large volume in the detector chamber. The change in fluid cross-sectional area caused loss in resolution and broadening of the sample peaks. The tubing between the outlet of the channel and the detector was extra-column volume that distorted the sample peaks.

Fraction Collector

The final stage of the ThFFF system is the fraction collector. This component is only necessary when purifying samples for further work. A fraction collector is simply a container used to collect the eluted samples at a given time. The collection must be timed

with the elution of each sample peak or coordinated with the detector so that samples are not mixed again. No fraction collection system was used in the research associated with this thesis.

Microchannel with Integrated Heater Fabrication

Microchannels for fluids are an important part of micromachined systems. Channels have been fabricated on a variety of substrates like glass, silicon, metals, and organics. They are typically fabricated using bulk, surface, or some other process such as molding. Kovacs [31] summarizes three important factors that must be considered when fabricating a channel: geometric constraints, channel interior surface materials and complexity of fabrication. These factors were considered in designing and fabricating the μ-ElFFF channel and again when modifying the μ-FFF channel design for improvement and compatibility with the μ-ThFFF channel.

μ-ElFFF Channel

Gale [29] first fabricated a micro channel for use in a micro electrical field-flow fractionation system (μ-ElFFF). The first channels were rectangular with dimensions that varied from 4cm to 5.4cm in length, 0.20mm to 6mm in breadth and 5μm to 50μm in width. Ten, parallel channels were fabricated on a single, 3-inch silicon wafer. The channel had a single input and single output port etched through the silicon wafer at each end of the channel. The walls were made from a photosensitive polyimide that was spun onto the wafer to the channel width desired. The channel was capped with a glass cover bonded to the polyimide walls with a cyanoacrylate glue.

Gale later made modifications to the shape of the channel to include tapered channel ends [242] and an extra port at the inlet and at the outlet for pressure measurements. The application of metals to the surface of the silicon and glass allowed electrodes to be formed for setting up the electric field.

While this channel fabrication method worked well for the μ-ElFFF channel, it did fit exactly with all the requirements for the μ-ThFFF channel. The basic design and fabrication procedure was used for the μ-ThFFF channel with some required modifications for compatibility issues and a modification of channel design for improvement in the glass-bonding step.

μ-ThFFF Channel

The channel used for the μ-ThFFF system was fabricated using common micromachining techniques. The basic design was adapted from the μ-ElFFF channel and modified to make it suitable for the thermal field and solvents associated with ThFFF. The μ-ThFFF system was fabricated with an n-type, [100], single side polished, 3-inch, silicon wafer. The front side of the wafer refers to the polished side. The details of the micromachining processes associated with each fabrication step are covered in this section.

The first step was to etch the input/output ports through the silicon wafer, Figure 27, using thin film deposition and etching techniques mentioned earlier. First, a silicon dioxide (SiO_2) mask was thermally grown as a mask for the wafer etching. The silicon etching was to be done with potassium hydroxide. The specific conditions would require an oxide thickness of approximately 1 μm.

Positive photoresist (*Shipley* 1813) was spun onto both sides of the wafer for the purpose of masking the silicon dioxide or nitride mask. Application and patterning of the photoresist was as follows:

1. Spin PR 1813 at 2500 rpm on the backside of the wafer.
2. Hard bake wafer at 120°C for 3 minutes.
3. Spin PR 1813 at 3000 rpm on the front side of the wafer.
4. Soft bake wafer at 100°C for 2 minutes and 15 seconds.
5. The soft baked resist on the font side of the wafer was exposed with the port mask using an Electronic Vision (EV 400) mask aligner.
6. Hard bake wafer at 120°C for 5 minutes.
7. Develop exposed photoresist regions with 352 Developer and rinse with DI water.
8. Etch the SiO_2 using one of two methods described below.
9. Remove PR 1813 from both sides using acetone, methanol and DI water rinse.

Both wet and dry etching was successfully used in patterning the 800 μm^2 ports in the silicon dioxide. The dry etch was used for both the nitride and oxide films and was accomplished using reactive ion etching (RIE). The process used CF_4 or SF_6 as the etch gas with 250 W of power. The process time was approximately 20 minutes for the nitride. An alternative approach to etching the oxide was the wet etching method. This method submerged the wafers in buffered oxide etch (BOE) for 15 minutes (~850 nm/min etch rate). The BOE is comprised of 170 mL DI water, 28 mL hydrofluoric acid (HF), and 113 gm ammonium fluoride (NH_4F).

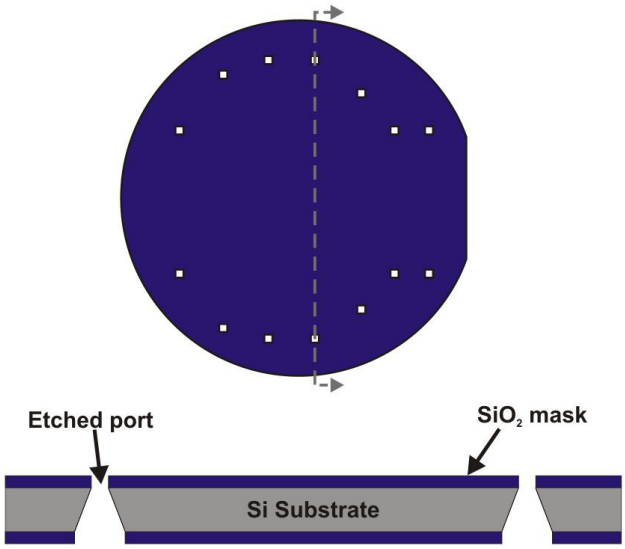

Figure 27. Top view and cross section (cut at dashed line) of the silicon wafer after the first process step, etching the input and output ports.

After the mask was defined, the ports were then anisotropically etched through the silicon wafer. Because of the <100> crystallographic plane on the surface of the wafer, the sidewalls were formed by the [111] plane. This plane forms an angle of 54.7° with the [100] plane. Because of this etch angle, the resulting port geometry on the front side of the wafer was 250 μm^2. The KOH etch was performed successfully with two different conditions. The first condition was a slow etch, approximately 24 hours. The conditions were 20% KOH at 55°C. A faster etch, approximately 3.5 hours, was done in 10% KOH at 90°C. The faster etch has rougher surface characteristics on the sidewalls. For both etches, the solution was stirred. The etch selectivity between the silicon dioxide and silicon increased, but the oxide film as defined earlier was still thick enough for the entire etch. The wafer was rinsed with DI water after the KOH etch.

The next step was to add the heater bands to the wafer, Figure 28. Two types of heaters, boron and titanium, were experimented with and successfully used. The boron heater was more robust, however, the titanium heater was easier to fabricate and control the resistivity.

The SiO_2 that remained from the KOH etch was then used as the mask for the boron diffused heaters. Patterning the SiO_2 was accomplished using the same method as for the ports but with a different mask. The boron furnace setup was similar to the oxide furnace setup in Figure 14b, except that instead of hydrogen gas, nitrogen gas was used. The wafer "boat" setup is shown in Figure 29. Prior to diffusion of the boron, the boron source wafers were aged under the following conditions: 800°C, 1.25 mL/min O_2, and 2.75 mL/min N_2, 7 hours. Boron was diffused at 1175 °C to a depth of 5 μm at a

concentration of approximately 4×10^{20} cm^{-3}. The time of diffusion was 7 hours with an oxygen flow rate of 0.46 mL/min and nitrogen flow of 3.80 mL/min. These process parameters estimate a boron doped region resistivity of 9×10^{-4} Ω-cm.

The titanium heater was deposited onto the backside of the wafer, on top of the oxide (electrical insulator), using sputtering techniques. The system was pumped to a base pressure of 5×10^{-6} Torr and a plasma was established in the chamber. The titanium was sputtered at 50 W for 20 minutes. The thickness was approximately 1000 Å. The titanium was patterned using the photolithographic methods for patterning the oxide except that in step 8, the titanium is etched instead of the oxide. The titanium is etched in 1% HF until all the titanium is removed in the exposed areas.

The walls of the channel were formed on top of the front side as shown in Figure 30. A negative photosensitive polymer epoxy (*SU-8*, MicroChem Corp.) was spun onto the front side of the wafer to a thickness of 25μm. The channels were defined in the *SU-8* by UV exposure and developing. Heat treatment of the channel walls ensured a strong bond and durability when exposed to the carrier fluid, which is typically an organic solvent.

The process steps for depositing a 25μm thick, SU-8, 5 film were obtained from a technical paper from Microchem Corp. and are as follows:

1. Spin SU-8, 5 onto the front side of the wafer.
    a. Ramp up to 1440 rpm at an acceleration of 200 rpm/sec.
    b. Hold at 1440 rpm for 15 seconds.

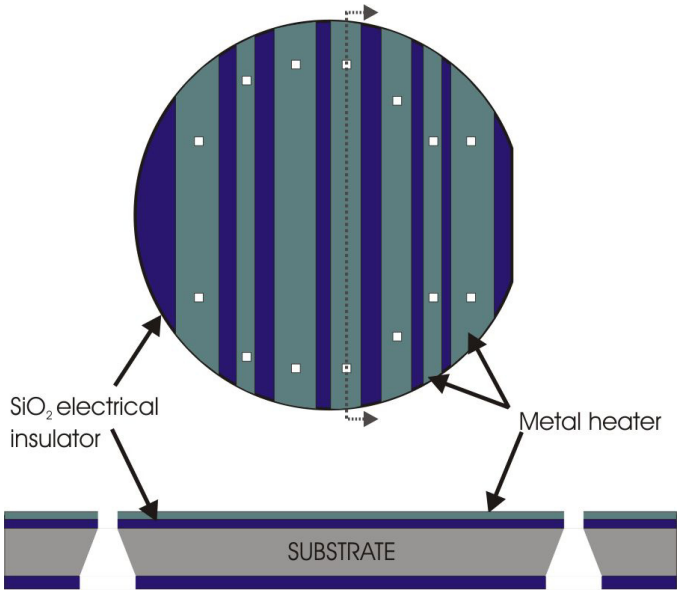

Figure 28. Schematic of the wafer after application of the heater bands. The heaters were made from both sputtered metal (Ti) and boron-doped regions.

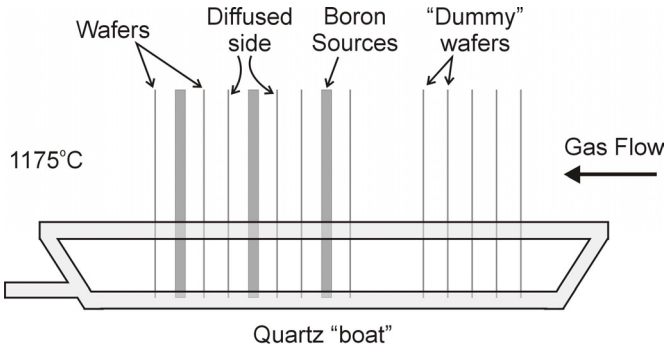

Figure 29. Boron wafer "boat" setup. The boron was diffused on one side of the wafers that are place on each side of the boron source.

2. Post spin bakes.
    a. Hot plate, 60°C for 5 minutes.
    b. Hot plate, 90°C for 6 minutes.
3. UV exposure in EV 400 aligner for 60 seconds.
4. Post exposure bakes.
    a. Hot plate, 50°C for 1 minute.
    b. Hot plate, 90°C for 1 minute.
5. Develop using SU-8 specific developer for approximately 3 minutes.
6. Rinse with developer and then DI water.
7. Post rinse bake at 120°C for 10 minutes.

The post rinse bake ensures a strong adhesion to the substrate and good resistance to the solvent. Some shrinking occurs, but is typically very small, see the results chapter.

One modification from the μ-ElFFF channel wall mask was made at this point. Initially, 10 channels were defined in the SU-8 with small spaces between them. The modification reduced the number of channels from 10 to 5. The extra space between channels allowed for better adhesion between the SU-8 and substrate. In addition, "adhesive trenches" were added around each of the channels. The number of channels is not represented accurately and the adhesive trenches are not shown in the process figures. These trenches were used in the bonding step, described next.

To complete the channel, a glass microscope slide was affixed to the top of the SU-8 walls and is shown schematically in Figure 31. The slide was adhered to the walls with an adhesive, which was required to withstand both thermal and chemical degradation and not increase the channel height significantly. Initially, a photosensitive,

medical grade, cyanoacrylate glue (*Loctite* 3301) was used for the bonding. However, this glue was dissolved by the solvents used in the ThFFF channel. A silicone was tried, but was too difficult to apply so that the channel thickness did not increase and was a constant width. Liquid SU-8, 10 was used successfully to bond the channel top. Bonding was done by filling in the adhesive trenches with the SU-8. These trenches prevented the adhesive from spilling over into the channel and reduced the extra width added to the channel by the adhesive. The SU-8 was exposed to a broad band UV light until cured. The SU-8 was then heat-treated.

After the channel was fabricated the fluidic and electrical interconnects were bonded to the wafer. This step is discussed in the packaging section. The complete system was then assembled and tested according to the methods in the next chapter.

Packaging

The purpose of micromachining a system may be for miniaturization of the system or improving parameters of a system through scaling factors. Although the device may be successfully fabricated using micromachining techniques it is of no use if it cannot be interfaced with the macroscale world or if the packaging increases the size considerably. Packaging has presented a challenge for many micromachined products. Packaging may include interfacing fluidic, electrical, electromagnetic, and other types of connections. The package itself may be important for isolation of the system from a harsh environment or for mechanical stability. For the case of μ-FFF systems, packaging has included both fluidic interconnects and electrical connections. This is true for both the ElFFF and ThFFF systems. The packaging for the μ-FFF system will need to be

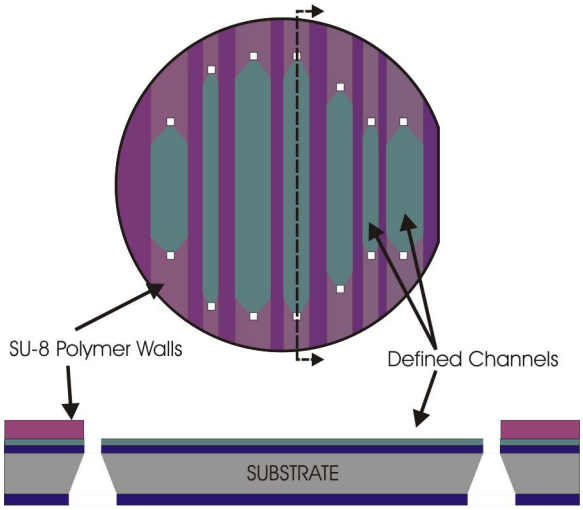

Figure 30. Schematic of SU-8 walls. SU-8 is a photosensitive epoxy that has good surface properties and excellent chemical resistance.

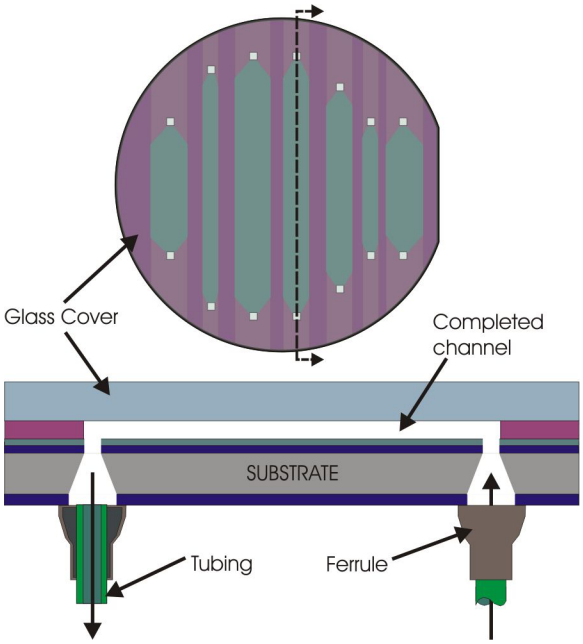

Figure 31. Schematic of completed channel after the glass slide was adhered to the channel walls and the fluidic interconnects bonded to the ports.

modified as future work of integration of other components such as the detector, heat sink, power supply, and integrated chips for analysis.

μ-ElFFF Packaging

Gale [242] developed a fluidic interconnect for pumping the carrier into the channel and directing it from the outlet to the detector or fraction collector. The packaging also included an injection port for sample introduction into the carrier stream. This injection port is shown in Figure 32 with the sample injection syringe inserted. With this setup, the point of injection is located at the inlet port, reducing the amount of extra-column length that the sample may traverse and thus reduce sample peak distortion. One problem that may exist is the possibility of disturbing the carrier flow during insertion and removal of the syringe because the syringe needle diameter is close to that of the inner diameter of the tubing in the system.

μ-ThFFF Packaging

The system developed for the μ-ElFFF system by Gale was used in the μ-ThFFF system with some minor modifications. Gale used a cyanoacrylate to bond the ferrule at the ports and the nut around the ferrule to the silicon substrate. Because of the solvents used in ThFFF systems, this glue does not work. The solution was simply to put a silicone seal around the ferrule/silicon substrate joint. Silicone has excellent solvent resistance properties once cured. Silicone alone, though, is not mechanically strong enough to support the movement at this joint caused by inserting and removing the syringe during injection. To strengthen the joint, the cyanoacrylate glue was applied to the nut and surrounding silicon substrate. The combination of the silicone seal and

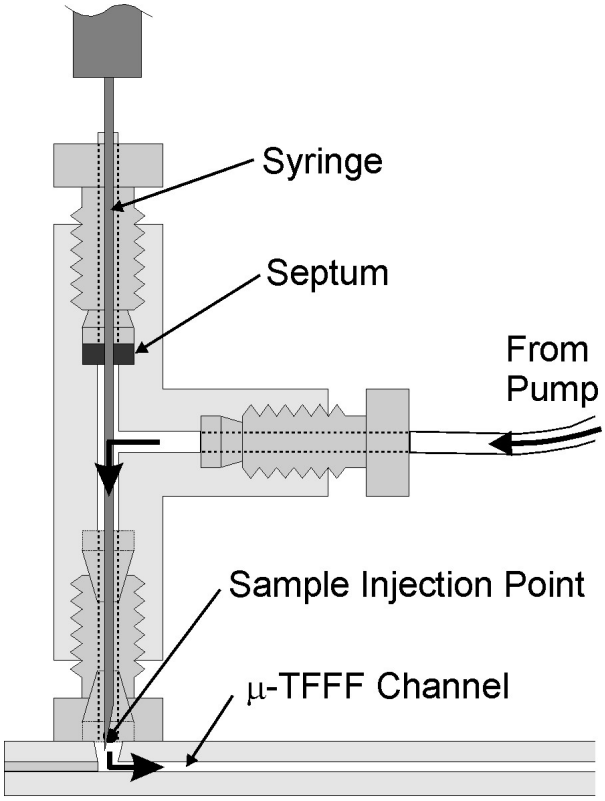

Figure 32. Injection port, fluidic interconnect system for μ-FFF channels.

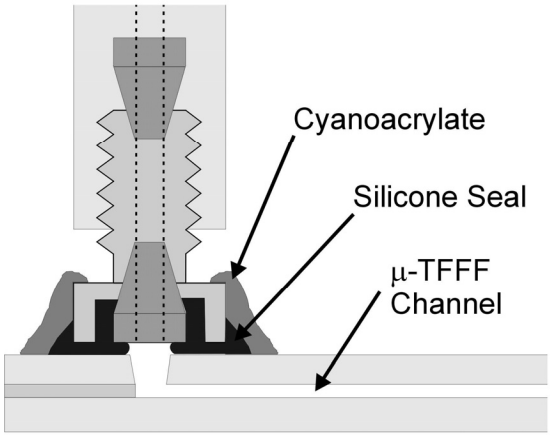

Figure 33. A cyanoacrylate adhesive-silicone seal combination modification of the injection system-substrate joint for the μ-ThFFF system.

cyanoacrylate glue, see Figure 33, provided the necessary joint to allow the use of Gale's sample injection system.

An improvement to this system was made by using an L-shaped injection port. This configuration is nearly identical to the tee shape but with fewer parts to assemble and glue and resulted in a lower profile so that the seal was less likely to break during injection (if the sample syringe was not inserted at precisely a right angle).

Still, another improvement to the entire system was the use of an automated injection valve; however, this solution was much more costly ($1000s compared to $10s for the previous setup). A six way valve with a 90 nL sweep volume was used to inject the sample. A capillary with a diameter of 25 microns was used for the injection loop to obtain a 1 μL injection volume. The major benefit of this system was the improvement in plate height, especially at low flow rates where mixing was much more of a problem in the L and T injection ports. In addition, the system was computer controlled to provide consistent injections each time. Besides cost, the other disadvantages of this system were seen when injecting PS samples, which would occasionally clog the capillary and/or delay the injection as an increased pressure was required to push it through the injection loop.

The 5 mL syringe was filled with the carrier fluid and connected to the injection port. The syringe was placed in the syringe pump, which controls the volume flow rate through the channel. The outlet port had only a ferrule bonded to it with 1/64-inch inner diameter tubing inserted in the ferrule. The tubing was made as short as possible and was connected to the external UV extinction detector. The outlet of the detector is piped to the fraction collector.

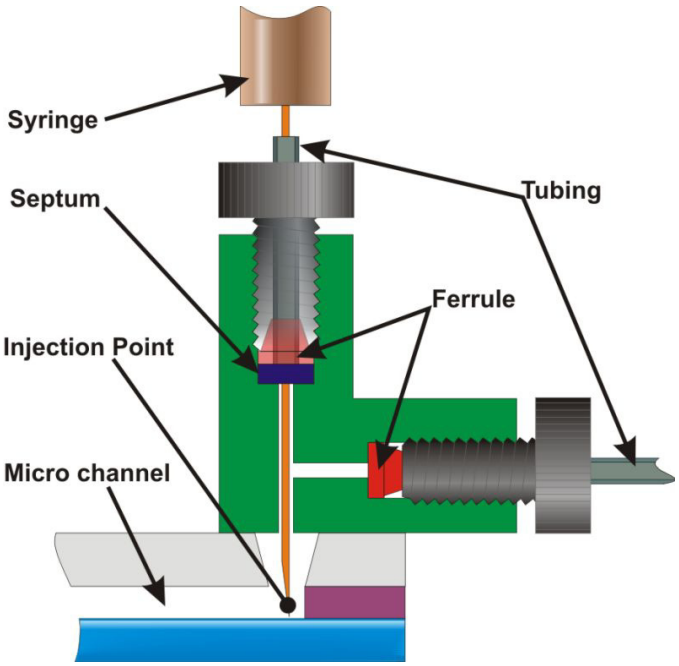

Figure 34. A slight improvement to the tee injection port is the L-shaped injection port due to its lower profile and easier setup.

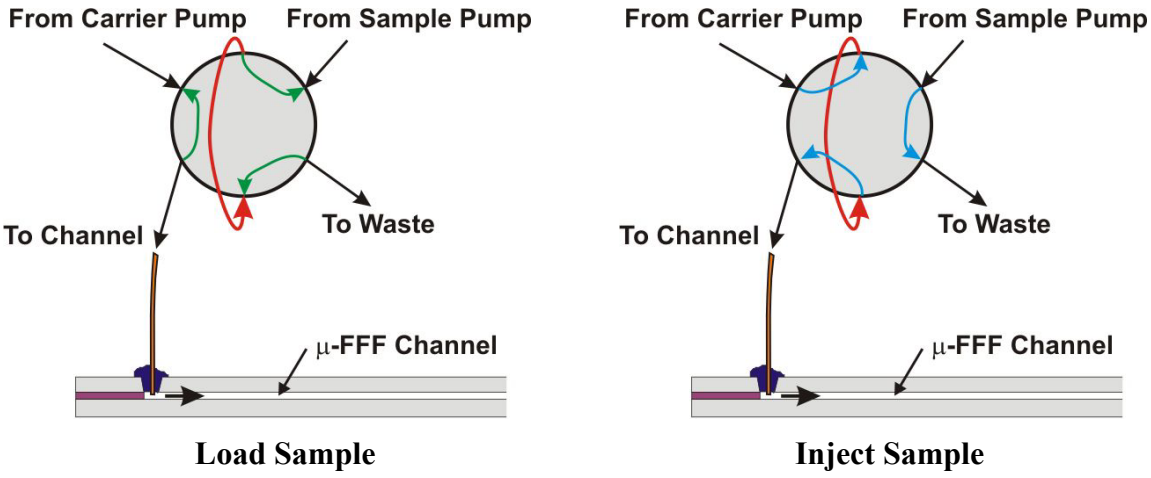

Figure 35. The automatic injection valve proved a significant improvement over the previous two sample introduction schemes, but also had trade-offs in the form of cost and inaccuracy in injection times due to pressure build-up in the injection loop.

The detector voltage signal was read by a multimeter. The multimeter was connected thorough a GPIB connection to the computer where data collection is done with a *LabView* virtual instrument (VI). Appendix A contains the VI code and GUI.

The electrical connections to the heater were made by bonding a short piece of copper wire to the surface of the heater at each end. An electrically conductive adhesive, "silver-paste," was used to bond the wires to the surface. It is applied in paste form and then baked at ~100°C to remove the solvent and increase conductivity. The DC power supply terminals were connected to the two wires along with a current and voltage meter.

The wafer was set on top of the aluminum top of the cooling chamber of the heat sink. Tap water was used as a coolant and the flow rate was increased until the hot wall temperature was steady. The temperature at the surface of the heat sink was measured with the thermocouple placed at a point midway between the ports on the heater surface.

Summary

The μ-ThFFF system is comprised of several components, but only the separation channel and heater are miniaturized in this work. However, the other components must be integrated with the miniaturized channel and heater through fluidic, electrical and thermal interconnects.

The channel and heater were fabricated on a three inch silicon wafer using common micromachining techniques. Processes such as bulk etching, thin film deposition, and photolithographic patterning were used to fabricate the channel and heater. The fabrication procedure was adapted from the μ-ElFFF channel fabrication procedure and modified as necessary to include the heater and make possible the use of harsh solvents that are typically used for the carrier fluid in ThFFF systems.

The fluidic interconnects were modified from the μ-ElFFF system design to account for the attacks from ThFFF carrier fluids. The power supply was connected to the heater with electrically conductive adhesive. The other components of the system were connected to the channel and heater to complete the system. Fluids were passed through the channels with no leaks. The heater was also successfully heated to various temperatures.

CHAPTER 4

MICRO ACFFF FABRICATION RESULTS

AND SYSTEM CHARACTERIZATION

Fabrication Results

A photograph image of the final microfabricated AcFFF system, font (transducer) and back (silicon) sides, is shown in Figure 36. The channel names of this figure oriented from top to bottom are *A*, *B*, *C*, *D*, and *E*. These channels are approximately 62 μm in width and varied in breadth (6, 4, 6, 2, and 4 mm, *A*-*E* respectively) and tip-to-tip lengths (4, 6, 6, 5, and 4 cm, *A*-*E* respectively). The active transduction area for each channel was 1.30, 0.93, 2.92, 2.10, and 1.72 cm^2, *A*-*E* respectively. The areas of the entrance and exit regions of channels *A*-*E* were: 0.076, 0.018, 0.174, 0.076, and 0.174 cm^2. The tubing between the injection port and entrance region was 150 μm inner diameter and 6 inches in length, or 2.69 μL. The total volumes from injection to detector, or void volume, for channels *A*-*E* were 11.25, 8.59, 21.85, 16.21, and 14.41 μL. These dimensions are summarized in Table 2. The masks for the process steps with the appropriate dimensions are shown and described in more detail in Appendix F.

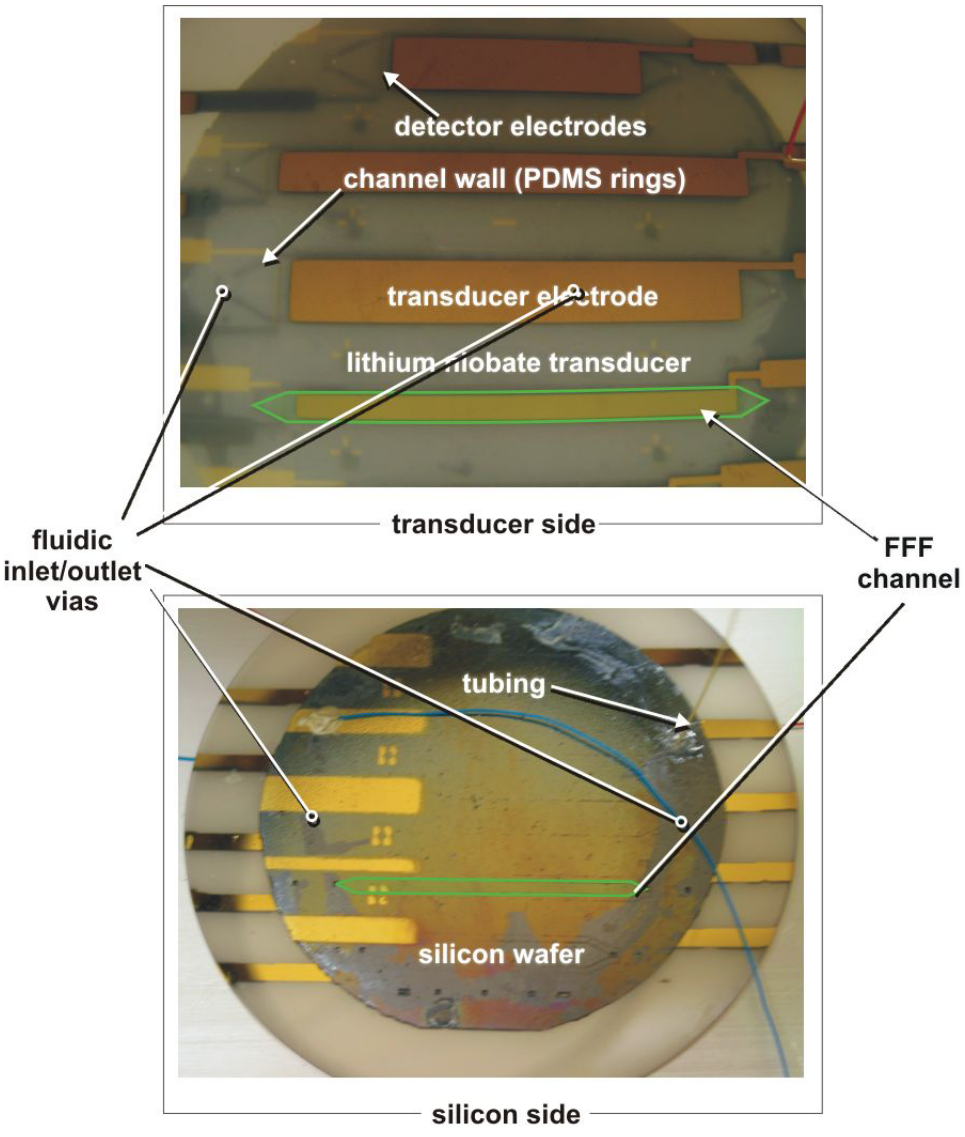

Figure 36. Photograph of five μ-AcFFF channels built onto a thinned 3-inch silicon wafer using laser ablated PDMS walls and a capped with the lithium niobate 4-inch wafer which serves as a channel wall and acoustic transducer. Also shown are integrated impedance detection electrodes and fluidic vias. One channel is outlined in green.

Table 2. Summary of physical dimensions for the μ-AcFFF channels *A*-*E*.

Parameter \ Channel	A	B	C	D	E
Width (μm)	62	62	62	62	62
Breadth (mm)	6	5	6	2	4
Length (cm)	4	6	6	5	4
Entrance/Exit Region Areas (cm^2)	0.076	0.018	0.174	0.076	0.174
Transducer Area (cm^2)	1.30	0.93	2.92	2.10	1.72
Precolumn Volume (μL)	2.69	2.69	2.69	2.69	2.69
Void Volume (μL)	11.25	8.59	21.85	16.21	14.41

In this figure are also noted the various components of the system: transducer electrodes, detector electrodes, lithium niobate wafer (transducer and top wall of channel), silicon wafer (acoustic reflector and bottom wall of channel), fluidic ports in silicon, tubing at channel inlet for carrier fluid and sample introduction, and PDMS channel walls which are sandwiched in between the top and bottom walls.

The thickness of the lithium niobate wafer was measured to be 525 μm using *Chicago* brand micrometer with 1 μm accuracy. The silicon wafer was thinned from approximately 380 microns, using an isotropic etch only on the rough side and measured using the micrometer to be 350 ± 2 μm. The height of the channels was measured using a *Wyko* optical profilometer.

The PDMS was mostly transparent to the spectrum of visible light which causes a problem in the profiilometry measurement. The profilometer works through an image recognition routine and computer algorithm that determines the presence of diffraction patterns in specific regions as a function of the *z*-axis position. These diffraction patterns

indicate a surface present. The algorithm does not work properly if a diffraction pattern occurs more than once in the same region during a sweep through the specified *z*-axis range. A transparent material on top of another material will cause such an event. Since the *z*-axis sweep is from higher to lower, this problem is overcome by simply reducing the range or stopping the sweep before the second set of diffraction patterns appear.

This measurement was also used to characterize the thickness versus spin rate of the Dow-Corning *Sylgard 184* PDMS on [1 × 2] $inch^2$ glass microscope slides (Corning brand). The PDMS was prepared as per the manufacturer's standard recipe of 1:10 parts of curing agent to base, degassed in a vacuum chamber, and cured on a hot plate at 100 °C for 4 hours. The uncured PDMS was spun onto the glass slide at a precise rotational rate. Prior to the hot plate assisted cure, the PDMS was allowed to reflow on a level plate for 1 hour to help eliminate defects from bubbles and the edge bead. After the cure period, a pattern was laser ablated into the PDMS and a portion of the PDMS was then physically removed. The step height and edge profile was measured and recorded. The thickness versus spin rate is shown in Figure 37. It follows closely with the expected power trendline. A regression of the data to this trendline yielded a scaling parameter of 129954 and a power of -1.050. The desired thickness for the acoustic system was 62 µm at a spin rate of approximately 1450 rpm. This spin rate was used in fabricating the µ-AcFFF system.

The parameters for laser ablation of the PDMS were determined through trial and error on the samples that were used for characterization of the spin curve previously noted. A commercially available carbon dioxide, CO_2, laser ablation unit,

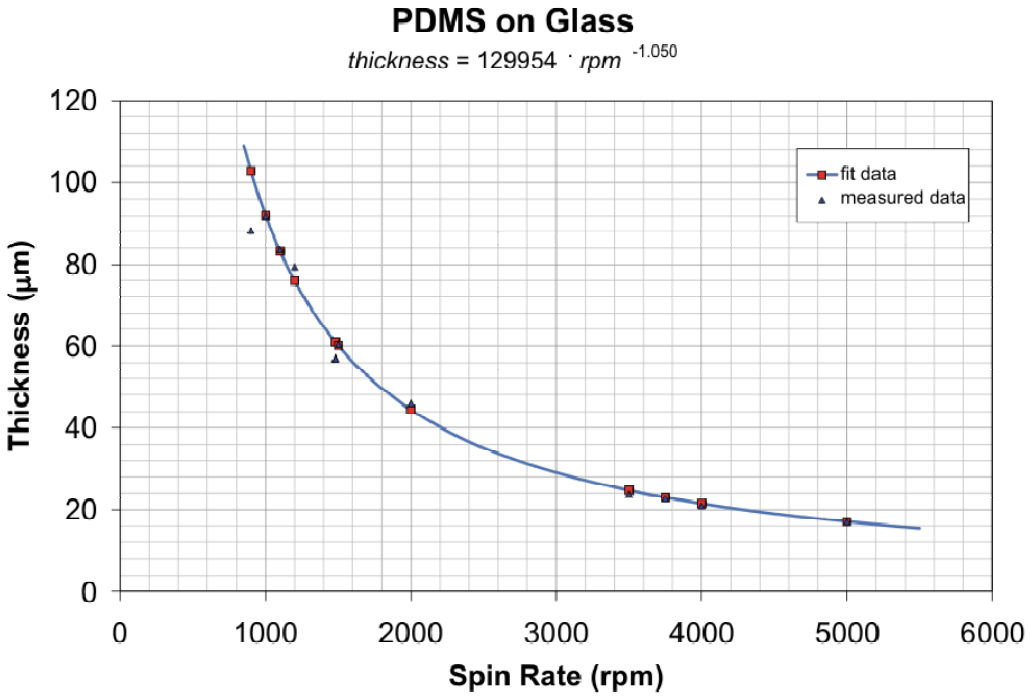

Figure 37. Thickness versus spin rate of Dow-Corning *Sylgard 184* PDMS on [1×2] in^2 glass slides (Corning).

(*Gravograph*/*New Hermes LX7500* with standard *2L* lens) and software (*Gravograph Gravostyle*) was used for defining the channel patterns in the PDMS layer. The lens had a 2 inch focal distance and resulted in a spot size of approximately 180 μm at the focal length. Alignment was made with respect to electrodes and fluidic ports in the silicon wafer by means of a low power LED laser spot from the same optical pathway of the cutting laser. The parameters that could be adjusted in this machine were: cut type (raster filled or vector outline), percent power (1-100%), percent speed (1-100%), number of passes (1-9) and change in focal distance per pass, N_2 assist (on/off with manual control of N_2 pressure), and resolution of steps (300-1200 dpi). The maximum laser power was 70 watts but the actual power was determined by a built-in algorithm based on the parameters and the length and complexity of cut (i.e. higher power and speed for long straight cuts and lower power and speed for corners and short cuts).

The pattern to be cut was designed using AutoCAD (see Appendix F) and imported into the *Gravostyle* software and placed so the alignment marks coordinates matched the physical location on the stage and the parameters were adjusted for the run. Up to eight sets of parameters could be set up for various patterns of the design. For the AcFFF system only two sets of parameters were used, one for the channel edge which was cut through to the wafer and one for the adhesive troughs which were intended to be only partially cut into the surface of the PDMS.

A silicon wafer with etched fluidic ports, detector electrodes and the patterned PDMS layer was photographed and is shown in Figure 38. This figure indicates several key landmarks on the wafer, electrodes and ports, which were used for alignment, as well

Table 3. Laser ablation parameters for two cuts used in the 62 μm thick PDMS layer of the AcFFF channels.

Cut	Vector / Raster	% Power	% Speed	No. of Passes	Pass adjustment	N2 Assist	DPI
Channel	Vector	10	20	1	0”	High	1200
Gasket	Vector	5	25	1	0”	High	1200

as the channel regions and high surface area gasket regions (or adhesive troughs). The laser settings for these two cuts are summarized in Table 3.

A step height of the PDMS on glass, post ablation, was measured using the procedure previously described. The result of the profile is shown in Figure 39. This two-dimensional slice is taken from the original three-dimensional data. This data set is represented in a 3D surface plot of which is shown in Figure 40 (*top*) and a top-down view in Figure 40 (*bottom*). Both surfaces appear to be sloping as indicated by the color gradients; however, this anomaly is simply due to the slight tilt of the optical profilometer stage relative to the lens. The data set was leveled in Figure 39. In each of the figures there is a gap, approximately 300 microns in width between the upper trace (PDMS) and the lower trace (glass surface). This gap was the location of the ablation laser trace and roughened the surface sufficiently as to prevent the diffraction pattern from being detected by the profilometer. In the 3D surface plot, Figure 40 (*top*) this gap is filled by an artificial floor (*deep blue color*).

While no profile is shown here, it was observed that the silicon substrate, silicon dioxide layer, nor the Ti/Au metal traces was not ablated to any degree at the settings

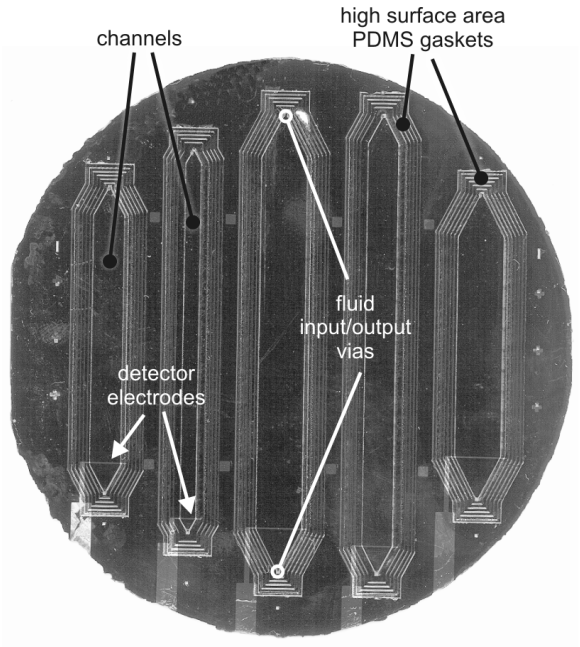

Figure 38. Photograph of patterned PDMS on a 3 inch silicon wafer prepared with fluidic vias and Ti/Au detector electrodes.

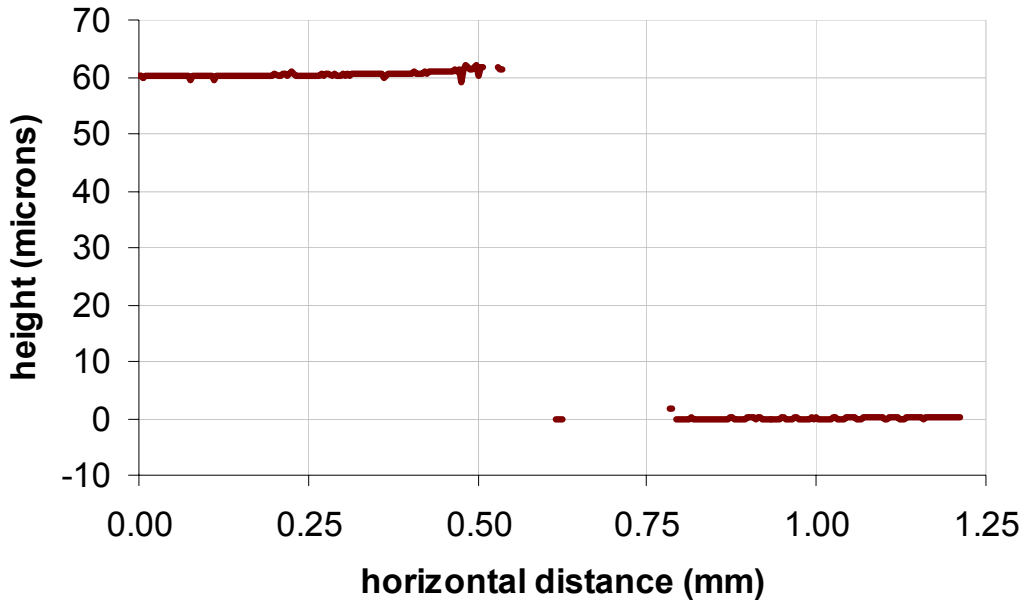

Figure 39. Step height profile of a laser ablated PDMS channel edge used in the fabrication of the microscale AcFFF system. The gap in between the floor and the top of the PDMS is where the ablation took place. The data are absent in this region because of the surface roughness due to the laser.

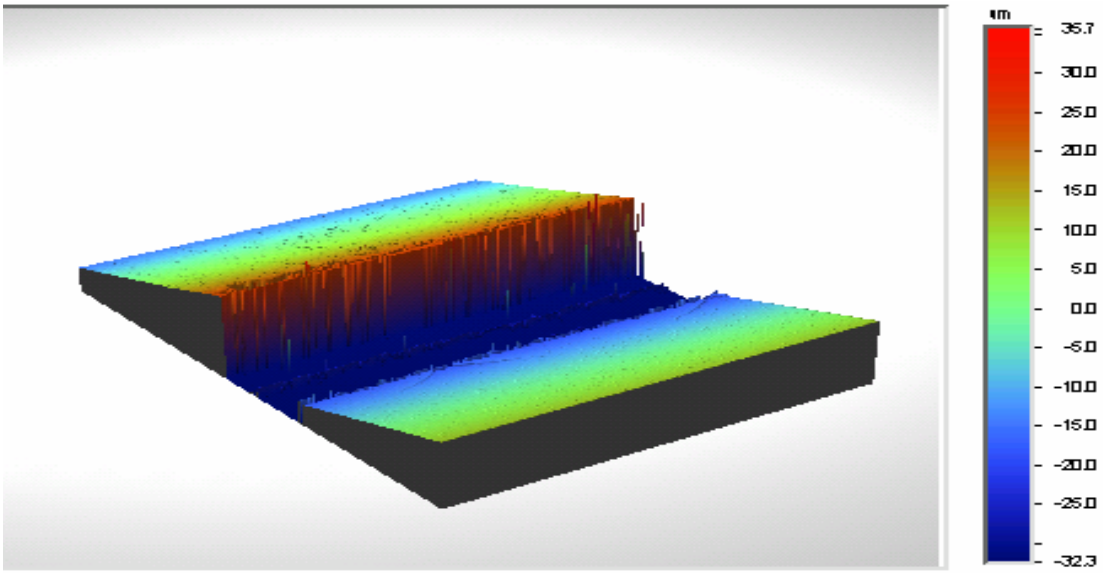

top

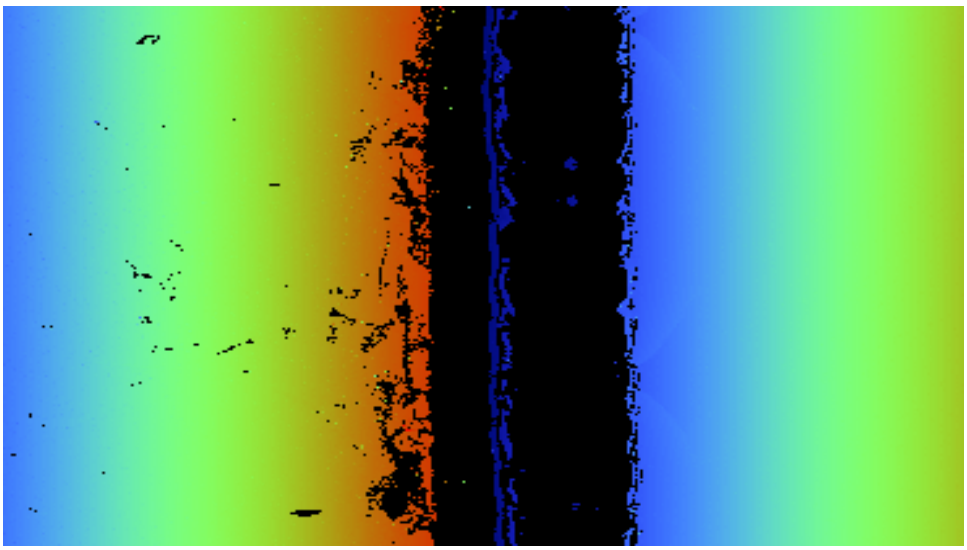

bottom

Figure 40. (*top*) 3D surface plot of data obtained from optical profiilometry of PDMS channel on silicon. The data has been leveled based on the silicon surface (lower level). (*bottom*) Top-down view of profile with colors representing the elevation. The absent data represented by the black regions was explained in the text.

used as described previously. These claims are made based on a magnified inspection of the materials from the processed wafer in Figure 38 as well as other subsequent wafers. It was possible to use CO_2 laser ablation to remove silicon (for fluidic ports); however, it was slow and inefficient because it required full power, low speeds and multiple passes.

Channel Characterization

The pressure/flow characteristics of the channel were evaluated by measuring the pressure at the inlet of the system as a function of the set flow rate using deionized (DI) water. The DI water was prepared from tap water through a series of two 2-micron filters, a *Barnstead* distillation unit, and a *Barnstead* deionization unit which included a bacteria filter. The DI water measured 17.2 MΩ-cm. The water was degassed by heating and then cooled to room temperature, 22 °C.

The channel walls of the both the capillary (precolumn) and the channel are assumed to be smooth. Under the conditions of the maximum useful flow rate, 30 mL/hr and channel cross-sectional dimensions, 0.31 mm^2, the Reynolds number was calculated to be 0.082 which is well within the laminar flow regime. The calculated flow rate for a simplified channel (the tapered end regions were ignored) of length 6 cm is 55 kPa. The tubing described earlier is expected to have a 40 kPa pressure drop with the same conditions.

The measured pressure at the inlet as a function of flow rate in the channel was recorded and plotted in Figure 41. The plot inset is a magnification of the lower flow rates and utilized the same trendline as in the original graph. The linear regression should yield a zero intercept according to Bernoulli's equation. However, this offset merely indicates an incorrect calibration offset of the pressure transducer and can be subtracted

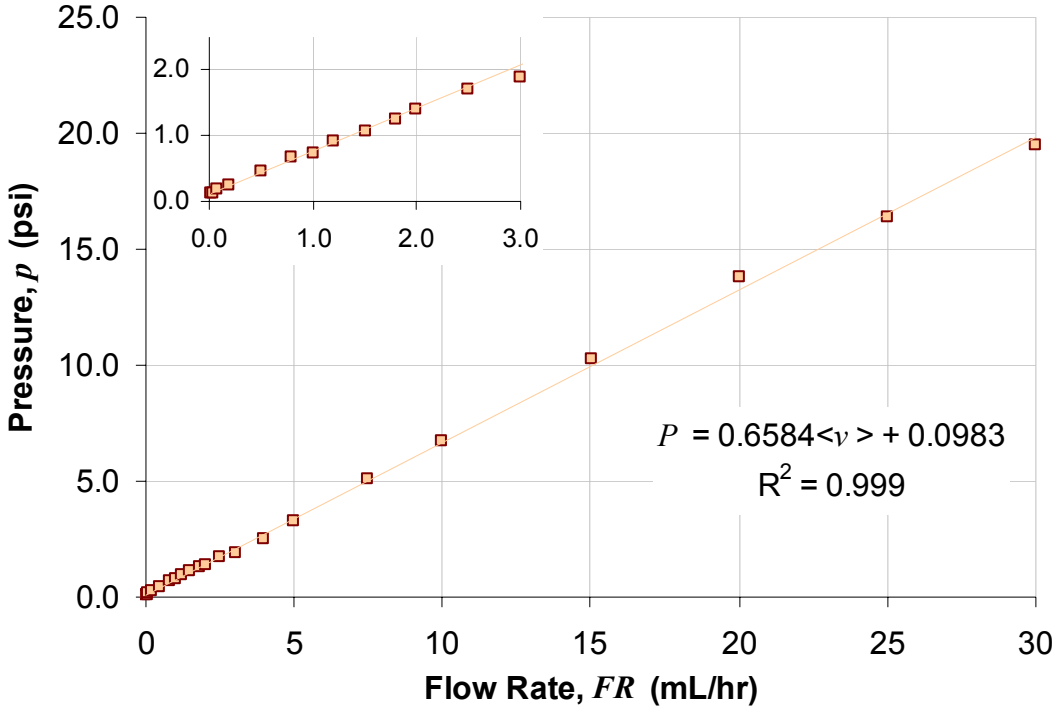

Figure 41. Pressure drop in the precolumn tubing and microchannel as a function of pressure driven flow rate. The non-zero intercept is due to incorrect calibration of the pressure transducer.

from the data set to obtain the accurate readings. At 30 mL/hr the pressure difference was approximately 20 psi (137 kPa). This is roughly close to the predicted 95 kPa. The difference can be accounted for in the simplicity of the model in neglecting the tapered ends and the sudden contraction and expansions located in the injection tee and the channel itself.

The flow rates between 10 and 30 mL/hr were useful during operation of the μ-AcFFF system. However, it was occasionally necessary to temporarily increase the pressure to well beyond this flow rate to clean the channel of residual sample or bubbles. The pressure sometimes exceeded 100 psi (the maximum of the pressure gauge). On a couple of occasions a leak formed by delaminating of the PDMS and lithium niobate. However, after clearing the carrier fluid and allowing the channel to dry, the PDMS resealed to the LN each time and the channel was again useful.

Acoustic Characterization

The system was modeled using an analogous transmission line, Figure 42. The passive layers were 2-port networks and the acoustic transducer a 3-port network with one electrical and two acoustic ports. A *Matlab* [243] program was used to calculate the electrical input impedance into the system and the results are shown in Figure 43. The predicted natural fundamental frequency and input impedance of the system located at zero phase and near minimum impedance was approximately 6.48 MHz and 200 Ω.

The system input impedance was also measured using an *Agilent 4294A* impedance analyzer. The analyzer was calibrated for both closed and open circuits prior to making any measurements. The frequency range was set from 1 MHz to 10 MHz with 201 samples linearly spaced. No point or trace averaging was set. The measurement

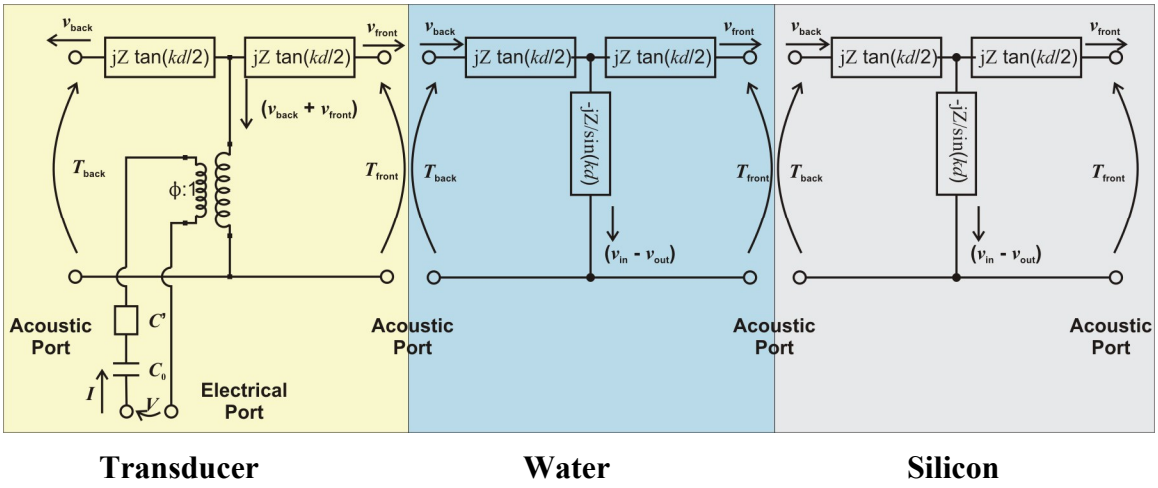

Figure 42. The Analogous transmission line model of the acoustic system including the KLM model of the transducer 3-port network. This model is described in more detail in the theory section.

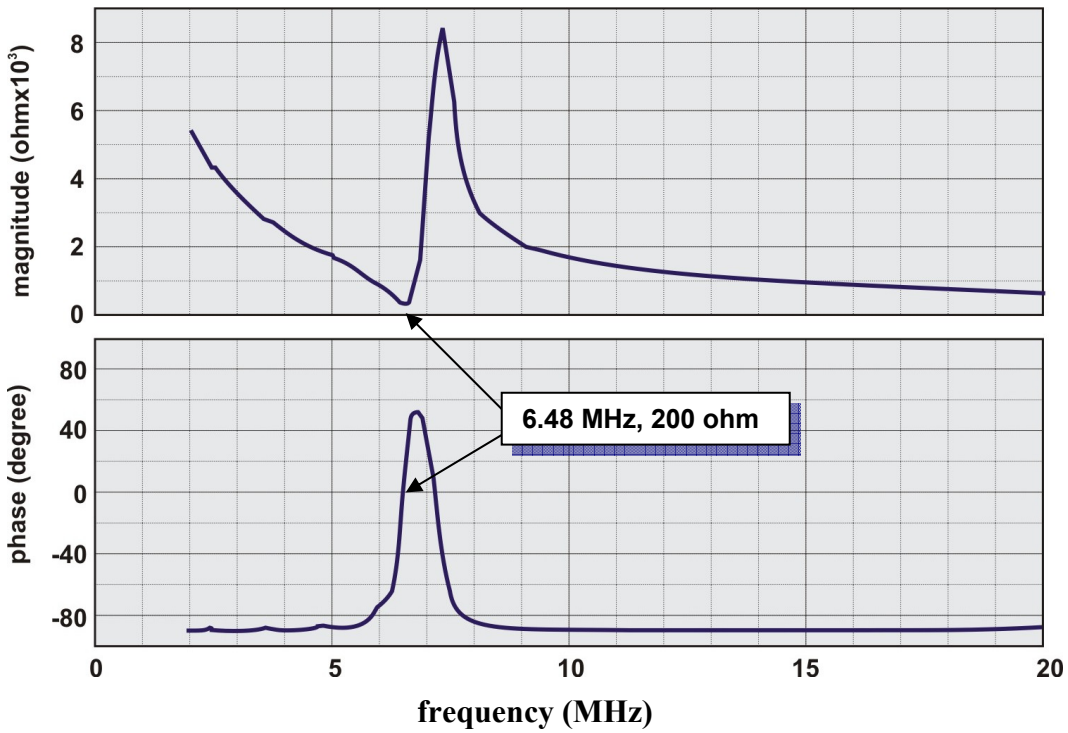

Figure 43. Results of the model shown above in Figure 42 in calculating the electrical input impedance of the AcFFF system. The resonant frequency was determined to be approximately 6.48 MHz and 200 Ω.

function was set to impedance magnitude (logarithmic scale) and phase (linear scale). The instrument Kelvin leads were clamped onto the 30 gauge wrapping wire bonded to the AcFFF transducer electrode bond pads. The channel was filled with DI water and the measurement was recorded to disk and plotted in Figure 44. At zero phase and near minimum magnitude the resonant frequency was determined to be 6.16MHz and 49 Ω. This value is slightly lower in both frequency and magnitude. These differences may be explained by way of transducer area. In the model the transducer area was not the same as the area of the transducer because of a last minute design/fabrication change. The change in area affects the capacitive portion of the impedance causing a discrepancy in the measured from the predicted.

System Setup

The system was setup according to Figure 24 and Figure 25 (Chapter 3) for the experiments listed following. The channel used for these experiments was channel A, which dimensions were reported in Table 2. The transducer was driven with the *Agilent 33250A* function generator operating at 1-10 volts peak-to-peak and 6.08 MHz. The detector electrodes were connected to the low frequency output from an *Agilent* function generator operating at 1-5 volts peak-to-peak and 2 kHz. The *Agilent 3458A* digital multimeter (DMM) was place in-line of the high potential electrode to measure the AC current. The DMM was set to 8.5 digits resolution and number of powerline cycles (NPLC) of 1.0. The NPLC controls the speed and accuracy of the measurement. The guard was not used and was set to ground.

The DMM data and control was interfaced with a PC through GPIB. The interface was controlled through *LabView 7.0* which program is detailed in Appendix A.

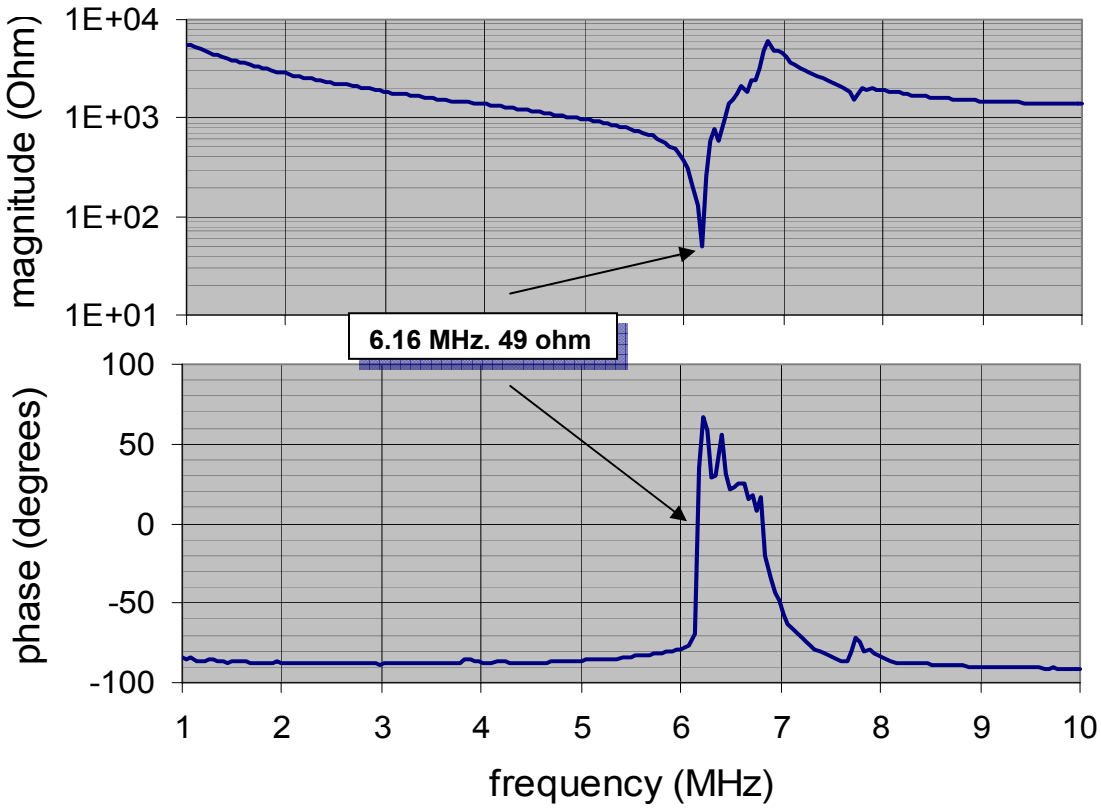

Figure 44. Electrical input impedance measurement of the AcFFF system with the channel filled with DI water. The natural fundamental frequency is at 6.16 MHz.

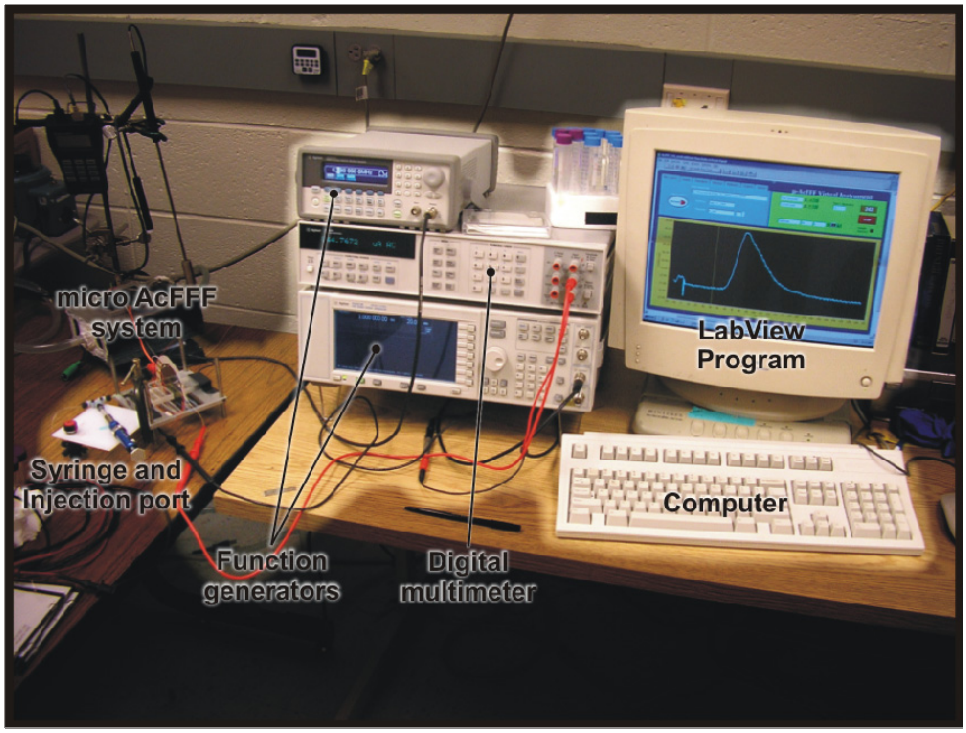

Figure 45. Acoustic system test setup with labeled instruments and components.

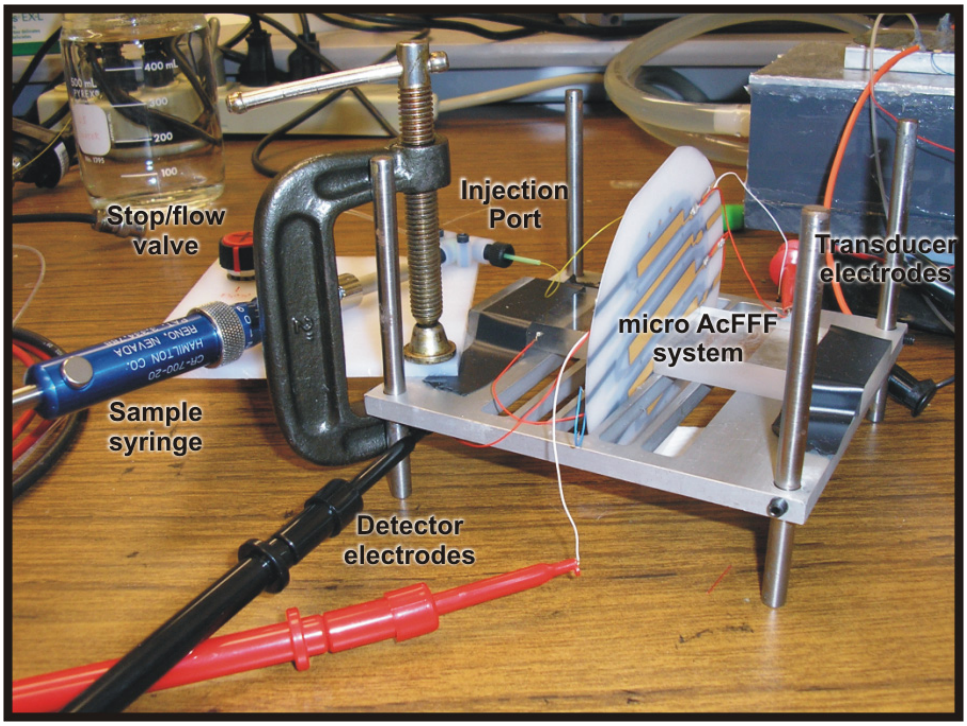

Figure 46. Close-up photo of AcFFF system and interconnects.

This program allowed for the user to control the DMM and function generator as well as collected the streaming data from the DMM and stored it to a file. The file header contained information with regard to the channel dimensions, flow rate, carrier, sample type, sample size, DMM parameters, transducer settings, and detector operation settings.

The flow rate was set manually using a syringe pump (*Linear 100*) and a 3-30 mL syringe. The smaller syringe allowed for the lower flow rates (<0.1 mL/hr) to be used in the plate height studies. The larger reservoir was useful during all other studies. The syringe was filled with either pure DI water or DI water with FL-70 surfactant added. The sample was introduced typically with a *Hamilton* syringe at sizes from 0.1 – 1.0 μL.

Band Broadening Measurements

The concentration of the sample was proportional to the displacement current measure across the channel between the detector wires. A sample peak is shown in Figure 47. The plate height of the sample was extracted using a Matlab program (Appendix E) and determined to be 0.729 cm. The flow rate for this sample was 10 mL/hr or an average carrier velocity in the channel active region of 1.12 cm/s. This peak is not purely Gaussian shaped as a perfect concentration profile is expected to be. The distortion is primarily in the tail, probably due to the injection routine.

The plate height was plotted as a function of various average carrier velocities and plotted in Figure 48. The expected trend of this data was a positive linear at high flow rates and a negative slope (not linear) at low flow rates according to the theory presented previously. There is typically a minimum plate height where these two curves meet. In this curve there appeared to be a minimum at about 0.001 cm/sec. At lower velocities diffusion appeared to be dominant. At velocities just higher there appeared to be a linear

trend. The plate height then drops again and was also quite low at very high flow rates and was difficult to discover a trend over the range of flow rates examined.

Single Component Retention

Various sizes of polystyrene beads in suspension (*Bangs Labs*) were injected into the system in 1.0 microliter boluses to determine retention. The diameters used were 110, 210, and 300 nm. The sample concentrations of the 110 to 300 nm solutions were diluted to 0.1 weight percent from the stock solution of 10 weight percent.

The system was setup with the *x*-direction (direction of field) normal to gravity, Figure 46, to eliminate any effects it may have on the particles, even though its effects on the smaller particles were estimated to be very small. The detector electrodes were driven with a 2 kHz, 5 volt peak-to-peak signal. This frequency and voltage were determined by Gale and Frazier [48] to be optimum for measuring polystyrene suspensions.

The transducer was operated at the fundamental resonant frequency as determined by the previous set of experiments. This frequency was 6.16 MHz, slightly different than the previously recorded measurement due to it being a different channel. The impedance of the function generator was adjusted to match the input impedance of the AcFFF system to ensure maximum power transfer. The voltage was 5 or 7 volts. The force on the sample is proportional to the voltage applied, so retention should be increased with increasing voltage and will be demonstrated in this section.

The first set of experiments included retention of 110 nm polystyrene, 210 nm polystyrene, and 300 nm polystyrene suspensions (termed PS 110, PS 210, and PS 310).

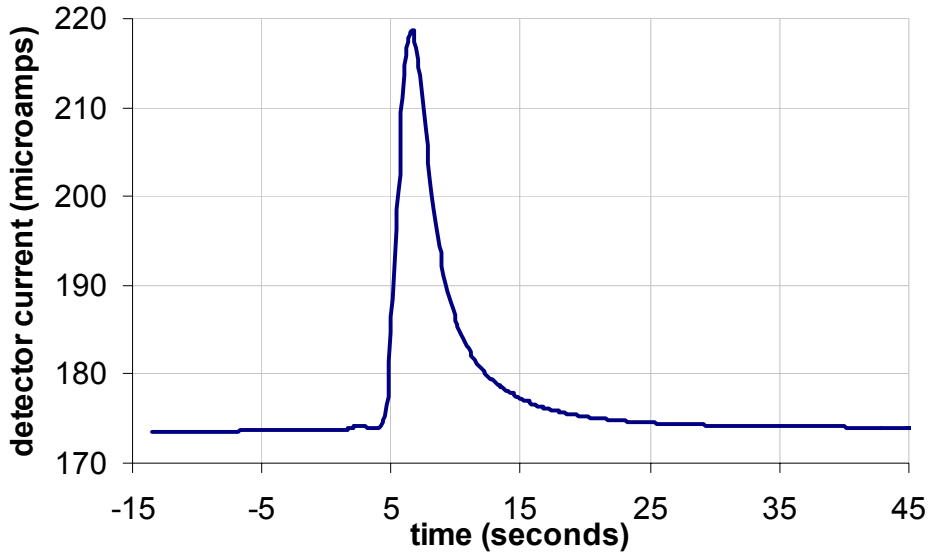

Figure 47. Void peak for plate height measurements. The sample was 0.5 µL of NaCl solution in DI water with FL-70 surfactant. The flow rate for this sample was 10 mL/hr and the time of injection was at 0 sec. The calculated plate height was 0.729 cm.

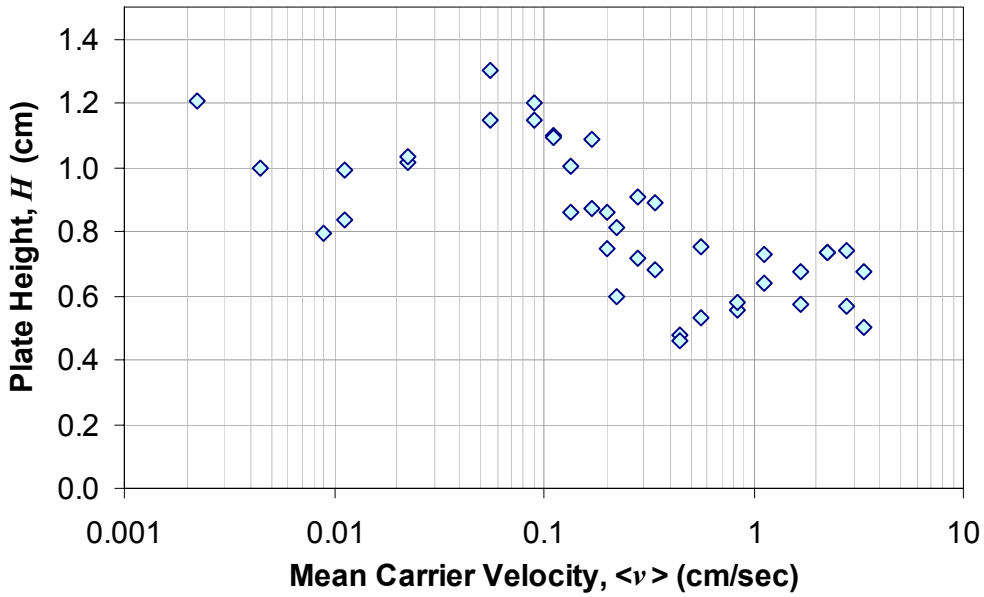

Figure 48. Plate height measurements in channel A of the AcFFF system as a function of carrier velocity in the channel.

These samples were injected into the stream at precisely zero seconds. The data began recording approximately 15 seconds prior to injection to establish a baseline.

The void peak was recorded by injecting PS 110 into a 0.5 mL/hr DI water stream with the transducer voltage turned off (0 volts). The data was recorded and presented in Figure 49 (*top left*). This peak was recorded at 151 seconds. The data in these in graphs have a much lower signal to noise ratio than in the previously recorded plate height data. The impedance change detected was much smaller than with the NaCl solution used to measure plate height. This effect places some limitations on the concentration of the sample. The upper limit of the sample concentration was based on the complex particle-particle interaction within the channel, especially during retention as the sample is further concentrated into bands. The seemingly unstable baseline was of little consequence in this first experiment as the peak was eluted at the expected time. The displacement current magnitude was on the order of forty microamps for DI water and the change in current as the sample passed through the detector was on the order of four to five tenths of microamps. The noise level was on the order of a tenth of a microamp.

The voltage of the transducer was turned on to 5 volts peak-to-peak and 6.16 MHz. The 1 μL PS 110 sample was then introduced into the 0.5 mL/hr of DI water carrier. The sample was retained to a degree and shown in Figure 49 (*top right*). The retention parameter calculated from this graph was 0.222 and the dimensionless sample layer thickness, λ, was determined to be 0.037 or 3.7% of the channel.

With the same conditions of 5 volts and 6.16 MHz, a 1 μL PS 210 sample was injected into the 0.5 mL/hr DI water carrier, Figure 49 (*bottom left*). The sample was

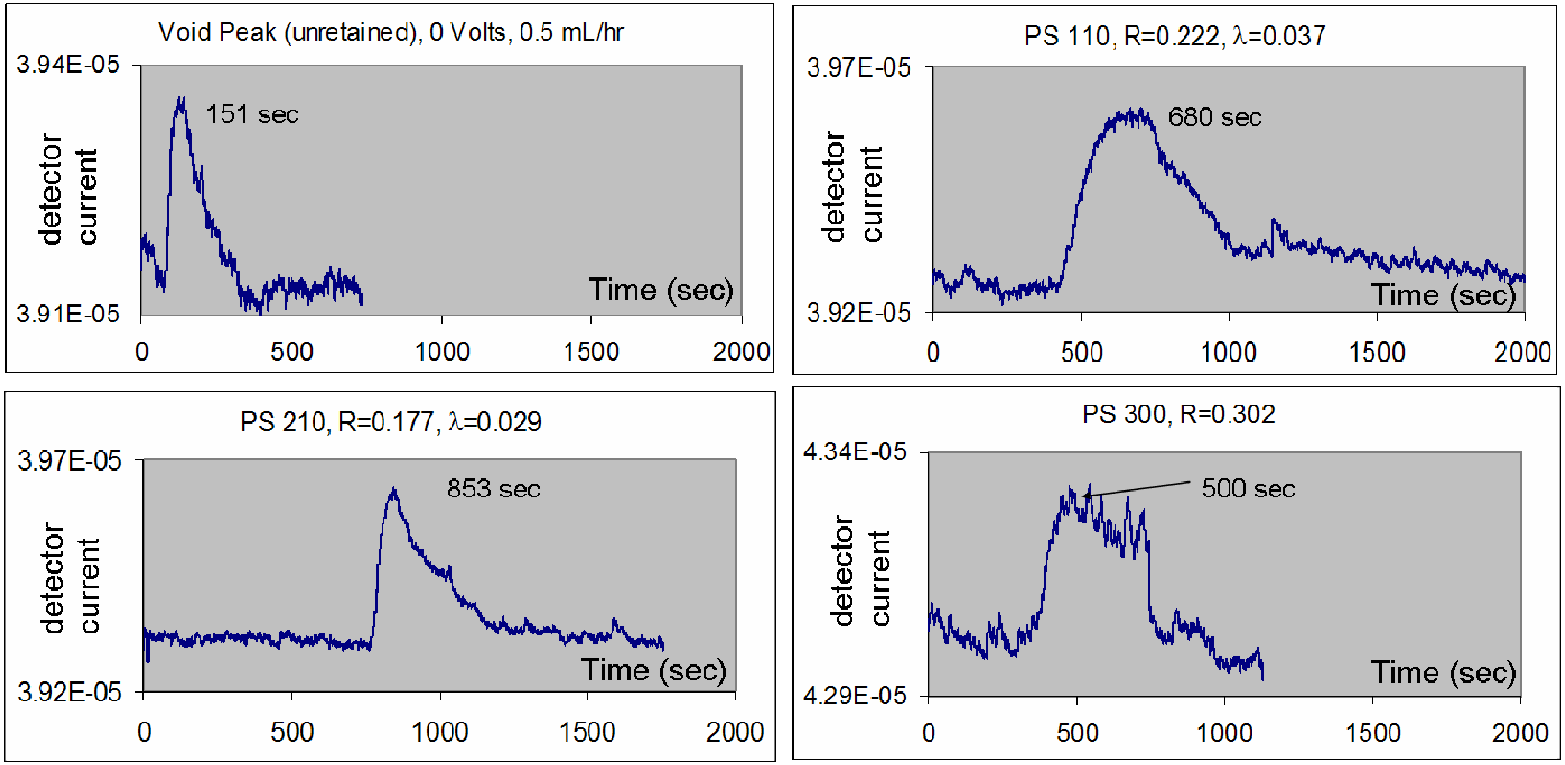

Figure 49. Single size PS particle suspension retention results. *Top left*, unretained PS or the void peak. *Top right*, 110 nm sample retained slightly more. *Bottom left*, 210 nm sample retained more with more distortion in the peak. *Bottom right*, 300 nm PS sample retained less, probably due to steric inversion.

retained more than the 110 nm sample, calculated to be 0.222 with a dimensionless layer thickness of 0.029. This peak was much sharper but tailed off significantly. The reason behind this distortion is not clear, but may be due to subtle differences in sample injection.

A third sample, PS 300 was also injected into the same DI carrier stream at 0.5 mL/hr. This time the voltage was also increased to 7 volts peak-to-peak. A higher retention was expected because of the increase in voltage and the increase in diameter. However, as can be seen in Figure 49 (*bottom right*) the highly distorted PS 300 peak was actually retained less than both the PS 110 and PS 210 peaks suggesting that the steric inversion point had been reached.

Further evidence that the steric inversion diameter was somewhere between the PS 110 sample and PS 300 sample is indicated in the lack of correlation between the calculated retention parameters and the theory. The theory for normal mode retention predicts the retention will increase with the exponent of the diameter cubed. In addition, the steric mode of retention is complicated also by a spatially varying field strength. By adjusting the scaling factor of the simplified steric retention equation a plausible scenario is obtained that closely predicts the values obtained. The scaling factor was estimated to be approximately 15.5 and the front port velocity of the transducer was estimated at 0.65 m/s. Using these values, a plot of the retention ratio for normal, steric, and a linear combination of the two versus particle diameter, can be formed, Figure 50. The retention time is also calculated from these equations and plotted as a function of diameter, Figure 51.

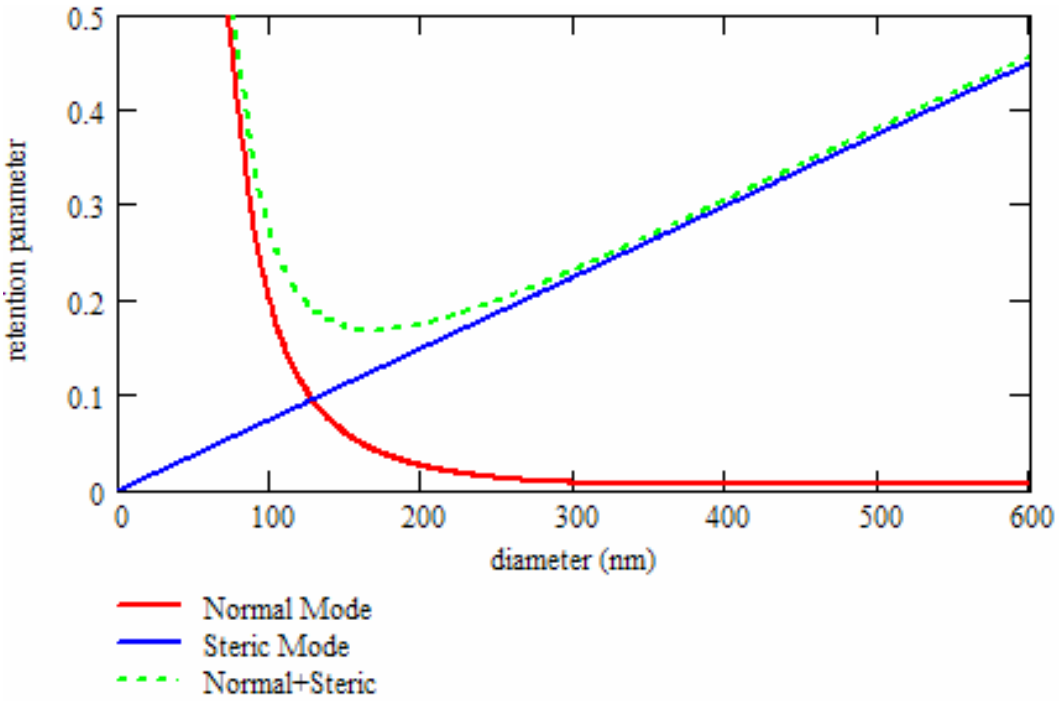

Figure 50. Retention ratio for normal, steric ($\gamma \approx 15.5$), and normal plus steric modes plotted as a function of sample diameter to describe the results.

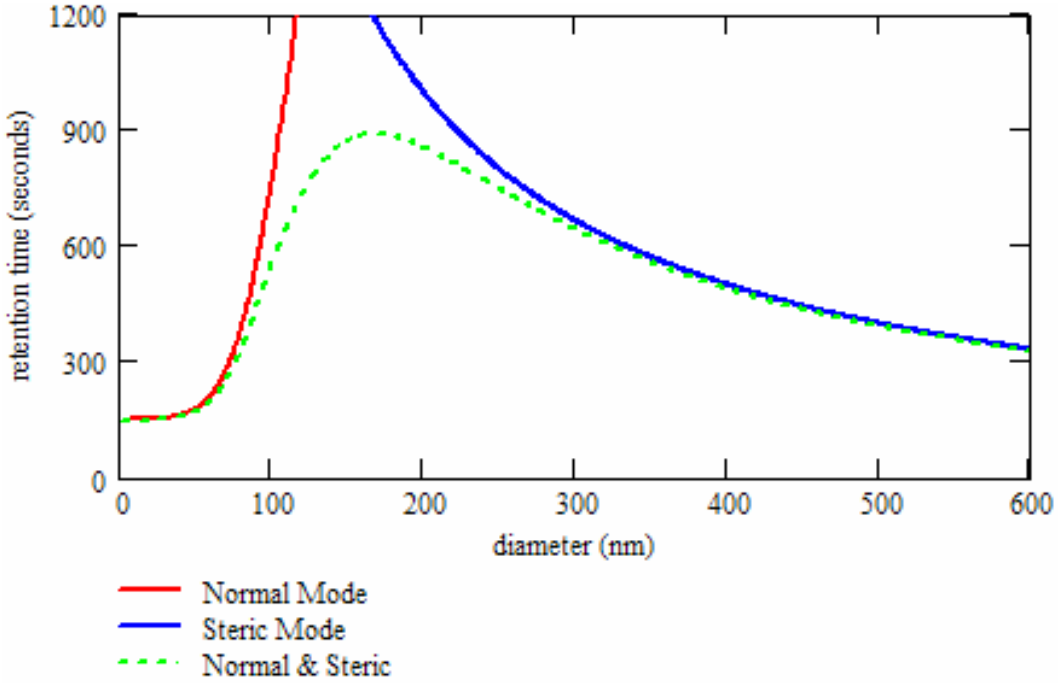

Figure 51. Retention time calculated based on the results of Figure 50. The green curve matches well with the results of Figure 49.

To check to see if retention increases under normal mode the voltage was adjusted from 5 volts to 7 volts peak-to-peak for the PS 210 sample. At the time of the experiments, it was unknown that this diameter was near the steric inversion point and so did not change retention according to the theory. However, the results of the experiments at the two voltages are still interesting, see Figure 52. The difference between the two data sets is a distortion in the peak. The starts of the peaks are approximately the same but the time at maximum was delayed at the higher voltage. This result indicated that the steric inversion point is near 200 nm. The probable explanation for the shift in the time at maximum peak is that the sample under a higher field strength may have experienced more particle-particle and particle-wall interactions than at lower field strengths, causing more band broadening and higher retention for those samples.

Multiple Component Separation

In addition to single particle retention, an attempt to characterize the system with respect to resolution of multiple component polystyrene suspension mixtures was made. However, it has now been recognized, due to the preceding results, that this attempt with PS 110, PS 210, and PS 300 was frivolous and the results conclude this statement.

The samples injected were mixtures of the above mentioned polystyrene samples. The sample size was 1 microliter in each experiment. The sample mixture used was PS 110, PS 210, and PS 300 nm), made using the equal parts of the diluted 0.1 weight percent solutions from the single component retention experiments. The concentration of each of the components in the mixture was then 0.033%. Two voltages were used, 5 and 7 volts peak-to-peak. The results of these two experiments is shown in Figure 53. In neither case is there a separation of any kind. This result follows the explanation of the

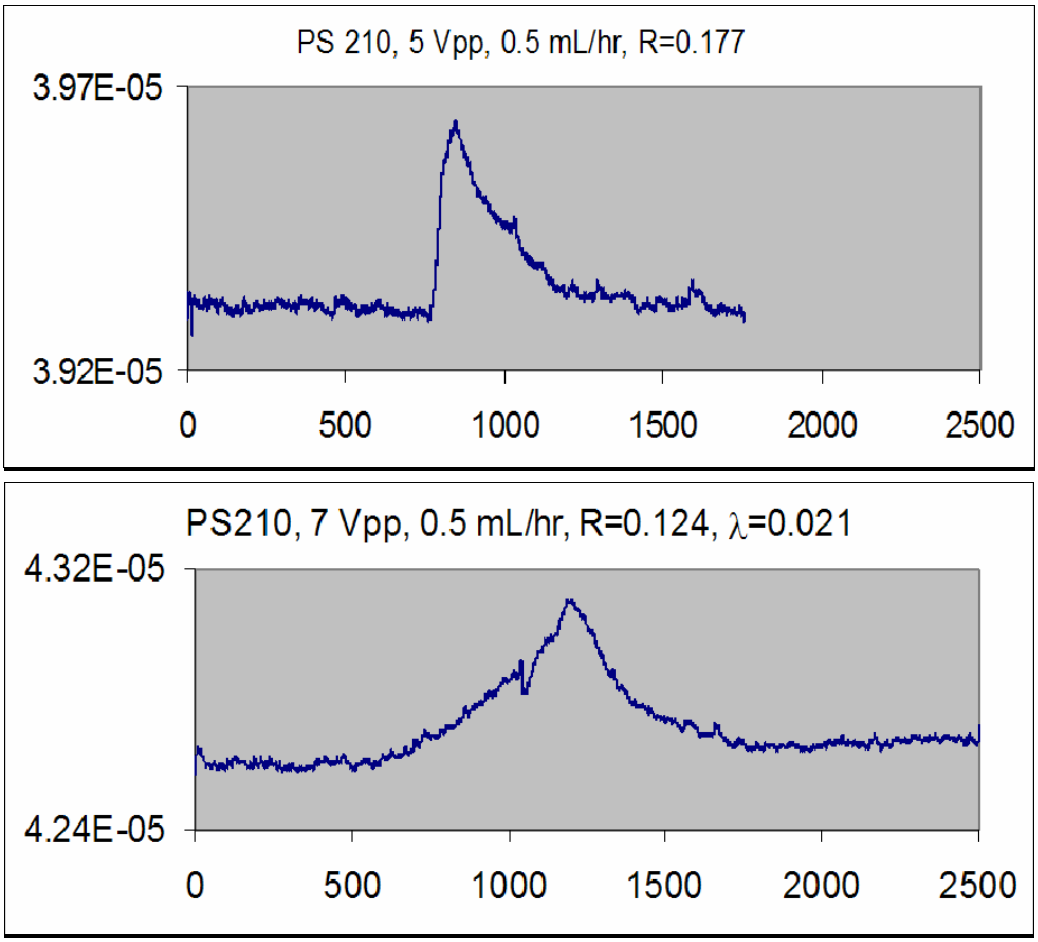

Figure 52. *Top*: PS 210 retained at 5 volts peak-to-peak in DI water at 0.5 mL/hr. *Bottom*: PS 210 retained at 7 volts peak-to-peak in otherwise same conditions.

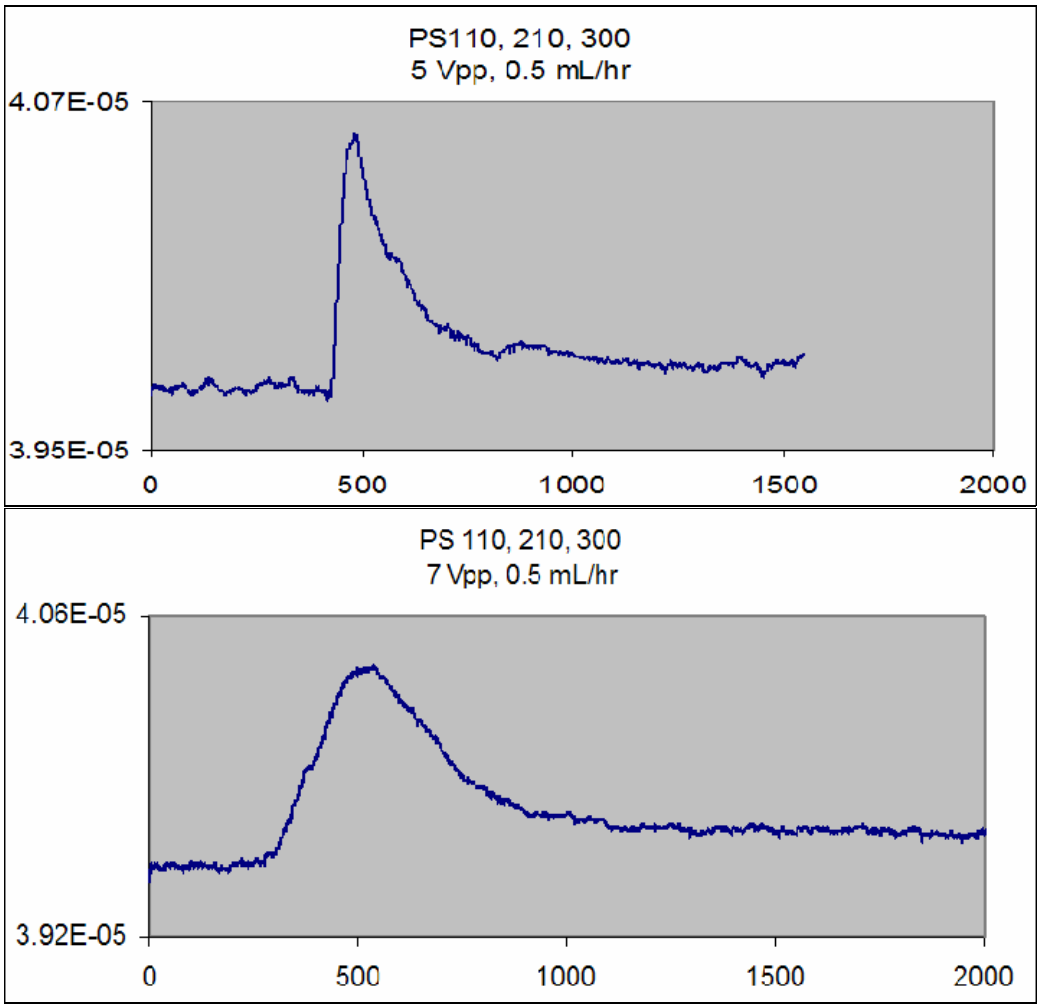

Figure 53. Multiple sample polystyrene mixture (PS 110, PS 210, PS 300) retained in AcFFF channel at 0.5 mL/hr of DI water. *Top*: The transducer voltage was 5 volts peak-to-peak. *Bottom*: The transducer voltage was 7 volts peak-to-peak. Neither sample was resolved due to the steric inversion being around 200 nm.

conclusion that the sample range tested is near the steric inversion point. Compared with the void peak in Figure 49 (*top left*) the sample is retained and much more spread out as a results of the slightly different retention times of the three samples. However, the column is not nearly long enough to allow the samples to resolve. Even with a much longer channel, the PS 110 and PS 300 samples would still likely not resolve due to their having nearly identical retention ratios.

Summary

The μ-AcFFF system was tested and characterized according to a number of tests. First, the fluidic channel pressure drop was measure at various flow rates and compared with Navier-Stokes theory, which was quite close after the incorrect calibration of the pressure gauge was taken into account. The acoustic system was characterized by measuring the electrical input impedance to discover the natural frequencies of the system. These results were compared with the KLM transmission line model investigated previously. The results were slightly different, but thought to be due only to a last minute change in the fabrication from the modeled system design which changed the capacitive portion of the impedance.

Several single component PS spheres were retained the channel. The order of the retention times followed neither the normal mode nor the steric mode of retention. This phenomenon was explained by predicting the steric inversion diameter to be located somewhere in the range of samples tested. Theory supported this claim. This claim was further supported in both the PS 210 retention experiment at different voltages and the multiple component sample separation, which did not resolve.

CHAPTER 5

MICRO THFFF FABRICATION RESULTS

AND SYSTEM CHARACTERIZATION

Fabrication Results

Channel Geometry and Dimensions

Two different mask patterns for the channels were used for this project. The first pattern equivalent to the pattern used by Gale in the μ-ElFFF channel. Ten channels were made in parallel on a single, 3-inch silicon wafer using the methods described in the previous chapter. A photograph of the wafer is shown in Figure 36.

These channels are approximately 25 μm in width and vary in breadth (2 mm, 4 mm, or 6 mm). The channels lengths also vary from 4 cm to 6 cm. The extra SU-8 removed on the edges was for electrical contacts in the μ-ElFFF channel.

The port and entrance region to a 4 mm breadth channel is shown in Figure 55. The walls of the channel are made from SU-8. They are cracked because of over development during processing. A very thin film of SU-8 remained in the channel after development. To correct these problems the post exposure bake steps should be followed exactly. The port was etched using KOH from the backside of the wafer and is 250 μm^2.

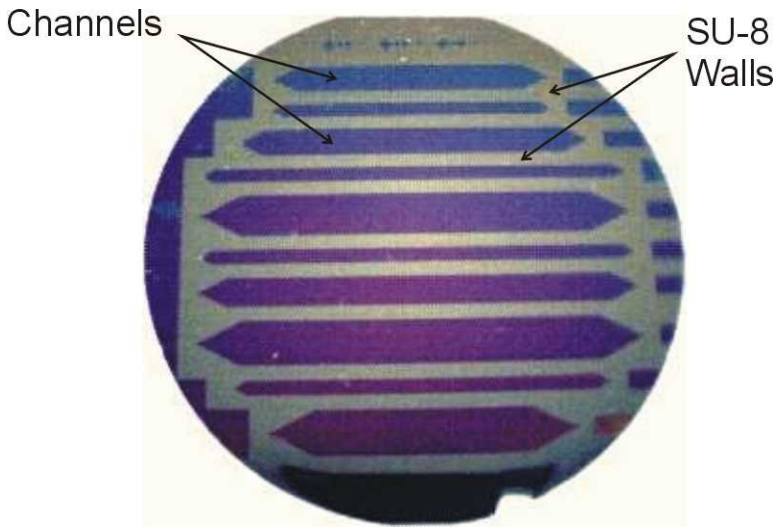

Figure 54. Photograph of 10 μ-ThFFF channels built on a silicon wafer using SU-8.

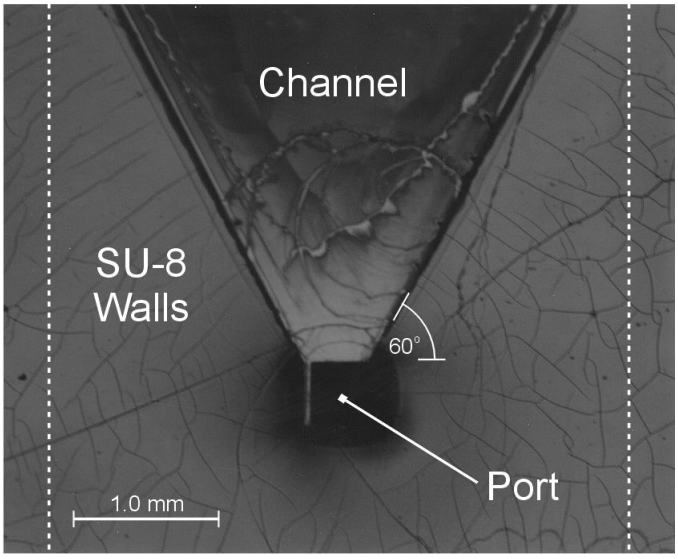

Figure 55. Magnified photograph of a port and tapered entrance region to a μ-ThFFF channel. The dashed lines indicate the heater region on the backside of the wafer.

For this particular channel, the boron doped heater was located on the channel side of the wafer. The SU-8 walls hide the boron-silicon border, which is approximately located at the dashed lines. The widths and breadths of several channels from a single wafer were measured with the *Tencor Instruments*, P-10 profilometer. The profiles are shown in Figure 56.

The maximum and minimum widths measured were 24.8 μm and 23.6 μm. The average wall width from the six walls shown (two scans of two walls each and two scans of one wall) was 24.2 ± 0.6 μm. The sidewalls appear to be sloped but, are actually vertical as shown in Figure 57. This is a scanning electron micrograph (SEM) of a structure (not the μ-ThFFF channel) fabricated using SU-8 on silicon substrate with the same procedure as for the μ-ThFFF channel walls. In Figure 57, the surfaces of both the silicon substrate and the SU-8 are very smooth and flat. The sidewalls are also very smooth. These characteristics help to reduce non ideality factors in the system performance and thus reduce the instrument contribution to the overall plate height.

The final step in fabricating the channel walls is a post development bake at approximately 90˚C for 10 minutes. This step is to remove all remaining solvent from the epoxy structure to ensure a better adhesion to the substrate and resistance to the solvents used in ThFFF. However, like other materials of this sort, this final bake step causes the material to shrink. Channel dimensions may be compromised in this step. The *Tencor Instruments*, P-10 profilometer was used to measure two channel dimensions both before and after this post development bake step. The two channels were 2 mm and 6 mm in breadth, representing the two extremes. The changes in channel width and breadth are found in Table 4. The change in breadth for both the narrow and wide

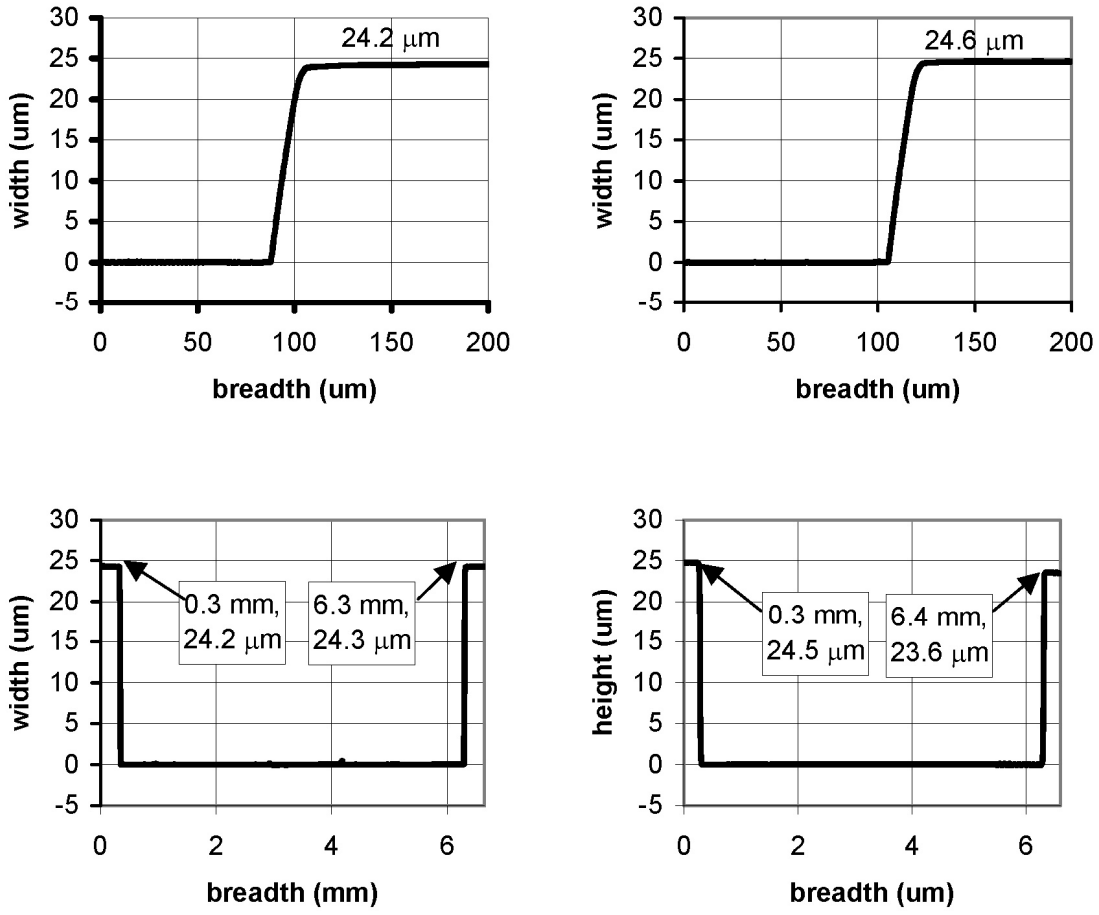

Figure 56. Profilometer scans of several channels from the same wafer. The slope of the sidewalls is due to the slope of the profilometer stylus (60˚). The sidewalls are, in reality, near vertical.

Table 4. Results from the SU-8 epoxy wall dimension shrinkage test. The two conditions were *before* and *after* heat treatment of the walls at 90˚C.

channel	dimension	before	after	change
NARROW (2 mm)	breadth, mm	1.965	1.961	-0.21%
	width, μm	24.19	24.51	1.32%
WIDE (6 mm)	breadth, mm	6.012	6.014	0.03%
	Width, μm	23.22	24.13	3.92%

Table 5. Summary of channel dimensions for the modified μ-FFF channels.

Channel	Width (mm)	Breadth (mm)	Length (cm)
1	25-50	4	4
2	25-50	2	5
3	25-50	6	6
4	25-50	4	6
5	25-50	6	4

channels was very small. This change may even be due to a profilometer measurement that was not oriented exactly perpendicular to the channel walls. The percent change in height for both channels was more significant, 1.32% for the narrow channel and 3.92% for the wide channel. These changes were still small compared to the change in height of the channel due to bonding the channel top to the walls.

Modification to the original μ-FFF channel design entailed reducing the number of channels to five to allow more spacing between channels and the addition of an adhesive trench. The extra SU-8 between channels allows for better adhesive properties of the wall to the substrate and provides a larger area for the adhesive when bonding the channel top to the walls. Table 5 summarizes the dimensions of the five channels. The

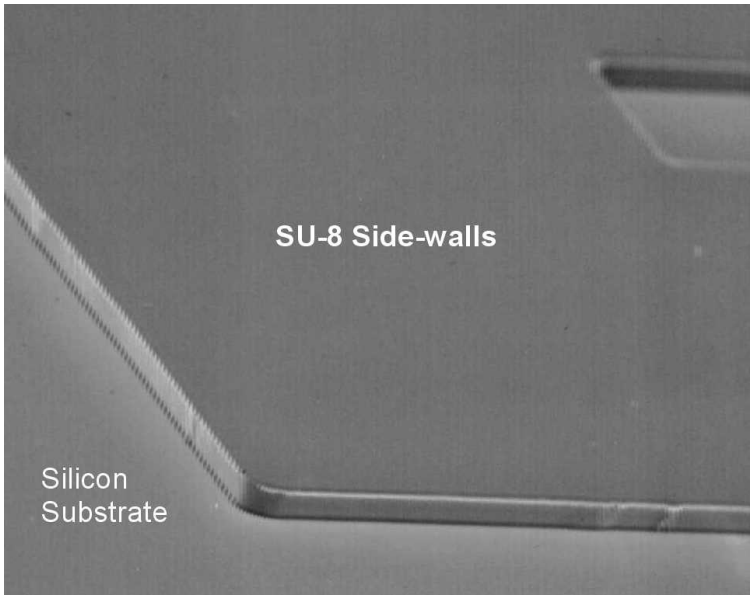

Figure 57. Scanning electron micrograph (SEM) of SU-8 deposited on a silicon substrate using the process

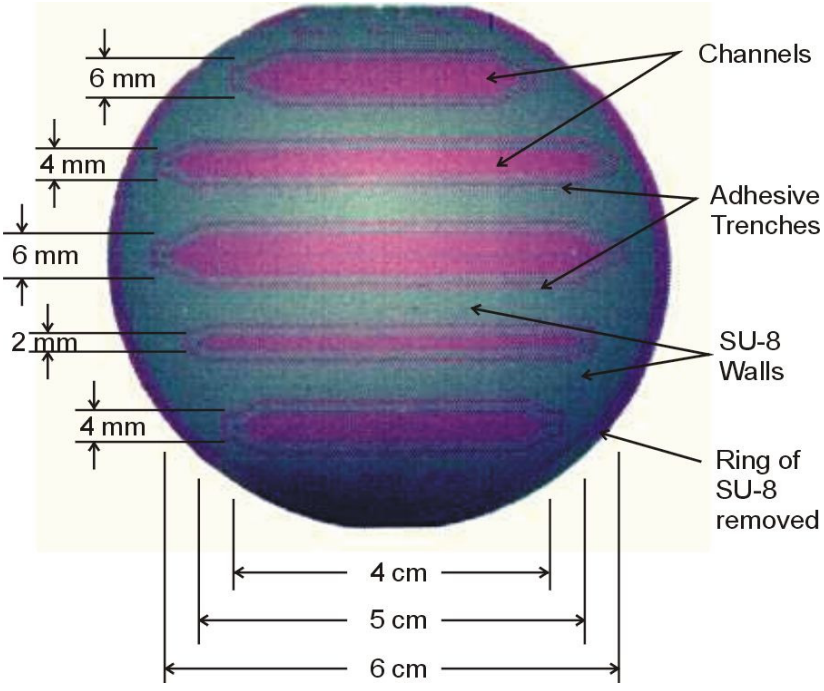

Figure 58. Photograph of five complete μ-ThFFF channels using the modified μ-FFF channel design. This design also included an adhesive trench around each of the channels.

adhesive trench around each was 1 mm in breadth. A photograph of an entire wafer containing the five channels is shown in Figure 58. The five channels run parallel from side to side. All five of the channels were successfully sealed and isolated from each other. A thin ring of SU-8 around the edge of the wafer was removed. Normally, when a thin film is spun onto a substrate, the surface tension at the edge of the substrate causes a slight bead to be formed at the edge. When the channel top is bonded to the walls, this bead can cause problems with forming a complete seal around the ThFFF channel. This ring mostly eliminated problems associated with this edge bead.

A three-dimensional profile of a port and entrance region for a channel fabricated using the modified design is shown in Figure 59. The profile was obtained from the *Tencor Instruments*, P-10 profilometer. The adhesive trench is shown in this figure and surrounds the channel. The sides of the walls appear wavy because the mask used for this channel was made from an ink-jet printer with a resolution of 1440 dpi which limits the resolution transferred to the SU-8. The mask used for the 10 channel design was an electron beam generated mask. The channel walls are approximately 25 μm in width. The adhesive trench is 500 μm in breadth. The surface of both the SU-8 walls and the silicon channel appears very smooth.

Heater Characterization

Two types of heaters were integrated with the μ-ThFFF channel. The first type tried was the boron-doped silicon heater. The boron was deposited at 1175˚C in regions on the silicon wafer where the silicon dioxide had been removed. These regions were doped with boron for 7 hours. Theory predicts a diffusion depth of 5 μm and a resistivity of 9×10^{-4} Ω-cm. The resistances of the heaters were measured from tip to tip using an HP

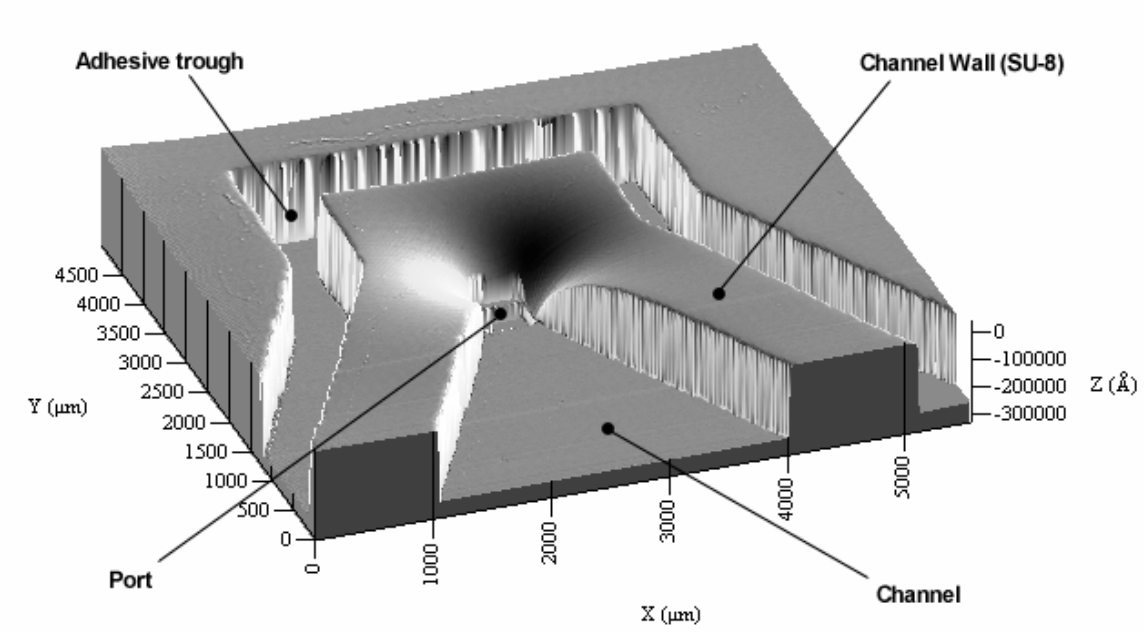

Figure 59. 3-D profile scan of a port and entrance region of the modified µ-FFF channel design. The design also includes an adhesive trench for bonding the channel top to the SU-8 channel walls.

multimeter. An image of the resulting heater and the corresponding measured resistances are shown in Figure 60. The resistivity, ρ, is calculated from the heater length, L, cross-sectional area, A, and the resistance, R, using the equation $\rho = (R \cdot A)/L$. From the three center channels with breadths of 4 mm, 2 mm, and 6 mm, the calculated resistivities are 1.55×10^{-4} Ω-cm, 1.54×10^{-4} Ω-cm, and 3.94×10^{-4} Ω-cm. These values are all lower than the predicted value but are within reason.

Several reasons are given for the difference. The exact amount of time in the furnace is not clear because of the heating up time and cooling time. The exact depth of diffusion is not well known either. Other factors, still, such as impurities may affect the diffusion rate of the boron into the silicon. Cross-talk between channels is possible as well as parallel resistance between the heater and adjacent, undoped regions.

To fully explore the extent of cross-talk between heaters and the thermal diffusion of heat to other regions of the silicon wafer, the heaters were examined with an infrared (IR) camera. The completed channel was placed on the cooling chamber and the electrodes connected to the power supply. The IR camera recorded the intensity of heat radiated from the wafer to a video tape. Still images were then digitally recorded on a computer using a video capture card.

One of these images is shown in Figure 61. In this figure the entire wafer is shown. The two electrical connections from a constant current power supply were connected to each end of the center boron-diffused heater. These connections as well as the active heater are indicated with arrows. The silicon regions appear brighter than the surrounding regions. This contrast is due to the difference in emissivity between the boron-doped and undoped regions of silicon. The brightness of the undoped regions

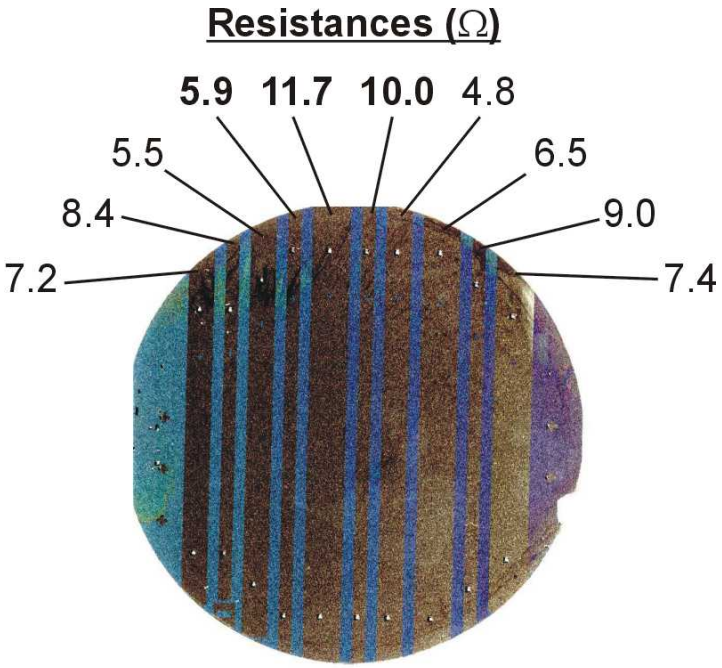

Figure 60. An image of the boron heaters diffused into the silicon wafer and the associated, measured resistance for each heater.

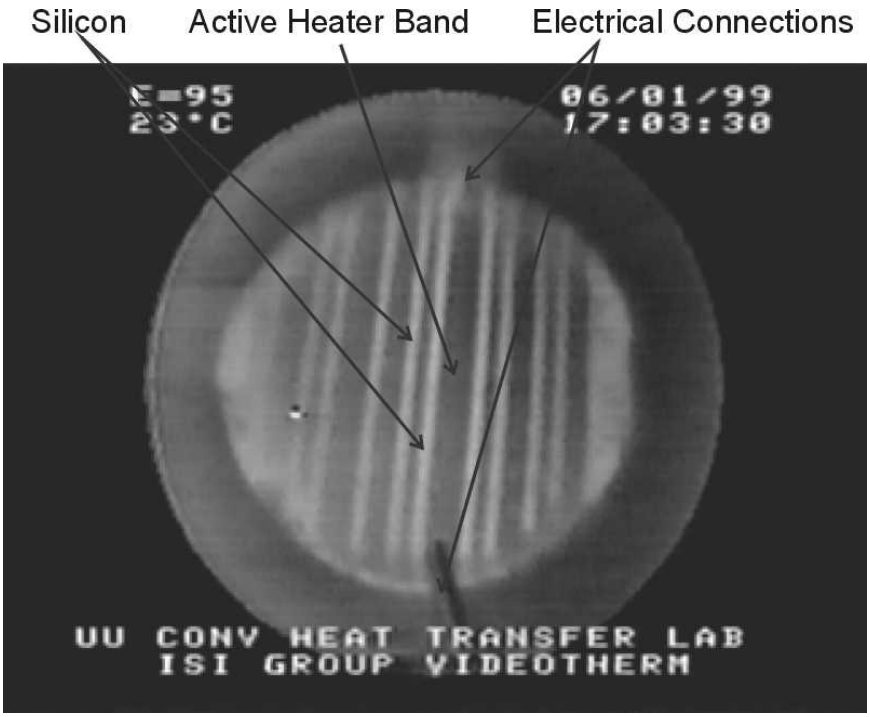

Figure 61. Infrared image of the wafer while applying a current through the center boron-diffused heater.

fades slightly farther away from the active heater. The heat conduction in silicon is very high, leading to the entire wafer temperature being increased.

The boron heaters were very robust and were able to sustain electrical currents of up to 2 amps for long periods of time. However, the boron diffusion method chosen was not the best for this purpose for several reasons. First, the processing time was quite long, approximately seven hours. Second, the concentration of boron in the silicon varied radially from the center of the wafer. However, from Figure 61, the variation in temperature due to this variation of the concentration gradient was very small because of the high thermal conductivity of the silicon. Third, this method will not work if other substrates, such as glass or plastic are used. Fourth, because of the high processing temperature, this method may also make other components impossible to integrate with the channel.

The second type of heater used was a titanium (Ti) metal deposited using sputtering techniques described in the previous chapter. These heaters were used on both the 10-channel and modified 5-channel designs. A photograph of the heater bands on a 5-channel design is shown in Figure 62. The heater bands in the modified design were widened slightly to overlap the channels by 1 mm on each side. The purpose for widening the heater bands past the boundaries of the channel is to ensure a constant temperature profile along the breadth of the channel from edge to edge.

The Ti based heater proved to be the better choice. Titanium can be sputtered onto a wide variety of surfaces and is typically limited by the etching step of the Ti. The substrate processing temperature for sputtering is much lower than that for thermal

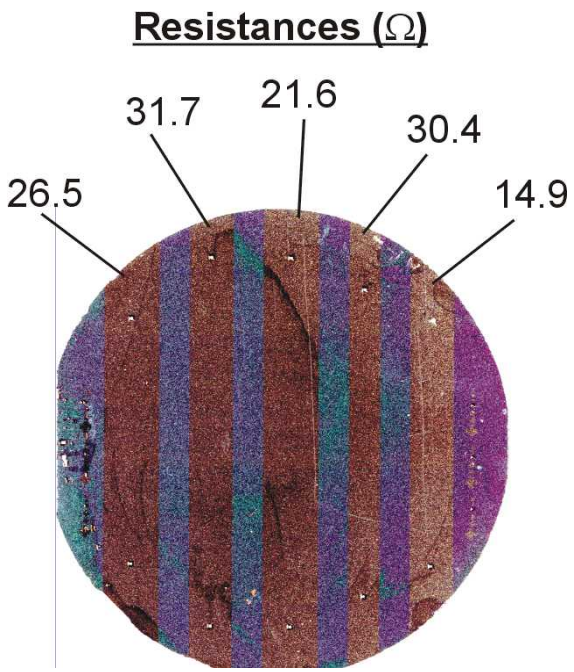

Figure 62. Image of the 5-channel modified heater design. The heaters are made by sputtering Ti metal onto the SiO2 film. The resistance, measured from port to port, is shown for each heater. The heaters are slightly wider than the breadth of the channels.

diffusion. The thickness of the metal in the heater element is easily controlled and is more uniform across the wafer. The Ti heaters had one disadvantage though. The eaters tended to degrade after approximately 10 hours of operation. This degradation was assumed to be from sustaining the current for extended periods of time.

Packaging

The final step in fabrication is to connect the peripheral components of the ThFFF system to the channel and heater. The interface between the micro-components and macro-components includes fluidic, electrical, and thermal connections. Packaging the μ-ThFFF system includes these interconnects.

The fluidic interconnect design was shown in Figure 32 and Figure 33. The design was tested and successfully resisted solvents such as methanol, acetone, tetrahydrofuran (THF), and dimethylsulfoxide (DMSO). The sample injection port and fluidic interconnects are shown in Figure 63. This design was successfully used to introduce samples at the inlet port to the μ-ThFFF channel. An *SGE* 1 μL syringe was used to inject polystyrene sample sizes that ranged from 0.05 μL to 1 μL. A *Hamilton* CR-700-20 syringe was used to introduce sample volumes in the range of 0.1 μL to 5 μL.

The electrical interconnects are also shown in Figure 63. These interconnects are simply made from short pieces of copper strand wire. The wire was bonded and electrically coupled to the heater by Silver Paste Plus, (*SPI Supplies,* West Chester, PA). The paste was cured at 90˚C for 10 minutes to allow for good electrical connections. The wires were mechanically secured to the silicon wafer using either the cyanoacrylate adhesive or the silicone. The wires were then connected to the power supply leads with alligator clips.

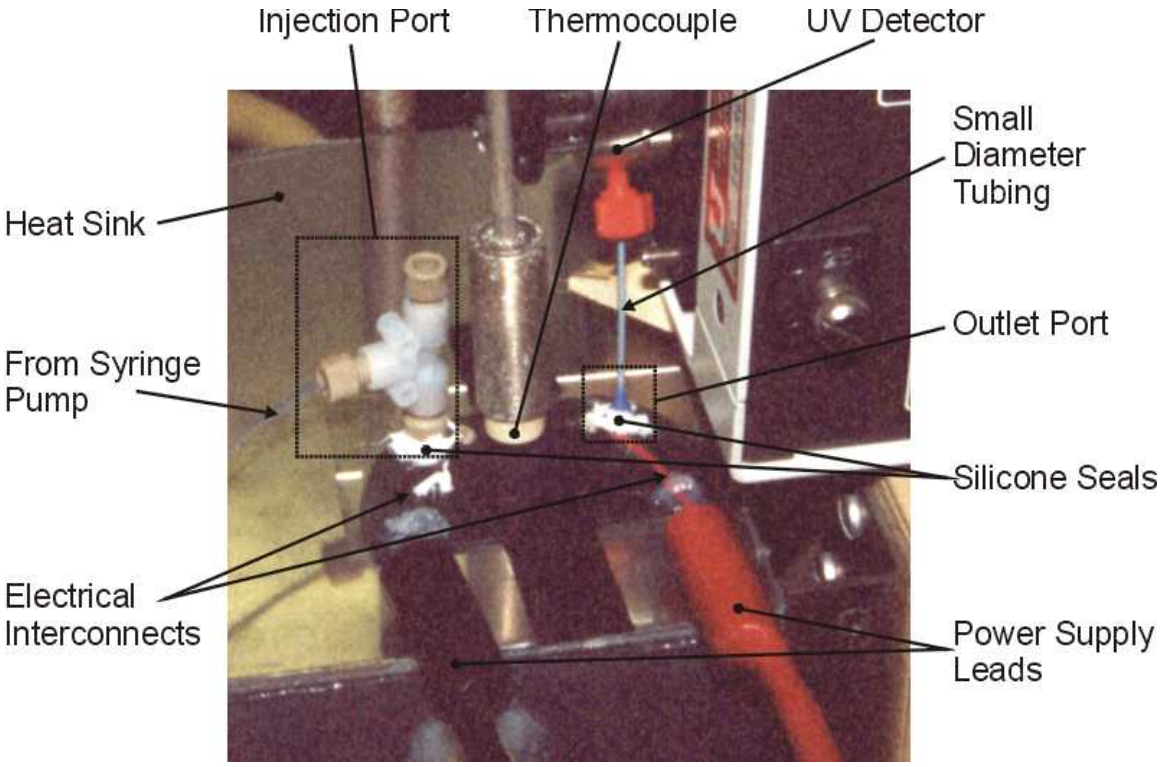

Figure 63. Photograph of the fluidic, electrical, and thermal interconnects from the micro-channel and heater to the other system macroscale components.

The thermal interconnects included both a J-type thermocouple and the heat sink as shown in Figure 63. The thermocouple was placed on top of the heater with a piece of electrical tape between the heater and the thermocouple to ensure electrical isolation. The thermocouple was plugged into a *Barnant* digital thermometer. The wafer was placed on top of the cooling chamber. Tap water, at approximately 10˚C, was passed through the chamber at a rate high enough to maintain the cold wall temperature.

After the interconnects were adhered to the μ-ThFFF channel and the heater, the peripheral components were then attached to the interconnects. The complete system is shown in Figure 64. Future work may include miniaturization of other macroscale components and integrating these components with the μ-ThFFF channel and heater.

μ-ThFFF System Characterization

The μ-ThFFF system is evaluated in this section. This evaluation will encompass the parameters commonly associated with ThFFF systems as described in the theory of Chapter 2. The primary goal of this research was to build a miniature ThFFF channel with integrated heater and demonstrate fractionation of samples containing particles with different physical sizes. Improvements in separation over macroscale ThFFF systems were explored only in theory. However, a comparison between the μ-ThFFF system and a macroscale ThFFF system in retention and separation of polystyrene particles in DI water is performed.

The important parameters of the ThFFF systems that will be considered in the evaluation are the void volume (V^0) and void time (t^0), retention (R) of polystyrene samples, plate height (H).

After fabrication of the μ-ThFFF channel and the integrated heater, the system was setup according to Figure 26. The final system setup was shown in Figure 64. A detail of the system setup and the experiment methods for each experiment follows in the next sections.

Experimental Setup

A *Becton-Dickenson* (B-D) 5 mL, plastic syringe was filled with the carrier fluid (typically DI water for this research) and placed in the syringe pump, *KD Scientific,* model 100. Polypropylene tubing (PP), 1/16" OD, was used to connect the *B-D* syringe to the injection port tee. The outlet of the channel was connected to the *Linear* UV-106 extinction detector with *Tefzel* tubing, *Upchurch Scientific*. This tubing had an extremely small inner diameter. From the UV detector, 1/16" PP tubing emptied to an open container. To prevent changes in channel pressure as the carrier fluid dropped from the end of the tubing, the end of the tubing was submerged in water. Samples were introduced into the channel as described in the previous section.

A *Hewlett-Packard*, HP E3611A power supply unit was connected to the electrical interconnects of the integrated heater using standard copper wire and alligator clips. The power supply unit had meters for both the voltage and the current.

The wafer was placed on top of the aluminum heat sink. The heat sink was connected to the laboratory water tap. The surface of the heat sink was typically at 11˚C. The J-type surface probe thermocouple was placed on the surface of the heater with a piece of electrical tape to electrically isolate the thermocouple from the heater. The thermocouple was plugged into a *Barnant*, model 100 thermometer. This thermocouple was also used for temporary temperature measurements of the heat sink surface.

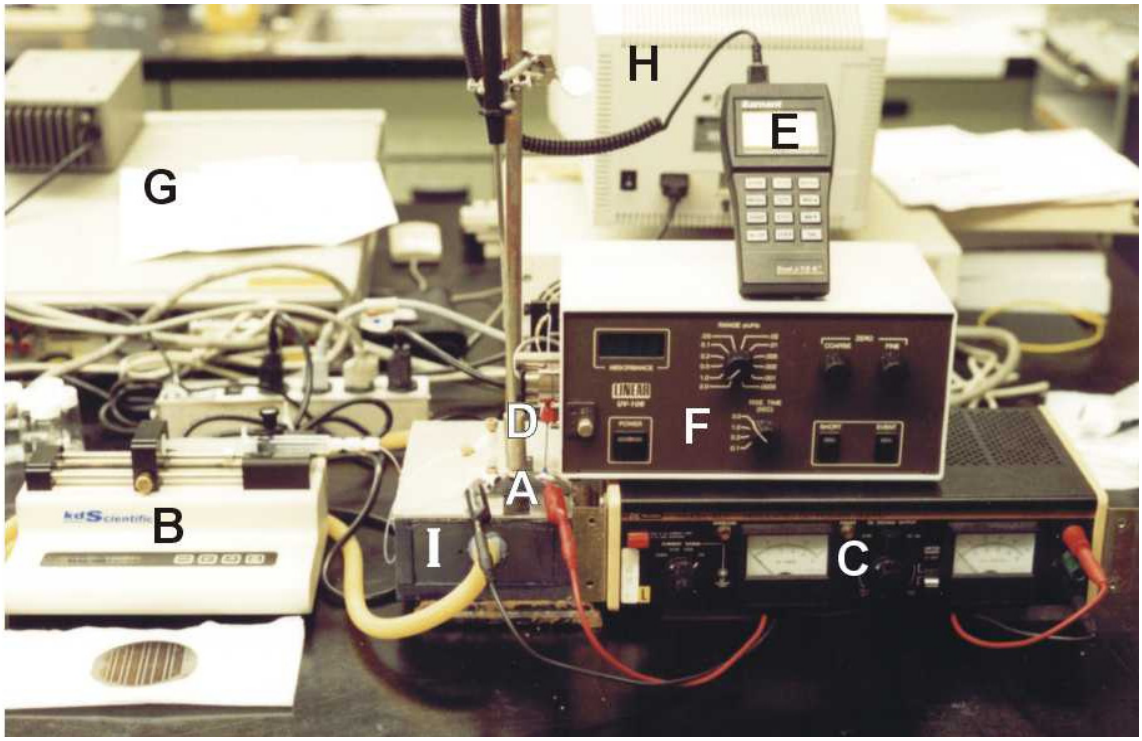

Figure 64. An image of the completed, assembled, μ-ThFFF system. A, micro channel; B, syringe pump; C, power supply; D, thermocouple; E, thermometer; F, UV extinction detector; digital multimeter; H, personal computer; I, heat sink.

The UV detector output was a voltage from 0-5 volts proportional to the relative absorbance of the carrier fluid. The signal was wired to an *Agilent* 3458A multimeter. The multimeter was connected to the computer with a GPIB cable. *LabView* software was used to control the multimeter and GPIB PC card and to plot the data acquired to the screen and log the data to the disk drive. The *LabView* G-program and setup is shown in Appendix A.

Experiments and Methods

The first test was to measure the void time (void volume) of the channel and plate height for an unretained sample. Three sets of experiments were used to characterize various arrangements of the μ-ThFFF system: *First*, a simple channel with off-chip UV absorbance detection and T-shaped injection port; *Second*, a channel with an on-chip electrical impedance detector and L-shaped injection port; *Third*, a channel with an on-chip electrical impedance detector and automated injection port. Not tested, but certainly considered for important future research is that of a channel with both integrated detection and sample injection.

A simple channel (heater only) with dimensions of 25 microns in width was used. The flow rate was set by the syringe pump to an accuracy of ±0.01 mL/hr. The flow rates used were 0.50, 0.75, 1.00, 1.25, 1.50 and 2.00 mL/hr. Stock grade acetone, 0.2 μL, 100%, was injected through the injection port with the *Hamilton* 10 μL syringe. The data from the *Linear* UV extinction detector were collected with the PC. The void time is the time at which the center of the acetone peak is detected. The void volume is the flow rate multiplied by the elution time.

The next step for improvement of the microfabricated ThFFF system was integration of a concentration-based detector. The detector used was based after one used by Gale in his μ-ElFFF system, a simple two wire impedance detector as described in the previous chapter. This integration was expected to dramatically decrease instrument contributions to band broadening by eliminating extra-column and detector volume. A channel similar to that in the first plate height experiment with the exception of the integrated detector was used. The flow rate was adjusted to give average carrier fluid velocities with a range of 0.772 – 2.57 cm/sec. The detector was operated at 2 kHz and 5 volts (peak-to-peak). To improve detectability, the sample was changed from acetone to a 0.068 N NaCl solution. The current was measured as a function of time. These data were used to calculate the plate height for each set velocity.

Another large contribution from the instrument to sample broadening is in the injection system. Ideally but also practically, an integrated injection system with on-chip pumps and valves that are so prevalent in microsystems would minimize plate height, allow for smaller sample sizes to be injected, and allow for tighter control of injection time and sample size. Integration of an injection port was beyond the scope of this project; however, the intermediate step toward this goal is the use of an off-chip automated injection valve.

The third plate height experiment was to demonstrate that by using an injection loop in conjunction with an automated timing system the plate height could be reduced. A channel similar to that used in the previous experiment was used in this experiment as described in the previous chapter. The sample size was 1 μL and the flow rate was

adjusted to give average velocities in the channel of 0.00514 – 1.54 cm/sec. The on-chip impedance detector was operated identical to that in the previous experiment.

The next experiment was to observe retention with a single component. For this experiment, 597 nm polystyrene beads suspended in DI water were injected into the channel with a temperature gradient established across the width of the channel. The temperature was set by first measuring the temperature of the surface of the cooling chamber and then adjusting the power output of the power supply unit until the temperature measured at the heater remained steady at the desired temperature. The hot wall temperature was set at 61.8 ˚C and the cold wall temperature was set at 15.8 ˚C. The carrier flow rate was set to minimize the plate height as determined from the previous experiment. This flow rate was approximately 1.25 mL/hr.

The last experiment was to determine if the system is capable of separating polystyrene spheres of different sizes. Several experiments were conducted for this purpose. The first experiments were operated under the same conditions as that for the single-component retention experiment. The last experiment was to compare the results with those obtained from a nearly identical experiment, using a macroscale ThFFF system. The velocity was set to 5.55 cm/min which corresponds to a flow rate of 1.00 mL/hr. The temperature gradient was 0.544 ˚C/μm with the cold and hot wall temperatures at 11.8 ˚C and 39.0 ˚C, respectively. The sample size injected was 0.5 μL of a 394 nm and 597 nm polystyrene particles.

The last experiment was to observe the relaxation time or the time required for the particles to reach spatial equilibrium under the applied thermal field.

Results and Discussion of Results

Void Volume, Void Time and Plate Height

From the first plate height experiment setup a sample of the detector response to 0.2 μL of acetone in DI water carrier is shown in Figure 65. The flow rate for this sample was 1.00 mL/hr with no temperature gradient applied across the channel. This peak represents the time at which the void peak would be eluted when a sample would be eluted. The void time in this case is ~63 seconds. The corresponding void volume is calculated to be 0.0175 mL. Eluted peaks are normally Gaussian shaped. Too much sample volume caused the peak distortion in this case.

The plate height calculated for this peak, using equation 19, is 0.44 cm. The channel length is 8 cm in this case. Half the length is the actual μ-ThFFF channel and the other half is the extra column tubing from the outlet to the detector. Integration of the detector would have a direct impact on this calculated value of H by reducing the column length as well as reduce the amount of peak distortion in the channel itself.

The flow rate of the carrier fluid was varied between 0.50 mL/hr and 2.00 mL/hr. The optimum flow rate to perform separations at is located at the minimum plate height. A second order polynomial was fit to the data. A second order polynomial was chosen because it best fit the data. The polynomial is then differentiated to find the minimum. For the data of Figure 66 the optimum flow rate is ~1.3 mL/hr. This optimum flow rate can theoretically be determined as described by Giddings [244]. For the acetone/water binary system the diffusivity, D, is approximately 2×10^{-5} cm^2/sec. The sample is unretained (R = 1.0), so the calculated theoretical value is around 0.12 mL/hr. For a small macromolecule with a value for $D = 2\times10^{-6}$ cm^2/sec, under moderate retention

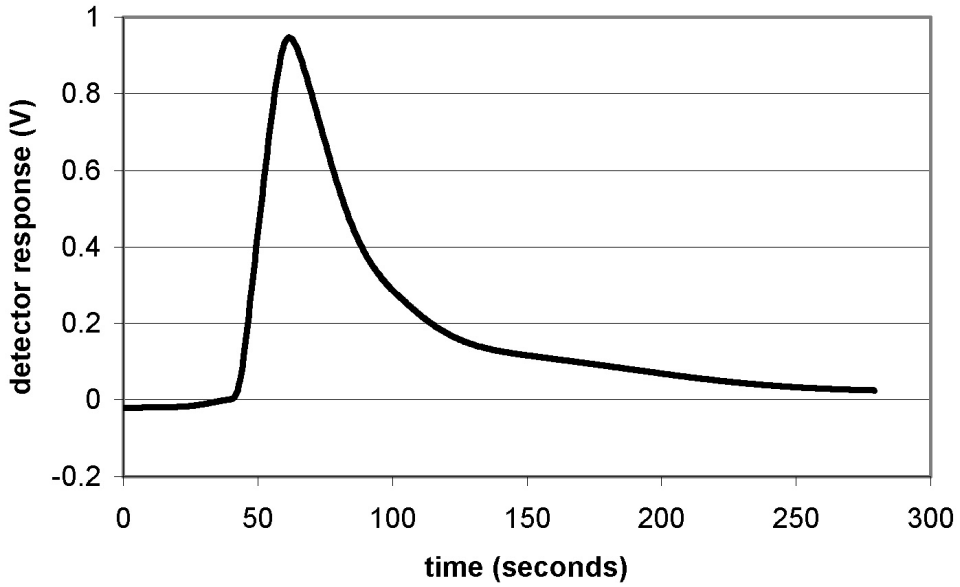

Figure 65. The detector response to a 0.2 µL sample of 100% acetone. The carrier flow rate was 1.00 mL/hr. No temperature gradient was applied.

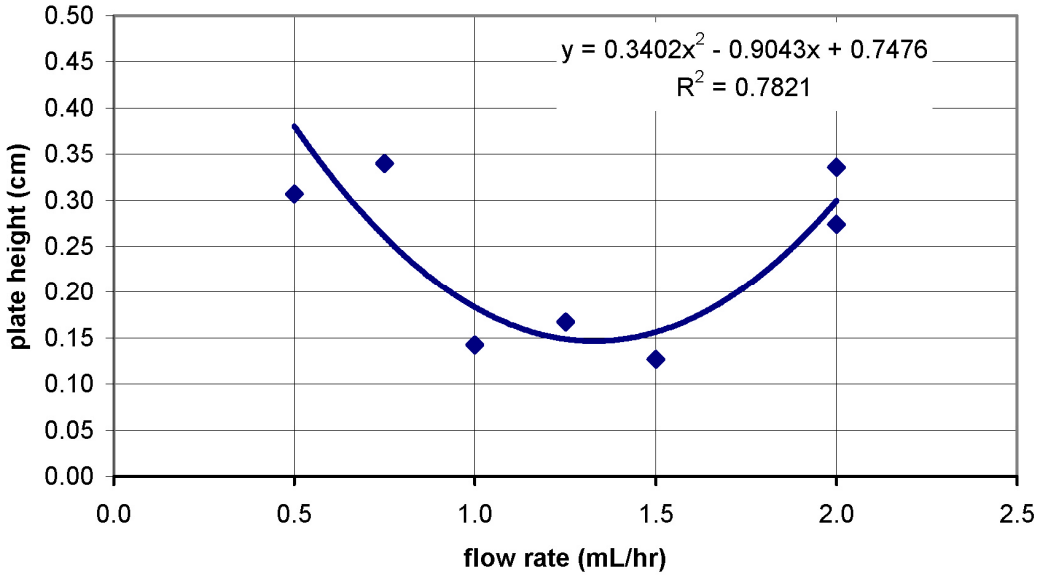

Figure 66. Plate height measurements as a function of the carrier flow rate. This measurement is used to determine the optimum carrier flow rate.

(R = 0.1), the optimum flow rate equal to that determined in this experiment. However, the optimum flow rate is linearly proportional to the diffusivity, D. Thus, for typical macromolecules ($D \approx 10^{-7}$ cm^2/sec), the optimum flow rate is much lower, approximately 0.06 mL/hr.

Results were obtained from the plate height experiments of the other two systems. These results are shown for the system with integrated detector and one with an automatic injection valve in Figure 14 and Figure 15, respectively. The plate height of the m-ThFFF system with an integrated detector is compared with the same system and an off-chip UV extinction detector. The effects of moving the detector and eliminating the post-column volume of the tubing and detection chamber was a reduction in the overall plate height. This graph shows only linear region and the extrapolated system plate height at zero velocity; it does not show the diffusion effects on plate height at low carrier velocity.

Figure 15 is used to compare the effects of different sample introduction schemes. The automatic injection valve had a clear advantage over the manual syringe injection through the L-shaped injection port. The T-shaped injection port was similar to the L-shaped as expected. The purpose of this experiment was to prove the advantage of moving toward integration of the injection system on-chip.

It can be safely assumed that plate height will continue to be minimized through the integration of the external components such as sample injection, valves, pumps, sorting channels and sample recovery wells, and sensors. This effort was not within the scope of this research but acknowledged as a reasonable and logical procedure.

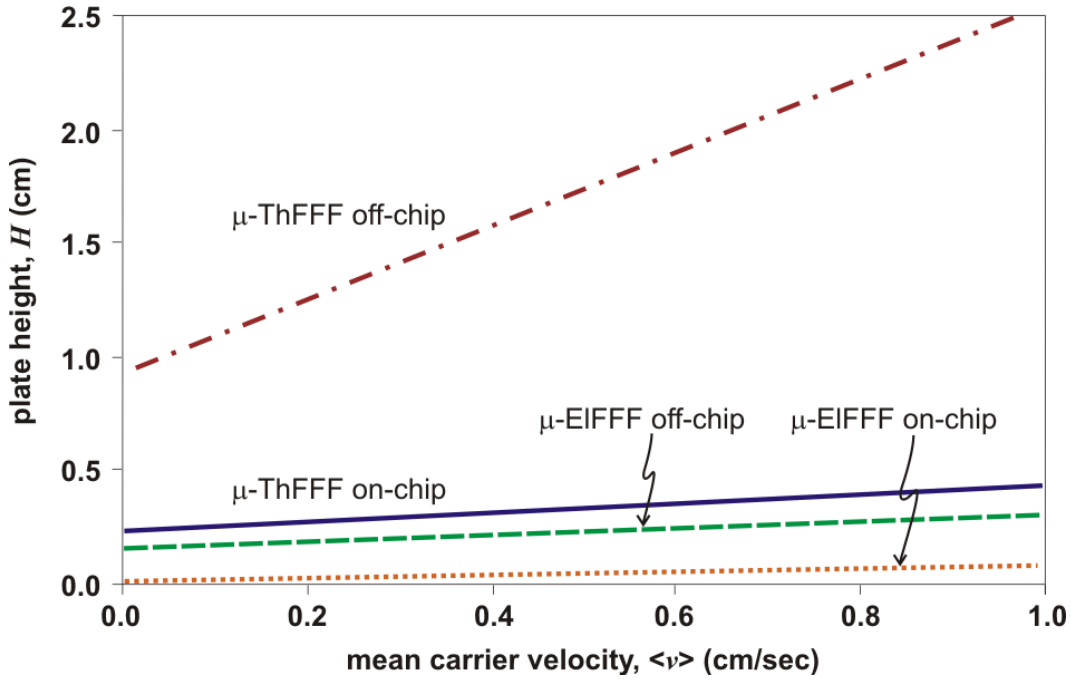

Figure 67. Plate height of microfabricated thermal FFF system with either an off-chip UV extinction detector or an on-chip integrated impedance detector. There is significant decrease in the system plate height with the on-chip detection. These results are compared with the previously microfabricated electrical FFF system.

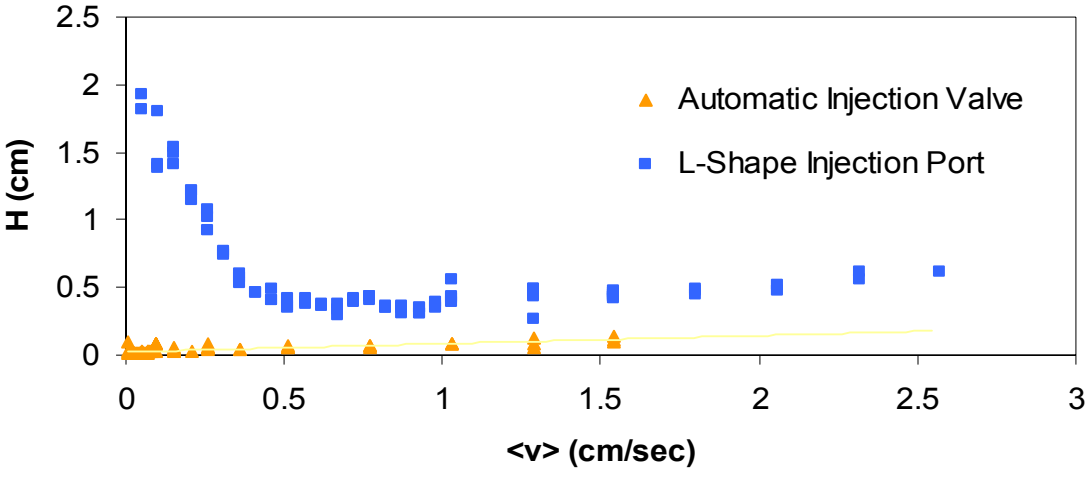

Figure 68. Plate height comparison between two types of sample injection schemes. The injection valve has minimal mixing at low flow rates and tighter control over the injection.

Retention of a single component

The result for the retention of a single component polystyrene (PS) sample is shown in Figure 69. The diameter of the PS beads was 597 nm. Three peaks are present. The void and 597 nm peak elution times were 29 seconds and 55 seconds, respectively. The third peak at 86 seconds represents the doublet formed by two 597nm particles. The retention ratios for this singlet and doublet samples are 0.53 and 0.34. The Soret coefficients (D_T/D) were calculated to be 2.37 K^{-1} and 3.66 K^{-1}. The diffusion coefficients were calculated to be 8×10^{-9} cm^2/sec and 4×10^{-9} cm^2/sec. The thermal diffusion coefficients were then calculated to be about 2×10^{-8} $cm^2/sec\cdot K$.

The average value for the thermal diffusion coefficient is compared to experimental results by Giddings. The extrapolated value from his data, corrected for the cold wall temperature difference, is 3×10^{-8} $cm^2/sec\cdot K$. The error may be due to extrapolation of the data acquired by Giddings. In the next experiment with separation multicomponent mixture of PS beads, the data will be shown to correlate better with Giddings results.

In the experimental methods section, it was mentioned that the temperature measurements for the hot and cold wall were made on the surface of the heater and the surface of the heat sink. By assuming these measurements to be the hot and cold wall, the thermal diffusion coefficient calculated for this retention experiment would be about 2×10^{-9} $cm^2/sec\cdot K$. This small value indicates that the hot and cold wall temperatures are not actually the measured temperatures. An investigation into the heat conduction through each of the materials confirms that this assumption is invalid. The calculations for the heat conduction are found in Appendix C. The temperature difference measured

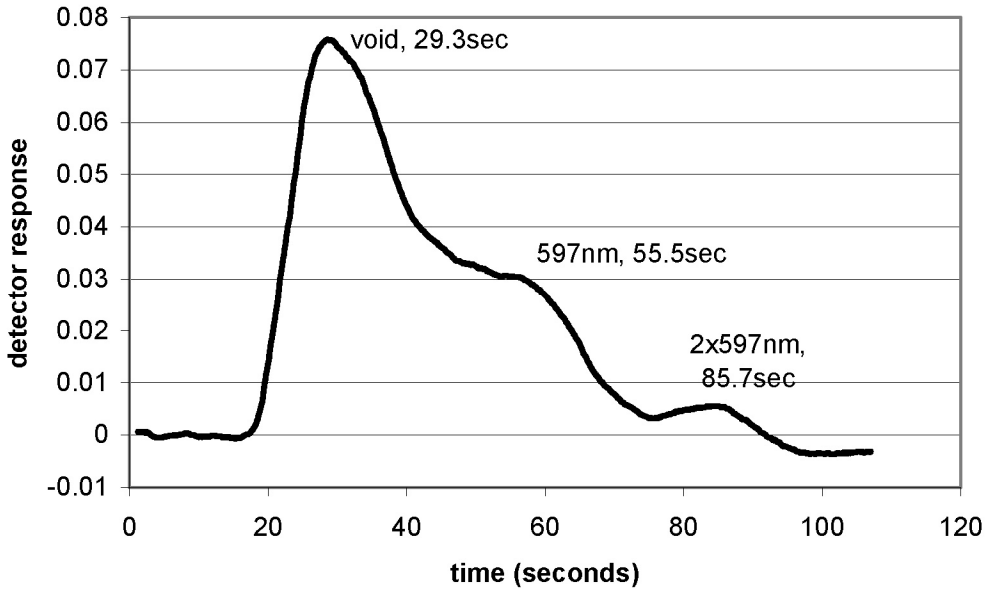

Figure 69. Retention of a 597 nm PS particle sample and its doublet in DI water.

was 46 ˚C. The actual temperature drop across the channel is only 4.8 ˚C. Using this value for the thermal diffusion coefficient calculation gives the correct value.

Because of the very small temperature gradient, the samples were only slightly retained in the system. Estimates of the layer thickness from the retention ratio, as given by equation 10, for the singlet and doublet peaks are 4.40 μm and 2.85 μm,

respectively. An increase in the temperature gradient directly affects the sample layer thickness and the retention of the sample and would, in turn, increase the resolution of the separation. However, the theoretical temperature difference could be increased to only ~5.7 ˚C without reaching the steric transition point for the doublet.

This increase in temperature difference can be accomplished simply by increasing the hot wall temperature. However, there are two points to consider when taking this route. The first is that there is a hot wall limit determined either by the sample (especially critical with biological samples) or by the solvent boiling point at the channel pressure. The second point is that the cold wall temperature also increases because of the system design. This temperature is reflected in predicting physiochemical properties. An alternative approach is to redesign the system to ensure the largest part of the temperature drop is across the channel and not one of the channel components.

Separation of Multicomponent Mixtures

A mixture of two sizes of PS beads, 394 nm and 597 nm, were separated in the μ-ThFFF system. The results of this separation are found in Figure 70. The temperature difference recorded was 45.2 ˚C with T_c = 15.8 ˚C. However, the actual temperature drop across the channel was calculated to be 4.7˚C with the cold wall at 56.3 ˚C as calculated according to Appendix C. The power consumption for this separation was

approximately 10 watts. This power is compared to a typical macroscale ThFFF system with two 1.5 kilowatt, rod heaters which means a reduction in power consumption of around 300 times.

Four distinct peaks are shown in the results from this separation in Figure 70. The first peak to be detected is the void peak. The elution time of this peak is about 29 seconds. The next two peaks to be eluted are the samples to be separated, the 394 nm and the 597 nm peaks. One other peak representing the 2×394 nm doublet is eluted next. The peaks of doublets formed by 394+597 nm and 2×597 nm are probably hidden in the baseline. In Table 6 are listed the elution time, retention ratio and Soret coefficient for each of the peaks in Figure 70.

From the Soret coefficients and the diffusivities the thermal diffusivities can be calculated. This value is independent of molecular weight for dissolved polymers but for the diameter of rigid particles. Giddings shows a trend of increasing thermal diffusion coefficient, D_T, with size and is reflected in the maximum diameter based selectivity of the system. This value should be unity if D_T is independent of size, but was calculated by Giddings to be around 1.50. The calculated thermal diffusion coefficient for these PS samples is about 2×10^{-8} $cm^2/sec \cdot K$. This value is compared with that determined by Giddings for PS spheres (~100-300 nm) in DI water, $1\text{-}3 \times 10^{-8}$ $cm^2/sec \cdot K$. The maximum selectivity for the μ-ThFFF system was calculated to be 0.99. This value is approximately unity, but is different from the macroscale system results. The reason for this discrepancy is not clear.

As in the single component retention experiment, the small temperature drop across the channel is the reason for the poor resolution. The sample layer thicknesses are

Table 6. Summary of physical and calculated parameters of peaks in the separation of 394 nm and 597 nm polystyrene particles.

Peak number	1	2	3	4
Diameter, d (nm)	Void	394	597	2×394
Elution time, t (sec)	29	40	61	76
Retention ratio, R	1.000	0.71	0.47	0.38
Soret coefficient (K^{-1})	-	1.79	2.73	3.40
Diffusivity, D (cm^2/sec)	-	1×10^{-8}	8×10^{-9}	6×10^{-9}

large enough to allow an increase in the thermal gradient before reaching the steric transition point. This increase will theoretically improve the retention and the resolution in the system. An increase in the temperature gradient will also make possible the resolution of smaller diameter materials. Giddings showed that the macro scale system could resolve a 30 nm PS particle from the void peak.

Other Results

Other sample sizes besides the 394 nm and 597 nm PS particles were attempted to be retained in the system. However, not all the results from the separation and retention experiments were successful. These results are presented in this section. No other sample materials have been attempted to be retained or separated in the μ-ThFFF system. In addition, no dissolved samples were experimented with in this system.

Single component retentions presented in this section include PS particles in DI water with diameters of 165 nm, 204 nm, 597 nm, and 944 nm. Although the 597 nm diameter particles were presented earlier, this graph shows a very poor resolution separation even though the operating conditions were similar. The reason for this difference for various experiments is not clear. The results from this retention are given

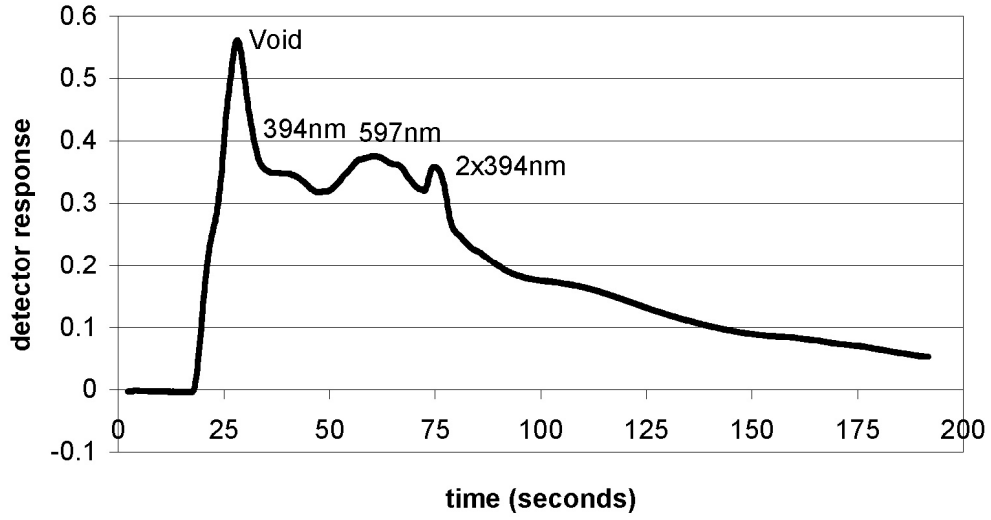

Figure 70. Separation of a binary component PS mixture. The operating parameters are: $\Delta T = 4.7$ ˚C, $T_c = 15.8$ ˚C, V = 1.25 mL/hr.

in Figure 71. One peak is visible in this figure. This peak is determined to be the 597 nm because the calculated D_T is about 1×10^{-8} $cm^2/sec \cdot K$, which falls within the values determined by the macro scale experiment mentioned earlier.

Results from the 165 nm, 204 nm and 944 nm PS particles are shown in Figure 72, Figure 73, and Figure 74. The process conditions for the 165 nm particles is $\Delta T = 3.0$ ˚C, $T_c = 41.5$ ˚C, V = 1.25 mL/hr. The peak is only slightly resolved from the void peak.

For the 204 nm particles the process conditions are $\Delta T = 5.3$ ˚C, $T_c = 69.7$ ˚C, V = 1.25 mL/hr. Three peaks are distinct in this graph. The two peaks following the void peak represent the single 204 nm and the doublet, 2×204 nm. The peaks are excellently resolved because the peaks are narrow. The reason for the variability in the plate height of the peaks between runs is not understood at this point, but is probably due to variances in the time and technique of injecting the samples into the stream.

To solve the problems due to variability in sample injection times and techniques, which are present between users as well as between samples from the same user, two methods can be incorporated. The first method is to use a constant rate syringe. Syringes such as these can deliver an accurate and precise volume of sample at a constant rate each time. However, variability may still exist in the time the syringe is removed from the injection port. The second method is to incorporate a sample injection loop with the system, either externally or integrated with the fluidic channel. This method ensures a constant volume and constant rate of sample introduction with only a minimal disturbance of the carrier flow. This method is probably more difficult to implement.

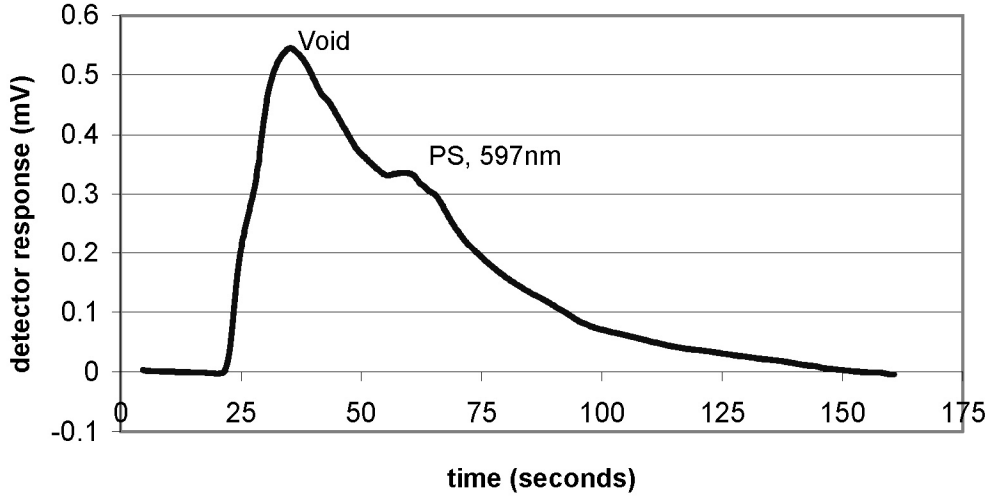

Figure 71. Single component retention of 597 nm PS in DI water. Although the process conditions were similar to Figure 69 the retention is much worse for unknown reasons.

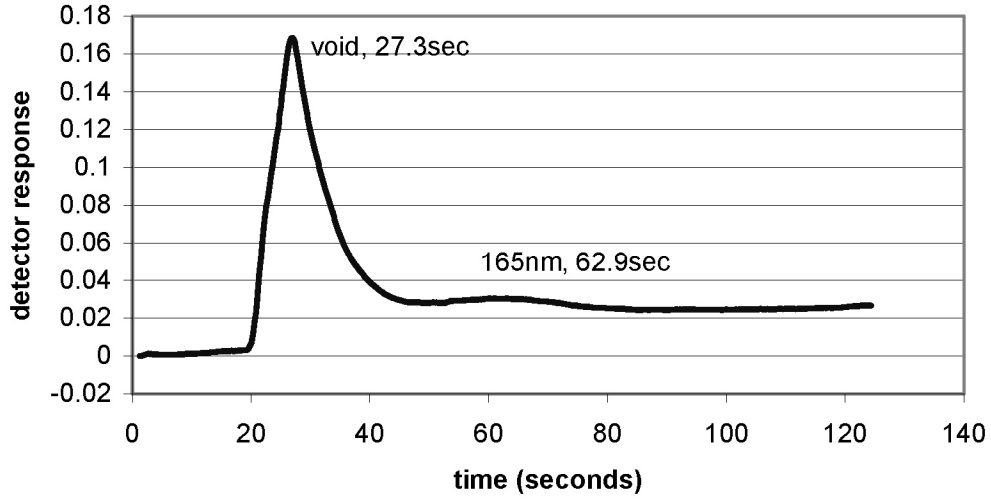

Figure 72. Single component retention of 165 nm PS in DI water, where $\Delta T = 3.0$ ˚C, $T_c = 41.5$ ˚C, V = 1.25 mL/hr.

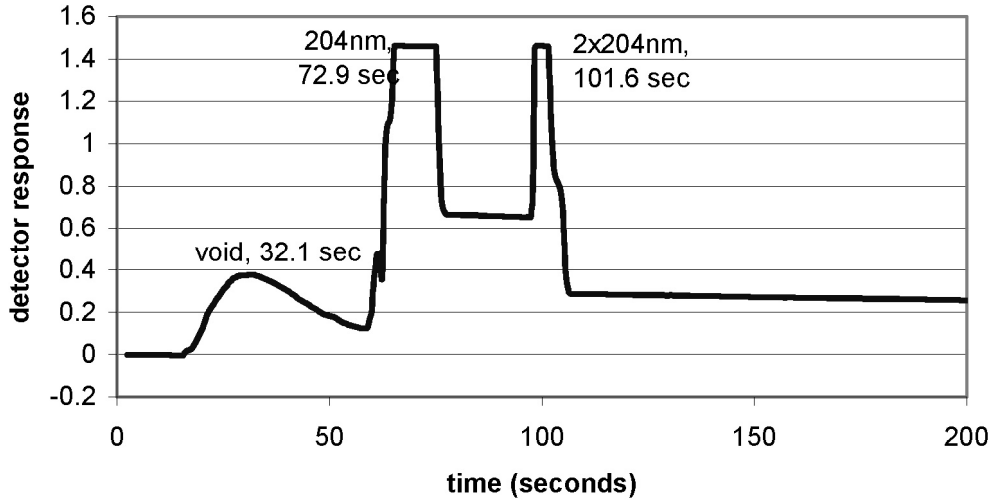

Figure 73. Single component retention of 204 nm PS in DI water, where $\Delta T = 5.3$ ˚C, $T_c = 69.7$ ˚C, V = 1.25 mL/hr. The peaks are clipped at 1.5 volts because of the limitation of the detector.

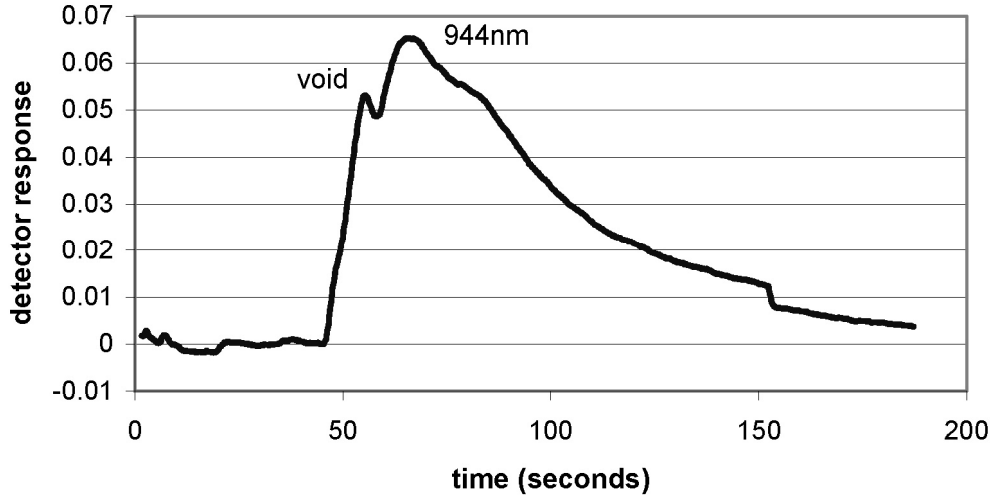

Figure 74. Single component retention of 944 nm PS in DI water, where $\Delta T = 1.25$ ˚C, $T_c = 21.3$ ˚C, and V = 1.5 mL/hr.

A single component retention of 977 nm PS in 0.1 μL of DI water is shown in Figure 74. The process conditions for this sample are $\Delta T = 1.25$ ˚C, $T_c = 21.3$ ˚C, and V = 1.5 mL/hr. The peak associated with the 977 nm particles is only slightly resolved from the void peak because of the small temperature difference applied.

In each of the separations a significant improvement in the retention of the sample would be accomplished with an increase in the temperature difference as noted earlier. A decrease in the channel width would also result in better retention of the sample peaks.

Comparison with Scaling Parameters

In Table 2.1, the scaling effects in general FFF channels and thermal FFF channels are compared. The potential advantage or disadvantage of scaling the channel is also discussed. In this section the experimental results obtained are compared with the theory predicted in Chapter 2 and summarized in Table 2.1. However, not all of the system parameters explored in theory were investigated experimentally. Only those parameters tried with experiment will be discussed.

One difficulty in comparing the predicted results with actual results is the lack of data from a macroscale ThFFF system in which the exact same experiments were conducted as were conducted in this thesis. Although the experiments conducted in this work were comparable to the previous work of Giddings, some significant differences may cause discrepancies when comparing data. One, plate height is dependent on the system user and the injection technique. Two, a duplication of the fractionation operating parameters were attempted, but were not consistent. For example, the temperature difference on the μ-ThFFF system was assumed to be from the points of measurement, but was later discovered to be very inaccurate. Three, the samples used in this study were

not exactly the same size or polydispersity as that used in Giddings experiments. This effect is seen in differences in plate height and required interpolation of Giddings results for comparison. Fourth, the carrier solution was not exactly the same. Giddings used doubly distilled water with a surfactant. This work used DI water available in the laboratory. These effects make the analysis of scaling effects difficult and limited.

A summary of the analysis of some of the scaling parameters from Table 2.1 is shown in Table 7. The retention ratio was predicted not to scale with the channel width. The value predicted by Giddings was approximated from the fractionation graph to be 0.05 for a 394 nm PS particle. The temperature drop was 65 K with T_c = 292 K. The conditions for the μ-ThFFF channel retention were ΔT = 4.7 K and T_c = 329 K. Since the retention is directly proportional to the cold wall temperature and inversely proportional to the temperature difference, the retention ratios cannot be compared directly. However,

Table 7. Analysis of scaling factors in the macro to micro ThFFF systems.

System Parameter	Predicted Scale Factor	Measured Scale Factor	Consistent?
Retention Ratio (R)	1	~1	Yes
Drift Velocity (U)	$\frac{1}{s}$	$\frac{1}{s}$	Yes
Required Sample Size	s^3	$> s^3$	Greater
Carrier Fluid Consumption	s^3	$> s^3$	Greater
Instrument Size	s^3	s^3	Yes

the ratio of the two retention values should be equal to the ratio of $(T_c/\Delta T)_{macro}$: $(T_c/\Delta T)_{micro}$, from equations 74 and 44 in Chapter 2. The results are in Table 8. Because of the approximations in determining the retention ratio for the macroscale system, these two ratios may reasonably be equal to each other. Thus, the retention ratio does not scale with channel height.

The drift velocity, U, of the particles under an applied thermal field is a function of the thermal diffusion coefficient, temperature difference, and channel width. Because the temperature difference and channel width are set by experimental conditions, the drift velocity is then a measure of the thermal diffusion coefficient. A plot of $U/\Delta T$ versus $1/w$ should reveal a straight line with the intercept equal to zero and the slope equal to the thermal diffusion coefficient. Including the point (0,0) in the linear regression of these data points gives a slope (D_T) = 2.16×10^{-8} $cm^2/sec\cdot K$ and an intercept of -5.55×10^{-8} cm/sec with $R^2 = 0.996$. This value for D_T is approximately the same as presented for both the macro and micro scale systems in the previous section. Thus, drift velocity, U, does scale inversely with channel width, w.

The sample size was significantly reduced. For the macroscale system, the sample was injected via a 28 μL injection loop. For the microscale system, the sample

Table 8. Comparison of corrected retention ratios from macro to micro scale.

Scale	R	$T_c/\Delta T$
Macro	0.054	4.49
Micro	0.714	70.0
Ratio	**0.075**	**0.064**

volume required was typically less than 0.2 μL. This volume reduction is actually greater than the predicted scaling with the three dimensions of the channel. This volume may vary according to the concentration of the PS in the sample.

The carrier fluid consumption was scaled higher than predicted. If the carrier velocity is kept constant the flow rate must be reduced in proportion to the cross-sectional area. The amount of fluid in the channel is also scaled with the three dimensions of the channel. The flow rate used by Giddings was 18 mL/hr with the void peak being eluted at approximately 3 minutes. The flow rate for the μ-ThFFF channel was 1.25 mL/hr with the void time at 28.5 seconds. This time is actually over six times faster than that of the macroscale system but uses more than 14 times less carrier. The size of the channel and heater are scaled approximately by the three dimensions of the instrument according to prediction.

Summary

The μ-ThFFF system was tested and compared with macroscale systems. Several single component PS spheres were retain the channel and the thermal diffusion coefficient of polystyrene spheres in DI water was determined. This coefficient was approximately 1-3 $\times 10^{-8}$ $cm^2/sec \cdot K$ and is consistent with that measured in a macroscale system. Some of the scaling factors such as the retention ratio, drift velocity, and volumetric parameters presented theoretically in Chapter 2 were found consistent with theory through experiments and comparisons of the macro and micro scale systems.

CHAPTER 6

CONCLUSION

Summary

FFF was introduced as a chromatographic-type separation system. The separations are chromatographic in nature because the samples migrate differentially along the separation pathway. The samples are then eluted at separate times. Several types of FFF techniques were described. Common subtechniques include electrical, flow, sedimentation, and thermal and less common may include dielectric, magnetic and acoustic. Thermal FFF has some unique advantages over other subtypes of FFF. These advantages are due to retention being a function of not only size or molecular weight, but also the physiochemical properties of the sample. Acoustic, the other type investigated, was not well research previously but also had certain attributes that made examination into this technique desirable.

The theory for generalized field-flow fractionation was expounded in detail. This theory was then extended to the acoustic field-flow fractionation subtechnique and also to thermal field-flow fractionation. Acoustic theory was also elucidated which included acoustic force on a compressible sphere, sound propagation in isotropic and anisotropic media, piezoelectric effect, equivalent transmission line model and the KLM transducer

model. This theory aided in the design of the various layers of the acoustic system to achieve the appropriate standing wave.

The system was then designed using standard microfabrication techniques and also utilized new methods such as laser ablation of PDMS to form the microchannels. The system was tested and characterized based on plate height, electrical input impedance, channel pressure drop, single component sample retention, and multiple component sample separation. The results correlated well with theory in nearly all aspects. The resonant frequency of the system was measured at 6.16 MHz and 50 Ω while the model predicted 6.18 MHz and 200 Ω. The pressure difference measured correlated well with Bernoulli's equation. Although the retention times of the single component samples did not follow in order, the theory explained the location of the apparent steric inversion point as the reason. The reasoning also explained the inability of the system to resolve PS 110, PS 210, and PS 300.

Important parameters such as void volume and time, retention, plate height, resolution, analysis time, and physical sizes associated with the channel were evaluated in terms of scaling effects for both the general form of FFF and specifically for ThFFF. Scaling channel geometry for general FFF was shown by Giddings not to be advantageous in many aspects. However, benefits for scaling ThFFF channel geometry have been shown to exist for nearly all system parameters.

The fabrication of microscale thermal field-flow fractionation channels and integrated heater was demonstrated in this work. In addition to the channel and heater, the interconnects to other components of the system were applied from the micro

electrical field-flow fractionation system and adapted to meet the specific needs of the thermal system. The entire μ-ThFFF system was assembled together and tested.

Testing of the μ-ThFFF system included determination of plate height as a function of carrier fluid velocity for unretained acetone samples, 0.2 μL. These plate height measurements are a high limit approximation because of the unretained sample and that the diffusion coefficient is much larger in small molecular weight samples. The minimum plate height measured was approximately 0.15 cm. The velocity that corresponded to a minimum plate height was approximately 1.25-1.30 mL/hr and was used as a starting point for retention experiments.

A single sample of polystyrene particles, 597 nm, suspending in DI water was then shown to be retained in the system when a thermal gradient was applied of about 0.1 ºC/μm. Peaks for the 597 nm sample and the 2×597 nm dimer were detected. From these experiments the thermal diffusion coefficient of the sample/solvent system was shown to be 1.7×10^{-8} cm/sec·K^{-1}, approximately equal to that determined from similar experiments with a macroscale ThFFF system.

A multicomponent mixture of polystyrene particles, 394 nm and 597 nm, were then separated from each other. The process conditions were similar to the single component retention experiment. The 394 nm, 597 nm and 2×394 nm peaks were resolved from each other. Peaks associated with other dimers were lost in the baseline. The thermal diffusion coefficient was calculated to be 2.18×10^{-8} cm/sec·K^{-1}, also within the range determined by similar macroscale ThFFF experiments. One discrepancy arose between the two systems in the maximum diameter based selectivity. The value

determined in the macroscale system was 1.5 whereas in the microscale system was around 1.0. The reason for this discrepancy is not clear.

This experiment was compared with the macroscale system as well. Some of the system parameters explored in the theory section were evaluated for accuracy with these experiments. Scaling effects in channel geometry in the experimental results agreed well with theory and in some instances, showed a greater improvement over theory.

Future Work

This work is merely a starting point for future work on the microscale acoustic and thermal FFF systems. In addition, the fabrication process used in this work may be one of many successful fabrication processes used for microscale separation systems. Because this work was based in part off the μ-ElFFF system, it is also an extension of the work to miniaturize FFF systems. Much research can be done in both of these areas.

The most important work at present for the thermal system is to further characterize the system using a larger temperature difference. If possible, a temperature gradient equivalent to the gradient used for the macroscale system experiments is desirable. This work may include a change in channel design to accomplish the majority of the temperature drop across the channel and not the components that comprise the walls of the channel. As for the acoustic system, the work should be focused in the area of characterizing other sample size and other sample types.

The success of miniaturizing the FFF system requires that all or nearly all of the system components be integrated with the system. This work included the the integration of the detector. However, other components such as the injection port, fluid pump, and analysis system can and should also be integrated with the channel.

Much work can still be done in the areas of microscale separation system and total analysis systems. In addition, there is still a lot of work left to do in the area of field-flow fractionation and chromatographic separation systems. Integration of these two technologies may help to solve many questions facing researchers today.

APPENDIX A

LABVIEW PROGRAM

AcFFF.vi

This VI opens and initializes a GPIB session, reads a number of measurements and returns all the data taken from the instrument's output buffer before checking for error(s) and closing the session. The order of returned data can be either in FIFO (first-in-first-out) or LIFO (last-in-first-out). The VI loops through this sequence over the time of the experiment and acquires a data point from the HP 3458A DMM. This datum is plotted versus time on a graph. The data is also stored to file if requested to do so by the user. Each LabView VI is organized through a front panel (interactive) and a block diagram (back panel or behind-the-scene). These sections are described in the next sections.

Notes: When controller requests data from the multimeter and its output buffer is empty in the FIFO or LIFO mode, a reading is removed from the memory and sent to the controller. This is the "implied read" method of recalling reading. The reading storage mode (LIFO or FIFO) is important only when you are using the "implied read" method of recalling readings. The mode has no affect on readings if the data is recalled from the memory without being removed.

Connector Pane

If the program is used in conjunction with another program this program is described by the following icon with the appropriate connectors. All other interfaces are internal to the program.

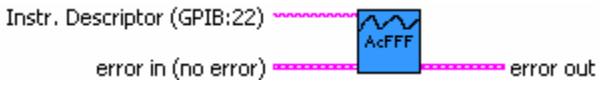

Front Panel

The program also allows for input of various experimental conditions including: file information, sample information, transducer operating conditions, detector operating conditions and physical attributes, multimeter settings, channel physical attributes, and automatic injector controls if used. These inputs and indicators are available for interaction with the user on the front panel, Figure 75.

Controls and Indicators

The details of each of the controls and indicators in the front panel are described in this section. Each item is indicated by an icon representative of the data type (e.g. text, Boolean, etc.) with the appropriate name and an optional description of the item.

abc Detector Electrode Materials

abc Instr. Descriptor (GPIB:22) A string that uniquely identifies the instrument to open or initialize. The grammar for the instrument descriptor is shown below. Parameters are shown in lower-case and optional parameters are shown in square brackets ([ ]).

Default Value: GPIB::22::INSTR

GPIB - GPIB[bd]::prim addr[::sec addr]

VXI - VXI[bd]::logical addr

GPIB-VXI - GPIB-VXI[bd][::prim addr]::logical addr

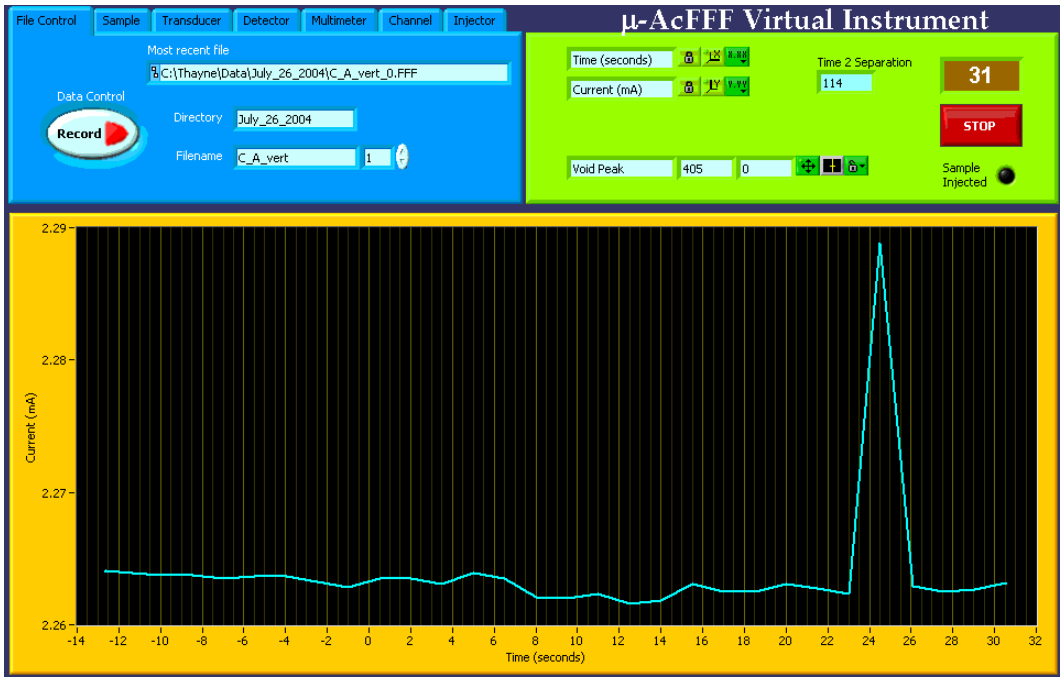

Figure 75. Front panel of the AcFFF virtual instrument.

Parameters (default value):

bd - GPIB board (0)

prim addr - GPIB primary address (1)

sec addr - GPIB secondary address (none)

logical addr - VXI logical address

EXAMPLE: A GPIB instrument on GPIB board 0, at primary address 5, and no secondary addressing.

GPIB::5

error in (no error) error in is a cluster that describes the error status before this VI executes. If error in indicates that an error occurred before this VI was called, this VI may choose not to execute its function, but just pass the error through to its error out cluster. If no error has occurred, then this VI executes normally and sets its own error status in error out. Use the error handler VIs to look up the error code and to display the corresponding error message. Using error in and error out clusters is a convenient way to check errors and to specify execution order by wiring the error output from one subVI to the error input of the next.

Valid Range:

Not Applicable

Default:

status= False (no error)

code = 0

source = empty string

status status is TRUE if an error occurred before this VI was called, or FALSE if not. If status is TRUE, code is a non-zero error code. If status is FALSE, code can be zero or a warning code.

Valid Range:

T: Error

F: No Error (default)

code code is the number identifying an error or warning. If status is TRUE, code is a non-zero error code. If status is FALSE, code can be zero or a warning code. Use the error handler VIs to look up the meaning of this code and to display the corresponding error message.

Valid Range:

Not Applicable

Default:0

source source is a string that indicates the origin of the error, if any. Usually source is the name of the VI in which the error occurred.

Default:

Empty String

Transducer Voltage (p-p)

Transducer Operating Frequency

Flow Rate

Carrier Fluid

Filename

Filenumber

DMM Measurement Function Pass the measurement function you want the DMM to perform. The driver sets the hp3458a>>Basic Operation>>Function property to this value.

Valid Values:

HP3458A_VAL_DC_VOLTS - DC Volts

HP3458A_VAL_AC_VOLTS - AC Volts (Analog)

HP3458A_VAL_DC_CURRENT - DC Current

HP3458A_VAL_AC_CURRENT - AC Current

HP3458A_VAL_2_WIRE_RES - 2-Wire Resistance

HP3458A_VAL_4_WIRE_RES - 4-Wire Resistance

HP3458A_VAL_AC_PLUS_DC_VOLTS - AC plus DC Volts (Analog)

HP3458A_VAL_AC_PLUS_DC_CURRENT - AC plus DC Current

HP3458A_VAL_FREQ - Frequency

HP3458A_VAL_PERIOD - Period

HP3458A_VAL_AC_VOLTS_RNDM - AC Volts (Random)

HP3458A_VAL_AC_VOLTS_SYNC - AC Volts (Sync)
HP3458A_VAL_AC_PLUS_DC_VOLTS_RNDM - AC plus DC Volts (Random)

HP3458A_VAL_AC_PLUS_DC_VOLTS_SYNC - AC plus DC Volts (Sync)

HP3458A_VAL_AC_CPL_DIRECT - AC Coupled Direct-Sampling

HP3458A_VAL_DC_CPL_DIRECT - DC Coupled Direct-Sampling

HP3458A_VAL_AC_CPL_SUB - AC Coupled Sub-Sampling

HP3458A_VAL_DC_CPL_SUB - DC Coupled Sub-Sampling

Default Value: HP3458A_VAL_DC_VOLTS

Notes:

(1) The AC Volts and AC plus DC Volts measurement functions have 3 types of RMS conversion technique: analog, random sampling, or synchronous sampling. Analog is the most common used.

(2) For the Frequency and Period measurement functions, use the hp3458a>>Miscellaneous Settings>>Frequency source property to specify the type of signal to be used as the input signal.

(3) The AC Coupled Direct-Sampling and AC Coupled Sub-Sampling measurement functions measure only the AC component of the input waveform.

(4) The DC Coupled Direct-Sampling and DC Coupled Sub-Sampling measurement functions measure the combined AC and DC components of the input waveform.

(5) The AC Coupled Sub-Sampling and DC Coupled Sub-Sampling measurement functions use a completely different trigger model from the other measurement functions. Use the VI hp3458a Configure Sub-Sampling Trigger to configure the trigger when you are in the AC Coupled Sub-Sampling or DC Coupled Sub-Sampling measurement functions.

Directory

Detector Waveform Shape Selects the shape of the selected arbitrary waveform, as follows.

Macro Name	Value	Description
ag33250a_OUTPUT_FUNC_SIN	0	Sinusoid
ag33250a_OUTPUT_FUNC_SQU	1	Square

ag33250a_OUTPUT_FUNC_TRI	2	Triangle
ag33250a_OUTPUT_FUNC_RAMP	3	Ramp
ag33250a_OUTPUT_FUNC_NOIS	4	Noise
ag33250a_OUTPUT_FUNC_DC	5	DC
ag33250a_OUTPUT_FUNC_USER	6	User


Detector Operating Frequency Sets the output frequency.


Detector Voltage (p-p) Sets the output amplitude.


Detector Offset Voltage Sets the dc offset voltage.


Data Control


Ring


Sample


Injection Time Control


width


Area End Region


Area Sep Column


Sample Volume


Transducer Electrode Materials


precolumn length


Detector Electrode Width


DMM Number of Digits


Count


Auto Injection


Infinite?


Repeat?


DMM Range (-1:Auto) Pass the measurement range you want to use. The driver sets the hp3458a>>Basic Operation>>Range property to this value.

Use positive values to represent the absolute value of the maximum expected

measurement. The value must be in units appropriate for the Measurement Function. For example, when you set the Measurement Function to HP3458A_VAL_DC_VOLTS, you must specify the Range in volts. Setting this parameter to 10.0 configures the DMM to measure DC voltages from -10.0 to +10.0 volts.

The driver reserves special negative values for controlling the DMM's auto-ranging capability.

Defined Values:

HP3458A_VAL_AUTO_RANGE_ONCE - Auto-range Once

HP3458A_VAL_AUTO_RANGE_OFF - Auto-range Off

HP3458A_VAL_AUTO_RANGE_ON - Auto-range On

Valid Manual Range: The valid manual range depends on the value you pass for the Measurement Function parameter as shown below

DC Volts - 0.1 to 1000.0 volts

AC Volts - 0.01 to 1000.0 volts

DC Current - 0.0000001 to 1.0 amperes

AC Current - 0.0001 to 1.0 amperes

2-Wire Resistance - 10.0 to 1.0E9 ohms

4-Wire Resistance - 10.0 to 1.0E9 ohms

AC plus DC Volts - 0.01 to 1000.0 volts

AC plus DC Current - 0.0001 to 1.0 amperes

Frequency - ** See Notes (1) below

Period - ** See Notes (1) below

AC Volts (Random) - 0.01 to 1000.0 volts

AC Volts (Sync) - 0.01 to 1000.0 volts

AC plus DC Volts (Random) - 0.01 to 1000.0 volts

AC plus DC Volts (Sync) - 0.01 to 1000.0 volts

AC Coupled Direct-Sampling - 0.01 to 1000.0 volts

DC Coupled Direct-Sampling - 0.01 to 1000.0 volts

AC Coupled Sub-Sampling - 0.01 to 1000.0 volts

DC Coupled Sub-Sampling - 0.01 to 1000.0 volts

Default Value: HP3458A_VAL_AUTO_RANGE_ON

Notes:

(1) The value you pass in is coerced to the lowest multiple of 10 value that can handle the specified value. For example if you pass in the value 15.0, it is coerced to 100.0.

(2) For the Frequency and Period measurement functions, this property determines the voltage or current threshold. The valid manual range depends on the frequency source you are set to. The frequency source is specified by the hp3458a>>Miscellaneous Settings>>Frequency source property. For example, if the frequency source is set to AC Volts, the valid manual range is the same as the AC Volts measurement function's.

(3) The AC Coupled Direct-Sampling, DC Coupled Direct-Sampling, AC Coupled Sub-Sampling, and DC Coupled Sub-Sampling measurement functions do not support HP3458A_VAL_AUTO_RANGE_ONCE, HP3458A_VAL_AUTO_RANGE_OFF, or HP3458A_VAL_AUTO_RANGE_ON.

(4) Setting this parameter to HP3458A_VAL_AUTO_RANGE_ONCE configures the DMM to auto-range once, turn auto-range off, and then remain at the current maximum range.

(5) Setting this parameter to HP3458A_VAL_AUTO_RANGE_OFF configures the DMM to stop auto-ranging and keep the range fixed at the current maximum range.

postcolumn length

Time Display Limit


Tab Control

stop

DMM Integration Time

pre column diameter

Channel

Stop Flow

Start Flow


error out error out is a cluster that describes the error status after this VI executes. If an error occurred before this VI was called, error out is the same as error in. Otherwise, error out shows the error, if any, that occurred in this VI. Use the error handler VIs to look up the error code and to display the corresponding error message. Using error in and error out clusters is a convenient way to check errors and to specify execution order by wiring

the error output from one subVI to the error input of the next.

Valid Range:

Not Applicable

Default:

status= False (no error)

code = 0

source = empty string

status status is TRUE if an error occurred, or FALSE if not. If status is TRUE, code is a non-zero error code. If status is FALSE, code can be zero or a warning code.

Valid Range:

T: Error

F: No Error (default)

code code is the number identifying an error or warning. If status is TRUE, code is a non-zero error code. If status is FALSE, code can be zero or a warning code. Use the error handler VIs to look up the meaning of this code and to display the corresponding error message.

Valid Range:

Not ApplicableDefault:0

source source is a string that indicates the origin of the error, if any. Usually source is the name of the VI in which the error occurred.

Default:

Empty String

Most recent file new file path is the path of the file to which the VI wrote data. You can use this output to determine the path of a file that you open using dialog. new file path returns Not A Path if the user selects Cancel from the dialog box.

Injection Light

expected void peak time

Finish Time

Loop Number

 XY Graph

 x-y

 Inject

 Time 2 Separation

Block Diagram

The “wiring” or flow of the graphical program is shown in the block diagram. The block diagram includes all of the front panel items listed in the previous section as well as some other items including: arithmetic operators, subroutines, file operation routines, system and device communication protocol and routines, and graphing routines. These behind-the-scene components are described in this section in the same way they were described in the previous section.

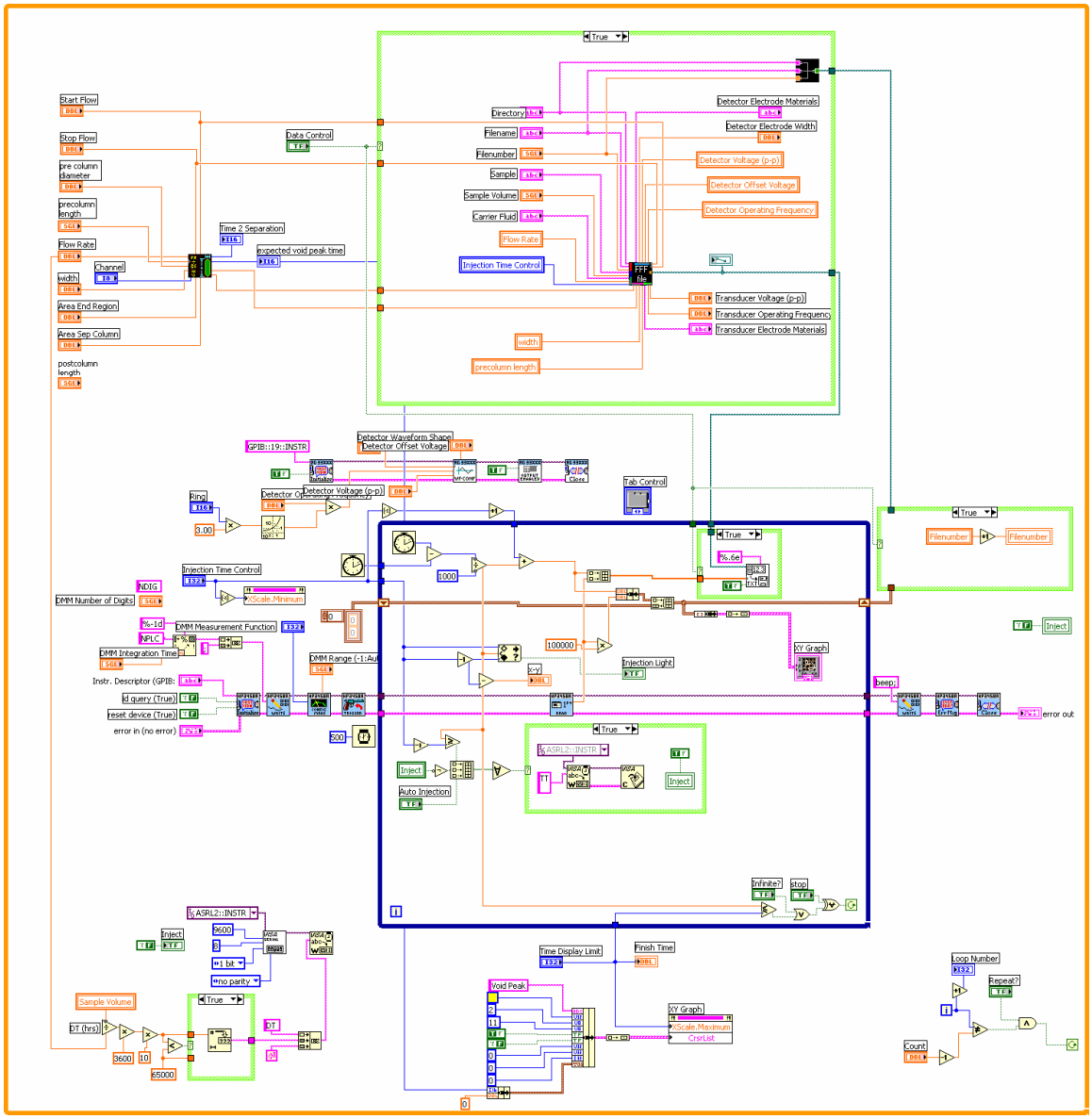

Figure 76. Block diagram showing the flow control of the g-program.

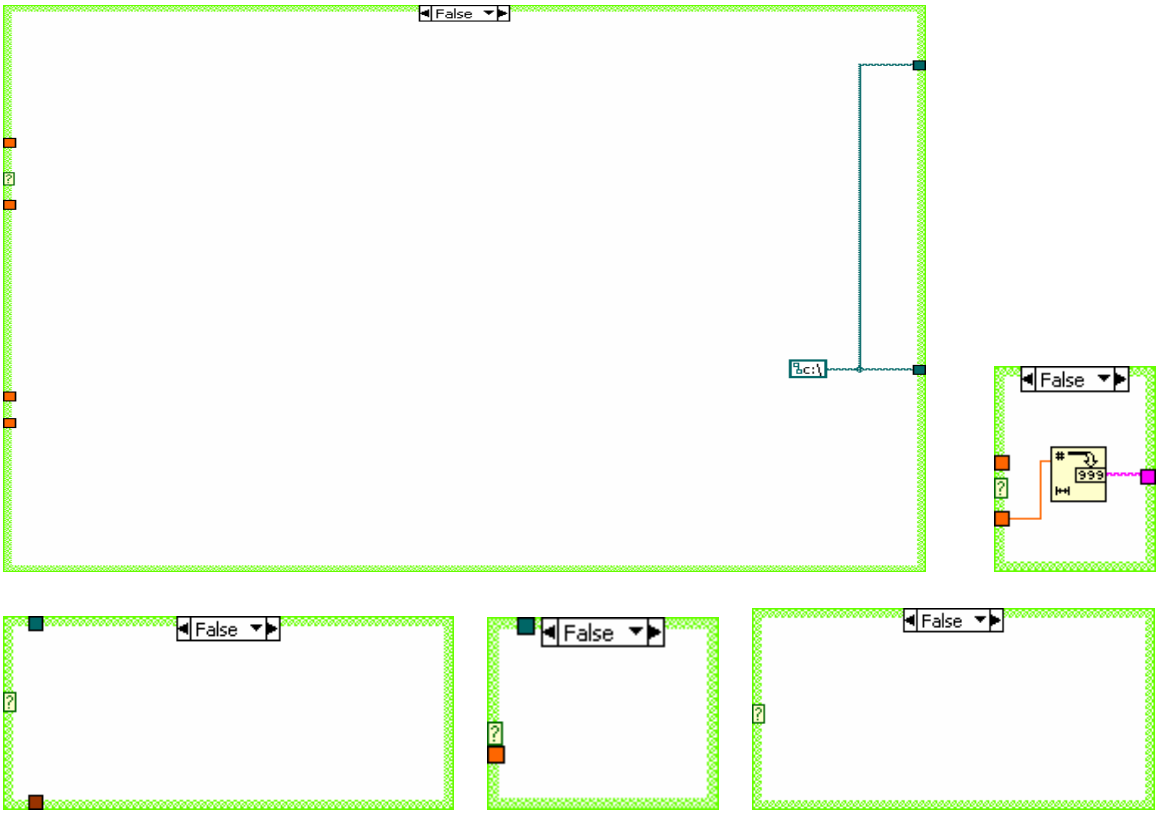

Figure 77. Alternative conditions for the Boolean expressions in the block diagram. True conditions were shown in Figure 76.

List of SubVIs and Express VIs with Configuration Information

Write To Spreadsheet File.vi

C:\Program Files\National Instruments\LabVIEW 7.0\vi.lib\Utility\file.llb\Write To Spreadsheet File.vi

hp3458a Initialize.vi

C:\Program Files\National Instruments\LabVIEW 7.0\instr.lib\hp3458a\hp3458a.LLB\hp3458a Initialize.vi

hp3458a Error Message.vi

C:\Program Files\National Instruments\LabVIEW 7.0\instr.lib\hp3458a\hp3458a.LLB\hp3458a Error Message.vi

hp3458a Close.vi

C:\Program Files\National Instruments\LabVIEW 7.0\instr.lib\hp3458a\hp3458a.LLB\hp3458a Close.vi

hp3458a Write Instrument Data.vi

C:\Program Files\National Instruments\LabVIEW 7.0\instr.lib\hp3458a\hp3458a.LLB\hp3458a Write Instrument Data.vi

FFF Data File Header Thayne.vi

F:\My Documents\Thayne\FFF.llb\FFF Data File Header Thayne.vi

hp3458a Configure Measurement.vi

C:\Program Files\National Instruments\LabVIEW 7.0\instr.lib\hp3458a\hp3458a.LLB\hp3458a Configure Measurement.vi

hp3458a Configure Trigger.vi

C:\Program Files\National Instruments\LabVIEW 7.0\instr.lib\hp3458a\hp3458a.LLB\hp3458a Configure Trigger.vi

hp3458a Read.vi

C:\Program Files\National Instruments\LabVIEW 7.0\instr.lib\hp3458a\hp3458a.LLB\hp3458a Read.vi

ag33xxx - Initialize.vi

C:\Program Files\National Instruments\LabVIEW 7.0\instr.lib\ag33xxx\ag33xxx.llb\ag33xxx - Initialize.vi

ag33xxx - Config Waveform.vi

C:\Program Files\National Instruments\LabVIEW 7.0\instr.lib\ag33xxx\ag33xxx.llb\ag33xxx - Config Waveform.vi

ag33xxx - Output Enabled.vi

C:\Program Files\National Instruments\LabVIEW 7.0\instr.lib\ag33xxx\ag33xxx.llb\ag33xxx - Output Enabled.vi

ag33xxx - Close.vi

C:\Program Files\National Instruments\LabVIEW 7.0\instr.lib\ag33xxx\ag33xxx.llb\ag33xxx - Close.vi

FFF_subVI_1.vi

F:\My Documents\Thayne\FFF.llb\FFF_subVI_1.vi

VISA Configure Serial Port

C:\Program Files\National Instruments\LabVIEW 7.0\vi.lib\Instr_visa.llb\VISA Configure Serial Port

VISA Configure Serial Port (Instr).vi

C:\Program Files\National Instruments\LabVIEW 7.0\vi.lib\Instr_visa.llb\VISA Configure Serial Port (Instr).vi

Channel Dimensions.vi

F:\My Documents\Thayne\FFF.llb\Channel Dimensions.vi

Position in Hierarchy

The program flow and dependence hierarchy of sub VIs is shown in Figure 78.

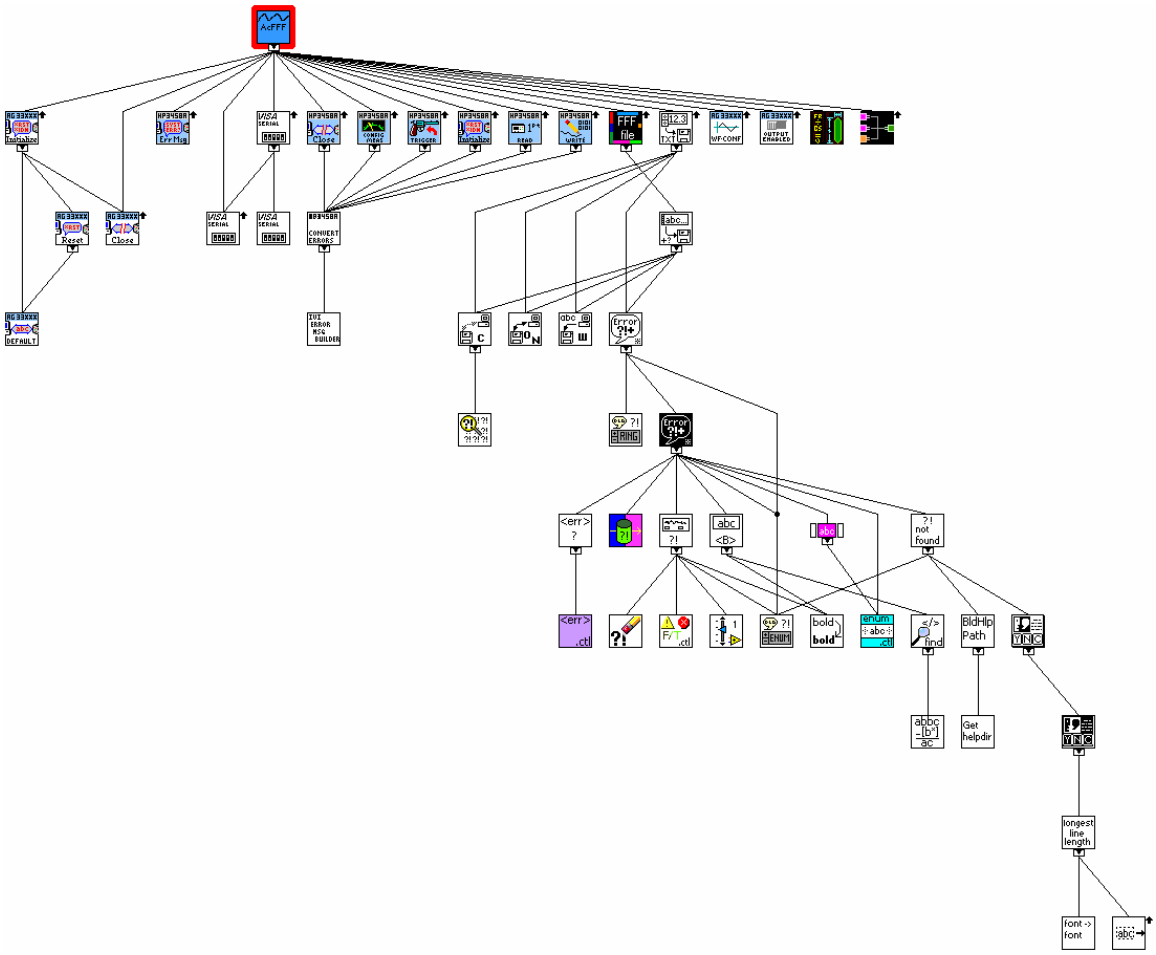

Figure 78. Dependence hierarchy of sub VIs in the AcFFF.vi LabView program.

APPENDIX B

SAMPLE DATA FILE

Data file as acquired by the LabView program in Appendix A. This data file is tab delimeted (two columns) ASCII encoded. There is a header that includes information of experimental conditions as input by the user and recorded by the computer.

Filename	A_PH_8.FFF
Date/Time	10/20/2004 9:07:00 AM
Sample Description	0.17 N NaCl
Sample Volume	0.500000
Sample Injection Time	15
Carrier Description	DI Water
Carrier Flow Rate (mL/hr)	30.000000
Channel Width (um)	62
Volume 2 Detector (uL)	11.246651
Total Channel Volume (uL)	11.720330
Precolumn Length (cm)	6.000000
Detector/Electrode Materials	Cr/Au
Detector Width (um)	75.000000
Detector Frequency (kHz)	2.000000
Detector Voltage (Vpp)	5.000000
Detector DC Voltage (V)	0.000000
Main Electrode Materials	Cr/Au
Main Electrode Frequency, MHz	6.080000
Main Electrode Voltage (V)	0.000000
Stop Flow Time (sec)	0.000000
Start Flow Time (sec)	0.000000
Time:	Detector:
-1.348400E+1	1.724741E-4
-1.228300E+1	1.725062E-4
-1.215800E+1	1.724947E-4
-1.203400E+1	1.725076E-4
-1.190800E+1	1.725179E-4

-1.178400E+1	1.725185E-4
-1.165800E+1	1.725277E-4
-1.153300E+1	1.725207E-4
-1.140700E+1	1.725162E-4
-1.128100E+1	1.725141E-4
-1.115600E+1	1.725153E-4
-1.103000E+1	1.725139E-4
-1.090500E+1	1.725075E-4
-1.078000E+1	1.725100E-4
-1.065200E+1	1.725047E-4
-1.052600E+1	1.725223E-4
-1.039900E+1	1.724853E-4
-1.027300E+1	1.724235E-4
-1.014700E+1	1.724038E-4
-1.002000E+1	1.723892E-4
-9.894000E+0	1.723847E-4
-9.766000E+0	1.723782E-4
-9.640000E+0	1.723895E-4
-9.513000E+0	1.723961E-4
-9.386000E+0	1.723905E-4
-9.260000E+0	1.723949E-4
-9.132000E+0	1.723986E-4
-9.005000E+0	1.723933E-4
-8.877000E+0	1.723921E-4
-8.750000E+0	1.723954E-4
-8.623000E+0	1.723877E-4
-8.495000E+0	1.723841E-4
-8.368000E+0	1.723882E-4
-8.240000E+0	1.723832E-4
-8.113000E+0	1.724087E-4
-7.985000E+0	1.723377E-4
-7.856000E+0	1.722905E-4
-7.727000E+0	1.722756E-4
-7.598000E+0	1.722676E-4
-7.470000E+0	1.722661E-4
-7.342000E+0	1.722665E-4
-7.213000E+0	1.722754E-4
-7.085000E+0	1.722789E-4
-6.956000E+0	1.722737E-4
-6.828000E+0	1.722650E-4
-6.700000E+0	1.722711E-4
-6.571000E+0	1.722714E-4
-6.443000E+0	1.722716E-4
-6.314000E+0	1.722694E-4
-6.186000E+0	1.722622E-4
-6.057000E+0	1.722599E-4
-5.929000E+0	1.722540E-4
-5.801000E+0	1.722513E-4
-5.672000E+0	1.722774E-4
-5.543000E+0	1.722281E-4
-5.414000E+0	1.721786E-4
-5.286000E+0	1.721623E-4
-5.157000E+0	1.721489E-4
-5.028000E+0	1.721480E-4
-4.900000E+0	1.721483E-4
-4.770000E+0	1.721498E-4
-4.641000E+0	1.721531E-4

-4.512000E+0	1.721529E-4
-4.382000E+0	1.721470E-4
-4.253000E+0	1.721513E-4
-4.123000E+0	1.721535E-4
-3.994000E+0	1.721501E-4
-3.865000E+0	1.721513E-4
-3.735000E+0	1.721534E-4
-3.606000E+0	1.721414E-4
-3.476000E+0	1.721416E-4
-3.347000E+0	1.721745E-4
-3.217000E+0	1.721241E-4
-3.088000E+0	1.720609E-4
-2.959000E+0	1.720453E-4
-2.829000E+0	1.720327E-4
-2.700000E+0	1.720238E-4
-2.570000E+0	1.720303E-4
-2.441000E+0	1.720408E-4
-2.312000E+0	1.720493E-4
-2.182000E+0	1.720554E-4
-2.053000E+0	1.720611E-4
-1.922000E+0	1.720575E-4
-1.794000E+0	1.720499E-4
-1.663000E+0	1.720486E-4
-1.534000E+0	1.720406E-4
-1.405000E+0	1.720278E-4
-1.275000E+0	1.720249E-4
-1.146000E+0	1.720171E-4
-1.015000E+0	1.720472E-4
-8.850000E-1	1.719698E-4
-7.540000E-1	1.719349E-4
-6.240000E-1	1.719184E-4
-4.940000E-1	1.719073E-4
-3.630000E-1	1.719045E-4
-2.330000E-1	1.719137E-4
-1.030000E-1	1.719255E-4
2.800000E-2	1.719304E-4
1.580000E-1	1.719317E-4
2.890000E-1	1.719196E-4
4.200000E-1	1.719358E-4
5.510000E-1	1.720163E-4
6.810000E-1	1.723403E-4
8.110000E-1	1.724248E-4
9.430000E-1	1.723103E-4
1.073000E+0	1.722122E-4
1.204000E+0	1.722187E-4
1.334000E+0	1.723039E-4
1.464000E+0	1.745755E-4
1.596000E+0	1.821155E-4
1.726000E+0	1.932566E-4
1.857000E+0	2.042973E-4
1.988000E+0	2.125978E-4
2.165000E+0	2.167316E-4
2.297000E+0	2.146603E-4
2.428000E+0	2.097185E-4
2.559000E+0	2.036305E-4
2.690000E+0	1.977866E-4
2.822000E+0	1.928550E-4

2.953000E+0	1.889634E-4
3.085000E+0	1.859755E-4
3.216000E+0	1.836599E-4
3.348000E+0	1.818420E-4
3.479000E+0	1.803933E-4
3.612000E+0	1.792094E-4
3.744000E+0	1.782853E-4
3.875000E+0	1.775199E-4
4.007000E+0	1.768857E-4
4.138000E+0	1.763515E-4
4.270000E+0	1.759041E-4
4.402000E+0	1.755167E-4
4.533000E+0	1.751903E-4
4.665000E+0	1.749044E-4
4.797000E+0	1.746454E-4
4.930000E+0	1.744218E-4
5.062000E+0	1.742230E-4
5.194000E+0	1.740479E-4
5.326000E+0	1.739168E-4
5.458000E+0	1.737412E-4
5.591000E+0	1.735505E-4
5.722000E+0	1.734138E-4
5.855000E+0	1.732960E-4
5.987000E+0	1.731912E-4
6.119000E+0	1.730978E-4
6.253000E+0	1.730165E-4
6.384000E+0	1.729468E-4
6.517000E+0	1.728716E-4
6.649000E+0	1.728094E-4
6.781000E+0	1.727515E-4
6.914000E+0	1.726886E-4
7.046000E+0	1.726298E-4
7.179000E+0	1.725720E-4
7.311000E+0	1.725185E-4
7.444000E+0	1.724728E-4
7.576000E+0	1.724633E-4
7.708000E+0	1.723812E-4
7.841000E+0	1.722730E-4
7.974000E+0	1.722212E-4
8.107000E+0	1.721760E-4
8.238000E+0	1.721388E-4
8.371000E+0	1.721150E-4
8.504000E+0	1.720919E-4
8.638000E+0	1.720610E-4
8.772000E+0	1.720378E-4
8.904000E+0	1.720090E-4
9.037000E+0	1.719907E-4
9.169000E+0	1.719691E-4
9.302000E+0	1.719573E-4
9.471000E+0	1.718957E-4
9.604000E+0	1.718998E-4
9.738000E+0	1.718946E-4
9.871000E+0	1.718346E-4
1.000500E+1	1.717496E-4
1.013800E+1	1.717108E-4
1.027200E+1	1.716871E-4
1.040500E+1	1.716707E-4

1.053800E+1	1.716598E-4
1.067200E+1	1.716555E-4
1.080500E+1	1.716477E-4
1.093900E+1	1.716469E-4
1.107200E+1	1.716238E-4
1.120600E+1	1.716162E-4
1.133900E+1	1.715973E-4
1.147200E+1	1.715867E-4
1.160600E+1	1.715740E-4
1.173900E+1	1.715653E-4
1.187300E+1	1.715624E-4
1.200600E+1	1.715544E-4
1.214100E+1	1.714642E-4
1.227500E+1	1.714277E-4
1.240800E+1	1.714087E-4
1.254200E+1	1.713955E-4
1.267500E+1	1.713894E-4
1.280900E+1	1.713871E-4
1.294200E+1	1.713860E-4
1.307600E+1	1.713789E-4
1.321000E+1	1.713752E-4
1.334400E+1	1.713664E-4
1.347800E+1	1.713610E-4
1.361100E+1	1.713492E-4
1.374600E+1	1.713310E-4
1.387900E+1	1.713191E-4
1.401400E+1	1.713122E-4
1.414700E+1	1.713342E-4
1.428100E+1	1.712792E-4
1.441600E+1	1.712212E-4
1.455000E+1	1.711914E-4
1.468500E+1	1.711743E-4
1.481900E+1	1.711637E-4
1.495300E+1	1.711740E-4
1.508700E+1	1.711747E-4
1.522100E+1	1.711732E-4
1.535600E+1	1.711704E-4
1.549000E+1	1.711555E-4
1.562500E+1	1.711427E-4
1.575900E+1	1.711396E-4
1.589400E+1	1.711358E-4
1.602800E+1	1.711262E-4
1.616200E+1	1.711168E-4
1.629700E+1	1.711136E-4
1.643100E+1	1.711120E-4
1.656600E+1	1.711096E-4
1.670000E+1	1.710273E-4
1.683500E+1	1.710001E-4
1.696900E+1	1.709799E-4
1.710300E+1	1.709627E-4
1.723800E+1	1.709615E-4
1.737200E+1	1.709667E-4
1.750800E+1	1.709644E-4
1.764100E+1	1.709621E-4
1.777700E+1	1.709546E-4
1.791100E+1	1.709535E-4
1.804500E+1	1.709453E-4

1.818000E+1	1.709400E-4
1.831500E+1	1.709390E-4
1.845000E+1	1.709380E-4
1.858400E+1	1.709309E-4
1.871900E+1	1.709225E-4
1.885400E+1	1.709573E-4
1.898800E+1	1.708657E-4
1.912400E+1	1.708250E-4
1.925900E+1	1.708161E-4
1.939400E+1	1.707988E-4
1.952900E+1	1.707877E-4
1.967500E+1	1.707916E-4
1.982000E+1	1.707898E-4
1.996600E+1	1.707791E-4
2.011200E+1	1.707784E-4
2.025600E+1	1.707738E-4
2.040600E+1	1.707637E-4
2.055500E+1	1.707611E-4
2.070400E+1	1.707642E-4
2.085100E+1	1.707555E-4
2.100300E+1	1.707542E-4
2.115400E+1	1.707426E-4
2.130400E+1	1.707367E-4
2.145700E+1	1.706538E-4
2.161000E+1	1.706348E-4
2.175900E+1	1.706231E-4
2.190800E+1	1.706190E-4
2.205700E+1	1.706166E-4
2.220900E+1	1.706259E-4
2.235800E+1	1.706217E-4
2.250800E+1	1.706230E-4
2.265700E+1	1.706203E-4
2.281200E+1	1.706130E-4
2.296600E+1	1.706063E-4
2.312000E+1	1.706037E-4
2.327400E+1	1.705943E-4
2.342900E+1	1.705935E-4
2.358300E+1	1.706198E-4
2.373400E+1	1.705264E-4
2.388800E+1	1.704937E-4
2.404300E+1	1.704830E-4
2.419800E+1	1.704769E-4
2.435200E+1	1.704770E-4
2.450600E+1	1.704860E-4
2.465600E+1	1.704906E-4
2.480700E+1	1.704877E-4
2.495700E+1	1.704882E-4
2.510800E+1	1.704898E-4
2.525800E+1	1.704827E-4

APPENDIX C

HEAT TRANSFER CALCULATIONS

The heat transfer through the μ-ThFFF system is shown in Figure 79. The temperature point T1 is the temperature of the heater and the temperature point T4 is the temperature of the heat sink. The three materials used and the thermal conductivity, *k*,

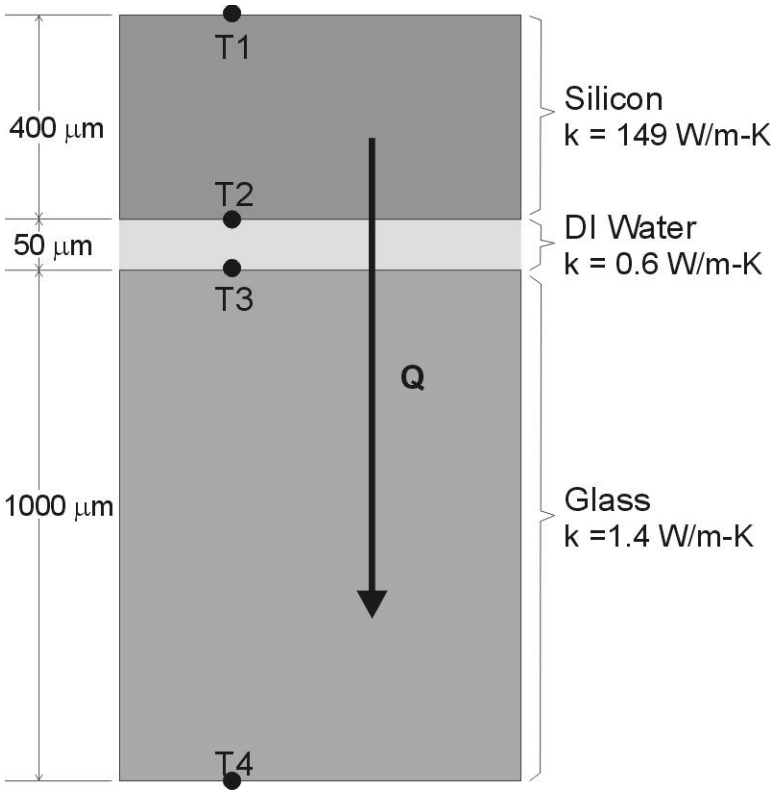

Figure 79. Schematic of heat transfer through the μ-ThFFF channel.

and width, w, are shown in this figure. Heat conduction, Q, is defined as positive from T1 to T4. The temperature difference across the channel is T3-T2.

For this sample calculation, the measured hot temperature, T1, is 61.0 °C and the measured cold temperature, T4, is 15.8 °C. The area of heat conduction is assumed to be the rectangular area of the channel (not including the tapered ends) which is calculated to be 2.1×10^{-4} m^2.

The heat conduction is governed by the following equations:

$$Q = \frac{1}{R_{tot}}(T4 - T1) \tag{86}$$

$$R_{tot} = \sum R_i = R_{silicon} + R_{water} + R_{glass} \tag{87}$$

$$R_i = \frac{w_i}{k_i}\frac{1}{A} \tag{88}$$

$$T2 = Q \cdot R_{silicon} + T1 \tag{89}$$

$$T3 = Q \cdot R_{water} + T2 \tag{90}$$

In these equations R_{tot} is the total equivalent resistance; R_i is the resistance for each material where i is silicon, water, and glass; and A is the area for heat transfer.

$$R_{silicon} = \frac{400\times10^{-6}\,\mathrm{m}}{149\,\mathrm{W/m\cdot K}}\frac{1}{0.00021\,\mathrm{m}^2} = 0.0128\,\mathrm{K/W}$$

$$R_{water} = \frac{50\times10^{-6}\,\mathrm{m}}{0.60\,\mathrm{W/m\cdot K}}\frac{1}{0.00021\,\mathrm{m}^2} = 0.3968\,\mathrm{K/W}$$

$$R_{glass} = \frac{1000\times10^{-6}\,\mathrm{m}}{1.40\,\mathrm{W/m\cdot K}}\frac{1}{0.00021\,\mathrm{m}^2} = 3.4104\,\mathrm{K/W}$$

$$R_{tot} = \sum R_i = R_{silicon} + R_{water} + R_{glass} = 3.811\,\mathrm{K/W}$$

$$Q = \frac{1}{3.811\,\mathrm{K/W}}(61.0\,\mathrm{K} - 15.8\,\mathrm{K}) = 11.9\,\mathrm{W}$$

$$T2 = 334.15\,\mathrm{K} - \left(11.9\,\mathrm{W} \cdot 0.0128\,\mathrm{K/W}\right) = 334\mathrm{K} = 60.8\,^{\circ}\mathrm{C}$$

$$T3 = 334\,\mathrm{K} - \left(11.9\,\mathrm{W} \cdot 0.3968\,\mathrm{K/W}\right) = 329.6\mathrm{K} = 56.4\,^{\circ}\mathrm{C}$$

$$\Delta T = (T3 - T2) = (60.8 - 56.4)\,^{\circ}\mathrm{C} = 4.7\,^{\circ}\mathrm{C}.$$

APPENDIX D

ACOUSTIC CALCULATIONS

This appendix is included for the purpose of showing an example calculation of the acoustic field flow fractionation system. Specifically, this program, written in *Mathcad* version 11, calculates the predicted elution time of polystyrene particles in pure water at room temperature. There are a number of parameters that are adjustable such as particle material properties, carrier material properties, transducer operating conditions, carrier flow rate, and others. The transducer includes a value for converting voltage to transducer face velocity. This value is predicted using a transmission line model of the acoustic system with a 3-port network model of the transducer such as the *Mason* or *KLM* model. The KLM model was described in this text in Chapter 2.

Mathcad is a graphical based math program capable of numerical calculations, which were required for determining the retention values. It has a set of built in units and automatically converts between these base units. Other units can be defined based on the core units.

This particlular example shows the separation conditions of the results found within this dissertation. The acoustic separation of three samples of polystyrene suspensions with mean diameters of 110 nm, 210 nm, and 300 nm.

Unit Definition

$nm := 10^{-9} \cdot m$ nanometer

$\mu m := 10^{-6} \cdot m$ micron

$aL := 10^{-18} \cdot L$ atoliter

Physical Constants and Standard Conditions

$T := 300 \cdot K$ Temperature

$k_b := 1.08 \cdot 10^{-23} \cdot \frac{J}{K}$ Boltzman's constant

$\varepsilon_0 := 8.65 \cdot 10^{-12} \cdot \frac{F}{m}$ Permittivity of free space

$f := 6.08 \cdot MHz$ Transducer operating frequency

$V_{amp} := 5 \cdot volt$ Transducer driving voltage

$u := 0.13 \cdot \frac{m}{s \cdot volt} \cdot V_{amp}$ Transducer face velocity

$A_{er} := 0.0764 \cdot cm^2$ Microchannel entrance region area

$A_{sr} := 1.3032 \cdot cm^2$ Microchannel separation region area

$w := 61.988 \cdot \mu m$ Microchannel width

$b := 4 \cdot mm$ Microchannel breadth

$l := 4 \cdot cm$ Microchannel length

$l_{pc} := 6 \cdot in$ Precolumn tubing length

$d_{pc} := 150 \cdot \mu m$ Precolumn tubing diameter

$FR := 0.5 \cdot \frac{mL}{hr}$ Flow rate of carrier fluid

$c_0 := 1$ Normalized concentration of sample

Material Properties

$\rho_{ps} := 1055 \frac{kg}{m^3}$ $\gamma_{ps} := 2.2 \cdot 10^{-10} \cdot Pa^{-1}$ Density and compressibility of polystyrene

$\rho_w := 1000 \frac{kg}{m^3}$ $\gamma_w := 4.4 \cdot 10^{-10} \cdot Pa^{-1}$ Density and compressibility of water

Calculations

$c_w := \frac{1}{\sqrt{\gamma_w \cdot \rho_w}}$ Speed of sound in water

$c_w = 1508 \frac{m}{s}$

$v_{mean} := \frac{FR}{w \cdot b}$ Mean carrier velocity

$v_{mean} = 0.056 \frac{cm}{s}$

$\Phi := \frac{5 \cdot \rho_{ps} - 2 \cdot \rho_w}{2 \cdot \rho_{ps} + \rho_w} - \frac{\gamma_{ps}}{\gamma_w}$ Density/compressiblity factor

$\Phi = 0.553$

$\lambda := \frac{c_w}{f}$ Acoustic wavelength in water

$\lambda = 248 \mu m$

$E := \frac{1}{2} \cdot \rho_w \cdot u^2$ Acoustic energy density

$E = 211.25 \frac{J}{m^3}$

$k := \frac{2 \cdot \pi}{\lambda}$ Wave propagation number in water

$k = 25340 m^{-1}$

$V(d) := \frac{\pi}{6} \cdot d^3$

Volume of particle, example for 300 nm.

$V(300 \cdot nm) = 14.137 aL$

$v(x) := 6 \cdot v_{mean} \cdot \left[\frac{x}{w} - \left(\frac{x}{w} \right)^2 \right]$

Velocity profile of carrier fluid in width (x) direction.

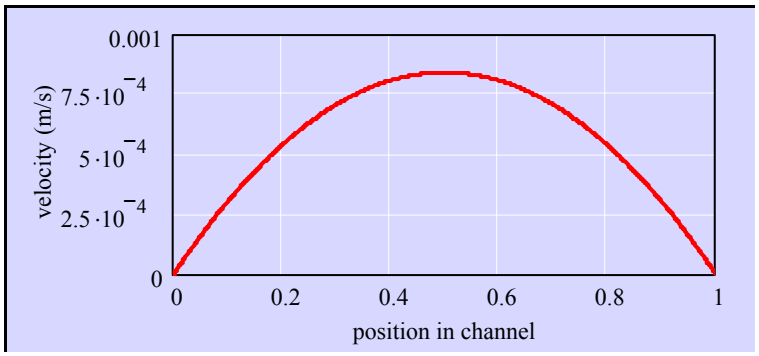

$F(x, d) := V(d) \cdot k \cdot E \cdot \Phi \cdot \sin(2 \cdot k \cdot x)$

Acoustic force on polystyrene particles of 110 nm, 210 nm, and 300 nm diameters.

$F_{max}(d) := V(d) \cdot k \cdot E \cdot \Phi$

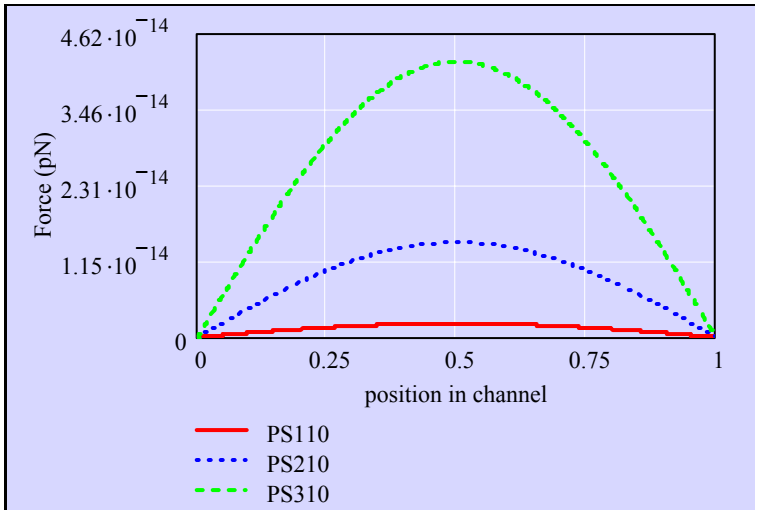

$$c(x,d) := c_0 \cdot e^{\frac{-F(x,d)}{2 \cdot k \cdot k_b \cdot T}}$$

Concentration profiles of polystyrene samples (110 nm, 210 nm, 300 nm) in water under the acoustic force shown above for 1/5 of the channel width.

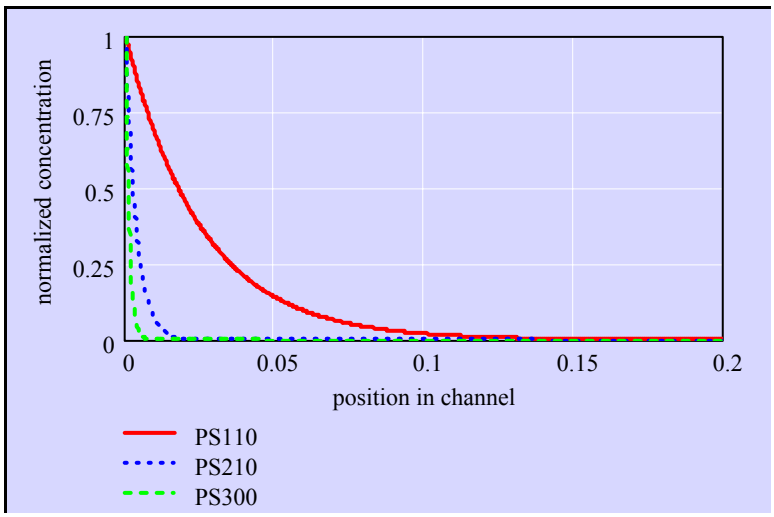

$$R(d) := \frac{\frac{1}{w} \cdot \int_0^w c(x,d) \cdot v(x)\, dx}{v_{mean} \cdot \frac{1}{w} \cdot \int_0^w c(x,d)\, dx}$$

Normal mode retention

$\gamma := 15.5$ $\quad d_{max} := 600$

Steric mode retention under high retention assumption.

$$Rs(d) := \frac{3 \cdot \gamma \cdot d}{w}$$

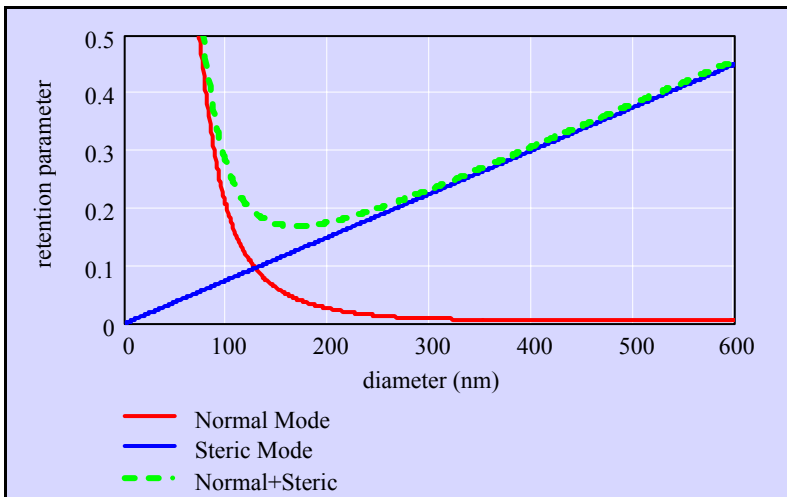

$$V_{pc} := \frac{\pi}{4} \cdot d_{pc}^{\,2} \cdot l_{pc}$$

$V_{pc} = 2.693\,mm^3$ Volume of precolumn tubing

$$V_0 := V_{pc} + \left(A_{er} + A_{sr}\right) \cdot w$$

$V_0 = 11.245\,mm^3$ Void volume

$$t_0 := \frac{V_0}{FR}$$ Void time or time of void peak elution

$$t_{Rn}(d) := \frac{t_0}{R(d)}$$ Normal mode retention time

$$t_{Rs}(d) := \frac{t_0}{Rs(d)}$$ Steric mode retention time

$$t_R(d) := \frac{t_0}{R(d) + Rs(d)}$$ Retention time

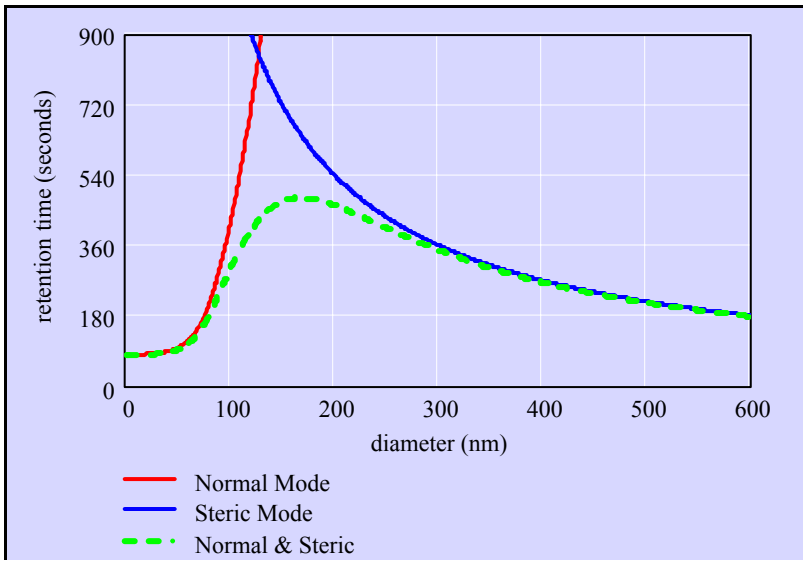

$t_0 = 81\,s$

$t_R(110\,nm) = 353\,sec$

$t_R(210\,nm) = 452\,sec$

$t_R(300\,nm) = 348\,sec$

APPENDIX E

MATLAB® PLATE HEIGHT PROGRAM

This program reads a data file (Appendix B) and calculates the plate height of the sample peak based on a gaussian shape. Flow rate, injection time and channel dimensions are extracted from the file header and appended, along with the calculcated plate height to a file containing all the data from the plate height experiments.

This particular program was setup to iterate the plate height calculation on 72 data files that had previously been recorded. This value can of course be adjusted to the data set available. The process for determining the plate height is: 1) determine maximum peak height, 2) locate the time at which the peak is maximum, 3) determine the peak half height, 4) locate the two points of time at the peak half height, 5) calculate number of theoretical plates and plate height according to theory.

PlateHeight.m

```
% Initialize
clear;                                          % Clear the variables

for i=1:72

% Get the Data
%name=input('What is the filename?  ChannelB_','s');  % Get the
filename
filename=['ChannelB_',num2str(i-1),'.fff'];  % Complete the filename
```

```
data=dlmread(filename,'\t',20,0);            % Get the data without the
header
%datetime=head(1,2);
%sample=head(1,3);
sampvol=dlmread(filename,'\t',[3 1 3 1]);
TI=dlmread(filename,'\t',[4 1 4 1]);
%carrier=head(1,6);
FR(i)=dlmread(filename,'\t',[6 1 6 1]);      % Carrier flow rate
(mL/hr)
width=dlmread(filename,'\t',[7 1 7 1]);
breadth=dlmread(filename,'\t',[8 1 8 1]);
length=dlmread(filename,'\t',[9 1 9 1]);
prelength=dlmread(filename,'\t',[10 1 10 1]);
%detector=head(1,12);
detwidth=dlmread(filename,'\t',[12 1 12 1]);
detfreq=dlmread(filename,'\t',[13 1 13 1]);
detvolt=dlmread(filename,'\t',[14 1 14 1]);
detdc=dlmread(filename,'\t',[15 1 15 1]);
%electrode=head(1,17);
elecfreq=dlmread(filename,'\t',[17 1 17 1]);
elecvolt=dlmread(filename,'\t',[18 1 18 1]);

% Manipulate the data
time=data(:,1);                              % Extract the time vector
from the data
signal=data(:,2);                            % Extract the signal
vector from the data
signal=signal-mean(signal(1:200));           % Move the signal baseline
to zero
area=width/10000*breadth/10;                 % Cross sectional area of
channel in cm^2
velocity(i)=FR(i)/area/3600;                 % Carrier fluid velocity
in cm/sec

% Find important parameters for calculating the plate height
sig_max=max(signal);                         % Find the signal peak
max_ind=find(signal==sig_max);               % Find the vector index of
the signal peak
max_length=size(max_ind);
if max_length(1,1) > 1
    max_mid=int8(max_length(1,1)/2);
    max_ind=max_ind(max_mid(1,1));
end
TP=time(max_ind)-TI;                         % Find the time at which
the signal peaks
sig_half=sig_max/2;                          % Find the half max value
(HMV) of the signal
half_ind=find(sig_half <= signal & signal <= sig_max);      % Find the
vector index of the signal HMV
vsize=find(half_ind==max_ind);               % Find the index of the
vector at maximum value
half_ind1=min(half_ind(1:vsize));            % Index of first signal at
HMV
half_ind2=max(half_ind(vsize:end));          % Index of second signal
at HMV
TW1=time(half_ind1)-TI;                      % First time at signal HMV
```

```
TW2=time(half_ind2)-TI;                          % Second time at signal
HMV

% Calculate the plate height
N=5.54*(TP/(TW2-TW1))^2;                         % Number of theoretical
plates
H(i)=length/N;                                   % Plate height
end

plateheight=zeros(i,2);
plateheight(1:end,1)=velocity.';
plateheight(1:end,2)=H.';
dlmwrite('plateheight.fff',plateheight,'\t');

% Plot the signal
plot(velocity,H,'o','MarkerEdgeColor','k','MarkerFaceColor','r');
% 2D plot of the signal versus time
title({'Plate Height versus Velocity for a 30 \mum on-chip Ti/Au
detector'});
text(0,10,{num2str(width),'\mum x ',num2str(breadth),'cm x
',num2str(length),'mm + ',num2str(prelength),'cm precolumn tubing.'});
xlabel('Carrier velocity (cm/sec)');
ylabel('Plate height (cm)');
```

APPENDIX F

PHOTO AND LASER MASK IMAGES

This section includes the photo and laser mask images used for fabrication of the acoustic and thermal FFF systems. The images are scaled down 3:5. Each image is described as to purpose and whether it is a photo mask or laser mask.

AcFFF

Top electrode

This mask is shown in Figure 80. It was a photo mask used for fabrication of a silicon stencil. The stencil was used for defining the metal layers on the backside or top of the LN wafer for operation of the transducer.

Bottom electrode

The bottom transducer electrode is the pair of the top electrode. It is also used for fabriation of a silicon stencil in defining the metal layers on the frontside or bottom of the LN wafer. It is shown in Figure 81. This mask also includes the electrical impedance detector electrode located on the top of the channel.

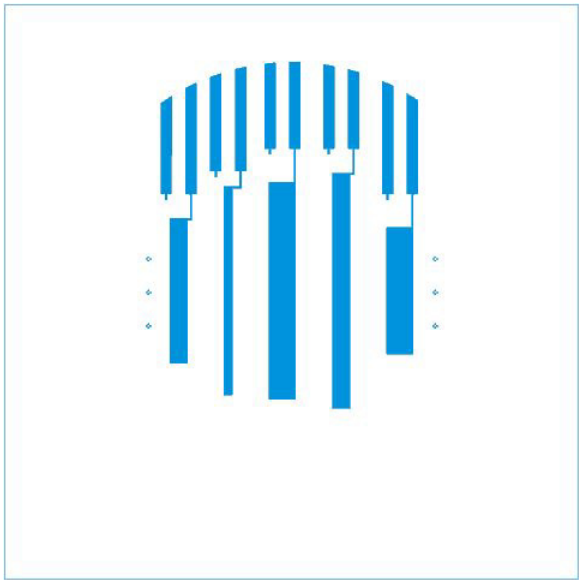

Figure 80. Top transducer electrode for AcFFF system.

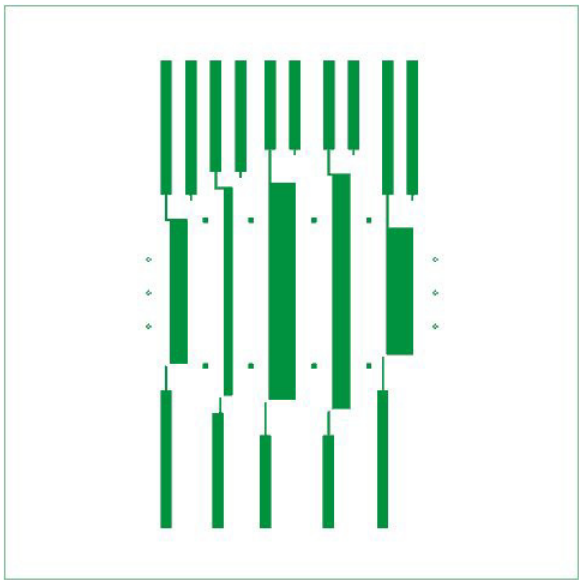

Figure 81. Bottom transducer electrode and top detector electrode for the AcFFF system.

Detector electrode

The complement of the top detector electrode is shown in Figure 82. It is located on the bottom of the channel directly opposite the top detector electrode. It was used to create a silicon stencil to be used as in the *top* and *bottom electrode* masks.

Fluidic ports

The fluidic ports to access the microchannel were etched through the silicon wafer using KOH or ICP-RIE. The photomask used to define the openings is shown in Figure 83. This is the same mask used for the ThFFF channel fluidic visa described later.

Channel walls

The mask for the channel walls is shown in Figure 84. It is not necessarily a mask but rather a pattern for the laser ablation machine to trace. The channel walls were defined in PDMS on the silicon wafer using this pattern.

ThFFF

Heaters

The integrated heaters for the thermal FFF systems were patterned using the mask shown in Figure 85. This photomask was used for either etching SiO_2 for boron diffusion barriers or for patterning metal electrodes.

Fluidic Ports

The fluidic vias for access to the channel were defined using the same mask as for the AcFFF system. This mask is shown in Figure 83.

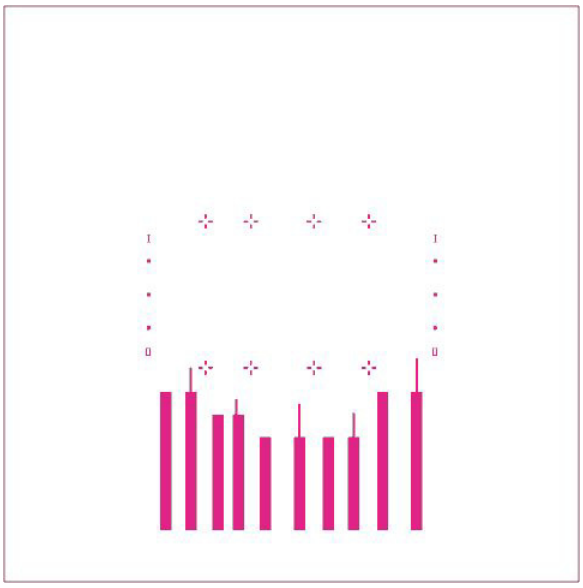

Figure 82. Detector electrode of the AcFFF system.

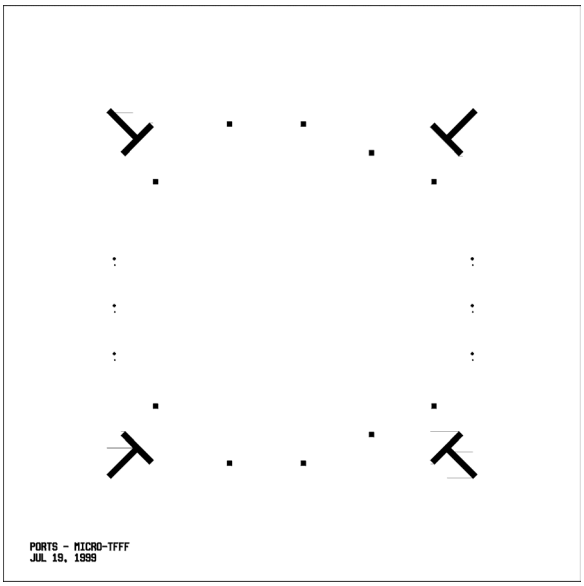

Figure 83. Fluidic ports for etching through the silicon wafer.

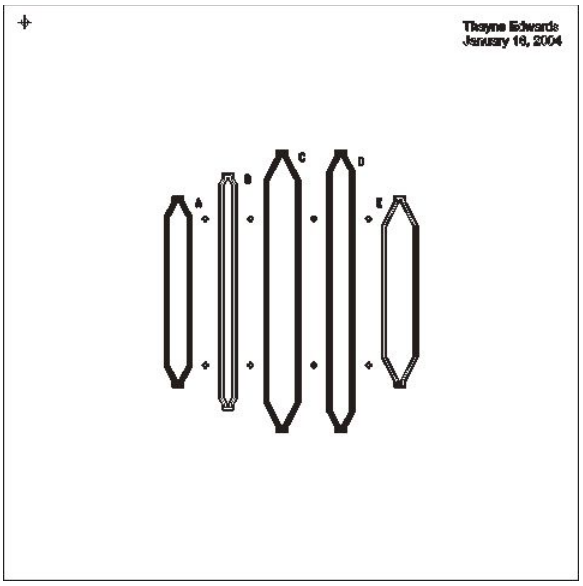

Figure 84. Laser pattern for defining channel walls in PDMS on silicon for the AcFFF system.

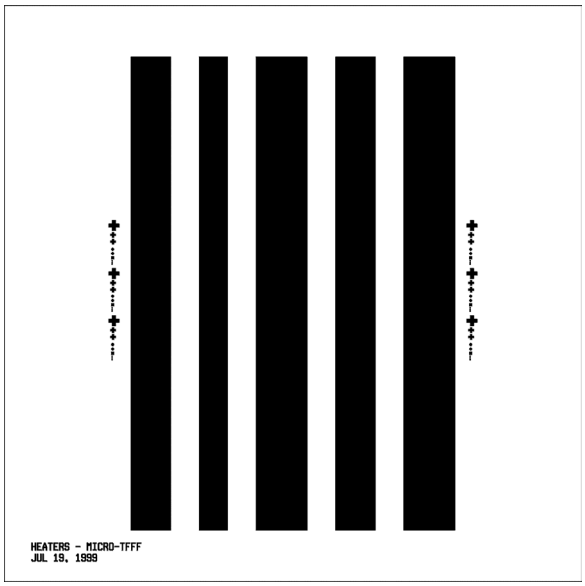

Figure 85. Heater photomask for the thermal FFF system. This mask was reduced at a 3:4 ratio.

Channel walls

The channel walls for the ThFFF system were not defined using the laser ablation method as with the AcFFF system. Instead, the walls were defined using a thick photoresist, *SU-8*, so the masks were photomasks. The photo mask is shown in Figure 86.

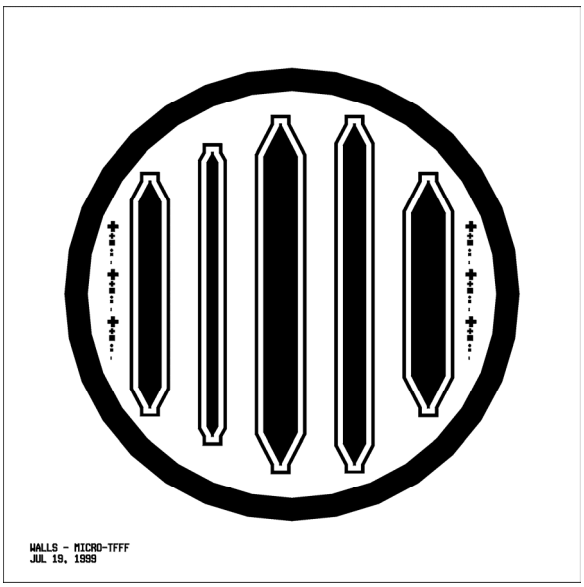

Figure 86. Channel walls photomask for the ThFFF system. This image was reduce at a 3:4 ratio.

REFERENCES

[1] Proceedings of micro-TAS ‘04*, Malmö, Sweden, September 26-30, 2004.*

[2] M. D. Weiss, *Biomedical instrumentation*. New York: Chilton Book Company, 1973.

[3] J. G. Webster, *Medical instrumentation: application and design*. New York: John Wiley and Sons, 1998.

[4] R. A. Normann, *Principles of bioinstrumentatio*n. New York: John Wiley and Sons, 1988.

[5] D.A. Christensen, *Ultrasonic bioinstrumentation*. New York, John Wiley and Sons, 1988.

[6] P.A. Belter, *Bioseparations: downstream processing for biotechnology*. New York: John Wiley and Sons, 1988.

[7] R.P. Oda, M.A. Strausbauch, A.F.R. Huhmer, N. Borson, S.R. Jurrens, J. Craighead, P.J. Wettstein, B. Eckloff, B Kline, and J.P. Landers, “Infrared-mediated thermocycling for ultrafast polymerase chain reaction amplification of DNA,” *Anal. Chem.*, vol. 70, pp. 4361-4368, Oct. 1998.

[8] D.J. Harrison, K. Fluri, K. Seiler, Z. Fan, C.S. Effenhauser and A. Manz, "Micromachining a Miniaturized Capillary Electrophoresis-Based Chemical Analysis System on a Chip", *Science*, vol. 261, pp. 895-897, 1993.

[9] J.C. Giddings, "A new separation concept based on a coupling of concentration and flow nonuniformities," *Sep. Sci.*, vol. 1, pp. 123-125, 1966.

[10] G.H. Thompson, M.N. Myers, and J.C. Giddings, "An observation of a field-flow fractionation effect with polystyrene samples," *Sep. Sci.*, vol. 2, pp. 797-800, 1967.

[11] G.H. Thompson, M.N. Myers, and J.C. Giddings, "Thermal field-flow fractionation of polystyrene samples," *Anal. Chem.*, vol. 41, pp. 1219-1222, 1969.

[12] S.L. Brimhall, M.N. Myers, K.D. Caldwell, and J.C. Giddings, "High temperature thermal FFF for the characterization of polyethylene," *Sep. Sci. Technol.*, vol. 16, pp. 671-689, 1981.

[13] G. Liu and J. C. Giddings, "Separation of particles in aqueous suspensions by thermal field-flow fractionation. Measurement of thermal diffusion coefficients," *Chromatographia*, vol. 34, pp. 483-492, 1992.

[14] S. L. Brimhall, M. N. Myers, K. D. Caldwell, and J. C. Giddings, "Study of temperature dependence of thermal diffusion in polystyrene/ethylbenzene by thermal field-flow fractionation," *J. Polym. Sci.: Polym. Phys. Ed.*, vol. 23, pp. 2445-2456, 1985.

[15] R. Sisson and J. C. Giddings, "Effects of solvent composition on polymer retention in thermal field-flow fractionation: retention enhancement in binary solvent mixtures," *Anal. Chem.*, vol. 66, pp. 4043-4053, 1994.

[16] M. E. Schimpf and J. C. Giddings, "Characterization of thermal diffusion of copolymers in solution by thermal field-flow fractionation," *J. Polym. Sci.: Part B: Polym. Phys.*, vol. 28, pp. 2673-2680, 1990.

[17] J. C. Giddings, "Factors influencing accuracy of colloidal and macromolecular properties measured by field-flow fractionation," *Anal. Chem.*, vol. 69, pp. 552-557, 1997.

[18] M. Martin, M.N. Myers, and J.C. Giddings, "Nonequilibrium and polydispersity peak broadening in thermal field-flow fractionation," *J. Liq. Chromatogr.*, vol. 2, pp. 147-164, 1979.

[19] S. Lee, "Application of thermal field-flow fractionation for characterization of industrial polymers," *J. Microcolumn Separations*, vol. 9(4), pp. 281-286, 1997.

[20] J. E. Belgaied, M. Hoyos, M. Martin, “Velocity profiles in thermal field-flow fractionation,” *J. of Chromatogr. A*, pp. 85-96, 1994.

[21] K. D. Caldwell, “FFF of biological materials,” in *Research instrumentation for the 21st centur*y, G. Beecher, Ed. Dordrecht, Netherlands: Martinus Nijhoff Publishers, 1987, pp. 89-116.

[22] G. H. Thompson, M.N. Myers, and J.C. Giddings, "An observation of a field-flow fractionation effect with polystyrene samples," *Sep. Sci.*, vol. 2, pp. 797-800, 1967.

[23] G. H. Thompson, M.N. Myers, and J.C. Giddings, "Thermal field-flow fractionation of polystyrene samples," *Anal. Chem.*, vol. 41, pp. 1219-1222, 1969.

[24] S. N. Semenov and K. I. Maslow, "Acoustic field-flow fractionation," *J. Chromatogr*., 446, 1988, pp. 151-156.

[25] M. Martin and P. S. Williams, in *Theoretical Advancement in Chromatography and Related Separation Techniques*, F. Dondi and G Guiochort (Eds.), NATO ASI Series C: Mathematical and Physical Sciences, Vol. 383, Kluwer, Dordrecht, The Netherlands, 1992, p. 534.

[26] N. Tri and R. Beckett, "Ultrasonic forces for particle separations," The eight international symposium on field-flow fractionation, Paris, France, Sept. 6-8, 1999.

[27] R. Beckett, "The use of acoustic forces of thin channel separations," The ninth international symposium on field-flow fractionation, Golden, CO, June 26-29, 2001.

[28] N. Tri and R. Beckett, "Acoustic field-Flow fractionation for particle separation," Ed. J. Cazes, *Encyclopedia of Chromatography*, accepted, 2000.

[29] B. K. Gale, K. D. Caldwell, and A. B. Frazier, "A micromachined electrical field-flow fractionation system," *IEEE Trans. Biomed. Eng*., vol. 45, no. 12, pp. 1459-1469, 1998.

[30] S. Middelhoek, "Celebration of the tenth transducers conference," in *Proc. Transducers '99*, Sendai, Japan, June 1999, pp. 12-15.

[31] G.T.A. Kovacs, *Micromachined transducers sourcebook*, New York: McGraw-Hill Companies, 1998, p. 1.

[32] D.J. Harrson, C. Skinner, S.B. Cheng, G. Ocvirk, S. Attiya, N. Bings, C. Wang, "From micro-motors to micro-fluidics: the blossoming of micromachining technologies in chemistry, biochemistry, and biology," in *Proc. Transducers '99*, Sendai, Japan, June 1999, pp. 12-15.

[33] M. A. Northrup, C. Gonzalez, D. Hadley, R. F. Hills, P. Landre, S. Lehew, R. Saiki, J. J. Sninsky, and R. Watson, "A MEMS-based miniature DNA analysis system," in *Proc. Transducers '95*, Stockholm, Sweden, June 25-29, 1995, pp. 764-767.

[34] P. Wilding, M. A. Shoffner, and L. J. Kircka, "Manipulation and flow of biological fluids in straight channels micromachined in silicon," *Clin. Chem*, vol. 40, pp. 1815-1818, 1994.

[35] M. Albin, R. Kowallis, E. Picozza, Y. Raysberg, C. Sloan, E. Winn-Deen, T. Woudenberg, and J. Zupfer, "Micromachining and microgenetics, what are they

and where do they work together?" in *Proc. IEEE Solid-State Sensor and Actuator Workshop*, Hilton Head, SC, June 2-6, 1996, pp. 253-257.

[36] R. C. Anderson, G. J. Bogdan, and R. J. Lipshutz, "Miniaturized genetic-analysis system," in *Proc. IEEE Solid-State Sensor and Actuator Workshop*, Hilton Head, SC, June 2-6, 1996, pp. 258-261.

[37] C. S. Effenhauser, A. Manz, and M. H. Widmer, "Glass chips for high-speed capillary electrophoresis separation with submicrometer plate heights*," Anal. Chem*., vol. 65, pp. 2637-2642, 1993.

[38] Z. H. Fan and D. J. Harrison, "Micromachining of capillary electrophoresis injectors and separators on glass chips and evaluation of flow at capillary interconnections," *Anal. Chem*., vol. 66, pp. 177-184, 1994.

[39] S. C. Jacobsen, A. W. Moore, and J. M. Ramsey, "Fused quartz substrates for microchip electrophoresis," *Anal. Chem*., vol. 67, pp. 2059-2063, 1995.

[40] H. Nakanishi, T. Nishimoto, N. Nakamura, S. Nagamachi, A. Arai, Y. Iwata, and Y. Mito, "Fabrication of electrophoresis devices on a quartz and glass substrates using a bonding with HF solution," in *Proc. IEEE Workshop on Micro Electro Mechanical Systems*, Nagoya, Japan, Jan. 26-30, 1997, pp. 299-304.

[41] D. E. Raymond, A. Manz, and H. M. Widmer, "Continuous sample preparation using free-flow electrophoresis on a silicon microstructure," in *Proc. Transducers '95*, Stockholm, Sweden, June 25-29, 1995, pp. 760-765.

[42] A. Manz, "Miniaturized chemical analysis systems based on electroosmotic flow," in *Proc. IEEE Workshop on Micro Electro Mechanical Systems*, Nagoya, Japan, Jan. 26-30, 1997, pp. 1-4.

[43] S. C. Terry, J. H. Jerman, and J. B. Angell, "A gas chromatographic air analyzer fabricated on a silicone wafer," *IEEE Trans. Electron. Devices*, vol. ED-26, pp. 1880-1886, 1979.

[44] R. R. Reston and E. S. Kolesar, "Silicon-micromachined gas chromatography system used to separate and detect ammonia and nitrogen dioxide--part I: design, fabrication, and integration of the gas chromatography system," *IEEE J. Microelectromech. Syst*., vol. 3, pp. 134-146, 1994.

[45] R. R. Reston and E. S. Kolesar, "Silicon-micromachined gas chromatography system used to separte and detect ammonia and nitrogen dioxide--part II: evaluation, analysis, and theoretical moedling of the gas chromatograph system," *IEEE J. Microelectromech. Syst*., vol. 3, pp. 147-154, 1994.

[46] G. Ocvirk, E. Verpoorte, A. Manz, H. M. Widmer, “Integration of a micro liquid chromatography onto a silicon chip,” in *Proc. Tranducers ’95*, Stockholm, Sweden, June 25-29, 1995, pp. 756-759.

[47] A. Manz, Y. Miyahara, J. Miura, Y. Watanabe, H. Miyagi, and K. Sato, “Design of an open-tubular column liquid chromatograph using silicon chip technology,” *Sensors and Actuators*, vol. B1, pp. 249-255, 1990.

[48] B. K. Gale, K. D. Caldwell, and A. B. Frazier, “A micromachined electrical field-flow fractionation system,” *IEEE Trans. Biomed. Eng*., vol. 45, no. 12, pp. 1459-1469, 1998.

[49] T. L. Edwards, B. K. Gale, and A. B. Frazier, “Micromachined thermal field-flow fractionation system,” in *Proc. Transducers ’99*, Sendai, Japan, June 7-10, 1999, pp. 742-745.

[50] J. Yang, Y. Huang, X.-B. Wang, F. F. Becker, P. R. C. Gascoyne, “Cell separation on microfabricated electrodes using dielectrophoretic/gravitational field-flow fractionation,” *Anal. Chem.*, vol. 71, pp. 911-918, 1999.

[51] M. A. Burns, C. H. Mastrangelo, T. S. Sammarco, F. P. Man, A. R. Kaiser, and D. T. Burke, “Microfabricated structures for integrated DNA analysis,” *Proc. Natl. Acad. Sci.*, vol. 93, pp. 5556-5561, 1996.

[52] B.K. Gales, Scaling effects in a microfabricated electrical field-flow fractionation system with integrated detector, University of Utah, Dept. of Bioengineering, August 2000.

[53] J.J. Gunderson and J.C. Giddings, "Chemical composition and molecular-size factors in polymer analysis by thermal field-flow fractionation and size exclusion chromatography," *Macromolecules*, vol. 19, pp. 2618-2621, 1986.

[54] J.C. Giddings, M.N. Myers, and J. Janca, "Retention characteristics of various polymers in thermal field-flow fractionation," *J. Chromatogr.*, vol. 186, pp. 37-44, 1979.

[55] J.C. Giddings, M. Martin, and M.N. Myers, "High speed polymer separations by thermal field-flow fractionation," *J. Chromatogr.*, vol. 158, pp. 419-435, 1978.

[56] J.J. Gunderson and J.C. Giddings, "Comparison of polymer resolution in thermal field-flow fractionation and size exclusion chromatography," *Anal. Chim. Acta*, vol. 189, pp. 1-15, 1986.

[57] J. C. Giddings, “Micro-FFF: Theoretical and practical aspects of reducing the dimensions of field-flow fractionation channels,” *J. Microcol. Se*p., vol. 5, pp. 497-503, 1993.

[58] J.C. Giddings, L.K. Smith, and M.N. Myers, "Surface barriers for retention enhancement in field-flow fractionation," *Sep. Sci. Technol.*, vol. 13, pp. 367-385, 1978.

[59] J. C. Giddings, M. R. Schure, M. N. Myers, and G. R. Velez, "End effects in field-flow fractionation: theory and means for reducing incremental zone broadening," *Anal. Chem.*, vol. 56, pp. 2099-2104, 1984.

[60] P. M. Shiundu and J. C. Giddings, "Influence of bulk and surface composition on the retention of colloidal particles in thermal field-flow fractionation,"*J. Chromatogr.*, vol. 715, pp. 117-126, 1995.

[61] C. A. Rue, M. E. Schimpf, "Thermal diffusion in liquid mixtures and its effect on polymer retention in ThFFF," *Anal. Chem.*, vol. 66, pp. 4054-4062, 1994.

[62] J.C. Giddings, M. Martin, and M.N. Myers, "High-resolution polymers separations in a four-pass hairpin thermal field-flow fractionation column," *J. Polym. Sci.: Polym. Phys. Ed.*, vol. 19, pp. 815-828, 1981.

[63] K.D. Caldwell, L.F. Kesner, M.N. Myers, and J.C. Giddings, "Electrical field-flow fractionation of proteins," *Science*, vol. 176, pp. 296-298, 1972.

[64] L.F. Kesner, K.D. Caldwell, M.N. Myers, and J.C. Giddings, "Performance characteristics of electrical field-flow fractionation in a flexible membrane channel,"*Anal. Chem.*, vol. 48, pp. 1834-1839, 1976.

[65] J.C. Giddings, G.C. Lin, and M.N. Myers, "Electrical field-flow fractionation in a rigid membrane channel," *Sep. Sci.*, vol. 11, pp. 553-568, 1976.

[66] J.C. Giddings, "Harnessing electrical forces for separation: CZE, IEF, FFF, SPLITT, and Other Techniques,"*J. Chromatogr.*, vol. 480, pp. 21-33, 1989.

[67] S. Levin, M.N. Myers, and J.C. Giddings, "Continuous separation of proteins in electrical split-flow thin (SPLITT) cell with equilibrium operation," *Sep. Sci.*, vol. 24, pp. 1245-1259, 1989.

[68] H. L. Lee and E. N. Lightfoot, "Preliminary report on ultrafiltration-induced polarization chromatography--an analog of field-flow fractionation," *Sep. Sci.*, vol. 11, pp. 417-440, 1976.

[69] J.F.G. Reis, E.N. Lightfoot "Electropolarization chromatography." *AIChE J.*, vol. 22, pp. 779-785, 1976.

[70] F.G. Reis, D. Ramkrishna, E.N. Lightfoot "Convective mass transfer in the presence of polarizing fields: dispersion in hollow fiber electropolarization chromatography." *AIChE J.*, vol. 24, pp. 679-686, 1978.

[71] A. S. Chiang, E. H. Kmiotek, S. M. Langan, P. T. Noble, J. F. G. Reis, and E. N. Lightfoot, "Preliminary experimental survey of hollow-fiber electro-polarization chromatography (electrical field-flow fractionation) for protein fractionation," *Sep. Sci.*, vol. 14, pp. 453-474, 1979.

[72] A.B. Shah, J.F.G. Reis, E.N. Lightfoot, R.E. Moore "Modeling electroretention of proteins during electropolarization chromatography." *Sep. Sci.*, vol. 14, pp. 475-497, 1979.

[73] J. M. Davis, F. R. F. Fan, and A. J. Bard, "Retention by electrical field-flow fractionation of anions in a new apparatus with annular porous glass channels," *Anal. Chem.*, vol. 59, pp. 1339-1348, 1987.

[74] W. Thormann, M. A. Firestone, M. L. Dietz, T. Cecconie, and R. A. Mosher, "Focusing counterparts of electrical field flow fractionation and capillary zone electrophoresis," *J. Chromatogr.*, vol. 461, pp. 95-101, 1989.

[75] K. D. Caldwell and Y.-S. Gao, "Electrical field-flow fractionation in particle separation . 1. monodisperse standards," *Anal. Chem.*, vol. 65, pp. 1764-1772, 1993.

[76] M. E. Schimpf, D. D. Russell, and J. K. Lewis, "Separation of charged latex particles by electrical field-flow fractionation," *J. Liq. Chromatogr.*, vol. 17, pp. 3221-3238, 1994.

[77] R. Mori, T. Nakagama, T. Hobo "Electrical field flow fractionation of sugars." *Kuromatogurafi*, vol. 15, pp. 270-271 (1994) (in Japanese) [CA 122:133578d].

[78] M. E. Schimpf and K. D. Caldwell, "Electrical field-flow fractionation for colloid and particle analysis," *Am. Lab.*, vol. 27(6), pp. 64-68, 1995.

[79] S.A. Palkar, R.E. Murphy, M.R. Schure "Charge/hydrophobicity fractionation with hyphenated electrical FFF/chromatography." *Polym. Mater. Sci. Eng.*, vol. 75, pp. 6-7, 1996.

[80] S. A. Palkar, M. R. Schure "Mechanistic study of electrical field-flow fractionation. I: on the nature of the internal field," *Analytical Chemistry*, pp. 3223-3229, 1997.

[81] S. A. Palkar, M. R. Schure, "Mechanistic study of electrical field-flow fractionation. II: the effect of sample conductivity on retention," *Analytical Chemistry*, 3230-3238, 1997.

[82] M. Dunkel, N. Tri, R. Beckett, K. D. Caldwell, "Electrical field-flow fractionation: a tool for characterization of colloidal adsorption complexes," *J. Microcolumn Separations*, vol. 9(3), pp. 177-183, 1997.

[83] S. A. Palkar, R. E. Murphy, M. R. Schure, "Charge and hydrophobicity fractionation of colloidal-size polymers using electrical field-flow fractionation and liquid chromatography," in *Particle Size Distribution III*, T. Provder Ed., ACS Symposium Series No. 693, American Chemical Society, pp. 196-206, 1998 [CA129:162031].

[84] J.C. Giddings and M.N. Myers, "Steric field-flow fractionation: a new method for separating 1-100 um particles," *Sep. Sci.*, vol. 13, pp. 637-645, 1978.

[85] M.N. Myers and J.C. Giddings, "A continuous steric FFF device for the size separation of particles," *Powder Technology*, vol. 23, pp. 15-20, 1979.

[86] J.C. Giddings, M.N. Myers, K.D. Caldwell, and J.W. Pav, "Steric FFF as a tool for the size characterization of chromatographic supports," *J. Chromatogr.*, vol. 185, pp. 261-271, 1979.

[87] K.D. Caldwell, T.T. Nguyen, M.N. Myers, and J.C. Giddings, "Observations on anomalous retention in steric field-flow fractionation," *Sep. Sci.*, vol. 14, pp. 935-946, 1979.

[88] M.N. Myers and J.C. Giddings, "Properties of the transition from normal to steric field-flow fractionation," *Anal. Chem.*, vol. 54, pp. 2284-2289, 1982.

[89] B.J. Compton, M.N. Myers, and J.C. Giddings, "A single particle photometric detector for steric field-flow fractionation," *Chem., Biomed., and Environ. Instru.*, vol. 12, pp. 299-317, 1982-83.

[90] K.A. Graff, K.D. Caldwell, M.N. Myers, and J.C. Giddings, "Characterization of fine coal particles by steric field-flow fractionation," *Fuel*, vol. 63, pp. 621-626, 1984.

[91] H. Meng, K.D. Caldwell, and J.C. Giddings, "Examination of residues from coal liquefaction by steric field-flow fractionation," *Fuel Process. Technol.*, vol. 8, pp. 313-320, 1984.

[92] R.E. Peterson II, M.N. Myers, and J.C. Giddings, "Characterization of steric field-flow fractionation using particles to 100 um diameter," *Sep. Sci.*, vol. 19, pp. 307-319, 1984.

[93] K.D. Caldwell, Z.Q. Cheng, P. Hradecky, and J.C. Giddings, "Separation of human and animal cells by steric field-flow fractionation," *Cell Biophys.*, vol. 6, pp. 233, 251, 1984.

[94] M. R. Schure, M. N. Myers, K. D. Caldwell, C. Byron, K. P. Chan, and J. C. Giddings, "Separation of coal fly ash using continuous steric field-flow fractionation," *Environ. Sci. Technol.*, vol. 19, pp. 686-689, 1985.

[95] T. Koch and J. C. Giddings, "High speed separation of large (> 1 um) particles by steric field-flow fractionation," *Anal. Chem.*, vol. 58, pp. 994-997, 1986.

[96] J.C. Giddings, X. Chen, K.-G. Wahlund, and M.N. Myers, "Fast particle separation by flow/steric field-flow fractionation," *Anal. Chem.*, vol. 59, pp. 1957-1962, 1987.

[97] S. Lee and J.C. Giddings, "Experimental observation of steric transition phenomena in sedimentation field-flow fractionation," *Anal. Chem.*, vol. 60, pp. 2328-2333, 1988.

[98] X. Chen, K.-G. Wahlund, and J.C. Giddings, "Gravity augmented high-speed flow/steric field-flow fractionation: simultaneous use of two fields," *Anal. Chem.*, vol. 60, pp. 362-364, 1988.

[99] M. H. Moon, M. N. Myers, and J. C. Giddings, "Evaluation of pinched inlet channel for stopless flow injection in steric field-flow fractionation," *J. Chromatogr.*, vol. 517, pp. 423-433, 1990.

[100] J.C. Giddings, M. H. Moon, P. S. Williams, and M. N. Myers, "Particle size distribution by sedimentation/steric FFF: development of a calibration procedure based on density compensation," *Anal. Chem.*, vol. 63, pp. 1366-1372, 1991.

[101] J. C. Giddings and M. H. Moon, "Measurement of particle density, porosity, and size distributions by sedimentation/steric field-flow fractionation. application to chromatographic supports," *Anal. Chem.*, vol. 63, pp. 2869-2877, 1991.

[102] P. S. Williams, M. H. Moon, J. C. Giddings, "Fast separation and characterization of micron size particles by sedimentation/steric field-flow fractionation: role of lift forces," in *Particle Size Analysis*, N. G. Stanley-Wood and R. W. Lines, Eds., Royal Society of Chemistry, Cambridge, UK, 1992.

[103] M. H. Moon and J. C. Giddings, "Extension of sedimentation/steric field-flow fractionation into submicron range: size analysis of 0.2-15 um metal particles," *Anal. Chem.*, vol. 64, pp. 3029-3037, 1992.

[104] M. H. Moon and J. C. Giddings, "Rapid separation and measurement of particle size distribution of starch granules by sedimentation/steric field-flow fractionation," *J. Food Sci.*, vol. 58, pp. 1166-1171, 1993.

[105] J. C. Giddings, "Retention (steric) inversion in field-flow fractionation: practical implications in particle size, density, and shape analysis," *The Analyst*, vol. 118, pp. 1487-1494, 1993.

[106] R. Beckett, Y. Jiang, G. Liu, M. H. Moon, J. C. Giddings, "Separation and behavior of nonspherical particles in sedimentation/steric field-flow fractionation," *Part. Sci. Technol.*, vol. 12, pp. 89-113, 1994.

[107] P. S. Williams and J. C. Giddings, "Theory of field programmed field-flow fractionation with corrections for steric effects," *Anal. Chem.*, vol. 66, pp. 4215-4228, 1994.

[108] B. N. Barman and J. C. Giddings, "Separation of colloidal latex aggregates by cluster mass and shape using sedimentation field-flow fractionation with steric perturbations," *Anal. Chem.*, vol. 67, pp. 3861-3865, 1995.

[109] P. S. Williams, M. H. Moon, Y. Xu, and J. C. Giddings, "Effect of viscosity on retention time and hydrodynamic lift forces in sedimentation/steric field-flow fractionation," *Chem. Eng. Sci.*, vol. 51, pp. 4477-4488, 1996.

[110] M. H. Moon and J. C. Giddings, "Upper particle size limit for high-speed analysis by sedimentation/steric field-flow fractionation (FFF) in thin channels," *Ind. Eng. Chem. Res.*, vol. 35, pp. 1072-1077, 1996.

[111] K. D. Jensen, S. K. Williams, and J. C. Giddings, "High-speed particle separation and steric inversion in thin flow field-flow fractionation channels," *J. Chromatogr.*, vol. 746, pp. 137-145, 1996.

[112] P. S. Williams, M. H. Moon, and J. C. Giddings, "Influence of accumulation wall and carrier solution composition on lift force in sedimentation/steric field-flow fractionation," *Colloids Surf. A: Physicochem. Eng. Aspects*, vol. 113, pp. 215-228, 1996.

[113] J.C. Giddings, F.J. Yang, and M.N. Myers, "Flow field-flow fractionation: a versatile new separation method," *Science*, vol. 193, pp. 1244-2145, 1976.

[114] J.C. Giddings, F.J. Yang, and M.N. Myers, "Theoretical and experimental characterization of flow field-flow fractionation," *Anal. Chem.*, vol. 48, pp. 1126-1132, 1976.

[115] J.C. Giddings, F.J. Yang, and M.N. Myers, "Flow field-flow-fractionation: a new method for separating, purifying, and characterizing the diffusivity of viruses," *J. Virol.*, vol. 21, pp. 131-138, 1977.

[116] J.C. Giddings, F.J. Yang, and M.N. Myers, "The flow field-flow fractionation channel as a versatile pressure dialysis and ultrafiltration cell," *Sep. Sci.*, vol. 12, pp. 499-510, 1977.

[117] F.J. Yang, M.N. Myers, and J.C. Giddings, "Peak shifts and distortion due to solute relaxation in flow field-flow fractionation," *Anal. Chem.*, vol. 49, pp. 659-662, 1977.

[118] J.C. Giddings, F.J. Yang, and M.N. Myers, "Flow field-flow fractionation as a methodology for protein separation and characterization," *Anal. Biochem.*, vol. 81, pp. 395-407, 1977.

[119] J.C. Giddings, G.C. Lin, and M.N. Myers, "Fractionation and size analysis of colloidal silica by flow field-flow fractionation," *J. Colloid Interface Sci.*, vol. 65, pp. 67-78, 1978.

[120] J.C. Giddings, G.C. Lin, and M.N. Myers, "Fractionation and size distribution of water soluble polymers by flow field-flow fractionation," *J. Liq. Chromatogr.*, vol. 1, pp. 1-20, 1978.

[121] J.C. Giddings, G.C. Lin, and M.N. Myers, "Fractionation and size distribution of water soluble polymers by flow field-flow fractionation," *J. Liq. Chromatogr.*, vol. 1, pp. 1-20, 1978.

[122] S. L. Brimhall, M. N. Myers, K. D. Caldwell, and J. C. Giddings, "Separation of polymers by flow field-flow fractionation," *J. Polym. Sci. Polym. Lett.*, Ed. 22, pp. 339-345, 1984.

[123] S.L. Brimhall, M.N. Myers, K.D. Caldwell, J.C. Giddings "Polymer characterization by flow field-flow fractionation." *Polym. Mater. Sci. Eng.*, vol. 50, pp. 48-52, 1984.

[124] K.-G. Wahlund, H. S. Winegarner, K. D. Caldwell, and J. C. Giddings, "Improved flow field-flow fractionation system applied to water soluble polymers: programming, outlet stream splitting, and flow optimization," *Anal. Chem.*, vol. 58, pp. 573-578, 1986.

[125] R. Beckett, Z. Jue, and J.C. Giddings, "Determination of molecular weight distributions of fulvic and humic acids using flow field-flow fractionation," *Environ. Sci. Technol.*, 21, 289-295, 1987.

[126] K.-G. Wahlund and J.C. Giddings, "Properties of an asymmetric flow field-flow fractionation channel having one permeable wall," *Anal. Chem.*, vol. 59, pp. 1332-1339, 1987.

[127] R. Beckett, J.C. Bigelow, J. Zhang, and J.C. Giddings, "Analysis of humic substances using flow field-flow fractionation," in *Influence of aquatic humic substances on fate and treatment of pollutants*, P. MacCarthy and I.H. Suffet, Eds., ACS Advances in Chemistry Series No. 219, ACS, Washington, D.C. 1988, Chapter 5.

[128] S.K. Ratanathanawongs, J.C. Giddings "Particle size characterization from 0.01 to 50 um by flow field-flow fractionation." *Polym. Mater. Sci. Eng.*, vol. 62, pp. 181-185, 1990.

[129] S. K. Ratanathanawongs, I. Lee, and J. C. Giddings, "Separation and characterization of 0.01-50 um particles using flow field-flow fractionation," in *Particle size distribution II*, T. Provder, Ed., ACS Symp. Series No. 472, American Chemical Society, Washington, DC, 1991, Chapter 15.

[130] M.-K. Liu, P. S. Williams, M. N. Myers, and J. C. Giddings, "Hydrodynamic relaxation in flow field-flow fractionation using both split and frit inlets," *Anal. Chem.*, vol. 63, pp. 2115-2122, 1991.

[131] J.C. Giddings, M.A. Benincasa, M.-K. Liu, P. Li "Separation of water-soluble synthetic and biological *Macromolecules* by flow field-flow fractionation." *Polym. Mater. Sci. Eng.*, vol. 65, pp. 21-23, 1991.

[132] S.K. Ratanathanawongs, J.C. Giddings "Particle size analysis using flow field-flow fractionation." *Polym. Mater. Sci. Eng.*, vol. 65, pp. 24-26, 1991.

[133] M. A. Benincasa and J. C. Giddings, "Separation and molecular weight distribution of anionic and cationic water soluble polymers by flow field-flow fractionation," *Anal. Chem.*, vol. 64, pp. 790-798, 1992.

[134] J. C. Giddings, M. A. Benincasa, M.-K. Liu, and P. Li, "Separation of water soluble synthetic and biological macromolecules by flow field-flow fractionation," *J. Liq. Chromatogr.*, vol. 15, pp. 1729-1747, 1992.

[135] S. K. Ratanathanawongs and J. C. Giddings, "Particle size analysis using flow field-flow fractionation," in *Chromatography of polymers: characterization by SEC and FFF*, T. Provder, Ed., ACS Symposium Series 521, American Chemical Society, Washington, DC, 1993, pp.13-20.

[136] M.-K. Liu and J. C. Giddings, "Separation and measurement of diffusion coefficients of linear and circular DNAs by flow field-flow fractionation," *Macromolecules*, vol. 26, pp. 3576-3588, 1993.

[137] M. H. Moon and J. C. Giddings, "Size distribution of liposomes by flow field-flow fractionation," *J. Pharm. Biomed. Anal.*, vol. 11, pp. 911-920, 1993.

[138] M.-K. Liu, P. Li, and J. C. Giddings, "Rapid protein separation and diffusion coefficient measurement by frit inlet flow field-flow fractionation," *Protein Sci.*, vol. 2, pp. 1520-1531, 1993.

[139] S.K. Ratanathawongs, J.C. Giddings "Characterization of core-shell carboxylated latex using sedimentation and flow field-flow fractionation," *Polym. Mater. Sci. Eng.*, vol. 70, pp. 26-27, 1993.

[140] S. K. Ratanathanawongs and J. C. Giddings, "Rapid size characterization of chromatographic silicas by flow field-flow fractionation," *Chromatographia*, vol. 38, pp. 545-554, 1994.

[141] A. M. Botana, S. K. Ratanathanawongs, and J. C. Giddings, "Field-programmed flow field-flow fractionation," *J. Microcol. Sep.*, vol. 7, pp. 395-402, 1995.

[142] P. Li and J. C. Giddings, "Isolation and measurement of colloids in human plasma by membrane-selective flow field-flow fractionation: lipoproteins and pharmaceutical colloids," *J. Pharm. Sci.*, vol. 85, pp. 895-898, 1996.

[143] S. Lee, S. P. Rao, M. H. Moon, and J. C. Giddings, "Determination of mean diameter and particle size distribution of acrylate latex using flow field-flow fractionation, photon correlation spectroscopy, and electron microscopy," *Anal. Chem.*, vol. 68, pp. 1545-1549, 1996.

[144] M.E. Miller, J.C. Giddings "Study of colloids by flow field-flow fractionation." *Polym. Mater. Sci. Eng.*, vol. 75, pp. 1-2, 1996.

[145] H. Lee, S. K. Ratanathanawongs Williams, J. C. Giddings, "Particle size analysis of dilute environmental colloids by flow field-flow fractionation using an opposed flow sample concentration technique," *Anal. Chem.*, vol. 70, pp. 2495-2503, 1998.

[146] J.C. Giddings, F.J.F. Yang, M.N. Myers, "Sedimentation field-flow fractionation," *Anal. Chem.*, vol. 46, pp. 1917-1924, 1974.

[147] F.J.F. Yang, M.N. Myers, and J.C. Giddings, "Programmed sedimentation field-flow fractionation," *Anal. Chem.*, vol. 46, pp. 1924-1930, 1974.

[148] J.C. Giddings, F.J.F. Yang, and M.N. Myers, "Application of sedimentation field-flow fractionation to biological particles: molecular weights and separation," *Sep. Sci.*, vol. 10, pp. 133-149, 1975.

[149] F.J. Yang, M.N. Myers, and J.C. Giddings, "High resolution particle separations by sedimentation field-flow fractionation," *J. Colloid Interface Sci.*, vol. 60, pp. 574-577, 1977.

[150] K.D. Caldwell, G. Karaiskakis, M.N. Myers, and J.C. Giddings, "Characterization of liposomes by sedimentation field-flow fractionation," *Colloids and Surfaces*, vol. 3, pp. 233-238, 1981.

[151] K.D. Caldwell, G. Karaiskakis, M.N. Myers, and J.C. Giddings, "Characterization of BSA microspheres by sedimentation field-flow fractionation," *J. Pharm. Sci.*, vol. 70, pp. 1350-1352, 1981.

[152] J.C. Giddings, G. Karaiskakis, and K.D. Caldwell, "Density and particle size of colloidal materials measured by carrier density variations in sedimentation field-flow fractionation," *Sep. Sci.*, vol. 16, pp. 607-618, 1981.

[153] G. Karaiskakis, M.N. Myers, K.D. Caldwell, and J.C. Giddings, "Verification of retention and zone spreading equations in sedimentation field-flow fractionation," *Anal. Chem.*, vol. 53, pp. 1314-1317, 1981.

[154] K.D. Caldwell, G. Karaiskakais, and J.C. Giddings, "Characterization of T4D virus by sedimentation field-flow fractionation," *J. Chromatogr.*, vol. 215, pp. 323-332, 1981.

[155] J.C. Giddings, G. Karaiskakis, and K.D. Caldwell, "Concentration and analysis of dilute colloidal samples by sedimentation FFF," *Sep. Sci.*, vol. 16, pp. 725-744, 1981.

[156] G. Karaiskakis, K.A. Graff, K.D. Caldwell, and J.C. Giddings, "Sedimentation field-flow fractionation of colloidal particles in river water," Intern. J. Environ. *Anal. Chem.*, vol. 12, pp. 1-15, 1982.

[157] J.C. Giddings, G. Karaiskakis, K.D. Caldwell, and M.N. Myers, "Colloid characterization by sedimentation field-flow fractionation. I. monodisperse populations," *J. Colloid Interface Sci.*, vol. 92, pp. 66-80, 1983.

[158] F.-S. Yang, K.D. Caldwell, and J.C. Giddings, "Colloid characterization by sedimentation field-flow fractionation. II. particle size distribution," *J. Colloid Interface Sci.*, vol. 92, pp. 81-91, 1983.

[159] F.-S. Yang, K.D. Caldwell, M.N. Myers, and J.C. Giddings, "Colloid characterization by sedimentation field-flow fractionation. III. emulsions," *J. Colloid Interface Sci.*, vol. 93, pp. 115-125, 1983.

[160] F.-S. Yang, K.D. Caldwell, J.C. Giddings, and L. Astle, "Stability of perfluorocarbon blood substitutes determined by sedimentation field-flow fractionation," *Anal. Biochem.*, vol. 138, pp. 488-494, 1984.

[161] K.D. Caldwell, B.J. Compton, J.C. Giddings, and R.J. Olson, "Sedimentation field-flow Fractionation: a method for studying particulates in cataractous lens," *Invest. Ophthalmol. Visual Sci.*, vol. 25, pp. 153-159, 1984.

[162] J. C. Giddings and F.-S. Yang, "Colloid characterization by sedimentation field-flow fractionation. IV. reinjection FFF for polydisperse systems," *J. Coll. Int. Sci.*,vol. 105, pp. 55-64, 1985.

[163] C. R. Yonker, K. D. Caldwell, J. C. Giddings, J. L. van Etten, "Physical characterization of PBCV virus by sedimentation FFF," *J. Virol. Methods*, vol. 11, pp. 145-160, 1985.

[164] J.C. Giddings, K.D. Caldwell, H.K. Jones, M.N. Myers "Determination of particle size distribution and complex colloids by sedimentation field-flow fractionation." *Polym. Mater. Sci. Eng.*, vol. 53, pp. 246-50, 1985.

[165] M. R. Schure, J.C. Giddings "Advances in the calculation of particle size distributions by sedimentation field-flow fractionation. *Polym. Mater. Sci. Eng.*, vol. 53, pp. 252-255, 1985.

[166] M.R. Schure, K.D. Caldwell, and J.C. Giddings, "Theory of sedimentation hyperlayer field-flow fractionation," *Anal. Chem.*, vol. 58, pp. 1509-1516, 1986.

[167] K. D. Caldwell, H. K. Jones, and J. C. Giddings, "Measurement of the size and density of colloidal particles by combining sedimentation field-flow fractionation and quasi-elastic light scattering," *Colloids Surf.*, vol. 18, pp. 123-131, 1986.

[168] J.C. Giddings, P.S. Williams, and R. Beckett, "Fractionating power in programmed field-flow fractionation: exponential sedimentation field decay," *Anal. Chem.*, vol. 59, pp. 28-37, 1987.

[169] H.K. Jones, K. Phelan, M.N. Myers, and J.C. Giddings, "Colloid characterization by sedimentation field-flow fractionation. V. split outlet system for complex colloids of mixed density," *J. Colloid Interface Sci.*, vol. 120, pp. 140-152, 1987.

[170] P.S. Williams, J.C. Giddings, and R. Beckett, "Fractionating power in sedimentation field-flow fractionation with linear and parabolic field decay programming," *J. Liq. Chromatogr.*, vol. 10, pp. 1961-1998, 1987.

[171] J. C. Giddings, K. D. Caldwell, and H. K. Jones, "Measuring particle size distribution of simple and complex colloids using sedimentation field-flow fractionation," in *Particle size distribution: assessment and characterization*, T. Provder, Ed., ACS Symposium Series No. 332, ACS, Washington, D.C. 1987, Chapter 15, pp 215-230.

[172] S.R. Springston, M.N. Myers, and J.C. Giddings, "Continuous particle fractionation based on gravitational sedimentation in split-flow thin cells," *Anal. Chem.*, vol. 59, pp. 344-350, 1987.

[173] R. Beckett, G. Nicholson, B.T. Hart, M. Hansen, and J.C. Giddings, "Separation and size characterization of colloidal particles in river water by sedimentation field-flow fractionation," *Wat. Res.*, vol. 22, pp. 1535-1545, 1988.

[174] S. Lee and J.C. Giddings, "Experimental observation of steric transition phenomena in sedimentation field-flow fractionation," *Anal. Chem.*, vol. 60, pp. 2328-2333, 1988.

[175] S. Lee, M.N. Myers, R. Beckett, and J.C. Giddings, "Particle separation and characterization by sedimentation/cyclical-field field-flow fractionation," *Anal. Chem.*, vol. 60, pp. 1129-1135, 1988.

[176] P.S. Williams, L. Kellner, R. Beckett, and J.C. Giddings, "Comparison of experimental and theoretical fractionating power for exponential field decay sedimentation field-flow fractionation," Analyst (London), vol. 113, pp. 1253-1259, 1988.

[177] H.K. Jones, B.N. Barman, and J.C. Giddings, "Resolution of colloidal latex aggregates by sedimentation field-flow fractionation," *J. Chromatogr.*, vol. 455, pp. 1-15, 1988.

[178] H.K. Jones and J.C. Giddings, "Separation and characterization of colloidal materials of variable particle size and composition by coupled column sedimentation field-flow fractionation," *Anal. Chem.*, vol. 61, pp. 741-745, 1989.

[179] M.E. Hansen, J.C. Giddings, and R. Beckett, "Colloid characterization by sedimentation FFF. VI. perturbations due to overloading and electrostatic repulsion," *J. Colloid Interface Sci.*, vol. 132, pp. 300-312, 1989.

[180] M.E. Hansen and J.C. Giddings, "Retention perturbations due to particle-wall interactions in sedimentation field-flow fractionation," *Anal. Chem.*, vol. 61, pp. 811-819, 1989.

[181] J.C. Giddings, B.N. Barman, and H. Li, "Colloid characterization by sedimentation field-flow fractionation. VII. colloidal aggregates," *J. Colloid Interface Sci.*, vol. 132, pp. 554-565, 1989.

[182] S. Lee, M.N. Myers, and J.C. Giddings, "Hydrodynamic relaxation using stopless flow injection in split inlet sedimentation field-flow fractionation," *Anal. Chem.*, vol. 61, pp. 2439-2444, 1989.

[183] M.R. Schure, B.N. Barman, and J.C. Giddings, "Deconvolution of nonequilibrium band broadening effects for accurate particle size distributions by sedimentation field-flow fractionation," *Anal. Chem.*, vol. 61, pp. 2735-2743, 1989.

[184] B.N. Barman, J.C. Giddings "Monitoring of colloidal aggregation by sedimentation field-flow fractionation." *Polym. Mat. Sci. Eng.*, vol. 62, pp. 186-90, 1990.

[185] B. N. Barman and J. C. Giddings, "Overview of colloidal aggregation by sedimentation field-flow fractionation," in *Particle size distribution II: assessment and characterization*, T. Provder, Ed., ACS Symp. Series No. 472, American Chemical Society, Washington, DC, 1991, Chapter 14.

[186] J. C. Giddings, M. N. Myers, M. H. Moon, and B. N. Barman, "Particle separation and size characterization by sedimentation field-flow fractionation," in *Particle size distribution*, T. Provder, Ed., ACS Symp. Series No. 472, American Chemical Society, Washington, DC, 1991, Chapter 13.

[187] J.C. Giddings, M. H. Moon, P. S. Williams, and M. N. Myers, "Particle size distribution by sedimentation/steric FFF: development of a calibration procedure based on density compensation," *Anal. Chem.*, 63, 1366-1372, 1991.

[188] R. Beckett, J. Ho, Y. Jiang, and J. C. Giddings, "Measurement of mass and thickness of adsorbed films on colloidal particles by sedimentation field-flow fractionation," *Langmuir*, vol. 7, pp. 2040-2047, 1991.

[189] J. C. Giddings and M. H. Moon, "Measurement of particle density, porosity, and size distributions by sedimentation/steric field-flow fractionation. application to chromatographic supports," *Anal. Chem.*, vol. 63, pp. 2869-2877, 1991.

[190] B.N. Barman, J.C. Giddings "Characterization of latex aggregates by sedimentation field-flow fractionation. *Polym. Mater. Sci. Eng.*, vol. 65, pp. 61-62, 1991.

[191] Y. Gao, M.N. Myers, B.N. Barman, and J.C. Giddings, "Continuous fractionation of glass microspheres by gravitational sedimentation in split-flow thin (SPLITT) cells," Part. Sci. Technol., vol. 9, pp. 105-118, 1991.

[192] P. S. Williams, T. Koch, and J. C. Giddings, "Characterization of near-wall hydrodynamic lift forces using sedimentation field-flow fractionation," *Chem. Eng. Commun.*, vol. 111, pp. 121-147, 1992.

[193] P. S. Williams, M. H. Moon, J. C. Giddings, "Fast separation and characterization of micron size particles by sedimentation/steric field-flow fractionation: role of lift forces," in *Particle size analysis*, N. G. Stanley-Wood and R. W. Lines, Eds., Royal Society of Chemistry, Cambridge, UK, 1992.

[194] B. N. Barman and J. C. Giddings, "Kinetics and properties of colloidal latex aggregates measured by sedimentation field-flow fractionation," *Langmuir*, vol. 8, pp. 51-58, 1992.

[195] M. H. Moon and J. C. Giddings, "Extension of sedimentation/steric field-flow fractionation into submicron range: size analysis of 0.2-15 μm metal particles," *Anal. Chem.*, vol. 64, pp. 3029-3037, 1992.

[196] B. N. Barman and J. C. Giddings, "Separation and characterization of polymeric latex beads and aggregates by sedimentation field-flow fractionation," in *Chromatography of polymers: characterization by SEC and FFF*, T. Provder, Ed., ACS Symposium Series 521, American Chemical Society, Washington, DC, 1993, pp. 30-46.

[197] M. H. Moon and J. C. Giddings, "Rapid separation and measurement of particle size distribution of starch granules by sedimentation/steric field-flow fractionation," J. Food Sci., vol. 58, pp. 1166-1171, 1993.

[198] J. C. Giddings and P. S. Williams, "Multifaceted analysis of 0.01 to 100 um particles by sedimentation field-flow fractionation," *Am. Lab.*, vol. 25, pp. 88-95, 1993.

[199] R. Beckett, Y. Jiang, G. Liu, M. H. Moon, J. C. Giddings, "Separation and behavior of nonspherical particles in sedimentation/steric field-flow fractionation," Part. Sci. Technol., vol. 12, pp. 89-113, 1994.

[200] J. C. Giddings, Y. Xu, M. N. Myers, "Enhancement of performance in sedimentation field-flow fractionation by temperature elevation," *Anal. Chem.*, vol. 66, pp. 3047-3053, 1994.

[201] . J. C. Giddings and J. Ho, "Accurate measurement of density of colloidal latex particles by sedimentation field-flow fractionation," *Langmuir*, vol. 11, pp. 2399-2404, 1995.

[202] Y. Jiang, J. C. Giddings, R. Beckett, "Direct measurement of protein adsorption on latex particles by sedimentation field-flow fractionation," in *Proteins at interfaces II, T. A. Horbett and J. L. Brash, Eds.*, ACS Symposium Series No. 602, American Chemical Society, Washington, DC, 1995, Chapter 29, pp. 405-419.

[203] B. N. Barman and J. C. Giddings, "Separation of colloidal latex aggregates by cluster mass and shape using sedimentation field-flow fractionation with steric perturbations," *Anal. Chem.*, vol. 67, pp. 3861-3865, 1995.

[204] P. S. Williams, M. H. Moon, Y. Xu, and J. C. Giddings, "Effect of viscosity on retention time and hydrodynamic lift forces in sedimentation/steric field-flow fractionation," *Chem. Eng. Sci.*, vol. 51, pp. 4477-4488, 1996.

[205] M. H. Moon and J. C. Giddings, "Upper particle size limit for high-speed analysis by sedimentation/steric field-flow fractionation (FFF) in thin channels," *Ind. Eng. Chem. Res.*, vol. 35, pp. 1072-1077, 1996.

[206] P. S. Williams, Y. Xu, P. Reschiglian, and J. C. Giddings, "Colloid characterization by sedimentation field-flow fractionation: correction for particle-wall interaction," *Anal. Chem.*, vol. 69, pp. 349-360, 1997.

[207] R. Beckett, D. Murphy, S. Tadjiki, D. J. Chittleborough, and J. C. Giddings, "Determination of thickness, aspect ratio and size distributions for platey particles using sedimentation field-flow fractionation and electron microscopy," *Colloids Surf. A: Physicochem. Eng. Aspects*, vol. 120, pp. 17-26, 1997.

[208] T. M. Vickrey and J. A. Garcia-Ramirez, "Magnetic field-flow fractionation: theoretical basis," *Sep. Sci.*, vol. 15, pp. 1297-1304, 1980.

[209] J. Gorse, T.C. Schunk, M.F. Burke "The study of liquid suspensions of iron oxide particles with a magnetic field-flow fractionation device." *Sep. Sci.*, vol. 13, pp. 1073-1085, 1984-1985.

[210] T. C. Schunk, J. Gorse, and M. F. Burke, "Parameters affecting magnetic field-flow fractionation of metal oxide particles," *Sep. Sci.*, vol. 19, pp. 653, 1984.

[211] S.N. Semenov, A.A. Kuznetsov "Flow fractionation in a transverse high-gradient magnetic field." *Zh. Fiz. Khim.*, vol. 60, pp. 424-428, 1986.

[212] S.N. Semenov "Flow fractionation in a strong transverse magnetic field." *Zh. Fiz. Khim.*, vol. 60, pp. 1231-1233, 1986.

[213] S. Mori, "Magnetic field-flow fractionation using capillary tubing," *Chromatographia*, vol. 21, pp. 642, 1986.

[214] S. R. Springston, M. N. Myers, and J. C. Giddings, "Continuous particle fractionation based on gravitational sedimentation in split-flow thin cells," *Anal. Che*m., vol. 59, pp. 344-350, 1987.

[215] Y. Gao, M. N. Myers, B. N. Barman, and J. C. Giddings, "Continuous fractionation of glass microspheres by gravitational sedimentation in split-flow thin (SPLITT) cells," *Part. Sci. Techno*l., vol. 9, pp. 105-118, 1991.

[216] H. C. Berg, E. M. Purcell, and W. W. Stewart, "A method for separating according to mass a mixture of m*acromolecules* or small particles suspended in a fluid, II. experiments in a gravitational field," *Proc. Nat. Acad, Sc*i., vol. 58, pp. 1286-1291, 1967.

[217] P. J. P. Cardot, J. Gerota, and M. Martin, "Separation of living red blood cells by gravitational field-flow fractionation," *J. Chromatog*r., vol. 568, pp. 93, 1991.

[218] A. Merino, C. Bories, J.-C. Gantier, and P.J.P. Cardot, "Isolation of microfilariae from blood by gravitational field-flow fractionation," *J. Chromatog*r., vol. 572, pp. 91-301, 1991.

[219] E. Urbenkov, A. Vacek, N. Novekov, F. Matulek, and J. Chmelik, "Investigation of red blood cell fractionation by gravitational field-flow fractionation," *J. Chromatog*r., vol. 583, pp. 27-34, 1992.

[220] J. Pazourek and J. Chmelik, "Optimization of the separation of micron-sized latex particles by gravitational field-flow fractionation," *Chromatographi*a, vol. 35, pp. 591-596, 1993.

[221] E. Urbankova, A. Vacek, J. Chmelik "Micropreparation of hemopoietic stemcells from the mouse bone marrow suspension by gravitational field-flow fractionation," *J. Chromatogr. B*, vol. 687, pp. 449-452, 1996.

[222] J. M. Davis and J. C. Giddings, "Feasibility study of dielectrical field-flow fractionation," *Sep. Sci. Techno*l., vol. 21, pp. 969-989, 1986.

[223] Y. Huang, X.-B. Wang, F. F. Becker, P. R. C. Gascoyne "Introducing dielectrophoresis as a new force field for field-flow fractionation," *Biophys.* J., vol. 73, pp. 1118-1129, 1997.

[224] G. H. Markx, R. Pethig, J. Rousselet, "The dielectrophoretic levitation of latex beads, with reference to field-flow fractionation." *J. Phys. D: Appl. Phy*s., vol. 30, pp. 2470-2477, 1997.

[225] X.-B.Wang, J. Vykoukal, F. F. Becker, and P. R. C. Gascoyne, "Separation of polystyrene microbeads using dielectrophoretic/gravitational field-flow-fractionation," *Biophys.* J., vol. 74, pp. 2689-2701, 1998.

[226] J. C. Giddings, “Factors influencing accuracy of colloidal and macromolecular properties measured by FFF,” *Anal. Chem.*, vol. 69, pp. 552-557, 1997.

[227] J. C. Giddings, Y. H. Yoon, K. D. Caldwell, M. N. Myers, and M. E. Hovingh, “Nonequilibrium plate height for field-flow fractionation in ideal parallel plate columns,” *Separation Science*, vol. 10, pp. 447-460, 1975.

[228] J. C. Giddings, “Nonequilibrium theory of field-flow fractionation,” *The Journal of Chemical Physics*, vol. 49, pp. 81-86, 1968.

[229] L. K. Smith, M. N. Myers, J. C. Giddings, “Peak broadening factors in thermal field-flow fractionation,” *Anal. Chem.*, vol. 49, pp. 1750-1756, 1977.

[230] B. K. Gale, K. D. Caldwell, and A. B. Frazier, "Electrical conductivity particle detector for use in biological and chemical micro-analysis systems," in *Proc. of SPIE: Micro FluidicDevices and Systems,* 1998, pp. 230-242.

[231] A. S. Said, *Theory and mathematics of chromatography*. Heidelberg, Germany: Dr. Alfred Huethig Publishers, 1981.

[232] K. Yosioka and Y. Kawasima, "Acoustic radiation pressure on a compressible sphere," *Acustica*, 5, 167-173, 1955.

[233] Kino, G.S. "Acoustic Waves: Devices, imaging, and analog signal processing," *Prentice Hall, Inc.,* New Jersey, pp. 44-45.

[234] Perry's Chemical Engineering Handbook, 5th ed. McGraw-Hill Companies, New York, NY, sec.17, pp. 45-47, 1965.

[235] A. C. van Asten, G. Stegeman, W. Th. Kok, R. Tijssen, H. Poppe, "Separation speed in thermal FFF," *Anal. Chem.*, vol. 66, pp. 3073-3080, 1994.

[236] W. Cao, P. S. Williams, M. N. Myers, J. C. Giddings, "Thermal field-flow fractionation universal calibration: extension for consideration of variation of cold wall temperature," *Anal. Chem.*, vol. 71, pp. 1597-1609, 1999.

[237] ??? Secondary Dispersion Effects in Thin Channels, reviewed for Journal of Chromatogrpahy A.

[238] S. K. Mohanty, M. R. Graff, S. K. Ravula, A. Han, and A. B. Frazier, "A micro stenciling process for wafer scale metallization of plastic substrates", *Micro Total Analysis Systems 2001*, J. M. Ramsey and A. van den Berg (eds.), pp. 387-388.

[239] B.H. Jo, L.M. Van Lerberghe, K.M. Motsegood, and D.J. Beebe, "Three-Dimensional Micro-Channel Fabrication in Polydimethylsiloxane (PDMS) Elastomer," *JMEMS*, 9, 1, March 2000, pp. 76-81.

[240] J. C. Giddings, "Parameters for optimum separation in field-flow fractionation," *Sep. Sci.*, vol. 8, pp. 567-575, 1973.

[241] G. T. A. Kovacs, *Micromachined Transducers Sourcebo*ok. New York: McGraw Hill, 1998, pp. 581-585.

[242] B. K. Gale, K. D. Caldwell, and A. B. Frazier, "Characterization of a micromachined electrical field-flow fractionation system" in *Proc. IEEE 1998 Solid-State Sensor and Actuator Workshop*, 1998, pp. 342-345.

[243] Percin, G., Leland Standford Junior University, 1997.

[244] J.C. Giddings, “Parameters for optimum separations in field-flow fractionation,” *Sep. Sci.*, vol. 8, 1973, pp. 567-575.